GEOLOGICA ULTRAIECTINA

Mededelingen van de
Faculteit Geowetenschappen
Universiteit Utrecht

No. 290

Structure and properties of fluid-filled grain boundaries under stress in geological materials

Reinier van Noort

The research described in this thesis was carried out under the program “Earth materials: properties and processes” of the Vening Meinesz Research School of Geodynamics (VMSG). The project was funded by the Netherlands Organisation for Scientific Research (NWO), grant number 814.01.001.

The research was carried out at:
Experimental Rock Deformation (HPT) Laboratory
Faculty of Geosciences, Department of Earth Sciences
Utrecht University
Budapestlaan 4
3584 CD Utrecht
The Netherlands

www.geo.uu.nl

ISBN: 978-90-5744-156-1

Structure and properties of fluid-filled grain boundaries under stress in geological materials

Structuur en eigenschappen van met vloeistof gevulde korrelcontacten onder mechanische spanning in geologische materialen

(met een samenvatting in het Nederlands)

Proefschrift

ter verkrijging van de graad van doctor aan de Universiteit Utrecht op gezag van de rector magnificus, prof.dr. J.C. Stoof, ingevolge het besluit van het college voor promoties in het openbaar te verdedigen op woensdag 4 juni 2008 des middags te 12.45 uur

door

Reinier van Noort

geboren op 7 augustus 1980, te Ede

Promotor: Prof.dr. C.J. Spiers

Co-promotor: Dr. C.J. Peach

No sound was there in that high presence chamber in Galing till in a minute's space the serving man returned with startled countenance, and, bowing before Lord Juss, said, "Lord, it is an Ambassador from Witchland and his train. He craveth present audience."

E. R. Eddison – The Worm Ouroboros (1922).

Members of the dissertation committee:

Prof. Dr. P.S.J. Van Cappellen
Department of Earth Sciences
Utrecht University

Dr. M.R. Drury
Department of Earth Sciences
Utrecht University

Prof. Dr. S. Nakashima
Department of Earth and Space Science
Osaka University

Prof. Dr. A. Putnis
Institut für Mineralogie
Westfälische Wilhelms-Universität Münster

Prof. Dr. F. Renard
Laboratoire de Géodynamique des Chaînes Alpines
Université Joseph Fourier, Grenoble
Physics of Geological Processes
University of Oslo

Table of Contents

Summary

Wetted grain boundaries in geological materials are of major importance in controlling the rheological behaviour of rock systems in a wide range of crustal environments. In particular, such grain boundaries provide fast diffusion pathways that enable the process of dissolution-precipitation creep, or intergranular pressure solution. This is an important mechanism of compaction of sedimentary rocks, of sealing, strength recovery and creep in active fault zones, and of bulk rock deformation under diagenetic, greenschist and blueschist metamorphic conditions. Gaining the capability to reliably model phenomena such as porosity evolution and hydrocarbon migration/trapping in sedimentary basins, the behaviour of earthquake faults, and crustal deformation in general thus requires a quantitative understanding of the kinetics of pressure solution and of how the structure and properties of fluid-filled grain boundaries control the rate of the process. However, despite much interest, these properties remain poorly constrained.

The work presented in this thesis concentrates on investigating the structure of fluid-filled grain boundaries in geological materials undergoing intergranular pressure solution, and on investigating the influence of this structure on pressure solution kinetics. This is achieved through the following main lines of attack:

- Experiments addressing the on the electrical impedance of single halite contacts undergoing pressure solution at room temperature and atmospheric pressure,
- Experiments on the impedance of single silica contacts undergoing pressure solution under hydrothermal conditions,
- Isostatic compaction experiments on granular quartz aggregates under hydrothermal conditions, with special focus on the grain boundary structures formed,
- Theoretical modeling of the influence of an island-channel grain boundary structure and internal elastic/plastic deformation on the "rate constant" for grain boundary dissolution controlled pressure solution.

Chapter 1 introduces the scope of the thesis. It opens with a brief discussion of the state of current knowledge on pressure solution in rock materials. An overview is then presented of what is currently known of the structure and physical properties of stressed grain boundaries from theoretical models (thermodynamics of surfaces) and experimental observations. From the framework thus created, outstanding questions are identified and the aims of the present work are defined.

Chapter 2 addresses the effects of crystallographic orientation on the structure and diffusive properties of grain contact surfaces and/or boundaries undergoing active pressure solution. To gain insight into this issue, electrical impedance/resistivity measurements were made on single halite-glass contacts using different halite crystal orientations and on [100] halite-halite contacts with different twist-misorientations. The contacts were loaded with stresses up to 15MPa in the presence of brine. The impedance measurements yielded the diffusive properties of the fluid-filled grain boundaries. In the halite-glass experiments, pressure solution of the halite clearly occurred, and impedance measurements yielded contact diffusivity product ($Z = D\delta_{av}C^*$) values of 5×10^{-19} to 1.3×10^{-17}m^{3}s^{-1}. The value of this grain boundary transport property was clearly influenced by contact orientation. Post-mortem

observations showed a rough grain boundary microstructure or texture that was controlled by crystallographic orientation, and it is inferred that this texture controls both the internal grain boundary structure and diffusive properties during pressure solution. In the halite-halite contact experiments, contact overgrowth by neck-growth was observed, proceeding at a higher rate for low contact misorientation than for high contact misorientation. The results imply that pressure solution may lead to the formation of a lattice-preferred orientation in rocks, as certain contacts will allow faster dissolution and diffusion than others, whereas in yet other contacts neck growth will occur. The results also imply that, partly due to the absence of neck growth, at lower stresses polymineralic rocks may deform faster by pressure solution than monomineralic rocks. Hence, care should be taken when applying data obtained from experiments on contacts between two dissimilar materials to contacts between two similar materials.

Whereas it is widely accepted that the structure of a grain boundary undergoing pressure solution can have a strong influence on the rate of diffusive transport in the grain boundary and hence on the pressure solution creep rate, the influence of grain boundary structure on internal grain boundary dissolution rates has rarely been considered. **Chapter 3** describes a model that investigates the influence of an island-channel grain boundary structure on the kinetics of dissolution controlled pressure solution for a purely elastic material. The model is derived from an approach based on internal grain boundary mass, energy and entropy balances, and enables the phenomenological rate coefficient for dissolution controlled pressure solution to be written in terms of the conventional free face dissolution rate constant. Using quartz as an example, the model described predicts that during dissolution-controlled pressure solution, average dissolution rates in a rough grain boundary (island-channel network) are slowed down by up to 13% compared to dissolution in a flat grain boundary containing a thin adsorbed fluid film, for example. An additional model is described in Chapter 3 that provides a criterion or "yield stress" for pressure solution, below which the process is prevented by surface energy driven grain boundary healing (progressive reduction of the contact area filled by connected fluid). This "yield stress criterion" for pressure solution offers a possible explanation for the cessation of pressure solution at low effective stresses and porosities, in nature and experiment. Using this "yield stress criterion" for pressure solution, limiting porosity depth curves are predicted for sandstones compacting by pressure solution, which show favorable agreement with porosity-depth data for quartz sandstones.

In **Chapter 4**, the grain boundary dissolution model described in Chapter 3 is extended to include the dissipation of energy by microscale plasticity in an island-channel structured grain boundary undergoing pressure solution. Simplified models are derived for the effects of plastic deformation on the rate constant for grain boundary dissolution, assuming either work hardening flow or time-dependent creep of highly stressed grain boundary islands. This model is then applied to quartz. It predicts that microscale plasticity at grain boundary islands can considerably slow down pressure solution in quartz. Though highly speculative at this stage, this effect may help explain the discrepancies between experimentally observed pressure solution rates for quartz and rates predicted assuming that grain boundary dissolution is governed by the conventional free face dissolution rate constant. When applied to pressure solution creep of sandstones or fault rocks in nature, our model predicts that grain boundary plastic deformation is probably not a significant effect at depths less than ~9-10km.

Summary

Whereas the preceding chapters focused on the properties of grain boundaries in halite and on theoretical analyses of grain boundary properties, **Chapter 5** concentrates on investigating the structure and diffusive properties of grain boundaries in silicate materials undergoing pressure solution. To achieve this, electrical impedance spectroscopy measurements were performed under hydrothermal conditions on single silica-glass–silica-glass and silica-glass–quartz contacts undergoing pressure solution. From these measurements, estimates of the average grain boundary fluid film thickness (δ_{av}) and of the average grain boundary diffusivity product ($Z = D\delta_{av}C^*$) for silica transport were made, with mean values of 380±140nm and $6.3\pm1.4\times10^{-18}$m^{3}s^{-1}, respectively. However, the average values for δ_{av} and Z obtained were likely influenced by cracking and irregular dissolution of the dissolving contact surfaces, and do not represent uniformly wetted grain boundary properties. Post-mortem SEM observations indicate that the contact surfaces established during pressure solution were internally rough with a (sub)micrometer amplitude. Taken together, our data support the notion that during pressure solution of quartz, grain boundary diffusion is relatively rapid, and that interface processes (dissolution and precipitation) are more likely to be rate limiting than diffusion in nature and experiment

Chapter 6 discusses isostatic compaction experiments performed on granular quartz under hydrothermal conditions (3-129μm initial grain size, 300-600°C, 200MPa fluid pressure, 25-100MPa effective pressure). Electron Backscatter Diffraction (EBSD) analysis was performed on one compacted sample, to detect if plastic deformation took place in the grains at high stress contact points. Single crystal quartz discs and mica plates were added to some samples to act as reference surfaces for studying contact structures formed during hydrothermal compaction. It is inferred from microstructural observations and mechanical data that whereas microcracking controlled pre-compaction at room temperature, the main compaction mechanism during hydrothermal isostatic compaction was pressure solution, though a limited effect of microcracking could not be excluded entirely. Dissolution was most likely the rate controlling process for pressure solution. Compaction rates depended linearly on the inverse of grain size (grain size coefficient of –0.97) and showed an apparent power law dependence on stress, with a coefficient of 3.4. The apparent activation energy for compaction was 105kJmol^{-1}. The EBSD analysis performed showed evidence limited plastic deformation at highly stressed grain contact points. The contact study performed using quartz single crystal discs or mica plates as reference surfaces showed that during hydrothermal compaction grain contacts were rough, with a micrometer scale island-channel type grain boundary structure. Many contacts also showed grain boundary microcracking. It is inferred that microcracking is an important mechanism for creating and maintaining contact roughness during quartz pressure solution. Extrapolation of our experimental compaction rates to natural conditions suggests that during burial and diagenesis of a sandstone, pressure solution starts to operate at depths of about ~1.5-2km, and may be the dominant compaction mechanism at depths greater than ~2.5-3km. This extrapolation gives good agreement with porosity-depth trends reported for natural, arenitic sandstones.

Finally, **Chapter 7** summarizes the main conclusions of this thesis, and documents suggestions for future work.

Summary

1. Introduction

1.1 Scope and motivation of the present study

The structure and physical properties of fluid-filled grain boundaries in geological materials are of major importance in controlling the rheological behaviour of wet rock systems in a wide range of crustal environments. In particular, wet grain boundaries provide fast diffusion pathways, and enable the process of dissolution-precipitation creep, or intergranular pressure solution (e.g., Weyl, 1959; Paterson, 1973, 1995; Rutter, 1976, 1983; Robin, 1978; Tada and Siever, 1989; Lehner, 1990, 1995). This is an important mechanism of compaction of sedimentary rocks (e.g., Houseknecht, 1988; Becker, 1995; Wahab, 1998), of sealing, strength recovery and creep in active fault zones (e.g., Angevine et al., 1982; Sleep and Blanpied, 1992, 1994; Karner et al., 1997; Renard et al., 2000; Bos and Spiers, 2002a, b; Yasuhara et al., 2005) and of bulk rock deformation under diagenetic, greenschist and blueschist metamorphic conditions (e.g., Elliot, 1973; Schwarz and Stöckhert, 1996; Wintsch and Yi, 2002; Lagoeiro and Fueten, 2008). Pressure solution is also likely to play a key role in controlling post-seismic stress relaxation and redistribution phenomena (Rutter and Mainprice, 1978; Renard et al., 2000; Bos and Spiers, 2002b).

In the context of both hydrocarbons exploration and geodynamics research, there is accordingly much interest in quantifying the kinetics of pressure solution and in understanding how the structure and properties of wetted grain boundaries control the rate of the process. These issues, notably the grain boundary structure and the properties of fluid-filled grain boundaries have been the topic of much discussion over the last few decades. Suggested structures vary from thin (~1nm) adsorbed films (Weyl, 1959; Rutter, 1976, 1983; Hickman and Evans, 1991, 1992, 1995; Renard and Ortoleva, 1997; Renard et al., 1997), to thin films short-circuited by fluid inclusions, channels or crack arrays (Gratz, 1991; Den Brok, 1998; Renard et al., 1999), to dynamically wetted island-channel networks (Elliott, 1973; Raj, 1982; Lehner, 1990; Schutjens and Spiers, 1999; Ghoussoub and Leroy, 2001). Recent experimental research has investigated both the structure and diffusive properties of load-bearing, fluid-filled grain boundaries in halite (De Meer et al., 2002, 2005), mica (Alcantar et al., 2003; Anzalone et al., 2006), and quartz (Meyer et al., 2006) at room temperature and atmospheric pressure. However, many important questions remain unanswered, and for most crustal rocks reliable, verified constitutive equations for creep by pressure solution are still lacking.

This thesis reports the results of a series of experiments and modeling exercises, aimed at exploring some of the outstanding questions about grain boundary structures and properties during pressure solution, and their influence on pressure solution kinetics. Experiments were done to investigate the structures and diffusive properties of pressure dissolving grain boundaries, and the effects of these on pressure solution creep rates, in halite at room temperature, and in silica glass and quartz at high temperatures and pressures, up to 500°C and 200MPa fluid pressure. Experimental techniques employed ranged from electrical impedance spectroscopy performed on pressure-dissolving mineral interfaces (halite, silica

glass, quartz), to compaction creep experiments performed on quartz sands, coupled with Electron Backscatter Diffraction (EBSD) to investigate grain contact plasticity. The modeling work reported in this thesis explores the influence that grain boundary structure, roughness, and internal elastic and plastic deformation have on dissolution controlled pressure solution rates, and is applied specifically to quartz.

1.2 Pressure solution creep in rock materials

1.2.1 The process and controlling kinetic factors

That mechanical forces or stresses can drive chemical reactions has long been known in geology (Sorby, 1863). One example of such interactions is the enhancement of mineral solubility at grain contacts under compressive stress, which, in the presence of a fluid phase that can penetrate grain boundaries, can result in the transport of material from high to low stress interfaces, causing creep (Sorby, 1908; Paterson, 1973; Durney, 1976; Robin, 1978; Lehner, 1990, 1995; Heidug, 1991). This is the deformation mechanism now known as dissolution-precipitation creep, or intergranular pressure solution. Intergranular pressure solution has long been recognised, from spectacular indentations and overgrowth microstructures as a mechanism for the compaction of granular silici-clastic and carbonate rocks (e.g., Weyl, 1959; Houseknecht, 1988; Tada and Siever, 1989; Becker, 1995; Wahab, 1998), and it has also been recognised as a source of diagenetic cement in sedimentary rocks (e.g., Houseknecht, 1988; Dewers and Ortoleva, 1990; Čyžienė et al., 2006). However, intergranular pressure solution is also a principal mechanism of bulk deformation of wet crustal rocks, controlling crustal rheology under a wide range of conditions varying from diagenetic to blueschist facies metamorphic where it can lead to mass transfer and slow ductile creep (Elliot, 1973; Rutter, 1976, 1983; Wright and Platt, 1982; Green, 1984; Tada and Siever, 1989; Schwarz and Stöckhert, 1996; Wintsch and Yi, 2002; Kawabata et al., 2007). Furthermore, it is an important mechanism controlling the creep and healing behaviour of wet active fault zones in the upper to middle crust (Hickman et al., 1995). During interseismic periods for example, intergranular pressure solution may result in the compaction of fault gouges, and in the growth and welding of grain contacts in fault gouges (e.g., Yasuhara et al., 2005; Tenthorey and Cox, 2006). This time-dependent fault strengthening, or fault healing, is believed to be important in determining post-seismic fault behaviour such as re-strengthening and seismic recurrence intervals (Angevine et al., 1982; Bos and Spiers, 2002b). Compaction, by reducing gouge porosity and permeability, may also lead to the pressurisation of pore water in the fault gouge, allowing failure at lower shear stresses, and hence weakening the fault (e.g., Sleep and Blanpied, 1992, 1994; Sleep, 1995; Lockner and Evans, 1995). Finally, pressure solution along laterally more extensive surfaces can lead to the formation of dissolution seams and stylolites (e.g., Sorby, 1908; Weyl, 1959; Heald, 1959; Gratier et al., 2005).

In a chemically closed system (i.e., a system with no long-range transport of dissolved matter), the mechanism of pressure solution consists of three processes operating in series.

The first is the dissolution of highly stressed solid material into the solvent. This can, depending on the structure of the grain boundary, occur either inside the grain boundaries by normal stress driven dissolution into an adsorbed thin fluid film (e.g., Weyl, 1959; Rutter, 1976, 1983), or at the margins of micro-scale load-bearing contact points or islands, within the grain boundaries, driven by elastic (and plastic) strain energy stored in the stressed solid (e.g., Tada et al., 1987; Lehner, 1990, 1995). Subsequently, the dissolved material is transported out of and away from the grain boundary by diffusion through the fluid phase (Rutter, 1976, 1983; De Meer et al., 2002, 2005; Alcantar et al., 2003), and the dissolved solid is deposited at grain boundary interfaces under low normal stress, or on pore walls at fluid pressure. As dissolution, diffusion and precipitation take place in series, the slowest of these processes will control the overall rate of pressure solution. In the case of an open system, dissolved material can also be transported into or out of the system by fluid flow and/or long-range diffusion through the pore fluid (Lehner, 1995; Gundersen et al., 2002). Under these conditions, dissolution, diffusion or the rate of mass removal from the system can control the rate of deformation (Lehner, 1995; Gundersen et al., 2002). Aside from the grain boundary diffusional mechanism described above, an undercutting mechanism, where dissolution only occurs on the edge of a pressure dissolving contact has also been proposed (e.g., Weyl, 1959; Tada and Siever, 1986). However, the prevalence of well-developed grain indentation and truncation microstructures in natural rocks suggests that grain boundary dissolution/diffusion creep mechanisms are the most important (e.g. see Tada et al., 1987) as an independent deformation mechanism and as a process coupled with phenomena such as grain boundary microcracking (e.g., Gratz, 1991; Dickinson and Milliken, 1995; Gratier et al., 1999; Chester et al., 2004; Chester et al., 2007).

1.2.2 Theoretical rate model for pressure solution

Simple theoretical equations for the creep rate due to grain boundary diffusional pressure solution can be derived using a variety of approaches, most recently based on non-equilibrium thermodynamic principles (e.g., Lehner, 1990). Numerous authors have derived such theoretical rate laws, and all have come to essentially the same result (Rutter, 1976; Raj, 1982; Lehner, 1990; Spiers and Schutjens, 1990; Shimizu, 1995). For axi-symmetric deformation of a dense material, for example, this is written:

$$\dot{\varepsilon} = \frac{G\kappa(T)}{d^m}\frac{(\sigma_1 - \sigma_3)\Omega_s}{RT} \tag{1.1}$$

Here, $\dot{\varepsilon}$ is the axial strain rate (s^{-1}), G is a geometric constant, d is grain size (m), $\sigma_1 - \sigma_3$ is the applied differential stress (Pa), Ω_s is the molar volume of the solid (m^3mol^{-1}), R is the gas constant ($Jmol^{-1}K^{-1}$), and T absolute temperature (K). For the special case of compaction of a regular pack of spherical grains, in both uniaxial and isostatic compaction, equation (1.1)

becomes:

$$\dot{\varepsilon} = \frac{G\kappa(T)}{d^m}\frac{\sigma_e \Omega_s}{RT} f(\phi) \tag{1.2}$$

In this equation, $\dot{\varepsilon}$ is the volumetric strain rate (s^{-1}), G is a geometric constant dependent on grain packing, $f(\phi)$ is a dimensionless function of porosity (ϕ) accounting for porosity dependent changes in grain contact area and pore wall area, and σ_e is the effective stress or effective isostatic pressure (Pa).

The "rate constant" $\kappa(T)$ in the above equations is the thermally activated rate coefficient of the rate controlling process (i.e., dissolution, diffusion or precipitation). For dissolution controlled pressure solution, this rate constant is the macroscopic rate coefficient for dissolution inside a grain boundary (I^*), which includes the effects of grain boundary roughness, and any processes operating in the grain boundary solid before it is dissolved (Lehner, 1990). When diffusion is the rate controlling mechanism, the rate coefficient $\kappa(T)$ is equal to $Z = D\delta_{av}S/\tau$, the grain boundary diffusivity product, with the solute diffusion coefficient in bulk fluid given by D, the average grain boundary width given by δ_{av}, the solute solubility in the grain boundary fluid given by S, and with τ giving the diffusion pathway tortuosity (usually assumed equal to 1 and neglected). Finally, for precipitation controlled pressure solution, $\kappa(T)$ is I_p, the rate coefficient for precipitation at free pore walls ($I_p = \kappa_+ \Omega_s$ where κ_+ is the geochemical rate coefficient for precipitation) and/or grain boundaries under low normal stress. The value of the grain size coefficient m is 1 for dissolution or precipitation controlled pressure solution, and 3 for diffusion controlled pressure solution. The above equations are based on an assumption ($e^x - 1 = x$), which is only valid for low stress. For higher stresses, $\sigma_e \Omega_s$ in equations (1.1) and (1.2) must be replaced by $\left[\exp\left(B\sigma_e \Omega_s / RT\right) - 1\right]$, where B accounts for stress concentrations at grain contacts in a porous aggregate (Niemeijer et al., 2002).

1.2.3 Previous experimental work on polycrystalline samples

Because of the importance of pressure solution for the rheology of the Earth's crust, a large amount of experimental work has been done investigating the kinetics and processes of pressure solution. Over the last few decades, experiments have been performed on halite (Spiers et al., 1990; Spiers and Schutjens, 1990; Spiers and Brzesowsky, 1993; Hickman and Evans, 1991, 1992, 1995; Schutjens and Spiers, 1999; Zubtsov et al., 2004), gypsum (De Meer and Spiers, 1995, 1999a, b; De Meer et al., 1997, 2000), calcite (Zhang et al., 2002; Zhang and Spiers, 2005) and quartz (Renton et al., 1969; Sprunt and Nur, 1976; De Boer et al., 1977; Gratier and Guiguet, 1986; Cox and Paterson, 1991; Den Brok and Spiers, 1991; Schutjens, 1991; Elias and Hajash, 1992; Dewers and Hajash, 1995; Rutter and Wanten,

2000; Niemeijer et al., 2002; Niemeijer and Spiers, 2002; He et al., 2003), focusing mainly on compaction creep. The aim of these studies was to demonstrate pressure solution as the main deformation mechanism, and to quantify pressure solution rates and rate constants.

However, except for pressure solution in halite, the results of these studies have not yielded well-constrained rate equations, but have shown that diffusion or reaction kinetics can be rate controlling. In halite aggregates, pressure solution rates are controlled by diffusion through the grain boundary fluid (Spiers et al., 1990; Spiers and Schutjens, 1990; Spiers and Brzesowsky, 1993; Spiers et al., 2004), with Z at room temperature in the range 3×10^{-20}-3×10^{-19} (Spiers et al., 1990; Spiers and Schutjens, 1990; Spiers and Brzesowsky, 1993) and showing an Arrhenius temperature dependence with apparent activation energy for creep of ~24.5kJmol^{-1} (Spiers et al., 1990). In gypsum, experiments show that the rate-controlling process for compaction by pressure solution is probably precipitation (De Meer and Spiers, 1999b), whereas in calcite both diffusion through the grain boundary fluid and precipitation have been inferred as rate-controlling processes, depending on factors such as pore fluid composition and compaction strain (Zhang et al., 2002; Zhang and Spiers, 2005). In quartz, for grain sizes up to at least 125μm, and temperatures up to at least 600°C, dissolution is the most likely rate-controlling process for pressure solution (Schutjens, 1991; Dewers and Hajash, 1995; Niemeijer et al., 2002). At lower temperatures (below ~250-300°C), though, and over timescales attainable in laboratory tests, microcracking is likely the dominant creep mechanism, rather than pressure solution (Schutjens, 1991; Chester et al., 2004; Chester et al., 2007).

So far, these bulk experiments have largely failed to yield constitutive equations for pressure solution in materials such as quartz and calcite, with reliable estimates of the rate constants for pressure solution (I^*,Z), mainly due to problems isolating pressure solution creep as the dominant compaction creep mechanism. The slow nature of pressure solution creep requires experiments to be performed at relatively high temperatures and pressures and/or on relatively fine-grained materials. In order to acquire a better understanding of the kinetics of pressure solution, a more fundamental understanding of the structure and physical properties of solid-fluid contacts under non-hydrostatic stress is therefore required, yielding independent data on rate constants such as I^* and Z which can be inserted into the theoretically based creep models such as equations (1.1) and (1.2) to quantify pressure solution. It is also important to develop an understanding of how the controlling grain boundary processes and associated rates are influenced by potentially coupled factors such as grain contact fracturing (e.g., Gratz, 1991; Den Brok, 1998; Gratier et al., 1999) and microplasticity (Lehner, 1990).

1.3 The structure and physical properties of grain boundaries during pressure solution: The state of knowledge to date

1.3.1 Grain boundary models

From pressure solution theory, the key quantities that we need to understand to quantify pressure solution are I^*, Z and I_p. With the exception of the precipitation rate constant I_p for pore wall precipitation, these quantities depend on the grain boundary structure. However, as indicated in the foregoing, our understanding of the structure and physical properties of fluid-filled grain boundaries is still very limited, with three distinct models being proposed for load-bearing grain boundaries during pressure solution. In the so-called thin film model, an adsorbed (~1nm) fluid film is maintained in the grain boundary either by conventional surface forces, i.e. through competition between Van der Waals, electric double layer and/or hydration forces providing a "disjoining pressure" (Weyl, 1959; Rutter, 1976, 1983; Israelachvili, 1986; Horn et al., 1989; Hickman and Evans, 1991, 1992, 1995; Renard and Ortoleva, 1997; Renard et al., 1997; Alcantar et al., 2003; Anzalone et al., 2006; Meyer et al., 2006), or (in quartz) by repulsive steric forces or bonding between hydrated silica gel layers (Vigil et al., 1994; Revil, 2001). In these thin film models, a molecular structuring of the fluid film is also often assumed (Rutter, 1976, 1983; Hickman and Evans, 1995) and an associated reduction in grain boundary diffusion coefficient compared to bulk diffusion of up to 5 orders of magnitude has been postulated (Rutter, 1976, 1983). Evidence for the structuring of fluid films through surface interaction effects has been found in films of (85-185nm) thickness in pressure dissolving halite-fluorite contacts (De Meer et al., 2005), between plates of borosilicate glass, between plates of quartz and flakes of muscovite (Nakashima et al., 2001), and in adsorbed films on free halite (100) faces (Arsic et al., 2004). However, reductions in grain boundary diffusion coefficient of a maximum of only ~1-2 orders of magnitude are indicated in such experimental studies (Hickman and Evans, 1995; Schutjens and Spiers, 1999; Nakashima et al., 2001; De Meer et al., 2002, 2005; Alcantar et al., 2003; Anzalone et al., 2006), and are estimated in recent models (Renard et al., 1997, Revil, 2001).

In the second grain boundary model, the existence of a thin fluid film is proposed, but short-circuited by a stable array of fluid inclusions, channels and/or cracks (Gratz, 1991; Den Brok, 1998; Renard et al., 1999). Dissolution occurs in the load-bearing thin film contacts, and dissolved material subsequently diffuses through these thin films into the open cracks. The fluid (with bulk properties) present in the constantly deepening cracks and fluid inclusions then provides a fast diffusion pathway for the removal of dissolved material from the grain boundary (e.g., Gratz, 1991; Gratier et al., 1999; Renard et al., 1999).

In the third model, the existence in the grain boundary of a non-equilibrium, dynamically wetted network of migrating interconnected channels of free fluid, separated by islands of solid-solid contact is assumed (Elliott, 1973; Raj, 1982; Tada et al., 1987; Lehner, 1990; Spiers and Schutjens, 1990; Schutjens and Spiers, 1999; Ghoussoub and Leroy, 2001). Here, the fluid in the channels, which is connected to the open pore fluid, allows for fast diffusion through the grain boundary, while the laterally dissolving islands bear intergranular tractions. In any solid-fluid system where the equilibrium dihedral angle $\theta_{eq} > 0$, such a rough,

dynamically wetted island-channel structure cannot constitute an equilibrium structure (Jin et al., 1994; Visser, 1999; Schenk and Urai, 2004). Moreover, since the load-bearing islands will be highly strained, they are expected to be removed by (strain-driven) dissolution (e.g., Bosworth, 1981; Meike, 1990). It has therefore often been questioned whether such a high-energy grain boundary can be maintained during long-term steady state deformation, as opposed to gradual flattening and/or healing driven by surface energy (e.g., Hickman and Evans, 1995). In most treatments it is assumed that a rough grain boundary structure can be maintained by local variations in the driving force for dissolution caused by the uneven distribution of stress/strain-induced or defect-related irregularities in free energy density (Lehner, 1990; Spiers and Schutjens, 1990; Koehn et al., 2006) or by crystal anisotropy effects (Spiers and Schutjens, 1990). As local variations in the driving force for dissolution must overcome surface energy driven healing effects for pressure solution to continue, there is considerable interest in assessing whether grain boundary healing might imply a yield stress for pressure solution.

1.3.2 Stability of solid-fluid interfaces under non-hydrostatic stress

Quite apart from the possibility that rough grain boundary island-channel structures can be maintained by local variations in the driving force for dissolution, such as stress/strain-induced or defect-related irregularities in free energy density, or by crystal anisotropy effects, recent theoretical modelling work has shown that grain boundaries may naturally roughen when under stress, even in purely elastic materials. Under hydrostatic conditions at equilibrium, the shape of a grain of soluble solid fully enclosed by its saturated solution is determined by the minimisation of the interfacial free energy of the solid-fluid interface (e.g., Müller and Saúl, 2004). For crystalline solids, the existence of sharply defined minima, or cusps, in the surface free energy for specific crystallographic orientations means that a faceted crystal is formed, with faces parallel to the orientations of minimum surface energy (Visser, 1999; Müller and Saúl, 2004). In a solid under non-hydrostatic stress, however, strain energy perturbation and resulting dissolution/precipitation transport can lead to the destabilisation of such low energy faces, specifically when the total relaxation of elastic energy by growth of a morphological perturbation is greater than the total increase in surface free energy that results (Srolovitz, 1989; Müller and Saúl, 2004). This type of instability is known as the Asaro-Tiller-Grinfeld instability (e.g., Asaro and Tiller, 1972). Such instabilities have been reported in experiments performed by Den Brok and Morel (2001) and Den Brok et al. (2002) on potassium alum single crystals loaded under saturated solution. In these experiments, regular grooves formed on free surfaces approximately perpendicular to the direction of maximum stress, and were dynamic rather than static, moving as the local stress field changed. Similar surface instabilities have been observed on the flat surfaces of uniaxially stressed sodium chlorate crystals in contact with saturated solution (Koehn et al., 2004; Bisschop and Dysthe, 2006).

Modelling studies (e.g., Ghoussoub and Leroy, 2001), based on stability analyses of free surfaces of stressed solids (such as the analysis of Srolovitz, 1989), show that in a grain boundary under normal stress, dissolution around originally cylindrical, fluid-filled cavities leads to undercutting of the dry contact regions, resulting in a thin fluid film penetrating along the grain boundary. Such penetrating thin films heal and disappear rapidly when the imposed

stress is removed (Ghoussoub and Leroy, 2001). It can further be argued, from the instability of free, flat solid-fluid interfaces of stressed solids, that a continuous thin fluid film cannot be stable in a stressed grain boundary, at least if the interface parallel stress differs from the pore pressure. The interfaces bounding such a film are then predicted to evolve toward corrugated surfaces (Ghoussoub and Leroy, 2001; see also the analysis by Gal et al., 1998), i.e., to develop a rough structure, of the type observed on free surfaces by Den Brok, Dysthe and co-workers (Den Brok and Morel, 2001; Den Brok et al., 2002; Koehn et al., 2004; Bisschop and Dysthe, 2006). On this basis, it seems likely that during pressure solution of even a homogeneous, isotropic and defect-free material, grain boundaries with a rough, unstable or dynamically wetted island channel structure, continuously reorganising in time can indeed exist (Ghoussoub and Leroy, 2001; Koehn et al., 2006). These instabilities, however, remain to be demonstrated in experiments on minerals such as quartz, under hydrothermal conditions.

1.3.3 Experimental observations on grain boundary structures and properties during pressure solution

In the last 10 years, a large amount of experimental work has been reported on the structures of fluid-filled grain boundaries undergoing pressure solution, in an attempt to elucidate the evolution of grain boundary roughness. However, this work has focused mainly on halite, as its solubility is high, and its room temperature dissolution/precipitation kinetics are rapid, rendering it easily studied. Post-experimental observations on grain boundaries in granular halite aggregates compacted by pressure solution, and on pressure solution indents made in halite, have shown rough grain boundaries with 0.1-10μm scale ridges and channels or with a shell-like island channel structure (Spiers and Schutjens, 1990; Spiers et al., 1990; Dysthe et al., 2003). However, these observations suffer from the disadvantage that the observed grain boundary structure may not be the same as that during active pressure solution (see Hickman and Evans, 1991, 1995). To avoid this problem, real time, in-situ observations of grain boundary roughness developed in pressure dissolving contacts between halite crystals and various other materials have been made using a wide variety of techniques, including light microscopy, Fourier Transform Infrared spectroscopy and synchrotron X-ray techniques. These observations generally show a dynamic grain boundary structure that evolves with time and/or decreasing stress, often to a smoother (suboptical) structure (Schutjens and Spiers, 1999; Martin et al. 1999; De Meer et al., 2005; Karcz et al., 2006; Dysthe et al., 2006). Imposing extra load on such a contact after smoothening of the structure generally leads to a new cycle of grain boundary roughening on the micrometer scale followed by smoothening (Schutjens and Spiers, 1999). Furthermore, the rough island-channel structure developed often shows clear crystallographic control on island-channel morphology (Schutjens and Spiers, 1999; Martin et al., 1999). In addition, the thickness of pressure dissolving, fluid-filled contacts between halite and fluorite is dependent on the crystallographic orientation of the contacting halite surface (De Meer et al., 2005). Such contacts show an average thicknesses of ~85-185nm and ~40nm during pressure dissolution on the (111) and (100) planes of halite, respectively, and are therefore rough at the suboptical scale. In contrast to these observations, stable nano-scale voids and cavities have been reported in a loaded halite-SiO_2 contact in the presence of brine (Jordan et al., 2005). However, pressure solution rates in these experiments were negligible (likely as a result of the relatively large contact sizes used), and the grain

boundary structure appears to have been dominated by healing effects. Smooth grain boundaries, with no optically visible contact roughness have been reported in experiments on pressure dissolving single contacts between convex halite lenses and silica plates (Hickman and Evans, 1991, 1995), though the possible existence of sub-optical roughness (see also De Meer et al., 2002, 2005) cannot be excluded.

Though there are a large number of observations of dynamically wetted, island-channel type grain boundaries in halite, several important questions remain. One of these is the influence of the crystallographic orientation, of the dissolving halite contact surfaces, on factors such as grain boundary fluid film thickness, and/or roughness. Another key point is the influence of the surface energy and solubility of the contacting object on grain boundary roughness and contact evolution. Contact microstructures are often investigated between halite and a relatively inert material such as silica glass, even though the nature of the contacting material is known to influence contact evolution, healing and (equilibrium) configuration through surface energy effects (e.g., Hickman and Evans, 1991; Bos and Spiers, 2000; Niemeijer and Spiers, 2006). Note for example that pressure solution creep rates are faster in mixed aggregates of halite and (inert) calcite than in pure halite aggregates (Zubtsov et al., 2004).

Unfortunately, the evidence for grain boundary structures during experimental pressure solution in quartz is much less extensive, and far less conclusive. Only a few observations on post-experimental grain boundary structures in granular aggregates compacted by pressure solution have been reported. These observations vary from contacts developing towards a flat (film) structure in experiments performed at low temperatures of 150°C (Dewers and Hajash, 1995), to a rough contact of islands (on a micrometer scale) separated by microcracks (~1μm wide) intersecting the grain boundary at 800°C (Den Brok, 1998), to an island-channel like structure with island dimensions of 0.05-3μm and estimated amplitudes of up to 100nm at 927°C (Cox and Paterson, 1991).

1.3.4 Grain boundary structure and internal dissolution/precipitation kinetics

It will be clear from the foregoing that the structure of fluid-filled grain boundaries is expected to exert a strong influence on the rate of diffusive transport in the grain boundary, and hence on diffusion controlled pressure solution. In particular, the effective grain boundary diffusivity ($Z = D\delta_{av}S/\tau$) is influenced by the degree of grain boundary wetting, the mean thickness of the fluid film (δ_{av}), the tortuosity of the diffusion pathway (τ, usually assumed equal to 1) and, in the case of thin fluid films, when thin enough, a possible structuring of the fluid and an associated reduction of the diffusion coefficient (D) or solid solubility (S) in the film. However, the influence that grain boundary structure might have on grain boundary dissolution (and precipitation) rates, and thus on the rate of dissolution (or precipitation) controlled pressure solution has not yet been considered, and it is generally assumed that the rate constant I^* for grain boundary dissolution is equal to I (e.g., Shimizu, 1995; Renard et al., 1999; Revil, 2001; Gundersen et al., 2002; Niemeijer et al., 2002; Revil et al., 2006). Here, $I = \kappa_+\Omega_s$, and κ_+ is the standard geochemical dissolution rate coefficient for a free surface (e.g., Rimstidt and Barnes, 1980). It is likely, though, that $I^* < I$, due to incomplete grain boundary wetting (island-channel structure), inelastic deformation of islands (island-

channel structure) and/or structuring of the fluid phase (thin film model) (Lehner, 1990). The usual assumption that $I^* = I$ would then lead to an overestimation of pressure solution rates in systems such as quartz, where dissolution is the rate controlling process for pressure solution (e.g., Niemeijer et al., 2002). The magnitude of this effect is unknown but may be large. Certainly, there is a significant discrepancy between measured intergranular pressure solution rates in quartz and rates predicted by theoretical rate models using $I^* = I$ (e.g., Niemeijer et al., 2002).

1.4 Aims of the present work

On the basis of the above it is clear that progress in quantifying pressure solution in geological materials required progress in understanding and quantifying grain boundary structures and properties during pressure solution creep. In particular, it is important to address the grain boundary dissolution rate constant I^* and the grain boundary diffusivity product $Z = D\delta_{av}S/\tau$, and the effects of grain boundary structure on these kinetic factors. The present thesis addresses these issues making use of experimental studies of pressure solution at individual grain boundaries and in polycrystalline aggregates, and through the development of simple models treating grain boundary dissolution kinetics. The specific aims are:

1) To investigate the influence of crystallographic orientation, lattice misorientation, and contact type on grain boundary structure and transport properties during pressure solution at halite-halite and halite-glass contacts in their own right and to gain fundamental insight in general.
2) To assess, using a simplified modelling approach, the influence of grain boundary structure on the rate of grain boundary dissolution (i.e. on I^*) in an elastic material, in which pressure solution rates are controlled by dissolution. This is of special interest for quartz.
3) To derive a model predicting the stress conditions under which a dynamically wetted island-channel structure can be maintained as opposed to healing by surface energy driven growth of islands.
4) To assess the influence of plastic deformation, at highly stressed contact points in a grain boundary with island-channel structure, on grain boundary dissolution rates (I^*).
5) To directly measure the grain boundary transport properties of single silica glass contacts undergoing active pressure solution at hydrothermal pressure and temperature, using a specially designed cell.
6) To determine the rate of compaction of granular aggregates of quartz by pressure solution creep, over a wide range of temperatures and effective pressures, along with the structure of pressure dissolving grain boundaries, and the associated rate controlling process, and comparing pressure solution rates obtained with the rates predicted by models for pressure solution.

Aim 1 is addressed in Chapter 2, aim 2 and 3 are addressed in Chapter 3, and aims 4 to 6 are addressed in Chapters 4-6 respectively. In Chapter 7 the general conclusions of this thesis are repeated, and suggestions are made for further work.

2. Effects of orientation on the diffusive properties of fluid-filled grain boundaries during pressure solution

This chapter was published as: Van Noort, R., C. J. Spiers and C. J. Peach (2006), Effects of orientation on the diffusive properties of fluid-filled grain boundaries during pressure solution, Phys. Chem. Miner. 34(2), doi:10.1007/s00269-006-0131-9. The original publication is available at www.springerlink.com

Abstract

An unresolved issue in the study of pressure solution in rock materials is the dependence of grain boundary structure and diffusive properties on the mutual orientation of neighbouring grain lattices. We report electrical measurements yielding the diffusivity of differently oriented halite–glass and halite–halite contacts loaded in the presence of brine. The halite–glass contact experiments show pressure solution of the halite and an effect of halite lattice orientation on grain boundary transport. Post-mortem observations show an orientation-dependent grain boundary texture controlled by the periodic bond chains in the halite structure. It is inferred that this texture determines the internal grain boundary structure and properties during pressure solution. In the halite–halite experiments neck-growth occurred, its rate depending on twist-misorientation. The results imply that deformation by pressure solution may lead to lattice-preferred orientation development, and that polymineralic rocks may deform faster at lower stresses than monomineralic rocks.

2.1 Introduction

The dominant mechanism of creep in much of the middle and upper crust is stress-induced, diffusive mass transfer, through water-bearing grain boundaries, or ''pressure solution'' (Elliott 1973; Rutter 1983). This mechanism is of major importance in controlling the compaction of sedimentary rocks (Tada et al., 1987; Revil, 2001), fault sealing, strength recovery and creep in active fault zones (Sleep and Blanpied, 1992; Hickman et al., 1995; Karner et al., 1997; Revil, 2001; Bos and Spiers, 2002a, 2002b) and bulk rock deformation under mid and even lower crustal conditions (Elliott, 1973; Rutter, 1983; Green, 1984). Over the last three decades pressure solution has been widely studied in nature (e.g., Rutter, 1983; Wintsch and Yi, 2002), theory (e.g., Lehner, 1995; Dysthe et al., 2002a) and experiments (e.g., Cox and Paterson, 1991; Rutter and Wanten, 2000; Niemeijer et al., 2002; Dysthe et al., 2002b, 2003; Chester et al., 2004; Zubtsov et al., 2004).

In a chemically closed system, pressure solution involves three processes operating in series: the dissolution of material within grain contacts under high normal stress, the diffusion of dissolved material through the grain boundary fluid phase, and precipitation on open pore walls or within grain boundaries under low normal stress (e.g., Raj, 1982; Rutter, 1983; Spiers et al., 1990; Lehner, 1995). The slowest of these processes will then determine the rate of deformation by pressure solution. However, though the importance of pressure solution is widely accepted, our understanding of the structure of wetted grain boundaries and, therefore, of the elementary diffusive and interfacial processes in such grain boundaries,

is still limited. Over the last few decades it has been argued that water may be present in grain boundaries in the form of (a) strongly adsorbed thin films (Weyl, 1959; Rutter, 1976, 1983; Hickman and Evans, 1991, 1992, 1995; Renard and Ortoleva, 1997; Renard et al., 1997), (b) isolated inclusion or connected crack arrays (Gratz, 1991), (c) dynamically stable, non-equilibrium, channel networks (Elliott, 1973; Raj, 1982; Jin et al., 1994; Schutjens and Spiers, 1999; Ghoussoub and Leroy, 2001; Den Brok et al., 2002; De Meer et al., 2005), or (d) intergranular gel layers (for silica, Vigil et al., 1994; Revil, 2001). However, a quantitative description of grain boundary properties, structure and internal kinetic processes that can reliably be extrapolated to describe intergranular pressure solution in geological materials, remains elusive.

Recently, De Meer et al. (2005) reported in situ Fourier transform infrared spectroscopy measurements on halite–fluorite bi-crystal contacts undergoing active pressure solution of the halite crystal, complemented by 'post-mortem' atomic force microscopy (AFM) observations of the contacts. Their results include the first independent determinations of the thickness of the fluid phase in a grain boundary undergoing pressure solution in any material, and of the apparent grain boundary diffusion coefficient. The average fluid film thicknesses measured varied from 85–185nm, for dissolution of the (111) halite face, to ~40nm for the (100) face. Film thicknesses were also observed to fluctuate in time and space, suggesting a dynamically stable island-channel network. The observed orientation dependence was tentatively ascribed to differences in dynamic surface structure between the rough (111) face and the flat (100) face. Similar conjectures regarding the effect of surface structure were put forward by De Meer et al. (2002), who performed electrical conductivity measurements on individual, ring-shaped halite–glass contacts undergoing active pressure solution. However, the detailed effects of crystallographic orientation on grain boundary structure and their role in controlling the rate of pressure solution are unknown. It is also unclear whether similar effects can be expected in other minerals, and whether an orientation dependence of grain boundary structure and properties may influence phenomena such as lattice preferred orientation development in rocks deforming by pressure solution (De Meer et al., 2005). A dynamically stable island-channel network was also observed by Karcz et al. (2006) for a contact between a halite (100) face and a silica glass sheet. Dysthe et al. (2002b, 2003) observed rough contacts forming between an inert indentor and halite single crystals in the presence of brine. The roughness on these contacts was observed to decrease with time. Schutjens and Spiers (1999) observed stressed, wetted halite–halite and halite–glass contacts. The roughness of these contacts increased as the stress on the contact was increased, and decreased as the experiment continued and contact stress decreased with increasing contact area.

This chapter attempts to clarify the influence that crystallographic orientation has on grain boundary structure during pressure solution of halite. We report electrical resistivity measurements made on ringshaped halite–glass contacts during active pressure solution of the halite, using three different loading orientations. We also report measurements on ringshaped halite–halite bi-crystal contacts in two different mutual orientations. Our results confirm that the grain boundary diffusivity of a halite–glass contact depends on the crystallographic orientation of the halite surface forming the contact. Our results also show that the type of contact, halite–glass or halite–halite bi-crystal, and, in the latter case, the

orientation mismatch between the crystals, strongly influence the development of the contact and its diffusive properties.

2.2 Theoretical background

We will begin by explaining the theory of how grain boundary diffusive properties relevant to pressure solution can be obtained from electrical measurements made on a pressure dissolving contact.

2.2.1 Relationship between grain boundary diffusive properties and electrical conductivity

The theoretical rate equation for axisymmetric deformation or compaction of a granular aggregate by grain boundary diffusion controlled pressure solution can be written (De Meer et al., 2005):

$$\dot{\varepsilon} = A(\phi)\frac{Z}{\tau}\frac{\sigma_e V_m}{RT}\frac{1}{d^3} \tag{2.1}$$

Here $\dot{\varepsilon}$ is axial strain rate (s^{-1}), $A(\phi)$ a geometric factor which depends on porosity in the case of a porous aggregate, τ tortuosity of the grain boundary fluid network, here assumed to be 1, σ_e effective axial or differential stress (Pa), V_m molar volume of the solid (m^3/mol), R the gas constant, T absolute temperature (K), and d grain size (m). In addition, $Z = D\delta_{av}C$ represents the grain boundary diffusivity product in which D is diffusion coefficient of the solute in the grain boundary fluid phase (m^2/s), δ_{av} average thickness of the wetted grain boundary (m) and C solubility of the diffusing species in the grain boundary fluid (m^3/m^3) (see also Table 2.1 for a list of all symbols with corresponding units used in this chapter). In the case of halite (a strong electrolyte), the grain boundary diffusion properties expressed here can be related to the electrical conductivity of grain boundaries using the Nernst–Einstein relation yielding the result:

$$\kappa = \frac{2F^2DC}{RT} \tag{2.2}$$

where κ is conductivity of the solution, and F Faraday's constant (De Meer et al., 2002). For a soluble salt such as halite, measurements of the conductivity of a grain boundary, or other pressure dissolving contact thus give a measurement of the product DC.

Symbol	Unit
$\dot{\varepsilon}$	Strain rate (s^{-1})
$A(\phi)$	Porosity dependent geometric factor (-)
τ	Tortuosity of grain boundary fluid network (-)
σ_e	Effective stress (Pa)
V_m	Molar volume of solid ($m^3 mol^{-1}$)
R	Gas constant ($JK^{-1}mol^{-1}$)
T	Absolute temperature (K)
d	Grain size (m)
Z	Grain boundary diffusivity product ($m^3 s^{-1}$)
D	Solute grain boundary diffusion coefficient ($m^2 s^{-1}$)
δ_{av}	Average grain boundary thickness (m)
C	Solute solubility ($m^3 m^{-3}$)
κ	Conductivity of the solution ($\Omega^{-1} m^{-1}$)
F	Faraday's constant (C)
r	Contact radius (m)
w	Contact width (m)
Ω	Electrical resistance of contact (Ω)
γ_{sl}	Liquid-solid interfacial energy (Jm^{-2})
γ_{ss}	Solid-solid interfacial energy (Jm^{-2})
θ_{eq}	Equilibrium dihedral angle

Table 2.1 List of all symbols with definitions and corresponding units.

2.2.2 Principle of present experiments

In the experimental setup used here, a conical lens is pressed coaxially into a circular hole in a halite single crystal disc. If pressure solution proceeds at the junction between the crystal and the lens, then a conical ring-shaped contact with radius r and width w is formed between the lens and the disc, as shown in Figure 2.1. The resistance (Ω) of the contact to radial ionic conduction through the grain boundary fluid allowing pressure solution to proceed is now given by:

$$\Omega = \frac{w}{2\pi r \delta_{av} \kappa} \tag{2.3}$$

Hence, combining equations (2.2) and (2.3), we find:

$$Z = D\delta_{av} C = \frac{V_m RT}{4\pi F^2} \frac{w}{r} \frac{1}{\Omega} \tag{2.4}$$

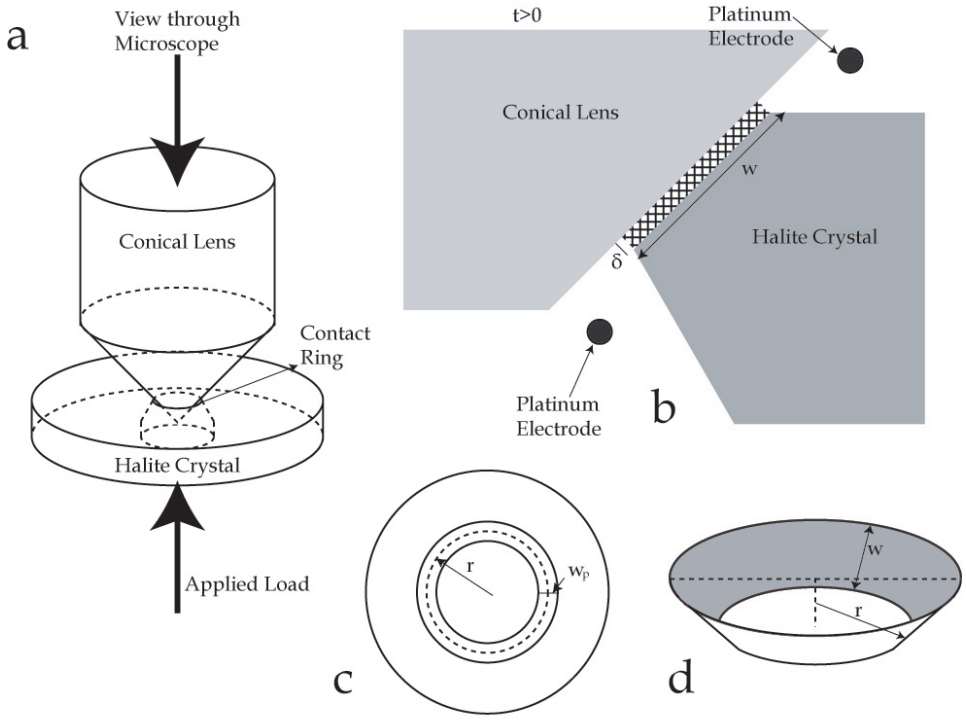

Figure 2.1 The geometry of the halite–glass contacts studied in the present experiments. (a) Schematic drawing of the glass lens penetrating the halite disc. (b) Cross-section through the halite–glass contact at t > 0. (c) Vertical view of the contact (as seen through the lens). (d) Three-dimensional shape of the dissolving contact (after De Meer et al., 2002).

where $V_m RT/4\pi F^2$ is constant at constant temperature (De Meer et al., 2002). As the resistance in the bulk solution on either side of the conical ring-shaped contact is negligible compared to the resistance of the (thin) contact itself, measuring the resistance of the circuit made by inserting electrodes into the solution on each side of the contact (see again Figure 2.1) yields Ω and thus Z. Note that when dissolution or precipitation is the rate controlling process for pressure solution, the rate of deformation depends on the relevant rate constant rather than Z. Nonetheless, the electrical resistivity of the contact then still depends on Z, and therefore equation (2.4) still applies.

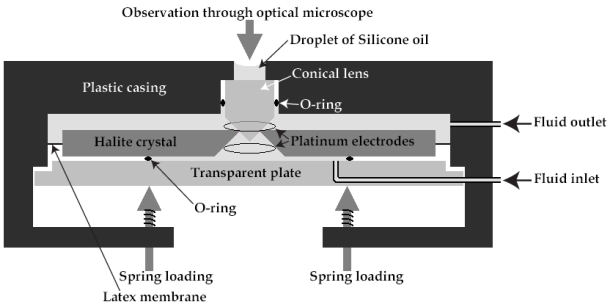

Figure 2.2 Schematic drawing of the experimental cell (after De Meer et al., 2002). The droplet of silicone oil was only present in the experiments with a halite lens.

2.3 Experimental method

2.3.1 Apparatus

We performed electrical resistivity measurements on halite–glass and halite–halite contacts at room temperature using the cell described by De Meer et al. (2002) (see Figure 2.2). This allows contact resistance and hence Z values to be determined in line with the principle described above. In this cell, a conical, ringshaped contact is formed between a halite single crystal disc, with a hole in the centre, and a conical lens made of either glass or a halite single-crystal, which is pressed into the hole in the halite disc. This contact forms the only connection between the two fluid reservoirs present in the cell. Two ring-shaped platinum electrodes, coated with platinum black to minimise polarisation effects, and placed close to the contact in each fluid reservoir, are used to measure the resistivity of the contact. Three adjustable, calibrated springs apply force to the lens and hence to the contact. The applied force remains constant within 2–4% during the experiments. The experimental temperature is monitored using a type K thermocouple placed in one of the fluid reservoirs, close to the contact. A digital programmable signal generator is used for generating the measurement current. The voltage drops across the contact, and across a 100kΩ ‘‘current sense resistor’’ placed in series with the cell, are logged using an A/D converter and a PC. A more elaborate description of the electrical circuit used in the experiments is provided by De Meer et al. (2002). The evolving contact is observed using an optical microscope, viewing through the glass or halite lens.

2.3.2 Sample orientation and preparation

In our halite–glass experiments, three different orientations of the halite crystal with respect to the loading direction and glass cone axis were investigated. These orientations were chosen such that the top surface of the halite single crystal disc used in the experiments was parallel to the (100), the (110), or the (111) lattice plane. Since the actual contacts in these experiments

were formed against the conical glass lens, which had an apex angle of 90°, these contacts were not parallel to the (100), (110), or (111) lattice planes. Rather, the contacts were conical rings at 45° to the indicated orientations.

The halite discs used in the experiments were cleaved from melt-grown cylindrical halite single crystals with a diameter of 25mm. For experiments with the top surface of the halite single crystal disc parallel to the (100) lattice plane, a hole was drilled into the disc, and thin slices were cleaved off the top and bottom surfaces of the crystal to remove the damaged outer layers and to provide a sharp-edged hole. For experiments with the top surface of the disc parallel to the (110) or (111) lattice plane, a 9mm diameter core was drilled from a larger crystal and then annealed in Argon at 700°C for at least 24h to remove damage. The core was then ground to a right cylinder, a hole was drilled into it as in the (100) experiments, and the cylinder was carefully ground to form a disc of the correct thickness. The top surface of the crystal was then lightly polished on a soft tissue moistened with demineralised water to produce a gleaming, optical quality surface. Note that one experiment (100NaCl) was done on an (100) oriented crystal ground to the correct thickness in the same way as the (110) and (111) crystals, rather than cleaved. This was done to check if the damage caused by the grinding influenced the development of the contact and the Z values measured.

Prior to each experiment the prepared crystal was annealed to remove any damage from the top surface. The halite discs used in the (100) orientation experiments were fitted into the cell directly. The smaller (9mm diameter) discs used in the (110) and (111) oriented experiments were each glued, using epoxy resin (Agomet P76), into a hole in the centre of a clear plastic disc, with the top surface of the crystal flush with the surface of the plastic disc. These plastic discs had the 25mm diameter required to fit the cell.

In the halite–halite experiments, instead of the glass lens, a halite single crystal lens with its axis parallel to the [100] direction was used. This lens was prepared by gluing a small, freshly cleaved prismatic crystal of halite into a PVC tube with Agomet P76 resin, and then grinding the crystal plus holder to the same conical tip as that of the glass lens. The conical surface was lightly polished with a tissue moistened with demineralised water to give it a gleaming, optically smooth finish. Annealing the glued lens was not possible. The halite discs used in the halite–halite contact experiments were prepared using the method described above for discs cut parallel to the (100) orientation.

2.3.3 Loading procedure and resistivity measurements

Once the cell was fully assembled, the annular contact was preloaded (dry) using three calibrated springs at the load chosen for testing (1 or 3N). This was done to ensure proper alignment of the sample and lens. Loads of 3N resulted in normal stresses across the contact of up to 15MPa after a contact ring had formed, though initially stresses must have reached higher values. The contact was then unloaded, the fluid reservoirs were filled with saturated brine and the spring load was reapplied, pressurising the brine, but not loading the contact. Contact between the lens and the crystal was established by carefully bleeding out the excess brine, until the load was entirely supported by the contact. At this point electrical resistivity measurements were started. A 1kHz sine wave burst (tests with a Solartron 1260A impedance analyser showed purely resistive behaviour at this frequency) with a duration of 6s, and a root

mean square amplitude of 100mV was sent through the contact at 200s intervals, and logging was started. The signal voltage of 100mV and 200s intervals were chosen to prevent heating of the fluid in the contact and possible internal dissolution effects. Such effects do occur at voltages of ≥500 mV but have no influence on contact evolution at lower voltages (see also De Meer et al., 2002). Also note that as the cell was placed in a circuit in series with a 100kΩ resistor, the actual voltage-drop across the cell was in most experiments considerably lower than 100mV (<70mV, depending on contact resistance).

In the halite–halite experiments, a single droplet of silicone oil was deposited on the flat outer surface of the lens in order to prevent dissolution/precipitation processes from taking place on the lens as a consequence of contact with the open air. Changes in the surface geometry of this droplet effectively changed the magnification with which the contact was viewed during the halite–halite experiments. Measuring the size of the rectangular cross-section of the halite lens crystal, which was held in epoxy and so did not change size during the experiments, allowed some correction for this problem. The average grain boundary diffusivity product determinations of the halite–halite contacts are still expected to be less accurate than the measurements of the halite–glass contacts. However, the errors are insignificant compared to the differences between individual experiments.

After each experiment, the stress was removed from the contact, and the cell was then opened as fast as possible (within ~2min) in order to minimise precipitation on the contact surface. Once the cell was opened, the crystal was rinsed vigorously with ethanol to remove any brine present on the surface, and the crystal was then stored in a low humidity (RH ≤ 20%) room.

2.4 Results

2.4.1 Observations on halite–glass contacts

Table 2.2 lists all experiments reported here. In each halite–glass experiment, a widening ring of contact was observed between the lens and the test crystal after loading in the presence of brine. Note that the concentric rings observed around the hole early in each experiment are machining grooves located on the conical surface of the hole drilled in the halite disc.

Experiment	Contact Type	Orientation
100NaCl	Halite–glass	Loading axis normal to (100)
110NaCla	Halite–glass	Loading axis normal to (110)
110NaClb	Halite–glass	Loading axis normal to (110)
111NaCl	Halite–glass	Loading axis normal to (111)
	Halite–halite	Loading axis normal to (100), 45 degree
	Halite–halite	Loading axis normal to (100), 0 degree

Table 2.2 List of all experiments reported here.

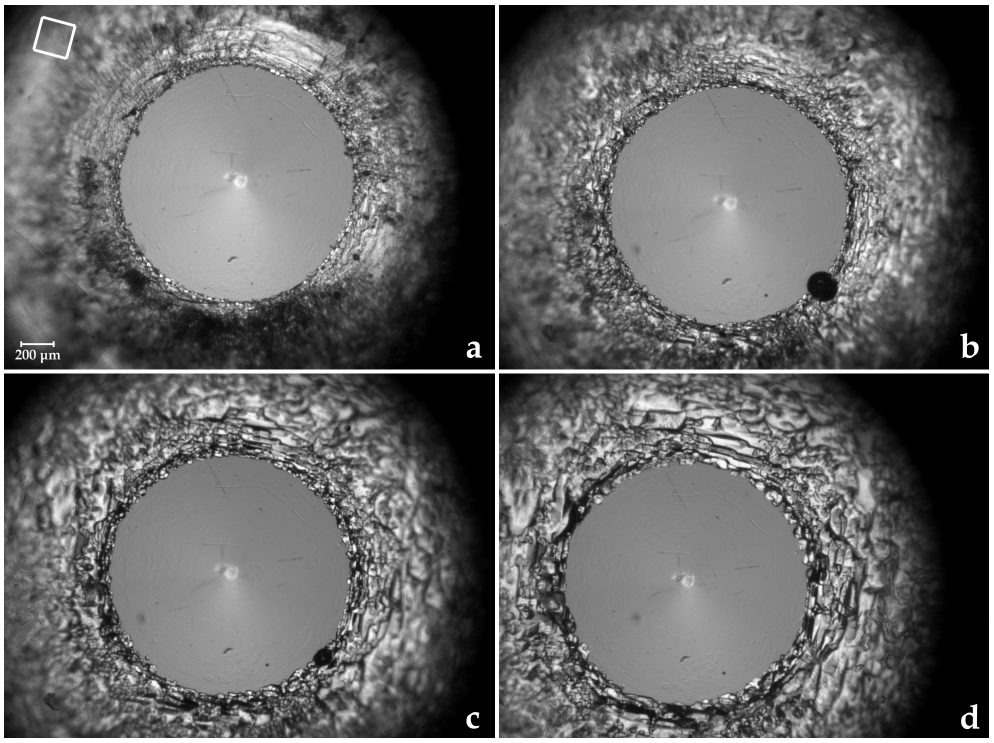

Figure 2.3 Development of the halite–glass contact in the 100NaCl experiment. (a) Start of the experiment. A contact ring has not yet formed. (b) After ~2 days. A contact ring is (just) visible. (c) After ~5 days. (d) End of the experiment; after ~12 days. A contact ring is present but obscured by overgrowths on the inside of the hole in and top surface of the halite disc. The bubble seen in (b) and (c) is located underneath the contact and so does not affect it.

Post-mortem (side-on) observation of the crystals from each halite–glass experiment showed that the contact rings had formed below the original top surface of the disc. This could be verified as part of this top surface did not come into contact with the brine in experiment 100NaCl. In the other halite–glass experiments the top surfaces of the plastic discs in which the samples were glued were used as references. These observations indicate that widening of the contact rings occurred as a result of the removal of halite from the contact, confirming that convergence between the glass lens and the halite single crystal disc did occur during each halite–glass experiment. Figure 2.3 shows the development of the contact ring in experiment 100NaCl. Overgrowths on the top surface of the halite disc and on the inner surface of the hole in it dominate the images, but a contact ring can just be distinguished after ~2 days. Despite some charging effects, the post-mortem SEM observations (see Figure 2.4) on the contact surface of the disc show a texture of small (micrometer scale) cubic kinks and longer steps parallel to the (100) directions, giving the surface a somewhat scaly appearance.

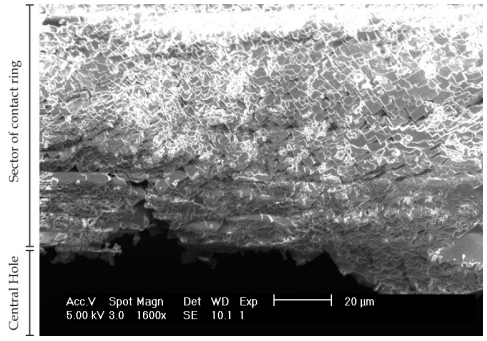

Figure 2.4 Post-mortem SEM SE micrograph of the surface of the contact ring on the halite disc, from experiment 100NaCl. Note the fine texture of small, parallel cubic steps. Unfortunately finer scale observations were not possible due to charging effects on the surface.

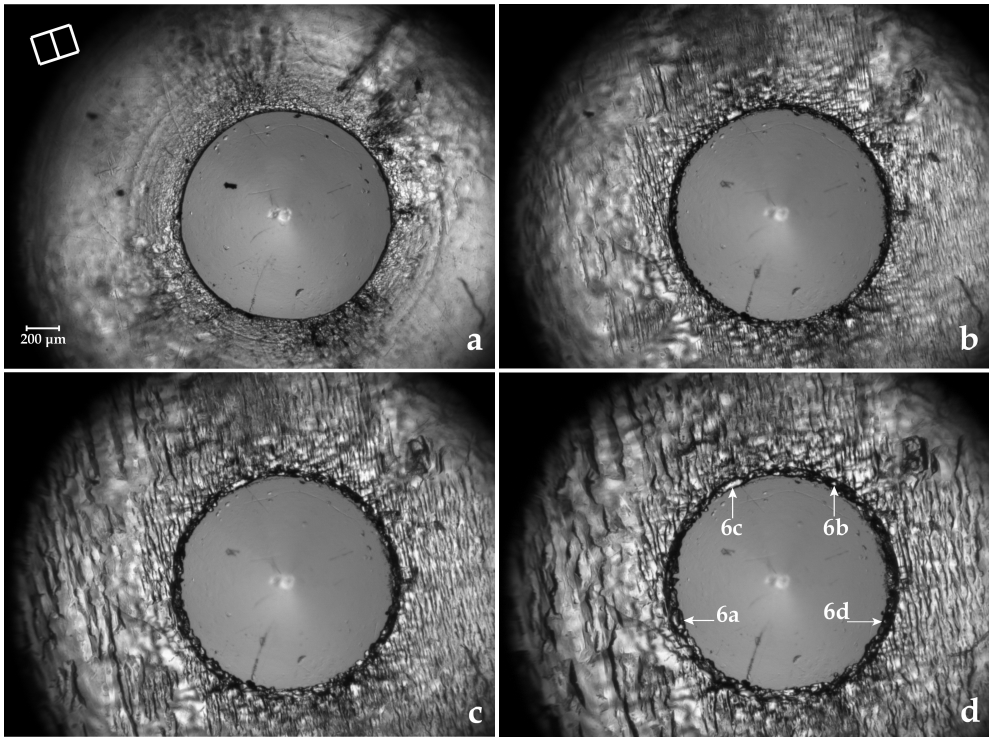

Figure 2.5 Development of the halite–glass contact in the 110NaCla experiment. (a) Start of the experiment. (b) After ~1 day. (c) After ~2 days. (d) After ~4 days. The arrows in (d) indicate the locations of the spots of roughness seen in Figure 2.6.

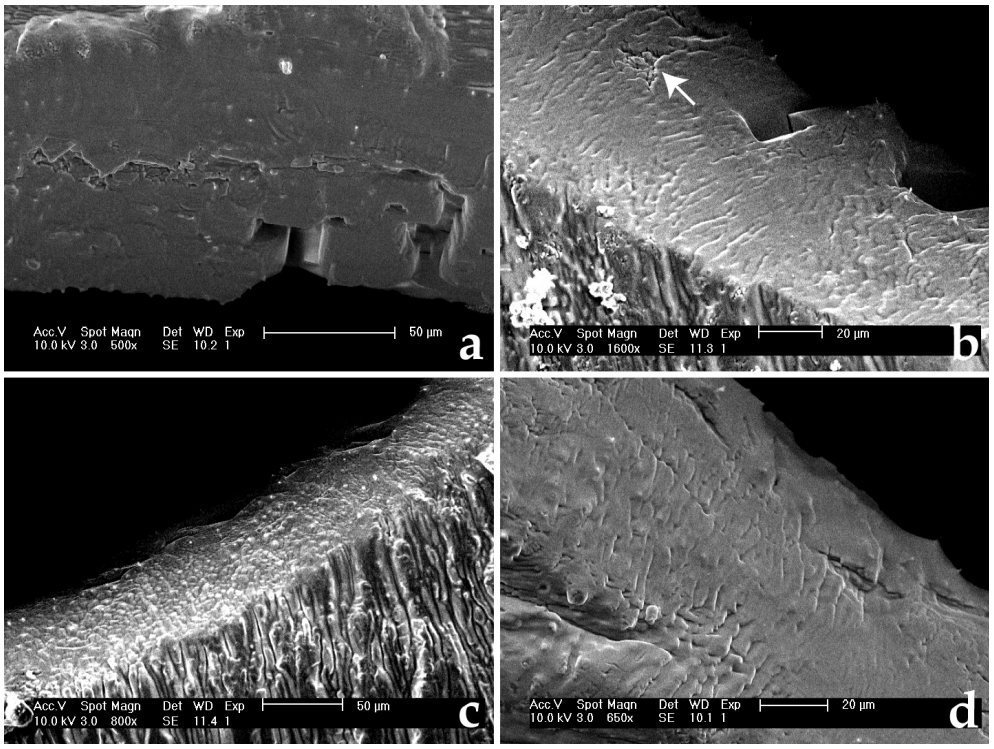

Figure 2.6 Post-mortem SEM SE images of the contact surface of the halite disc from experiment 110NaCla. (a, b) Irregular voids associated with the "light spots" indicated in Figure 2.5d as 6a and 6b. Note the otherwise very smooth contact surface in (a) which is sub-parallel to a {100} form. (c) An area of roughness that appears as a "light spot" in Figure 2.5d (indicated 6c). (d) The grooves (sub-)parallel to the (100) orientation (location indicated as 6d in Figure 2.5d).

In the (110) experiments (Figure 2.5) a contact ring formed, with overgrowths parallel to the {100} form along the inner rim of the hole and on the top (110) surface of the halite disc. The crystallographic control suggested by the surface overgrowths is also visible in the contact ring, with the parts of the contact aligned with the {100} form being considerably flatter than the rest of the contact (the uniform, dark parts of the contact are optically flat). Also observed is the movement towards and inclusion into the contact ring of spots of bright contrast from outside the ring. Post-mortem SEM observation has shown these to be related to patches of roughness on or irregular voids (up to 100–200µm long) in the halite contact surface (Figure 2.6). These rougher areas move towards the contact ring until they are assimilated into the contact, at which point they cease moving, though their shape does change gradually. Assimilation of all such features into the contact occurred around 2 days after the start of experiment 110NaCla, and around about 1 week after the start of experiment 110NaClb. Post-mortem SEM observation confirms a dependence of the degree of roughness

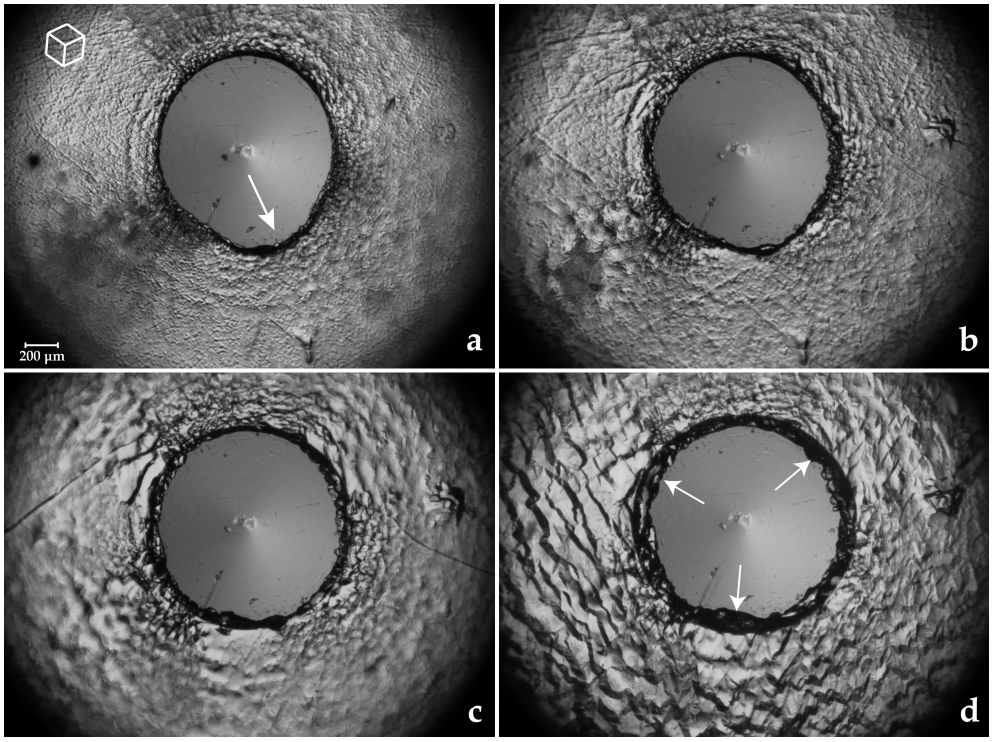

Figure 2.7 Development of the halite–glass contact in the 111NaCl experiment. (a) Approximately 1h after the start of the experiment; note the embayment indicated by the white arrow. (b) After ~1 day. (c) After ~4 days. (d) After ~11 days. White arrows indicate smoother sections sub-parallel to the {100} forms.

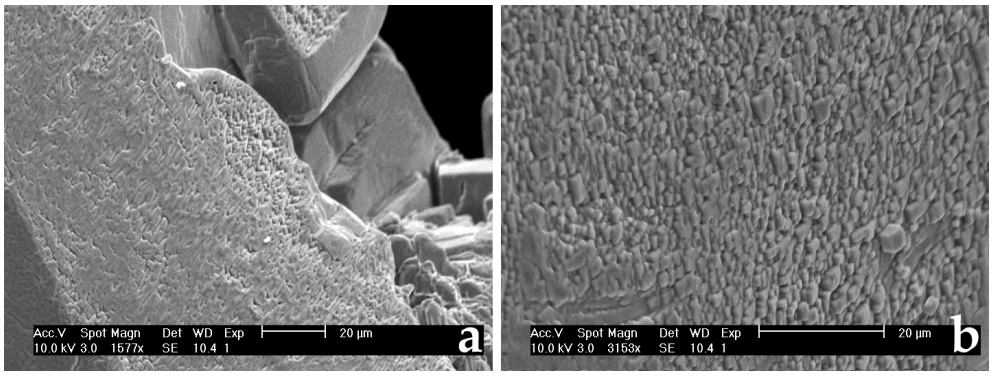

Figure 2.8 Post-mortem SEM SE images of the halite disc from experiment 111NaCl. Both pictures (a, b) show a rough texture on the contact surface.

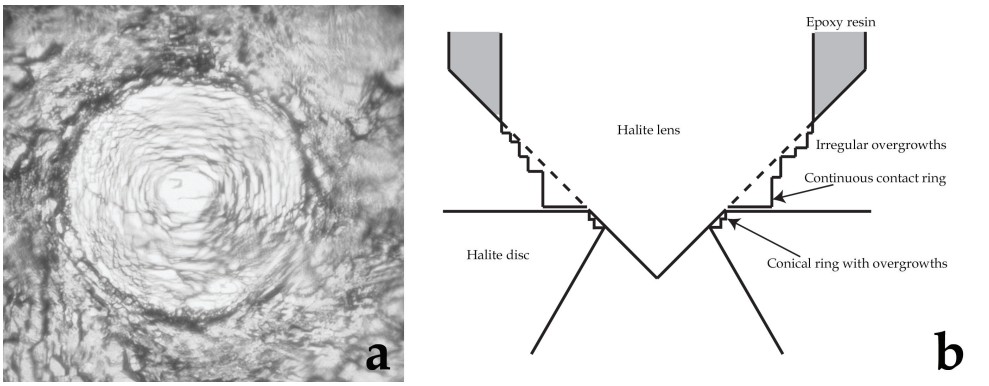

Figure 2.9 (a) The halite–halite contact in the 2NaCla experiment (45° axial rotation) after ~4 days. The contact ring is obscured by overgrowths on both the top surface of the halite disc and the conical surface of the halite lens. The inner diameter of the contact is ~1.1mm. (b) A schematic cross-section through the contact between the halite lens and disc.

of the contact surface upon crystallographic orientation, with the two sectors of the contact ring parallel to the (100) and (010) planes being smoother and flatter than the other regions. Figure 2.6d shows some grooves in the contact surface of the disc that are parallel to the (100) orientation.

In experiment 111NaCl, an embayment in the contact ring was formed at the set-up stage by a small piece of crystal breaking off. However, dissolution of the contact caused the ring to grow beyond this cavity, effectively eliminating it after ~3 days (Figure 2.7). The widening contact ring is clearly visible in Figure 2.7a–d. Furthermore, overgrowths parallel to the {100} forms progressively developed on the top surface of the crystal. The internal structure of the contact ring shows a threefold symmetry with smoother sections sub-parallel to the {100} forms and rougher sections between them. Post-mortem SEM observations made on the 111NaCl contact ring (Figure 2.8) show surface roughness on the micrometer scale over the entire contact ring. This roughness consists of irregular crystallographically controlled grooves and ledges (Figure 2.8a) or has a crystallographically controlled cobbled appearance (Figure 2.8b).

2.4.2 Observations on halite–halite contacts

Figure 2.9 shows the contact developed in experiment 2NaCla, i.e., between two halite crystals rotated by 45° relative to each other about the [100] axis, after ~4 days. The roughness observed around the contact is located on both the conical surface of the halite lens and the top surface of the halite disc. A widening, outward spreading contact ring was observed to develop with time. Post-mortem SEM observations (Figure 2.10) on the crystal disc used in the experiment show a conical ring developed at the contact between lens and disc, covered with crystallographically controlled overgrowths on a scale of 10–50μm with even larger

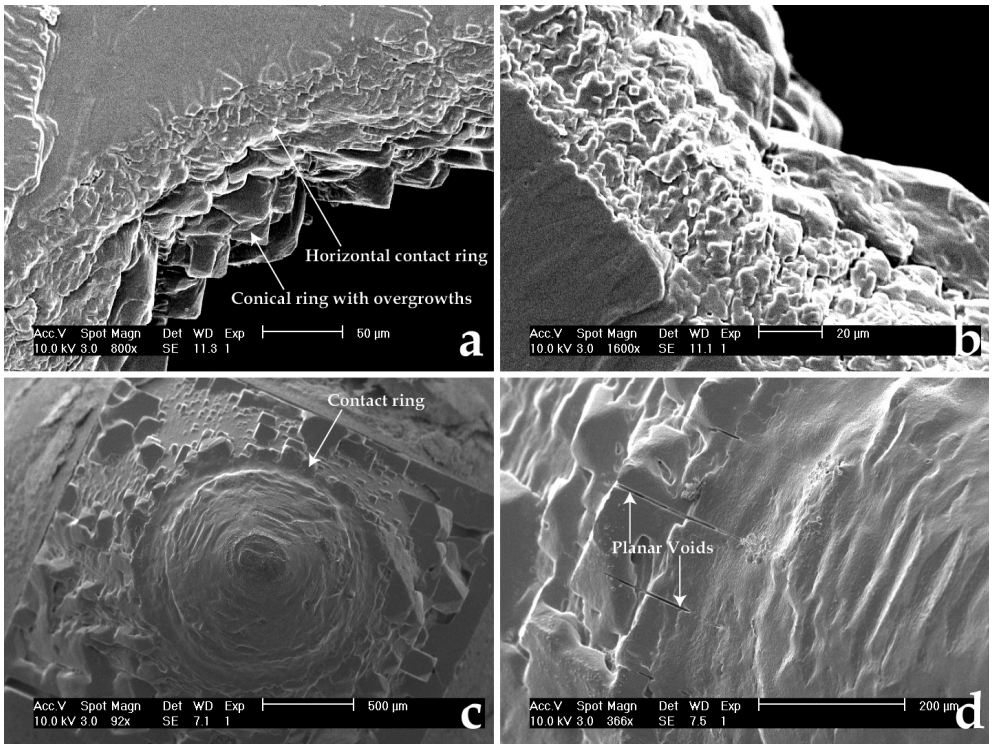

Figure 2.10 Post-mortem SEM SE images of the halite disc from experiment 2NaCla (a, b) and on the halite lens (c, d). A contact ring has formed parallel to the top surface of the halite disc. This ring has a somewhat fingered appearance (see c). (c) Also clearly shows the rectangular cross-section of the halite crystal used as a lens inside the epoxy resin holder.

overgrowths near the inner edges of the hole. Around the hole, on the top surface of the halite disc, a rim containing asperities and channels is observed. Optical observation of the lens crystal showed that during the experiment a collar of salt was deposited on the conical surface of the lens, down to the contact ring (Figure 2.9b). SEM observations on the lens show irregular, crystallographically controlled overgrowths on most of the conical surface of the lens, and a continuous ring around the tip of the lens (Figures 2.9b, 2.10c, d). Figure 2.10d shows a number of planar voids parallel to a (001) face and perpendicular to the contact orientation, which would have been connected to the contact during the experiment.

Figure 2.11 shows the development of the contact in experiment 2NaClb, i.e., between two halite crystals that are loaded with their crystallographic axes aligned in parallel. The ring-shaped contact in experiment 2NaClb is initially hard to see, but after ~6 days a clear, and rapidly outward growing contact zone, with an octagonal outer rim, could be seen. Post-mortem SEM observations (Figure 2.12) did not show a conical contact ring of the type

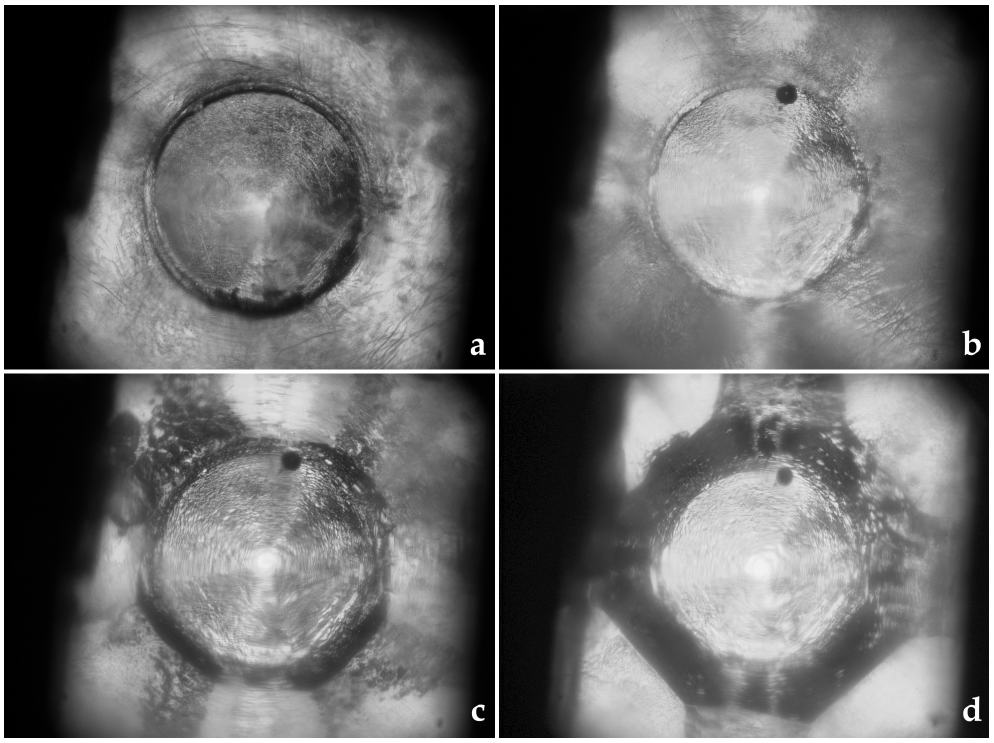

Figure 2.11 Development of the halite–halite contact in the 2NaClb experiment. (a) At the start of the experiment. The second ring around the contact is probably a scratch on the surface of the lens caused by the polishing. (b) After ~2 days. (c) After ~6 days. The octagonal shape of the contact has started to appear. (d) At the end of the experiment, after ~10 days. The contact has an inner diameter of ~1.2mm.

observed in the halite–glass experiments. Instead, along the edge of the hole in the crystal disc a rim of well-aligned coarse (10s of micrometer scale) cubic overgrowths is found (Figure 2.12a). The observed octagonal contact was formed on the top surface of the halite disc, perpendicular to the direction of observation. The optically flat surface of this contact actually has an intricate structure of blocky asperities (Figure 2.12b) seen with the SEM. On the surface of the halite lens, a collar of salt bordered by crystal planes has grown during the experiment. This corresponds to the octagonal contact feature observed optically during the experiments. The contact surface on the halite lens is significantly less rough than the corresponding surface on the disc (Figure 2.12c).

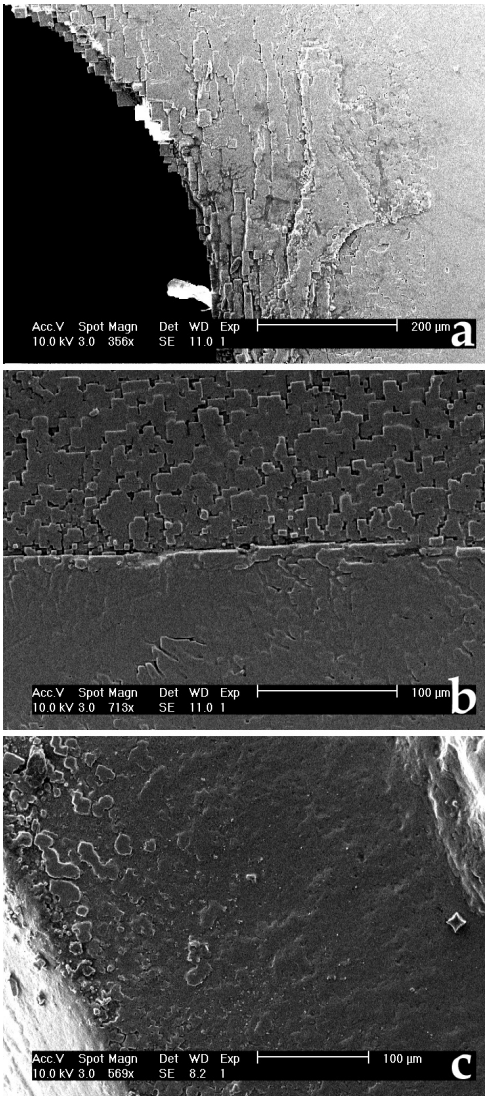

Figure 2.12 Post-mortem SEM SE images of the crystal from experiment 2NaClb. (a) A contact ring as observed in the other experiments did not form during this experiment or was no longer present at the end. (b) The contact surface on the halite disc. The optically flat surface shows an intricate orthogonal, structure of asperities. A sharp edge separates the octagonal contact from the completely flat halite (100) surface next to it. (c) The contact surface on the halite lens appears quite flat showing some structure on the edge of the contact.

2.4.3 Resistivity measurements

Figure 2.13 shows plots of contact resistance versus time for all experiments reported (Table 2.2). Most resistance versus time curves for the halite–glass runs show a rapid initial increase in contact resistance to a peak value, followed by a decrease in resistance to a lower value, which remains roughly stable for the rest of the experiment. For the 100NaCl and 110NaCla experiments the peak is reached after ~1–2 days. The 110NaClb and 111NaCl experiments

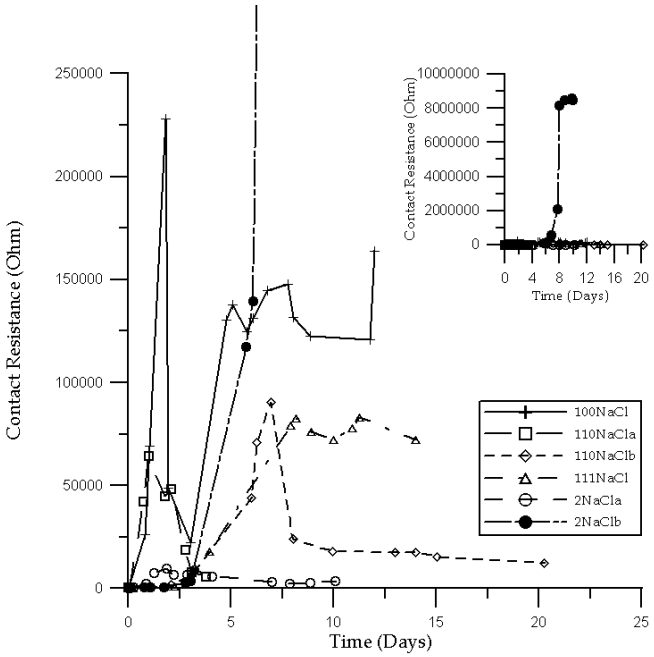

Figure 2.13 Contact resistance versus time plots for the experiments reported here.

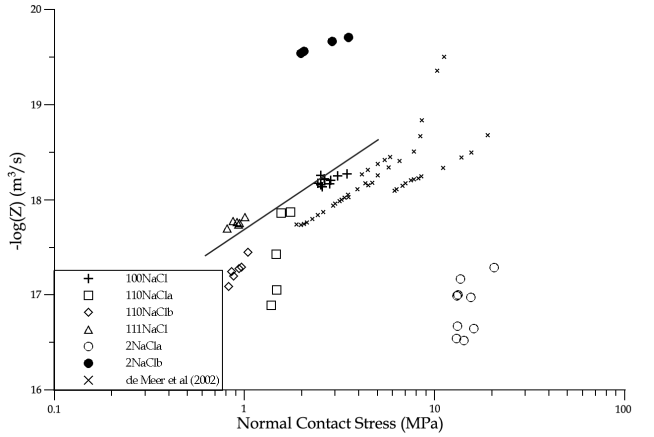

Figure 2.14 Plot of –log(Z) versus normal contact stress for the experiments reported here and by De Meer et al. (2002). Note that pre-peak values are not shown as the (effective) w and therefore Z could not be determined reliably.

do not reach this maximum until after at least 7 days. In the case of the 111NaCl experiment, this delay was caused by elimination of the embayment in the contact rim that formed while the experiment was set up. The strong drop in contact resistance in the 100NaCl experiment was caused by human interference; a bubble of air had formed near the contact ring and in an attempt to expel this bubble new brine was introduced into the cell thus disturbing the evolving halite–glass contact ring.

In experiment 2NaCla (a halite–halite contact with a 45° twist), a peak resistance was reached after ~2 days. This was followed by a period with a roughly stable, lower resistance. The contact resistance in the 2NaClb experiment (0° twist) remained low for ~3 days and then increased rapidly to values of about 8.5MΩ (reached after ~8 days), remaining constant thereafter.

In Figure 2.14, values for the grain boundary diffusivity product (Z) for all our experiments are shown versus the normal stress acting across the contact, together with the data of De Meer et al. (2002). The Z values have been obtained using equation (2.4) and making use of the resistances, widths and radii of the contacts, measured as a function of time. Note that the pre-peak measurements are not included, as an accurate determination of contact width (w) was not possible early in the experiments, and because at this stage a closed contact had probably not formed yet. Note also that while the contact rings in the halite–glass experiments were conical, the contact rings in the halite–halite experiments were observed to be horizontal (and thus perpendicular to the direction of observation). Figure 2.14 shows that for experiments 100NaCl, 111NaCl and 2NaClb the logarithms of the grain boundary diffusivity products increase more or less linearly with decreasing log normal stress following similar trends. In contrast a different, linear trend is observed for experiments 110NaCla and 110NaClb, and no such trend is apparent for experiment 2NaCla. The Z values for halite–glass contacts found here range from 5.5×10^{-19} to 1.3×10^{-17} m^3/s, whereas for halite–halite contacts values of ~1.0×10^{-17} and ~2.4×10^{-20} m^3/s are found for experiments 2NaCla and 2NaClb, respectively.

2.5 Discussion

Using electrical resistivity measurements, we have investigated the dependence of the grain boundary diffusivity product Z of halite–glass contacts during pressure solution on the orientation of the halite crystal. We have also investigated the contact behaviour of two differently aligned halite–halite contacts. We would like to re-emphasise that due to the apparatus used, measurements on a single orientation were not possible and measurements were made on a conical contact ring with an apex angle of 90° and with its axis perpendicular to the top surface of the halite crystal disc – either a (100), a (110) or a (111) plane. Also note that between experiments there are small differences in initial hole shape and size, rim sharpness, degree of contact wetting, and, in certain orientations, the evolution of grooves and similar contact features. Therefore, while similar experiments can be performed, it is impossible in practice to precisely reproduce data from different experiments. This means that there is some variability in the grain boundary diffusivity products reported, but it is unlikely to influence the observed trends in the data seen in Figures 2.13 and 2.14 and discussed below.

In the following, we will discuss the behaviour of the contacts in the halite–glass experiments. We will compare our results with the results of other workers and look at the influence of crystallographic orientation on grain boundary diffusivity products in these contacts. We will then discuss the behaviour of halite–halite contacts, and a comparison will be made between

these two different types of contact based on surface energy considerations. Finally, we will compare the microstructures observed on our contacts with the microstructures observed by other workers on contacts from pressure solution or recrystallisation experiments, and on contacts in natural recrystallised marbles.

2.5.1 Behaviour in the halite–glass experiments

In experiment 100NaCl, an initial increase in contact resistance is observed, caused by the dissolution of contact points and the closure of free-fluid pathways, which results in the formation of a narrow continuous contact. This increase is followed by a drop in contact resistance caused by the removal of a bubble by flushing the contact with fresh brine. Contact resistance then increases again, but values stay below the observed peak. This is most likely a consequence of an increase in contact area and a resulting decrease in contact normal stress, leading to higher grain boundary thickness and or diffusivity (De Meer et al., 2002).

If we now compare our 100NaCl experiment on a polished halite crystal with the experiments by De Meer et al. (2002) who used cleaved halite discs, our in situ observations show that polishing the top surface has a very strong influence on how well the contact ring can be observed. A clear dark ring, as reported by De Meer et al. (2002), is not observed here, as overgrowths on the top surface of the halite disc dominate our observations. The grain boundary diffusivity products measured in our experiment fall in the range $5–7\times10^{-19}m^3/s$, which lies well within the range of 3×10^{-20} to $2\times10^{-18}m^3/s$ as reported by De Meer et al. (see Figure 2.14). Polishing the top surface of the halite disc thus did not influence the grain boundary diffusivity products of the contacts in these experiments. We infer that the rough appearance of the contact ring is caused solely by roughness on the top and bottom surfaces of the halite disc, and not by roughness on the contact surface. As polishing does not influence the diffusivity measurements, the diffusivities measured on differently oriented crystals as reported here can be usefully compared to the values measured on cleaved halite discs.

The post-mortem SEM observations on the contact rings from experiments 100NaCl and 111NaCl show that both the contact surfaces are covered in closely packed, parallel kinks and steps thus giving the contact surface a scaly or cobbled appearance. Crystallographic orientation seems to have had a strong influence on the formation of the (post-mortem) roughness of these contact surfaces. Figure 2.14 shows that the 100NaCl and 111NaCl data fall on a parallel trend (black line) to the trend that can be drawn through the data of De Meer et al. (2002). This indicates that in our experiments a similar dependence of Z on normal stress is found. Furthermore, it shows that this same trend is found in more than one set of orientations, indicating that grain boundary diffusion in grain boundaries with similarly rough (post-mortem) textures is comparable.

Figure 2.13a shows that in both our (110) experiments a peak in resistance is reached, again caused by the dissolution of contact points and the closure of free fluid pathways, resulting in the formation of a narrow continuous contact, followed by a strong decrease in contact resistance. In Figure 2.14, it can be seen that the two earliest Z values of experiment 110NaCla lie on the same trend as the Z values for the (100) and (111) experiments and the experiments of De Meer et al. (2002). However, the remaining 110NaCla and the 110NaClb

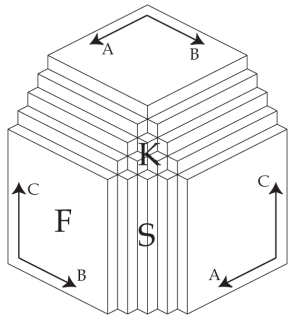

Figure 2.15 The structure of faces in the Hartman–Perdok theory for a cubic crystal (after Hartman and Perdok, 1955). A, B and C indicate three periodic bond chains (PBC's; principal directions of growth). F, S and K indicate a flat face (parallel to at least two PBC's), a stepped face (parallel to one PBC) and a kinked face (not parallel to any PBC's), respectively.

values are relatively high (3.7×10^{-18} to 1.3×10^{-17}m^3/s versus 1.4×10^{-18}m^3/s before the drop) and lie on different trends; increasing more strongly with decreasing normal stress or with progression of the experiment. During the (110) experiments, spots of bright contrast, which post-mortem SEM observations showed were related to areas of increased roughness and irregular voids, were assimilated in the contact ring. Optical observations showed that the timing of this assimilation approximately coincides with the decrease in contact resistance. SEM observations also revealed the existence of grooves inside the contact sub-parallel to the (100) orientation of the salt disc. None of the larger scale roughness features found in the (110) experiments (grooves, irregular voids) were found on the contact surfaces of experiments 100NaCl and 111NaCl. Even though these SEM observations are post-mortem, optical observations made during the experiments did reveal the presence of some anomalies around the contact ring. The fact that these anomalies can be related to irregular voids and rough patches in the post-mortem SEM observations indicates that it is likely that these roughness features were present in a similar form in the stressed contact. Once these grooves and other large-scale roughness features formed in the contacts, they provided free fluid pathways for diffusion, thus leading to an increase in the observed average grain boundary diffusivity product of the contact rings. Different degrees of contact roughness formed in experiments 110NaCla and 110NaClb could explain the differences in contact diffusivity between these two experiments. It is unlikely that the grain boundary diffusivity products measured in experiments 100NaCl and 111NaCl were influenced by grooves and similar coarse roughness features on the contacts as no such features were observed.

It has already been mentioned that the two Z values obtained in the 110NaCla experiment, before the drop in contact resistance, fall on approximately the same trend as the values measured in the (111) and (100) experiments (see Figure 2.14). The Z values measured after the drop in contact resistance fall on a steeper trend. This may indicate that there is a stronger dependence of Z on normal stress in these contacts, but the effect could also be caused by increasing contact roughness with time, independently of the normal stress across the contact. This would suggest a contact structure that evolves with time (c.f. Dysthe et al., 2003).

The orientations of the contact rings on the salt crystals in our experiments coincide mainly with K-forms or kinked forms in the Hartman–Perdok theory of crystal growth (Hartman and

Perdok, 1955)—see Figure 2.15. Post-mortem SEM observations revealed all surfaces in these orientations to be rough and to have a cobbled or scaly appearance. Part of the contact ring in the (100) experiments is parallel to the {110} form. This is an S-form (stepped form), and it has a stepped appearance in the post-mortem SEM observations with steps on a micrometer scale comparable to the scale of the kinks observed elsewhere on the contact ring. In the (110) experiments, part of the contact is parallel to the {100} form and this F-form (flat form) indeed appears as a flat face in our SEM observations. Crystallographic orientation thus seems to have a strong control on the orientation and texture of the postmortem roughness of pressure dissolved surfaces. Unfortunately our study cannot fully confirm if crystallography has an equally strong influence on the surface relief of the contact during pressure solution. However, the fact that the grooves, irregular voids and rough patches were only observed in the (110) experiments indicates that the orientation of the contact must have had some influence on their formation. De Meer et al. (2005) report that the thickness and the grain boundary diffusivity product of a fluid film between a halite and a fluorite surface depend on the orientation of the crystal. They found a fluid film thickness of 85–185nm for the (111) halite face and a thinner film of ~40nm for the (100) halite face. A value in the range 8.7×10^{-11} to $1.0\times10^{-10}m^2/s$ was found for the diffusion coefficient through the (111) contact, but for the (100) face a diffusion coefficient could not be derived (dissolution was observed to be slower). The structure of the (100) fluid film in their investigation was inferred to be a rough island-channel network, but on a finer scale than the (111) film. Postmortem AFM observations on the contact surface of the crystal used in the (111) experiment of De Meer et al. (2005) showed the existence of a roughness with an amplitude of 150–200nm (similar to the fluid film thicknesses measured) on a length scale of ~10μm (De Meer et al., 2005). This is similar in scale to the post-mortem roughness observed on our (K-type) contact surfaces. Hickman and Evans (1991, 1995) report thin fluid films with a thickness of <30nm for their halite (100)–glass contacts. Schenk et al. (2006) studied recrystallisation in halite aggregates using a cryo-SEM. They also observed fluid-filled grain boundaries with a thickness of <30nm (on migrating (100) faces).

Our own results coupled with the work done by De Meer et al. (2005) thus indicate that there is a dependence of grain boundary diffusivity product on the type (F-, S- or K-face) of halite face against which the halite–glass (or halite–fluorite) contact is formed. Unfortunately, our attempts at measuring the resistivity of contacts with a specific orientation, using a glass lens with a roof-shaped tip in the described apparatus, failed. Therefore, only conical ring-shaped contacts could be investigated. Comparison of the (110) experiments with the other experiments nonetheless shows that diffusion through the rougher (110) contacts was up to one order of magnitude faster. The roughness of a pressure dissolving contact surface, at least in post-mortem SEM observations seems to be controlled by crystallography, with F-, S- and K-faces having markedly different structures, and with steps and kinks on the contact surfaces being parallel to the principal {100} orientations.

Another explanation for the variation of contact roughness with orientation would be the effect of orientation dependent dislocation activity or density. The main slip system in NaCl at room temperature is the <110>{110} system (slip along {110} planes). It is expected that when dislocation activity is the main factor determining contact roughness, the roughness will be mainly oriented parallel to {110} planes. However, we observed contact roughness

parallel to the {100} orientation. Therefore, dislocation-related effects are considered not to be the main cause of the orientation dependence of contact roughness.

If we compare the range of grain boundary diffusivity products we found (2×10^{-18} to $5\times10^{-19}m^3/s$) in our 100NaCl and 111NaCl experiments with those of others we find that our values fall in the range found by De Meer et al. (2002), but are somewhat higher than the 5×10^{-20} to $5\times10^{-19}m^3/s$ found by Schutjens and Spiers (1999) for halite–halite contacts and the 4×10^{-20} to $2\times10^{-19}m^3/s$ found by Hickman and Evans (1995) for halite–glass contacts at 50°C (recalculating their values to room temperature using an activation energy of 24.5 kJ/mol (Spiers et al., 1990) decreases these values by about a factor 2). Our 110NaCl experiments give higher values still but, as discussed above, these values were largely controlled by the grooves and other roughness features on the contact rings.

Dysthe et al. (2002a) did molecular dynamics simulations on thin fluid films between calcite (104) faces. The simulation most relevant to our measurements (1km depth) indicated a wall separation of more than 8nm (the maximum for their simulation). Estimating a grain boundary diffusivity product for halite diffusion at room temperature from their water self-diffusion coefficient gives a value of $\sim2.7\times10^{-18}m^3/s$ (Vanýsek, 2006; Atkins and de Paula, 2002; Wang, 1951). This is comparable to the values we found for our 100NaCl and 111NaCl contacts, though, as indicated by Dysthe et al. (2002a), their model is much simplified and their simulations were mainly aimed at investigating the evolution of grain boundary diffusivity with depth.

2.5.2 Behaviour in the halite–halite experiments

A second series of experiments was done in which two different halite–halite contacts were investigated. In experiment 2NaCla the orientation of the halite single crystal disc is twisted approximately 45° along the [100] axis relative to the orientation of the lens. SEM observations on the crystal and the lens showed that a narrow contact ring has formed parallel to the top surface of the halite disc by precipitation on the halite lens surface. This continuous ring that was seen to grow outward during the experiments is quite regular when compared to the overgrowths on the rest of the conical lens surface. This seems to indicate that the ring was formed by some sort of neck growth mechanism, whereas the more irregular crystal growth elsewhere on the conical surface was driven by surface energy anisotropy. There is no evidence for convergence of the two crystals by contact dissolution during this experiment. Hickman and Evans (1991, 1992) also reported neck growth to operate in their salt-on-salt experiments. The occurrence of precipitation mainly on the lens surface, and not on the halite disc surface is in agreement with surface energy considerations, as the top surface of the disc was a (100) F-face, whereas most of the conical lens surface orientations were parallel to either S- or K-faces. The contact ring on the lens has a fingered appearance with fingers parallel to the [100] directions of the lens crystal. A similar contact was observed to grow in the halite–halite contact experiments of Hickman and Evans (1991, 1992). The high grain boundary diffusivity products (5×10^{-18} to $3\times10^{-17}m^3/s$) are about one order higher than measured for the halite–glass contacts. This can be explained by the presence in the contact surface of the lens of planar voids perpendicular to this surface, parallel to the (001)

plane. These voids provided free fluid channels through which faster diffusion could occur, and thus influenced the contact diffusivity measurements. As these voids are located in the overgrowths on the lens, and as they are oriented parallel to the direction of growth of these overgrowths, they are likely to be some sort of growth features such as inclusions. An effect of twist-misorientation on the grain boundary diffusivity product cannot be excluded.

In experiment 2NaClb the halite disc and lens were aligned with zero twist. An octagonal contact develops, again by what appears to be some sort of neck-growth process rather than convergence of the crystals, with deposition occurring on the lens surface. The rate at which this contact spreads is much higher than in experiment 2NaCla. The appearance of this contact ring occurs just prior to the observed rapid increase in contact resistance. Post-mortem SEM observation reveals a smooth, flat contact surface on the lens, but a rough surface of parallel-sided, micrometer scale, rectangular asperities on the halite disc. Outside of the presumed original contact surface on the disc, a smooth, flat surface is observed. It seems very unlikely that the rough surface formed after the experiment only where there was originally a contact, with such a sharp transition between flat and rough sections. Therefore it is assumed that this roughness was also present in the contact during the experiment. The grain boundary diffusivity product in the halite–halite contact, $2.0–2.9\times10^{-20}$m^3/s, is 2–3 orders of magnitude lower than in the other halite–halite contacts and ~1.5 orders of magnitude lower than measured in our halite–glass contacts.

2.5.3 Comparison of halite–glass and halite–halite experiments

We will now try to analyse and explain the different behaviours of halite–glass and halite–halite contacts, and the influence of relative orientation of the two crystals in a halite–halite contact. We observed relatively fast neck growth for a contact between two well-aligned halite crystals, slower neck growth for a 45° twist-misorientation halite–halite contact and no neck growth for halite–glass contacts. Hickman and Evans (1992, 1995) reported similar findings. For equilibrium at unstressed grain boundaries in isotropic materials the Young–Dupre relation applies:

$$2\gamma_{sl}\cos\left(\frac{\theta_{eq}}{2}\right) = \gamma_{ss} \tag{2.5}$$

Here γ_{sl} represents solid–liquid interfacial energy, γ_{ss} solid–solid interfacial energy and θ_{eq} equilibrium dihedral angle. A lower γ_{ss} value thus means a higher dihedral angle and therefore, in an otherwise unchanged setup, a stronger driving force for neck growth. In the case of an interface between two (chemically) identical materials, such as our halite–halite contacts, the nature of the interface, and thus γ_{ss}, depends on the misorientation of the two solids. A grain boundary with a low misorientation angle (<10–15°) can be considered as an array of dislocations and for such a boundary γ_{ss} is proportional to the dislocation line length per unit area and hence to the angular misorientation (Porter and Easterling, 1992). For boundaries with a higher misorientation, γ_{ss} becomes independent of the misorientation

angle, and has a value of approximately $\frac{1}{3}\gamma_{sv}$; γ_{sv} being the solid–vacuum equilibrium interfacial energy (Porter and Easterling, 1992). Note that for non-isotropic solids the surface free energy would also depend on the orientation of the interface. The differences in neck-growth velocity observed in our halite–halite experiments thus are well explained by the above equation. It seems reasonable to expect that a contact between halite and glass (two very dissimilar materials) has a higher interfacial energy than a high angle halite–halite boundary. This implies that for halite–glass contacts there is less driving force for neck growth then for halite–halite contacts. This could then explain why pressure solution rather than neck growth occurred during our halite–glass experiments (c.f. Schutjens and Spiers, 1999).

2.5.4 Grain boundary structures: Comparison with previous observations

SEM observations on the contacts from our experiments showed grain boundary structures on most contacts consisting of micrometer scale kinks or steps, grooves, asperities and channels, all strongly controlled by crystallography. This gives these contacts a scaly, cobbled or blocky appearance. In experiments 110NaCla, 110NaClb and 2NaCla, larger grooves or voids and patches of increased (larger scale) roughness are observed. In experiments 110NaCla and 110NaClb, the contact planes parallel to the (100) faces are flat, whereas in both halite–halite experiments networks of asperities and channels are observed on the (100) contact faces of the single crystals. In experiment 2NaCla, this network consists of irregular asperities and channels, whereas in experiment 2NaClb it consists of an intricate structure of blocky asperities.

Cox and Paterson (1991) performed pressure solution experiments on quartz aggregates at very high temperatures (1200K). They report microstructures with ~0.5μm wide, 0.1μm high ridges and plateaus on many of their grain interfaces. They do not report any strong crystallographic control on the development of these microstructures. Den Brok (1998) reports pressure solution experiments on quartz performed at 1073K. He shows a contact structure consisting of 3–5μm wide asperities with ~1μm wide channels in between. These channels are formed by microcracks and the author reports that the directions of these microcracks are controlled by crystallography. The scale of the roughness observed by Den Brok for pressure-dissolved quartz contacts is similar to the scale of the roughness we observed in halite–glass and halite–halite contacts. Furthermore, his experiments, like ours, showed a crystallographic control on contact roughness. In the pressure solution experiments of Dysthe et al. (2003), gold wires were used to indent halite single crystals. The microstructures of the contacts were studied under the microscope and all contacts showed a shell-like or island-channel structure with 2– 6μm large plateaus separated by channels (1μm deep) and pits (3μm deep). A crystallographic control on contact roughness is not discussed. Still, the contact structures observed by Dysthe et al. (2003) are very similar to the contact structures observed in this study. The morphological similarities between the contact structures observed in the experiments of Cox and Paterson (1991), Den Brok (1998) and Dysthe et al. (2003), and the contacts seen in our experiments suggest that in all cases these structures were controlled by similar processes, i.e., some non-equilibrium interaction between surface energy driven ‘‘healing’’ and irregular dissolution at stress concentrations.

Schenk and Urai (2004) studied the structure of grain boundaries formed during experimental static recrystallisation of halite. Mixtures of halite crystals in brine were compressed at high stress (150MPa) for a few minutes and then annealed at room temperature, allowing the samples to recrystallise. Grain boundary structures were studied in a SEM. The deformed, not recrystallised grains showed rough (micrometer scale) grain walls with cracks 10s of micrometers long. Recrystallised grains (and their imprints) on the other hand had smoother grain walls, with some parallel ridges a few micrometers apart, which were interpreted to be related to dislocation networks in the old grains. The structures observed on grain boundaries formed under stress are comparable to the structures reported by us. However, the structures of grain boundaries formed during static recrystallisation are quite different. Schenk et al. (2005), studying natural, recrystallised marble mylonites observed smooth grain boundaries with triangular, crystallographically controlled pores. There is also evidence of a connected network of triple-junction tubes. This grain boundary structure is very different from the grain boundary structures formed during pressure solution that are described above, but similar to the recrystallised grain boundary structures described by Schenk and Urai (2004). These smooth structures seem to represent an equilibrium configuration, whereas the rough grain boundary structures observed in pressure solution experiments (e.g., this study; Dysthe et al., 2003) and on plastically deformed grains (Schenk and Urai, 2004) represent non-equilibrium structures.

2.5.5 Implications

Our experiments on halite–glass contacts have shown that there is a dependence of electrical resistivity and hence diffusive properties on the orientation of the contact relative to the halite lattice. Post-mortem SEM observations coupled with in situ optical observations show that contact roughness also depends on contact orientation. The implication is that a rougher contact has a higher grain boundary diffusivity product. This further implies that diffusion and hence diffusion controlled pressure solution are slower on contacts of certain orientations (F-faces) than on others. In addition, on boundaries with low solid–solid interfacial energy, neck growth will occur, as seen in our halite–halite contact experiments. Contrary to conventional expectations, this means that pressure solution in halite may lead to the formation of a lattice-preferred orientation. Similar effects can be expected to occur during pressure solution creep of other rock materials, especially for minerals with a strongly PBC-controlled dissolution and growth habit. Furthermore, as grain boundary structure and fluid film thicknesses vary with orientation of the contact, it seems reasonable to suppose that additional seismic and electrical anisotropy effects can be expected in water-bearing rocks that (already) show lattice-preferred orientations.

The differences in contact development between our halite–glass and our halite–halite contact experiments imply that care should be taken when applying data acquired from contacts between two different minerals to contacts between two similar minerals. Intergranular pressure solution may occur at lower stresses and higher rates in polymineralic rocks than in monomineralic rocks, since the latter are more prone to neck growth or grain boundary healing. This has also been noted by other workers for halite–glass contacts (Hickman and Evans, 1991, 1995) and halite–calcite granular mixtures (Zubtsov et al., 2004).

2.6 Conclusions

Our halite–glass contact experiments coupled with the work done by De Meer et al. (2005) indicate that for halite–glass and halite–fluorite contacts there is a dependence of the grain boundary diffusivity product (Z) on the type of halite face (F-, S- or K-face) that forms the contact. SEM observations show that contact surfaces parallel to F-, S- and K-faces have markedly different post-mortem structures. However, the grain boundary diffusivity products for contacts with similar roughness are of similar magnitude. The assimilation of larger scale roughness features such as irregular voids and grooves into the contact ring was observed to have a strong influence on the average grain boundary diffusivity product, increasing this by up to an order of magnitude in our experiments.

Our experiments have not enabled us to determine the diffusive properties of contacts with a single orientation. Nonetheless, our results do support the notion that orientation is important in determining contact diffusivity, primarily through a PBC-dependent crystallographic control on contact roughness. Our halite–halite contact experiments show that interfacial energies have a strong influence on the rate of neck-growth. Furthermore, the diffusivity products of halite–halite grain boundaries appear to be different from those of halite–glass boundaries and may have been influenced by grain boundary misorientation. Our results imply that pressure solution may lead to the formation of a lattice-preferred orientation in rocks, as certain contacts will allow faster dissolution and diffusion than others, whereas in yet other contacts neck-growth will occur. This lattice-preferred orientation plus resulting preferred orientation of wetted grain boundaries can in turn lead to seismic and electrical anisotropy. A comparison between the results from our halite–glass and halite–halite experiments implies that at lower stresses polymineralic rocks may deform faster by pressure solution than monomineralic rocks. Hence, care should be taken when applying data obtained from experiments on contacts between two dissimilar materials to contacts between two similar materials.

3. Influence of grain boundary structure on dissolution controlled pressure solution and retarding effects of grain boundary healing

This chapter was published as: Van Noort, R., H. J. M. Visser and C. J. Spiers (2008), Influence of grain boundary structure on dissolution controlled pressure solution and retarding effects of grain boundary healing, J. Geophys. Res. 113, B03201, doi:10.1029/2007JB005223.

Abstract

It is widely accepted that the structure of a grain boundary undergoing pressure solution can have a strong influence on the rate at which diffusive transport in the grain boundary occurs. However, the influence of grain boundary structure on internal grain boundary dissolution rates has received little attention, despite evidence that dissolution controlled pressure solution in quartz is slower than expected assuming dissolution kinetics appropriate for free surfaces. In this chapter, three hypothetical steady state grain boundary structures are defined and the influence of these structures on dissolution controlled pressure solution rates in an elastic solid are considered by deriving simple models based on internal grain boundary mass and energy balances. It is found that average dissolution rates in a rough grain boundary (island-channel network) are slowed down by up to 13% compared to dissolution in a flat grain boundary containing a thin fluid film. This can only partly account for the discrepancy between models and experiments reported in the literature. In addition a model is derived providing a criterion or "yield stress" for pressure solution, below which the process is prevented by surface energy driven grain boundary healing (progressive reduction of the contact area filled by connected fluid). This "yield stress criterion" for pressure solution offers a further explanation for reduced rates or cessation of pressure solution at low effective stresses in nature and experiment. Using this criterion, limiting porosity depth curves are predicted for sandstones compacting by pressure solution, which show favorable agreement with porosity-depth data for quartz sandstones.

3.1 Introduction

Intergranular pressure solution is an important mechanism of time-dependent deformation and compaction in wet rocks and fault zones in the middle and upper crust (Elliott, 1973; Rutter, 1983; Tada et al., 1987; Renard et al., 1999, 2000; Revil, 2001; Bos and Spiers, 2002a, 2002b). In a chemically closed system, creep by intergranular pressure solution involves three processes operating in series. These processes are dissolution of the stressed solid into the grain boundary fluid phase, diffusion of dissolved material out of the grain boundary through this fluid, and deposition of the dissolved solid onto free pore walls (e.g., Raj, 1982; Rutter, 1983; Lehner, 1990). In an open system, dissolved material can also be transported in or out of the system by fluid flow and/or long-range diffusion (Lehner, 1995; Gundersen et al., 2002).

The structure of grain boundaries undergoing pressure solution has been much debated over the last few decades. Grain boundary models vary from (a) thin (~1nm) fluid films

maintained by conventional surface forces, i.e., competition between Van der Waals, electric double layer and/or hydration forces (Weyl, 1959; Rutter, 1976, 1983; Hickman and Evans, 1991, 1992, 1995; Renard and Ortoleva, 1997; Renard et al., 1997; Alcantar et al., 2003; Meyer et al., 2006), or by repulsive steric forces acting between protruding silicic "hairs" (Revil, 2001) to (b) dynamically wetted island-channel networks (Elliott, 1973; Raj, 1982; Lehner, 1990; Schutjens and Spiers, 1999; Ghoussoub and Leroy, 2001; De Meer et al., 2002, 2005; Dysthe et al., 2003; Van Noort et al., 2006, Chapter 2), to (c) thin films of the type mentioned above short-circuited by fluid inclusions, channels or crack arrays (Gratz, 1991; Den Brok, 1998; Renard et al., 1999).

These grain boundary models are illustrated in Figure 3.1. Much of the debate on which of the models applies to the structure of actively pressure dissolving grain boundaries has focused on whether or not dynamically wetted island-channel networks can persist in a dynamically stable condition or will be eliminated by grain boundary healing phenomena (e.g., Hickman and Evans, 1995). Much attention has also been directed at the extent to which grain boundary structure might reduce diffusion rates in grain boundaries undergoing pressure solution.

The type of structure present in grain boundaries undergoing intergranular pressure solution is expected to exert a strong influence on the rate of diffusive transport in the grain boundary, as the effective grain boundary diffusivity, expressed as the product $\tau D\delta C$, is influenced by the degree of grain boundary wetting, the mean thickness of the fluid film (δ), the tortuosity of the diffusion pathway (τ) and, in the case of thin fluid films, a possible structuring of the fluid and an associated reduction of the diffusion coefficient (D) or solid solubility (C) in the film (Rutter, 1976, 1983; Hickman and Evans, 1995; Alcantar et al., 2003; De Meer et al., 2005). Early estimates of the grain boundary diffusion coefficient (D) in a thin fluid film, based on changes in fluid viscosity induced by molecular structuring of the adsorbed film, were about 5 orders of magnitude lower than in bulk water, (Rutter, 1976, 1983). More recent work on diffusion controlled pressure solution in halite suggests that, whether of thin fluid film or island-channel type, fluid-filled grain boundaries undergoing pressure solution are characterised by a diffusion product τDC about one to two orders of magnitude lower than the value for diffusion in a film of uniform thickness ($\tau = 1$) with bulk solution properties (Hickman and Evans, 1995; Schutjens and Spiers, 1999; Renard et al., 1999; De Meer et al., 2002, 2005; Van Noort et al., 2006, Chapter 2). Assuming C is not affected by film thickness, a similarly modest reduction of diffusivity values has been predicted for uniform thin films in quartz (e.g., Renard et al., 1999; Revil, 2001), and have been measured for the diffusion of ions through thin water films between mica surfaces (Alcantar et al., 2003). Such rather high values imply that in materials with relatively slow surface reaction kinetics, such as quartz, grain boundary dissolution may often control the rate of intergranular pressure solution, notably at porosities of more than ~20% where the total surface area of grain contacts is smaller than the total pore wall area. However, aside from a note by Lehner (1990) on the likelihood of some reduction of dissolution rate coefficient in stressed grain boundaries compared with dissolution at free surfaces, the effect of grain boundary structure on the rate of dissolution controlled pressure solution has not yet been considered.

In this chapter, three hypothetical steady state grain boundary structures will be examined and the influence of these structures on dissolution controlled pressure solution rates in elastic solids will be investigated by deriving expressions for the ratio I^*/I, where I^* is the macroscopic rate constant for grain boundary dissolution during pressure solution, and I is the standard geochemical dissolution rate coefficient for a free surface ($I = k_+\Omega$). Our approach is based on a consideration of internal grain boundary mass and energy balances. It is found that for the conditions considered the dissolution rates for an island-channel grain boundary can be expected to be slowed down by up to 13% compared to dissolution rates derived assuming a thin film structure with $I^* = I$. Since much previous discussion of the structure of grain boundaries during pressure solution has focused on whether or not a non-equilibrium (dynamically wetted) island-channel network can exist stably (e.g., Hickman and Evans, 1991, 1992, 1995; Schutjens and Spiers, 1999; Ghoussoub and Leroy, 2001; De Meer et al., 2002, 2005; Jordan et al., 2005; Karcz et al., 2006; Koehn et al., 2006), we go on to derive a model predicting the stress conditions under which a dynamically wetted island-channel structure can be maintained as opposed to healing by surface energy driven growth of islands. This model predicts the existence of a "yield stress" for pressure solution, below which the process is slowed down and ultimately prevented by grain boundary healing (c.f. Revil, 2001, and Revil et al., 2006).

3.2 Theoretical background

Numerous authors have derived theoretical relations for the strain rate ($\dot{\varepsilon}$) due to dissolution controlled pressure solution in a closed system consisting of an aggregate of regular grains penetrated by a pore fluid phase (e.g., Raj, 1982; Lehner, 1990, 1995; Niemeijer et al., 2002). These equations all take a similar form. This is given by Niemeijer et al. (2002) and Spiers et al. (2004) for the case of uniaxial compaction creep of a porous aggregate as:

$$\dot{\varepsilon} = G\frac{I^*}{d}\left[\exp\left(\frac{B(\phi)\sigma_e\Omega_s}{RT}\right) - 1\right]f(\phi) \approx G\frac{I^*}{d}\frac{B(\phi)\sigma_e\Omega_s}{RT}f(\phi) \tag{3.1}$$

where the approximation ($e^x - 1 \approx x$) is valid for low effective stresses σ_e (Niemeijer et al., 2002). Here G is a geometric constant dependent on grain packing, d is the grain size (m), R is the gas constant (Jmol^{-1}K^{-1}), T is absolute temperature (K), Ω_s is the molar volume of the solid (m^{3}mol^{-1}), and $f(\phi)$ and $B(\phi)$ are dimensionless functions of porosity accounting for porosity-dependent changes in grain contact area and stress concentration. Recall that the kinetic coefficient I^* (ms^{-1}) is the macroscopic rate constant for grain boundary dissolution during pressure solution. In all previous treatments of dissolution controlled pressure solution (e.g., Lehner, 1990, 1995; Niemeijer et al., 2002; Gundersen et al., 2002), I^* is defined either implicitly or explicitly through the dissolution velocity relation:

$$\bar{V} = I^*\left[\exp\left(\frac{\Delta\bar{\mu}}{RT}\right) - 1\right] \approx I^*\left(\frac{\Delta\bar{\mu}}{RT}\right) \tag{3.2}$$

which gives the velocity of grain boundary dissolution $\bar{V}$ (ms^{-1}), i.e., the rate with which the contact approaches the center of the grain, in terms of the interfacial chemical potential drop $\Delta\bar{\mu}$ (Jmol^{-1}) between the stressed solid in the grain boundary wall ($\bar{\mu}_{gb}$) and the solid dissolved in the grain boundary fluid (μ_s). As shown by Lehner (1990, 1995), $\bar{\mu}_{gb}$ should be thought of as the average chemical potential of the solid at the inner margin of the grain boundary zone (on S'_{gb} in Figure 3.1) rather than at the solid-fluid interface, while I^* is a kinetic coefficient that accounts for all dissipative processes occurring in the grain boundary zone, including not only dissolution, but also phenomena such as plastic deformation of the solid phase. I^* also accounts for effects of partial wetting of the grain boundary zone, in the case of an island-channel structure.

In computing rates of dissolution controlled pressure solution it is generally assumed that $I^* = I$, where I is defined through the relation:

$$v_{dis} = I\frac{\Delta\mu}{RT} \tag{3.3}$$

for the velocity of dissolution of a solid with excess chemical potential $\Delta\mu$ over its dissolved equivalent (Shimizu, 1995; Renard et al., 1999; Revil, 2001; Gundersen et al., 2002; Niemeijer et al., 2002). Strictly speaking, however, this assumption is incorrect since in general $I^* < I$, due to incomplete grain boundary wetting (island-channel structure), inelastic deformation of islands (island-channel structure) and/or structuring of the fluid phase (thin film model) (Lehner, 1990). Significantly, models based on the assumption $I^* = I$ seem to overestimate experimental pressure solution rates by more than half an order of magnitude (Niemeijer et al., 2002), as well as overestimating natural pressure solution rates (e.g., Revil, 2001; Gundersen et al., 2002). Clarification of the role of grain boundary structure on dissolution controlled pressure solution is therefore needed.

3.3 Conservation equations for grain boundaries undergoing pressure solution

We approach the problem of dissolution controlled pressure solution by considering the effect that three different, hypothetical grain boundary structures have on the macroscopic rate constant for dissolution in the grain boundary during the process of pressure solution. The models considered are 1) the thin film model, 2) a cylindrical island-channel model, and 3) a bar-shaped island-channel model. In each case, a loaded, fluid-filled contact between

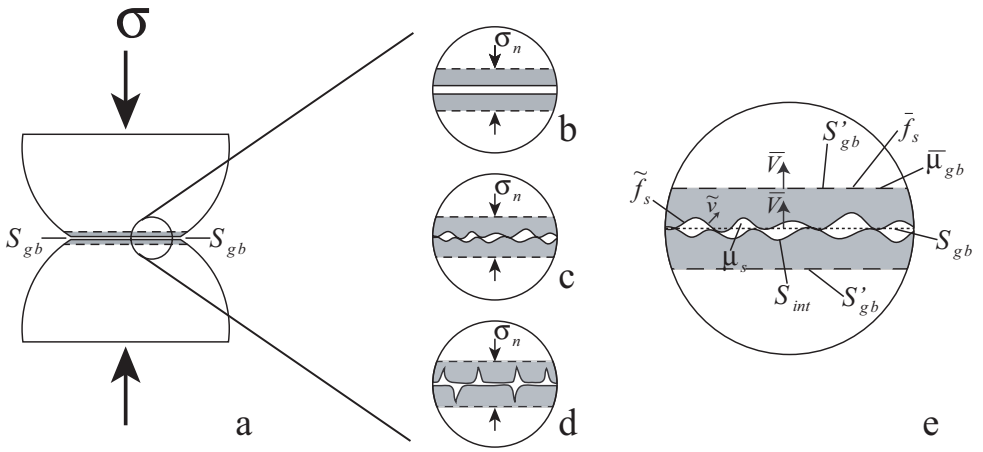

Figure 3.1 A pressure-dissolving grain contact and its internal structure viewed at grain scale (a) and at the scale of representative elementary volumes (b-e). (b) A thin film grain boundary (e.g., Hickman and Evans, 1995). (c) An island-channel network (e.g., Lehner, 1990). (d) A thin film short-circuited by crack arrays (e.g., Renard et al., 1999). (e) A close-up of the island-channel network in shown in (c), showing the various quantities used in equation (3.4) (after Lehner, 1990). The grain boundary zones are indicated in grey. S_{gb} *indicates the nominal (grain scale) grain boundary,* $\bar{V}$, $\bar{f}_s$ *and* $\bar{\mu}_{gb}$ *are the average dissolution rate normal to* S_{gb}*, the average Helmholtz free energy, and the average chemical potential on it. The surfaces* S'_{gb} *represent the margins of the grain boundary zone.* S_{int} *is the actual solid-fluid interface,* $\tilde{v}$ *and* $\tilde{f}_s$ *are respectively the local dissolution rate normal to* S_{int}*, and the Helmholtz free energy on* S_{int}*, and* μ_s *is the chemical potential of the solid dissolved in the grain boundary fluid.*

two soluble, isotropic solid grains deforming by pressure solution is considered, assuming a steady state process. Taken on average, the grain boundary structure is assumed to be constant, though locally the island structure considered will vary with time (a dynamically stable, steady state structure). Following Lehner (1990), at the grain scale the grain boundary can be considered as a surface (S_{gb}) on which smoothly varying values of free energy and normal contact stress (σ_n) can be defined (see Figure 3.1). This applies for the thin film and the island-channel models. For the island-channel model, it is assumed that the roughness is maintained as a result of non-uniform dissolution associated with defects (e.g., dislocations and impurity atoms), heterogeneities in solid deformation, and crystallographically controlled interface kinetics (Spiers and Schutjens, 1990).

3.3.1 Energy/entropy balance

Focusing now on a representative elementary volume of grain boundary with island-channel structure (Figures 3.1c, 3.1e), then along the solid-fluid interface (S_{int}), micro-scale values of free energy vary continuously and the normal stress is equal to the fluid pressure (P_f), as illustrated in Figure 3.1e. The average free energy $\bar{f}_s$ of the solid, and the average normal stress σ_n for the grain boundary element, are defined on the surfaces S'_{gb} at the margin of the grain boundary zone. The energy/entropy balance for such a zone is given by Lehner (1990) as:

$$\frac{\bar{V}S'_{gb}}{\bar{\Omega}}\left[\left(\bar{f}_s + \sigma_n\bar{\Omega}\right) - \mu_s\right] = \int_{S_{\text{int}}} \frac{\tilde{v}}{\tilde{\Omega}}\left[\left(\tilde{f}_s + P_f\tilde{\Omega}\right) - \mu_s\right]ds \tag{3.4}$$

In this relation $\bar{f}_s$ represents the Helmholtz free energy of the solid averaged along S'_{gb}, $\tilde{f}_s$ represents the local values of the Helmholtz free energy along S_{int}, ds represents an infinitesimal small element of S_{int}, and μ_s represents the chemical potential of the solid in the grain boundary fluid. Since steady state is assumed, the movement of solid material out of the grain boundary zone into solution, through S_{int} (at velocity $-\tilde{v}$ normal to S_{int}), is balanced by bulk grain material moving into the grain boundary zone through S'_{gb} (at velocity $-\bar{V}$ normal to S_{gb}), keeping the total mass of solid in the grain boundary zone constant. Note that the left hand side of equation (3.4) represents the energy input into the grain boundary zone through S'_{gb}, while the right hand side represents the amount of energy output from the grain boundary zone by dissolution of solid along S_{int} (Lehner, 1990).

The equality in equation (3.4) shows that during grain boundary dissolution at an average velocity $\bar{V}$ (ms^{-1}), the higher work rate of the normal stress at the grain boundary margin compared to that of the internal fluid pressure is compensated for by a transfer of excess free energy ($\tilde{f}_s - f_s$) across the phase boundary by dissolving highly stressed and/or strained material from the islands and channels (Lehner, 1990). In the present treatment, the solid in the grain boundary zone is allowed to deform elastically. We will consider the effects that plastic deformation in the grain boundary zone has on pressure solution rates in Chapter 4. Here, our analysis for a grain boundary with an island-channel structure is also applied to a grain boundary with a thin fluid film structure (Figure 3.1b versus Figures 3.1c–3.1e). The only difference is that, for the thin fluid film case, S_{int} is a flat solid/fluid interface and the fluid must be non-hydrostatically stressed with a component normal to S_{int} equal to σ_n.

3.3.2 Mass balance for the thin film model

In the case of the thin film model, a continuous adsorbed film of "fluid" present in the grain boundary supports the normal stress across the contact (see Figure 3.2), as described above.

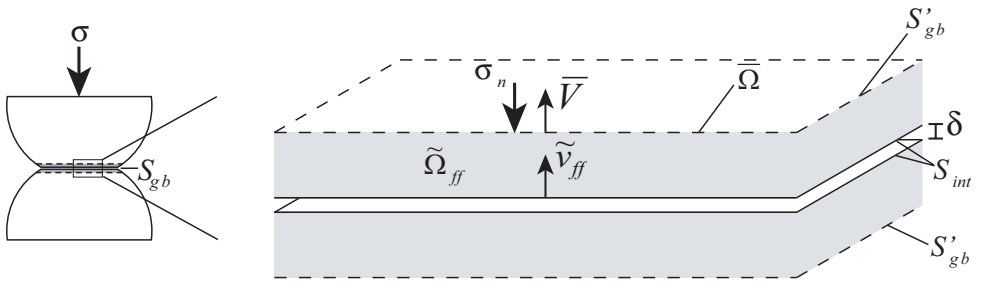

Figure 3.2 The grain boundary structure assumed in the thin fluid film model. An element of the grain boundary zone is indicated in grey. $\bar{V}$ *indicates the (macroscopic) rate with which the grain boundary zone moves towards the centre of the grain;* $\tilde{v}_{ff}$ *indicates the actual rate of dissolution at the solid-fluid interface* S_{int}. S'_{gb} *are translations of* S_{gb}*, the (grain scale) grain boundary plane, bounding a representative element of grain boundary volume.* δ *is the fluid film thickness.* $\bar{\Omega}$ *and* $\tilde{\Omega}_{ff}$ *indicate the average solid molar volume on* S'_{gb} *and the actual solid molar volume in the grain boundary volume element.*

Since this "fluid" film is held in the grain boundary by surface (adsorption) forces it is non-hydrostatically stressed. As the film is continuous, dissolution occurs over the entire solid/fluid interface, at a velocity $\tilde{v}_{ff}$ (ms^{-1}). Since conservation of mass (expressed in moles) dictates that the amount of solid material moving into the grain boundary zone is equal to the amount of solid material dissolving from it per unit time, we can write:

$$\frac{\bar{V}A}{\bar{\Omega}} = \frac{\tilde{v}_{ff}A}{\tilde{\Omega}_{ff}} \tag{3.5}$$

where A is the area of the grain boundary element considered, $\bar{\Omega}$ is the molar volume of the solid at the grain boundary margin (on S'_{gb}) and $\tilde{\Omega}_{ff}$ the molar volume of the solid in the grain boundary zone (at the solid-fluid interface).

3.3.3 Mass balance for the island-channel models

In the island-channel models, a network of either cylindrical or bar-shaped islands separated by fluid-filled channels is considered (see Figures 3.3 and 3.4). In such a geometry, two distinct dissolution sites can be distinguished, namely island margins and channel roofs and/or floors. Lateral dissolution of the islands is assumed to occur at average velocity $\tilde{v}_i$ (ms^{-1}) and results in the total island mass decreasing, whereas the channels deepen at average velocity $\tilde{v}_c$ by dissolving the channel roofs and floors, effectively recreating island mass (roughness). However, within the assumption of steady state pressure solution, the grain

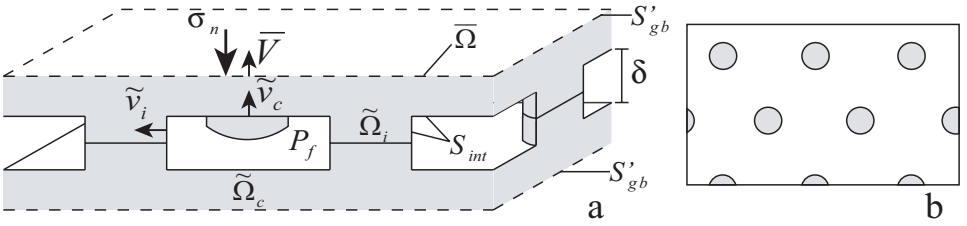

Figure 3.3 A schematic drawing of the grain boundary structure assumed in the island-channel model with cylindrical islands. An element of grain boundary is shown in grey. $\bar{V}$ *indicates the (macroscopic) rate with which the grain boundary zone moves towards the centre of the grain, perpendicular to* S'_{gb}*;* $\tilde{v}_c$ *and* $\tilde{v}_i$ *respectively indicate the average rate of dissolution on channel floors/roofs and of the island margins, perpendicular to the solid-fluid contact* S_{int}*.* $\bar{\Omega}$*,* $\tilde{\Omega}_c$ *and* $\tilde{\Omega}_i$ *are respectively the average solid molar volume on* S'_{gb}*, the solid molar volume in the channel floors/roofs (on* S_{int}*) , and the solid molar volume in the islands (on* S_{int}*).* δ *represents the grain boundary width. (b) A plan view of the island-channel geometry.*

boundary geometry on average remains constant. This implies that $\tilde{v}_c$ and $\tilde{v}_i$ must be related such that the mass of solid in the islands remains constant on average. If the area fraction of grain boundary occupied by solid island contact is α, and the island height is δ, we can therefore write for a grain boundary element of area A (m^2):

$$\frac{\tilde{v}_c A}{\tilde{\Omega}_c}\alpha = \frac{\tilde{v}_i A}{\tilde{\Omega}_i} M \frac{\delta}{2} c_i \tag{3.6}$$

where M (m^{-2}) represents the average number of islands per square meter of contact, $\tilde{\Omega}_c$ and $\tilde{\Omega}_i$ are the molar volumes of the solid on S_{int} at channel and at island sites respectively. For the cylindrical islands model, the mean island circumference, c_i is given by $c_i = 2\pi r_i$, where $r_i = \sqrt{\alpha/M\pi}$ is the mean island radius. For the bar-shaped islands model the mean circumference of the island bars depends on the aspect ratio (length/width) s of the bar-shaped islands through $c_i = 2\left(\sqrt{\alpha s/M} + \sqrt{\alpha/Ms}\right)$ or, if only dissolution on the long side of the bars is considered (effectively assuming continuous bars), $c_i = 2\sqrt{\alpha s/M}$. Equation (3.6) is equivalent to the statement that in the time taken to remove an island, another will be created by formation or deepening of a surrounding channel. Furthermore, since the mass of solid entering the grain boundary zone ($\bar{V}A/\bar{\Omega}$) must equal the total mass of solid dissolving from the grain boundary per unit time, we have

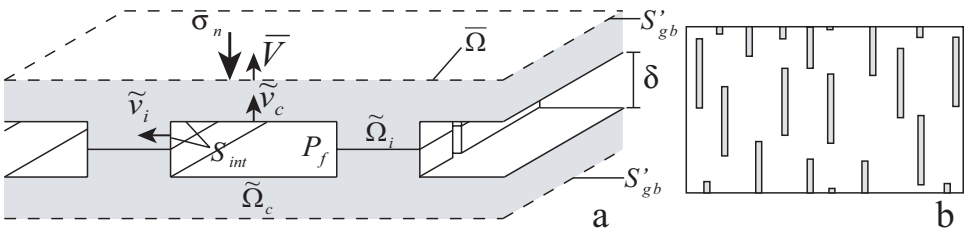

Figure 3.4 A schematic drawing of the grain boundary structure assumed in the island-channel model with bar-shaped islands. An element of grain boundary is shown in grey. $\bar{V}$ *indicates the (macroscopic) rate with which the grain boundary zone moves towards the centre of the grain, perpendicular to* S'_{gb}*;* $\tilde{v}_c$ *and* $\tilde{v}_i$ *respectively indicate the average rate of dissolution on channel floors/roofs and of the island margins, perpendicular to the solid-fluid contact* S_{int}*.* $\bar{\Omega}$*,* $\tilde{\Omega}_c$ *and* $\tilde{\Omega}_i$ *are respectively the average solid molar volume on* S'_{gb}*, the solid molar volume in the channel floors/roofs (on* S_{int}*) , and the solid molar volume in the islands (on* S_{int}*).* δ *represents the grain boundary width. (b) A plan view of the island-channel geometry.*

$$\frac{\bar{V}A}{\bar{\Omega}} = \frac{\tilde{v}_c A}{\tilde{\Omega}_c}(1-\alpha) + \frac{\tilde{v}_i A}{\tilde{\Omega}_i} M \frac{\delta}{2} c_i \tag{3.7}$$

3.4 Grain boundary dissolution kinetics

We now proceed to derive models for the ratio I^*/I for the different grain boundary structures discussed above.

3.4.1 The thin film case

Equation (3.5) describes the mass balance for the thin film grain boundary model. Making use of the energy/entropy balance derived by Lehner (1990) for a grain boundary element (equation (3.4)), and assuming that dissolution is the only dissipative process operating in the grain boundary and that all dissipated heat is conducted away so that isothermal conditions are maintained, we can write:

$$\frac{\bar{V}A}{\bar{\Omega}}\left[\left(f_s + \sigma_n \bar{\Omega}\right) - \mu_s\right] = \frac{\tilde{v}_{ff} A}{\tilde{\Omega}_{ff}} \Delta\tilde{\mu}_{ff} \tag{3.8}$$

Here, $\Delta\tilde{\mu}_{ff}$ is the difference between the average chemical potential $\bar{\mu}_{gb}$ of the (elastically deformed) solid in the grain boundary zone and chemical potential μ_s of the dissolved solid in the fluid. In the case of dissolution controlled pressure solution in a porous aggregate, diffusion and precipitation will be so easy that μ_s is approximately equal to the chemical potential of the (undeformed) solid at pore walls, so that $\mu_s \approx f_s + P_f\bar{\Omega}$ (Lehner, 1990, 1995). Combining (3.5) and (3.8) we then find that:

$$\Delta\bar{\mu} = \left(f_s + \sigma_n\bar{\Omega}\right) - \mu_s = \Delta\tilde{\mu}_{ff} \tag{3.9}$$

Using equation (3.2), we can therefore write for the entire grain boundary contact:

$$\bar{V} = I^* \frac{\left(f_s + \sigma_n\bar{\Omega} - \mu_s\right)}{RT} \tag{3.10}$$

Hence, assuming that the thickness and structure of the adsorbed grain boundary fluid film in itself does not influence the rate of dissolution of the solid grain, and by comparing equations (3.10) and (3.3) we of course obtain $I^*/I = 1$. Note however, that if I^* is somehow affected by fluid film thickness or the state of the non-hydrostatically stressed fluid this might not hold.

3.4.2 The island-channel network case

Rewriting the conservation of energy and entropy embodied in Lehner's relation (3.4), using the mass balance for the island-channel network model defined in equation (3.7) for this grain boundary model, with either cylindrical or bar-shaped islands, yields:

$$\frac{\bar{V}A}{\bar{\Omega}}\left[\left(f_s + \sigma_n\bar{\Omega}\right) - \mu_s\right] = \frac{\tilde{v}_c A}{\tilde{\Omega}_c}(1-\alpha)\Delta\tilde{\mu}_c + \frac{\tilde{v}_i A}{\tilde{\Omega}_i}M\frac{\delta}{2}c_i\Delta\tilde{\mu}_i \tag{3.11}$$

If we combine equation (3.6) with equation (3.7), we can easily show that $\bar{V}/\bar{\Omega} = \tilde{v}_c/\tilde{\Omega}_c$. Using this result and applying the mass balance in equation (3.6), equation (3.11) can now be rewritten to:

$$\left(f_s + \sigma_n\bar{\Omega}\right) - \mu_s = \Delta\tilde{\mu}_c\left[(1-\alpha) + \frac{2\alpha^2}{M\delta c_i}\frac{\tilde{\Omega}_i}{\tilde{\Omega}_c}\right] \tag{3.12}$$

Finally, putting this expression into (3.10) and combining the result with (3.3), using (3.6) and (3.7), it is seen that:

$$\frac{I^*}{I} = \frac{1}{\left[(1-\alpha) + \frac{2\alpha^2}{M\delta c_i}\frac{\tilde{\Omega}_i}{\tilde{\Omega}_c}\right]}\frac{\bar{\Omega}}{\tilde{\Omega}_c} \tag{3.13}$$

When using this result, it is important to realise, however, that restrictions are imposed on the grain boundary geometry by the energy balance expressed in equation (3.12). Specifically, as $\mu_s \approx f_s + P_f\bar{\Omega}$ and neglecting grain scale gradients in f_s, we find from (3.12) and (3.6):

$$(\sigma_n - P_f)\bar{\Omega} = \Delta\tilde{\mu}_i\left[(1-\alpha)\frac{M\delta c_i}{2\alpha}\frac{\tilde{\Omega}_c}{\tilde{\Omega}_i} + \alpha\right] \tag{3.14}$$

As the islands are assumed to be purely elastic columns with Young's modulus E (Pa), they support an effective average stress of $\sigma_{isl,eff} = \sigma_n - P_f/\alpha$. Omitting $P_f\left(\tilde{\Omega}_i - \bar{\Omega}\right)$, which is negligible as P_f is relatively low, the excess chemical potential of the solid in the islands due to elastic strain is then given by:

$$\Delta\tilde{\mu}_i = \frac{\left[(\sigma_n - P_f)/\alpha\right]^2}{2E}\tilde{\Omega}_i \tag{3.15}$$

which on inserting into equation (3.14) gives:

$$(\sigma_n - P_f)\bar{\Omega} = \frac{\left[(\sigma_n - P_f)/\alpha\right]^2}{2E}\left[(1-\alpha)\frac{M\delta c_i}{2\alpha}\tilde{\Omega}_c + \alpha\tilde{\Omega}_i\right] \tag{3.16}$$

Equation (3.16) is an important result as it implies that at a given effective contact stress, and assuming a steady state structure, the constants determining the grain boundary geometry are not independent. In the case of cylindrical islands, two of the three structural parameters M, δ, and α are independent. In the case of bar-shaped islands, three of the four structural parameters M, δ, α and s are independent.

3.5 Model predictions for grain boundary geometry and the ratio I^*/I

Comparing the outcomes of our three models, we see that, except for possible effects of confinement and associated structuring of the grain boundary "fluid" (e.g., De Meer et al., 2005) on interfacial reaction rates, a thin film boundary is likely to have no effect on the rate of dissolution controlled pressure solution ($I^* = I$). The cylindrical and bar-shaped island models do show an effect. The equations obtained for the ratio I^*/I in these cases (equation (3.13), with $c_i = 2\pi\sqrt{\alpha/M\pi}$ for cylindrical islands and $c_i = 2\left(\sqrt{\alpha s/M} + \sqrt{\alpha/Ms}\right)$ for bar-shaped islands) are very similar to each other, with only small geometry-related differences (different c_i). Both island-channel models thus show an increase in I^*/I for increasing thickness δ and increasing number of islands per unit area M, so that the larger the solid-fluid contact area of the islands is compared with their volume, the faster grain boundary dissolution occurs. The bar-shaped island model also shows a dependence on island aspect ratio s, with I^*/I increasing with increasing s values and with square islands giving the lowest values for I^*/I, close to the values found for cylindrical islands.

As mentioned above, equation (3.16) does not allow the parameters determining grain boundary geometry to be varied independently. Therefore, concentrating on quartz, we will first attempt to place constraints on M, δ and s, and then we will look at how α varies with these parameters for chosen grain boundary stresses. Then we will discuss the resulting values of I^*/I.

To our knowledge, the grain boundary width (δ) has never been measured directly for actively pressure-dissolving quartz contacts. Cox and Paterson (1991) report observations of ridges and channels on contacts between quartz grains after pressure solution. They estimated the ridges to be up to 10^{-7} m high. Generally, it is estimated that in quartz δ probably has a value in the range 10^{-9} to 10^{-7}m (e.g., Shimizu, 1995; Renard and Ortoleva, 1997; Nakashima, 1995; Spiers et al., 2004). Likewise, values for island density M are not commonly available, and are estimated here to lie between 10^{10} and 10^{13}m^{-2}. The minimum figure here assumes that for any contact to be in mechanical equilibrium, at least three load bearing islands are required. The maximum estimate of M is assumed to be limited by roughness related to dissolution of dislocations, the density of which rarely exceeds 10^{13}m^{-2} in natural quartz (Wintsch and Dunning, 1985). In the micrograph presented by Cox and Paterson (1991) of ridges and channels on a quartz contact, the ridges have lateral dimensions of approximately 0.05–0.2μm by 1–3μm. This indicates an aspect ratio (s) of about 5–50.

In order to compare the predictions of our model with compaction experiments on quartz, such as those of Niemeijer et al. (2002), we choose a relatively high effective normal contact stress of $\sigma_n = 495$MPa and a fluid pressure of $P_f = 200$MPa for investigating how α and I^*/I vary within the above ranges of M, δ and s. Assuming cubic packed spherical grains (Niemeijer et al., 2002), this is equivalent to the average effective contact stress supported at ~30% porosity in the 100MPa effective pressure experiments of Niemeijer et al. (2002). Finally, for quartz we take $E = 76.5$GPa. In our calculations, we assume the grain scale

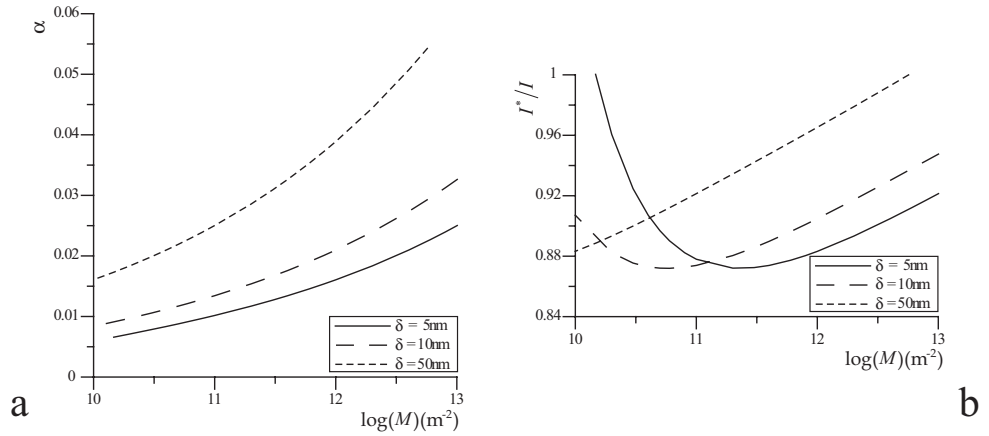

Figure 3.5 Plots of (a) α vs. log(M), and (b) I^*/I vs. log(M) for the cylindrical islands model, using $\delta = 5$, $\delta = 10$, and $\delta = 50$nm.

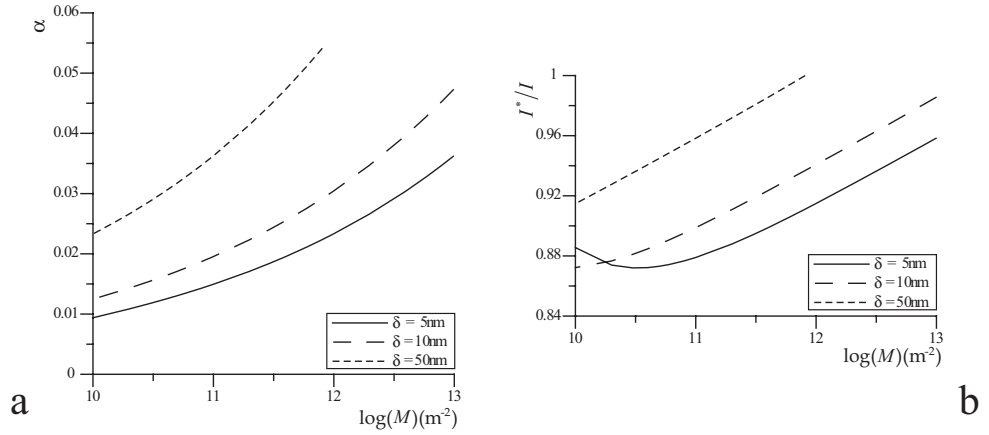

Figure 3.6 Plots of (a) α vs. log(M), and (b) I^*/I vs. log(M) for the bar-shaped islands model, using $\delta = 5$, $\delta = 10$, and $\delta = 50$nm.

gradients in molar volume to be negligible ($\tilde{\Omega}_c = \bar{\Omega}$). The dependence of α and I^*/I on M and δ (5, 10, and 50 nm) computed from equations (3.16) and (3.13), for a grain boundary geometry with cylindrical islands is shown in Figure 3.5. Figure 3.6 shows the dependence obtained for a grain boundary with bar-shaped islands, assuming $s = 20$.

Figures 3.5 and 3.6 demonstrate that the values of α predicted by equation (3.16) are very low (mostly less than 5%). Our model thus predicts that pressure dissolving grain contacts

in quartz will be characterised by a small number of highly stressed/strained, widely spaced contact points or islands that are continuously being dissolved and re-made elsewhere as mass is gradually removed from the entire interface. For the conditions examined, I^*/I falls in the range 0.87–1. This range is insensitive to normal contact stress. At high values of M (generally more than 10^{13}m^{-2}) our model breaks down and I^*/I ratios of more than 1 are predicted. This is a consequence of the simplified nature of our grain boundary model. At low values of M, below ~10^{11}m^{-2}, an increase in I^*/I is predicted, which is caused by very high island stresses and associated changes in the molar volume. The small, widely separated islands implied by the low α value predicted by our model, and the stresses supported at islands can be compared with indenter tests on quartz. Quartz is known to support indentation stresses of several GPa without fracturing (e.g., Hartley and Wilshaw, 1973; Masuda et al., 2000).

At this point, we should note that the observations available on the geometry of pressure dissolving grain boundaries in quartz do not seem consistent with the low α values predicted by the model. From Figure 3b of Cox and Paterson (1991) the fraction of the contact area taken up by islands appears to be about 0.2–0.5. We therefore suggest that in a real contact dissolving by pressure solution only a fraction of the island area present actually supports load at any instant. As these highly stressed points are dissolved or even fail and then dissolve (as elastic energy is converted into surface damage which then dissolves), new highly stressed contact points form at different locations. This is analogous to the way that force is carried by only a few highly stressed grain contacts or contact chains in a loaded granular material (e.g., Mair and Hazzard, 2007). For our model this means that only the fraction of the contact area taken up by load-bearing contact points is determined by equation (3.16), while the total area fraction of islands might be significantly larger.

Niemeijer et al. (2002) report experimental dissolution controlled pressure solution rates that are more than half an order of magnitude slower than predicted by their pressure solution creep model (equation (3.1), applied assuming $I^* = I$). The I^*/I ratios calculated here for the influence of an island-channel grain boundary structure on the rate of dissolution controlled pressure solution yield a maximum reduction of only 13% ($I^*/I = 0.87$). On this basis, we suggest that other mechanisms may further reduce dissolution rates in a pressure dissolving grain boundary, such as dissipation by plastic deformation or failure of the highly stressed islands. These effects will be addressed in Chapter 4. At porosities around 10–15%, a rapid drop in strain rate was observed in the experiments of Niemeijer et al. (2002). Niemeijer et al. (2002) suggest explanations such as a change in pressure solution rate-limiting process, dissolved copper from the capsule slowing down the dissolution of quartz, neck growth or grain boundary healing. The possibility that this rapid drop in strain rate was caused by the onset of grain boundary healing is investigated below.

3.6 Grain boundary healing under stress

We now derive a model to predict under what conditions an active island-channel structure can be maintained in a fluid-filled grain boundary under stress, as opposed to healing due to surface energy effects. We approach the problem by deriving a criterion for the growth of grain boundary islands in a manner analogous to neck growth between two solid particles (Figure 3.7). Neck growth is the widening of a contact between two grains driven by the small negative radius of curvature at the edge of the contact (e.g., Hickman and Evans, 1991, 1992). We first consider neck or island growth under hydrostatic conditions, and then examine the effects of a normal stress imposed on such a contact. Our starting point is the condition for chemical equilibrium at any point on the interface between a solid grain and its solution. This is written (Heidug, 1991; Visser, 1999):

$$\mu_{se} = f_s + P_f \Omega_s + \gamma_{sl}\left(1/r_1 + 1/r_2\right)\Omega_s \tag{3.17}$$

where μ_{se} is the equilibrium potential of the solute in solution (equal to the potential of the solid), γ_{sl} is the solid/liquid interfacial free energy, and r_1 and r_2 are the principal radii of interfacial curvature. Chemical equilibrium at the intersection of a solid-solid grain boundary between two (isotropic) grains and a solution phase is described by the Young-Dupre´ relation (Porter and Easterling, 1992; Holness, 1992, 1993):

$$\gamma_{ss} = 2\gamma_{sl}\cos\left(\frac{\theta_{eq}}{2}\right) \tag{3.18}$$

Here γ_{ss} is the solid-solid interfacial free energy and θ_{eq} is the equilibrium dihedral angle. When the intersection is removed from equilibrium, that is when the dihedral angle at the contact margin is not equal to the equilibrium value ($\theta \neq \theta_{eq}$) (see Figure 3.7b), a force acts on the intersection causing the solid-solid contact or neck between the grains to either spread (neck growth) or retreat (marginal dissolution). As pointed out by Visser (1999), this thermodynamic force F (Nm^{-1}) is given by:

$$F = 2\gamma_{sl}\left(\cos\frac{\theta}{2} - \cos\frac{\theta_{eq}}{2}\right) \tag{3.19}$$

Equations (3.17) and (3.19) imply that in a solid-fluid aggregate under fully hydrostatic conditions (pressure in solid = pressure in fluid = P_f), the only significant driving forces for mass transfer are surface energy related, caused by spatial variations in the radius of curvature of the solid in contact with the fluid and by departures from the equilibrium dihedral angle at

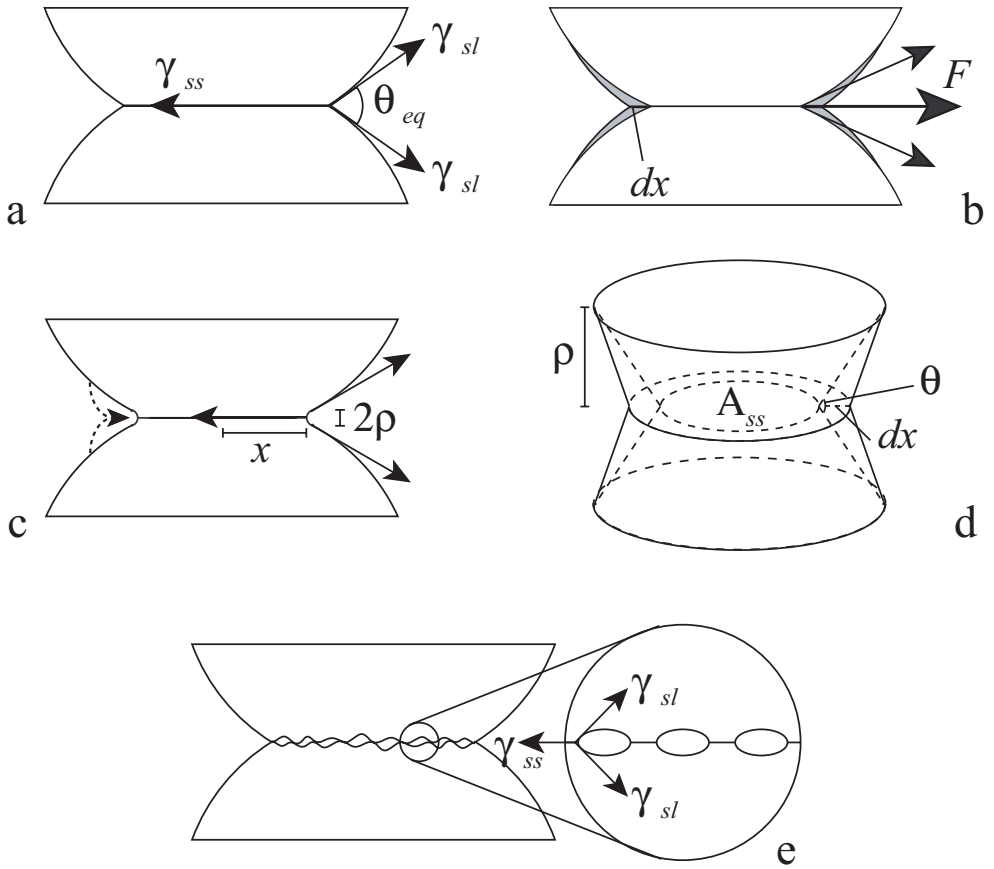

Figure 3.7 A contact between two solid grains and a fluid. (a) Equilibrium state; the dihedral angle is equal to the equilibrium dihedral angle θ_{eq}, and the solid-solid (γ_{ss}) and solid-liquid (γ_{sl}) interfacial energies are balanced. (b) Non-equilibrium state; the dihedral angle θ is not equal to the equilibrium dihedral angle θ_{eq} (here $\theta < \theta_{eq}$), and a resulting thermodynamic force F drives neck growth. Distance x is the solid-solid contact radius; dx indicates the growing neck (grey region). (c) The geometry of the growing neck (after Visser, 1999), where ρ is the radius of curvature of the solid-fluid interface at the neck. The arrows indicate possible transport paths from source (pore wall) to sink (neck) regions. (d) Simplified geometry of the growing neck whereby for small values of dx we find $dA_{ss} \approx 2\pi x dx$ and $dA_{sl} \approx -4\pi x dx \cos(\theta/2)$. (e) Schematic drawing of the neck growth model applied to healing of an island-channel structure grain boundary.

grain contacts. For aggregates in which the solid-solid-fluid contacts have non-zero dihedral angles, this means that the system is driven, via neck growth phenomena, to a structure in which all fluids are present in pores located at triple junctions and no fluid is contained in the grain boundaries (Visser, 1999; Schenk and Urai, 2004). An island-channel grain boundary structure is not, therefore, an equilibrium structure, and in order to maintain such high-energy grain boundaries without healing, local driving forces caused by the uneven distribution of stress and stress-induced irregularities in free energy density must overcome surface energy effects (Lehner, 1990; see also Koehn et al., 2006). In the present model, when surface-energy-driven neck growth at grain boundary islands dominates, this causes healing of the grain boundary, whereas when dissolution of the islands dominates, a dynamically pressure-dissolving island-channel network can exist.

3.6.1 Chemical potential for neck growth under hydrostatic conditions

Following the approach of Lehner (1990), for a solid-fluid aggregate deforming at constant stress, fluid pressure (P_f), mass and temperature, conservation of energy and entropy requires that:

$$\gamma_{ss}\dot{A}_{ss} + \gamma_{sl}\dot{A}_{sl} + \dot{\Phi} = \sigma_{ij}\dot{\varepsilon}_{ij} + P_f\dot{\phi} + \sum\dot{\Delta}_k \tag{3.20}$$

where γ_{ss} and γ_{sl} represent the solid-solid and the solid-liquid interfacial energies (Jm^{-2}), $\dot{A}_{ss}$ and $\dot{A}_{sl}$ represent the rates of change in solid-solid and solid-liquid interfacial areas per unit volume of the system ($m^{-1}s^{-1}$), $\dot{\Phi}$ is the rate of change of the free energy of the solid phase per unit volume of the total system ($Jm^{-3}s^{-1}$), the scalar product $\sigma_{ij}\dot{\varepsilon}_{ij}$ of the Cauchy stress tensor σ_{ij} and the strain rate tensor $\dot{\varepsilon}_{ij}$ $(i,j = 1,2,3)$ is the rate of mechanical work done upon the system ($Jm^{-3}s^{-1}$), P_f times the rate of change of the porosity ($\dot{\phi}$) is the work done in expelling fluids from the pore space ($Jm^{-3}s^{-1}$) and $\sum\dot{\Delta}_k$ is the total energy dissipation rate for the k irreversible processes operating within the system ($Jm^{-3}s^{-1}$). In a fully hydrostatic system, where no deformation or compaction occurs and where the free energy of the solid phase is constant and uniform, but in which $\theta_{eq} > 0$, the interfacial energy terms will drive neck growth by diffusive transport from pore walls to necks. Equation (3.20) thus modifies to:

$$\gamma_{ss}\dot{A}_{ss} + \gamma_{sl}\dot{A}_{sl} = \dot{\Delta}_{ng} \tag{3.21}$$

where $\dot{\Delta}_{ng}$ is the dissipation rate due to neck growth (Js^{-1}). This equation shows that the dissipation due to neck growth ($\dot{\Delta}_{ng}$) is provided by changes in the solid/solid/liquid interfacial areas. Assuming that the dissipation term $\dot{\Delta}_{ng}$ is solely the result of the redistribution of mass

between neck and grain surface regions (i.e., assuming negligible dissipation by fluid flow and solute diffusion), it can be written for a single contact in terms of the driving force (F) times flux (J) relation:

$$\dot{\Delta}_{ng} = JF \tag{3.22}$$

Using equation (3.19) for F, it follows that, when neck growth occurs at a velocity $\dot{x}$ (ms^{-1}) at the margin of a contact with contact radius x (m) between two spherical grains as shown in Figure 3.7b, we can write $J = 2\pi x\dot{x}$ so that

$$\dot{\Delta}_{ng} = 2\pi x\dot{x}F = 2\pi x\dot{x}2\gamma_{sl}\left(\cos\frac{\theta}{2} - \cos\frac{\theta_{eq}}{2}\right) \tag{3.23}$$

However, the rate of dissipation of energy by surface energy driven dissolution- reprecipitation can also be described in terms of the material flux times the average change in chemical potential per unit volume of material transported from source to sink sites (e.g., from the pore wall to the contact margin). For the neck growth geometry of Figure 3.7c, we can accordingly write:

$$\dot{\Delta}_{ng} \approx 2\rho\dot{x}2\pi x\frac{\Delta\mu}{\Omega_s} \tag{3.24}$$

where $\Delta\mu$ represents the average difference in chemical potential between the solid at the pore wall and at the contact margin, and ρ is the radius of curvature at the margin.

Moreover, considering the simple geometry for the contact region shown in Figure 3.7d, using equation (3.18) for γ_{ss}, and noting that $\dot{A}_{ss} \approx 2\pi x\dot{x}$ and $\dot{A}_{sl} \approx -4\pi x\dot{x}\cos(\theta/2)$, we can also write equation (3.21) as:

$$\dot{\Delta}_{ng} = 2\pi x\dot{x}2\gamma_{sl}\left(\cos\frac{\theta}{2} - \cos\frac{\theta_{eq}}{2}\right) \tag{3.25}$$

Combining either equations (3.23) and (3.24), or equations (3.24) and (3.25), we now find:

$$2\rho\dot{x}2\pi x\frac{\Delta\mu}{\Omega_s} = 2\pi x\dot{x}2\gamma_{sl}\left(\cos\frac{\theta}{2} - \cos\frac{\theta_{eq}}{2}\right) \tag{3.26}$$

and thus:

$$\Delta\mu = \frac{\gamma_{sl}}{\rho}\Omega_s\left(\cos\frac{\theta}{2} - \cos\frac{\theta_{eq}}{2}\right) \tag{3.27}$$

for the chemical potential drop driving transport from grain walls to necks, causing neck growth. It follows that since the equilibrium potential at a pore wall is given by (3.17), then the chemical potential at a neck can be given:

$$\mu_n = f_s + P_f\Omega_s - \frac{\gamma_{sl}}{\rho}\Omega_s\left(\cos\frac{\theta}{2} - \cos\frac{\theta_{eq}}{2}\right) \tag{3.28}$$

3.6.2 Neck growth under non-hydrostatic stress

The above expression for the chemical potential drop ($\Delta\mu$) driving neck growth under hydrostatic conditions can now be expanded to neck growth in systems under non-hydrostatic stress, i.e., where grain contacts transmit stresses in excess of P_f. Using equations (3.17) and (3.28) for the potential at source and sink sites, the potential drop is written:

$$\Delta\mu = \left(f_p + P_f\Omega_p + \frac{4\gamma_{sl}}{d}\Omega_p\right) - \left[f_m + P_f\Omega_m - \frac{\gamma_{sl}}{\rho}\Omega_m\left(\cos\frac{\theta}{2} - \cos\frac{\theta_{eq}}{2}\right)\right] \tag{3.29}$$

Here, the subscripts p and m indicate values in the solid at the pore wall and the contact margin respectively. As $4\gamma_{sl}\Omega_p/d$ is generally small, and assuming that the difference in molar volume between the pore wall and the margin is also negligible, the following approximation for the driving force for neck growth is found:

$$\Delta\mu = \frac{\gamma_{sl}}{\rho}\Omega_s\left(\cos\frac{\theta}{2} - \cos\frac{\theta_{eq}}{2}\right) - (\Delta f_s + P_f\Delta\Omega_s) \tag{3.30}$$

where Δf_s is the difference in Helmholtz free energy between the contact margin and the pore wall. When the neck is stressed and deforms elastically (or plastically) this causes an increase in Δf_s and thus a decrease in the driving force for neck growth ($\Delta\mu$). As $\Delta\Omega_s$ (the difference in solid molar volume between the contact margin and the pore wall) is generally small (~1%), the term $P_f\Delta\Omega_s$ can be neglected at low pore pressures. It becomes significant when P_f is high compared to the effective stress $\sigma_e = \sigma - P_f$, such as in the experiments of Niemeijer et al. (2002).

3.6.3 Grain boundary healing

Our next step is to apply this description for the driving force for neck growth under non-hydrostatic stress to healing of a stressed grain boundary with an island-channel structure at the contact between elastic solid grains (see Figure 3.7e). Individual islands in the contact can be considered small necks, where ongoing growth will result in grain boundary healing. The driving force for grain boundary healing is accordingly found by rewriting (3.30) (neglecting the term $P_f \Delta\Omega_s$) and approximating ρ (the radius of curvature at the margin) using $\rho = \frac{1}{2}\delta$ (half the grain boundary width). We will assume the islands to be purely elastic columns that support an average effective normal stress of $\sigma_{isl} = (\sigma_n - P_f)/\alpha$ where α is the total island area fraction including both load-bearing and non load-bearing points. This means we ignore our conclusion in section 3.5 that the normal stress transmitted across grain boundaries is concentrated at a few small contact points during ongoing pressure solution, while the remaining island area is more or less stress free. This is reasonable for deriving a healing criterion, as healing will start at islands that are not load-bearing, causing them to grow, so that the stress becomes more evenly distributed. Assuming that f_s is uniform elsewhere within the grain, Δf_s in (3.30) is hence approximated by the elastic strain energy term:

$$\Delta f_s = \frac{\left[(\sigma_n - P_f)/\alpha\right]^2}{2E}\Omega_s \tag{3.31}$$

and the driving force for grain boundary island growth is given:

$$\Delta\mu = \frac{2\gamma_{sl}}{\delta}\Omega_s\left(\cos\frac{\theta}{2} - \cos\frac{\theta_{eq}}{2}\right) - \frac{\left[(\sigma_n - P_f)/\alpha\right]^2}{2E}\Omega_s \tag{3.32}$$

A positive driving force indicates island growth and grain boundary healing, whereas a negative driving force indicates that net dissolution of the islands occurs, presumably leading to an unstable island-channel network through an uneven distribution of irregularities in free energy density and stress concentration (Lehner, 1990; Visser, 1999).

On this basis, the stress conditions at which grain boundary healing is expected to dominate over wetting of the grain boundary by undercutting of the islands can be obtained from the condition $\Delta\mu > 0$, or:

$$(\sigma_n - P_f) < \sigma_{crit} = 2\alpha\sqrt{E\frac{\gamma_{sl}}{\delta}\left(\cos\frac{\theta}{2} - \cos\frac{\theta_{eq}}{2}\right)} \tag{3.33}$$

For compaction of a granular aggregate, this gives the mean effective normal contact stress $(\sigma_n - P_f) = B(\phi)\sigma_e$ below which healing dominates over dynamic wetting. Recall here that $B(\phi)$ is a dimensionless function of porosity accounting for porosity-dependent changes in grain contact area and stress concentration (see equation (3.1)). Equation (3.33) thus represents a yield stress (σ_{crit}) below which deformation by intergranular pressure solution will not proceed. Finally, note that the equilibrium state at $(\sigma_n - P_f) = \sigma_{crit}$ is an unstable one, as any increase in α (neck growth) will result in a decrease in island stress and thus an increase in net driving force for growth of the islands. Conversely, any decrease in α will cause an increase in island stress and thus island dissolution.

In the above application of neck growth theory to derive equation (3.33), the chemical potential of the solute in the grain boundary fluid is implicitly assumed to be equal to the chemical potential at free pore walls, as expected for an aggregate of solid grains deforming by dissolution controlled pressure solution (Lehner, 1990). This assumption is valid for the onset of grain boundary healing during dissolution controlled pressure solution. According to our model, during the early stages of grain boundary healing, the islands will grow but dissolution will continue in the channels, ultimately forming isolated fluid inclusions at these sites. At this final stage, the effective normal contact stress required to re-initiate pressure solution will increase to a value greater than σ_{crit} at the onset of healing. This occurs because pressure solution requires rewetting of the grain boundary by marginal dissolution of the now larger islands by the fluids trapped in grain boundary inclusions, as described and modeled by Ghoussoub and Leroy (2001).

So far, we have assumed that P_f is low enough to neglect the term $P_f \Delta\Omega_s$ in equation (3.30). However, at high P_f, $P_f \Delta\Omega_s$ is no longer negligible, and therefore equation (3.33) is no longer valid. For purely elastic materials, changes in molar volume $\Delta\Omega_s$ due to loading can be estimated using Hooke's law. Inserting the $P_f \Delta\Omega_s$ term thus obtained into equation (3.30), and setting $\Delta\mu = 0$, this equation can readily be solved for the critical effective contact stress σ_{crit} using a numerical iteration method.

3.6.4 Healing predictions and comparison with data from nature and experiment

We will now compare the criterion derived above predicting a "yield stress" for pressure solution to the pressure solution experiments of Niemeijer et al. (2002). Also, we will calculate values of this yield stress for pressure solution in nature to obtain limiting ϕ versus depth curves.

Niemeijer et al. (2002) report a rapid decrease in pressure solution rates at porosities below ~10–15% in their quartz compaction experiments performed at temperatures of 400–600°C, fluid pressures of 150–250MPa and effective pressures of 50–150MPa. One possible cause for this decrease is the onset of grain boundary healing at those porosities (Niemeijer et al., 2002). Using the criterion derived here (equation (3.33)), we can now investigate whether or not the observed decrease in pressure solution rates was likely to have been caused by grain

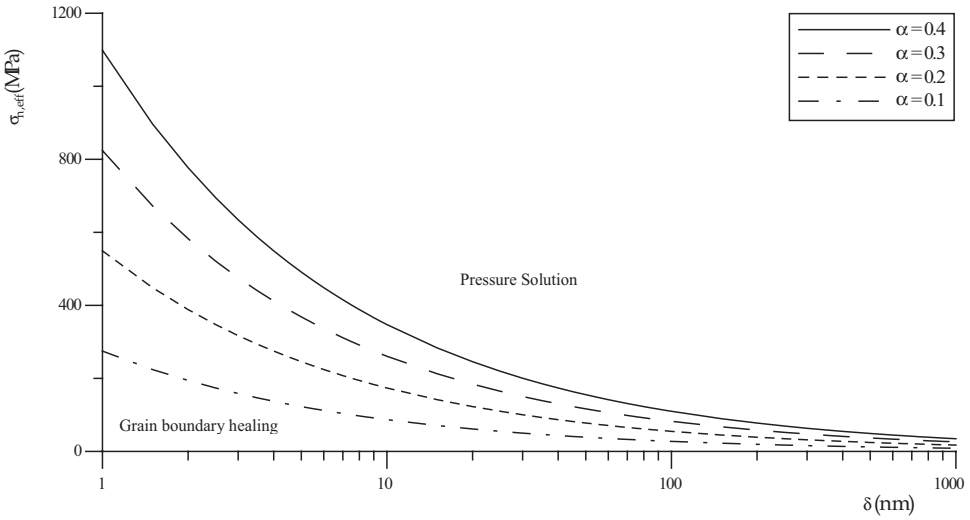

Figure 3.8 A plot of critical contact (normal) stress for dissolution of islands in the grain boundary (and thus for pressure solution) versus grain boundary width for values of α *between 0.4 and 0.1, at* $\left(\cos(\theta/2) - \cos(\theta_{eq}/2)\right) = 0.17$ *(*$T = 500\,°C$*).*

boundary healing. The following values were used for the Young's modulus and the solid-liquid interface energy of quartz $E = 76.5$GPa and $\gamma_{sl} = 0.145\text{Jm}^{-2}$ (Hiraga et al., 2002). This surface energy value was calculated by them from quartz dihedral angles developed in pelitic schists equilibrated at temperatures below 300°C. The equilibrium quartz-water dihedral angle is estimated from the data of Holness (1993) to be ~68° at a temperature of 500°C and fluid pressure of 400MPa. At 800°C and pressures below 600MPa, the pressure dependence of the dihedral angle is small (Holness, 1992). At temperatures of 500°C and fluid pressures of 150-250MPa, $\left(\cos(\theta/2) - \cos(\theta_{eq}/2)\right)$ will accordingly be about 0.17, assuming θ to be zero in a wetted grain boundary. Figure 3.8 shows σ_{crit} plotted as a function of δ for different values of α. For $\delta = 50$nm and $\alpha = 0.2 - 0.4$, the critical effective contact stress lies in the range 78–155MPa. Using the cubic packed spherical grains model of Niemeijer et al. (2002), the contact normal stress in their 100MPa effective stress experiments is expected to remain above these values down to porosities of about ~6.9%. This would suggest that grain boundary healing is not a likely cause for the decrease in compaction rates observed by Niemeijer et al. However, because of the high fluid pressure in the experiments of Niemeijer et al. (2002) ($P_f = 200$MPa), $P_f \Delta\Omega_s$ is of significant magnitude and cannot be neglected. Solving equation (3.30) including the term $P_f \Delta\Omega_s$ numerically, as discussed above, then gives critical stresses of 232MPa for $\alpha = 0.4$ and 116MPa for $\alpha = 0.2$. These

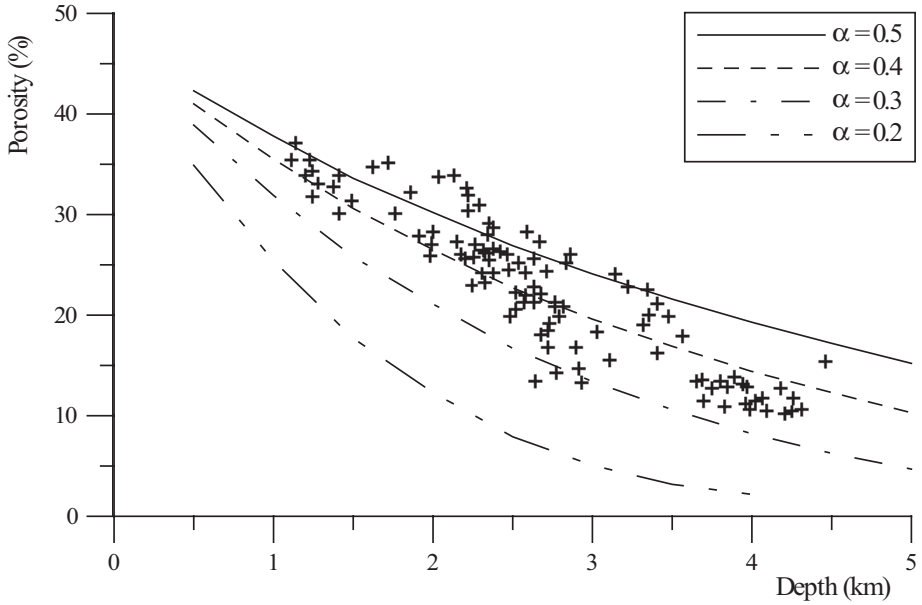

Figure 3.9 Curves of minimum achievable porosity versus depth for sandstones compacting by pressure solution only, assuming lithostatic rock pressure, hydrostatic pore fluid pressure and a geothermal gradient of 25ºCkm^{-1}. Crosses indicate porosity measurements on well-sorted arenitic sandstones from the Norwegian continental shelf (Ramm, 1992).

contact stresses are expected to occur at porosities of ~15.5% and 2.5%, suggesting that grain boundary healing might be a possible cause for the decrease in compaction rates seen in the experiments reported by Niemeijer et al. (2002). Further study of their resulting microstructures is required to confirm if healed grain boundaries are widespread.

If we now apply our criterion for grain boundary healing to a sandstone compacting under upper or mid-crustal conditions, we can calculate the porosity at which the onset of grain boundary healing would be expected, as grain boundary stresses become too low to enable grain boundary wetting. The aggregate geometry model used to do this here is that of an aggregate of initially spherical grains with a simple cubic packing, as used by Niemeijer et al. (2002). The porosity with depth curves displayed in Figure 3.9 were calculated for various values of α, with $\delta = 50\text{nm}$, assuming compaction by pressure solution (accommodated by grain boundary sliding) in a basin characterised by lithostatic rock pressure ($\rho_l = 2200\text{kgm}^{-3}$), hydrostatic fluid pressure ($\rho_w = 1000\text{kgm}^{-3}$) and a geothermal gradient of 25°Ckm^{-1}. For these curves, γ_{sl} was estimated as a function of temperature by linear interpolation between the value given by Hiraga et al. (2002) at 300°C and the value of 0.35Jm^{-2} reported for ambient temperature and pressure by Parks (1984). Values for $\left(\cos(\theta/2) - \cos(\theta_{eq}/2)\right)$ were estimated by linear extrapolation of a fit to the equilibrium

dihedral angles reported for 200–600°C by Holness (1993) and Hiraga et al. (2001).

For comparison, Ramm (1992) reports porosity measurements on well-sorted arenitic sandstones taken at different depths (1–4.5km) from the Norwegian continental shelf, from areas of near-hydrostatic pore pressures. It can be seen that our model neglecting $P_f \Delta\Omega_s$, which is reasonable for upper crustal conditions, agrees quite well with observed porosities for values of α between 0.3 and 0.4. For $\delta = 5$nm, identical porosity-depth curves are predicted for values of α $1/\sqrt{10}$ times the indicated values ($\alpha = 0.063, 0.095, 0.126$ and 0.158). If, in view of the uncertainties in our estimates of γ_{sl} and θ_{eq}, we assume $\gamma_{sl} = 0.35\text{Jm}^{-2}$ and an equilibrium dihedral angle of 40°, good agreement between predicted and observed porosities is found for values of α between 0.2 and 0.3. Note that pressure solution is expected to be the dominant mechanism of compaction from depths of about 2.5–3km, whereas mechanical compaction is expected to dominate at shallower levels (Ramm, 1992). A further study of the sandstones described by Ramm to assess whether grain boundary healing indeed occurred, would confirm if pressure solution was halted by healing as predicted by our model. If the minimum porosity that a rock can reach when compacting by pressure solution is indeed limited by the onset of grain boundary healing, this could explain why models of rock compaction by pressure solution based on experimentally determined pressure solution rates (such as equation (3.1)) generally overestimate average pressure solution rates in nature, determined assuming continuous compaction during burial. Inhibition of healing by the presence of micas at grain contacts might also explain the observations that phyllosilicates enhance pressure solution rates (e.g., Hickman and Evans, 1995; Bos and Spiers, 2000). Further comparison of our model to compaction trends in sandstones of various ages, and subjected to different basin geotherms and P_f-depth profiles is necessary to validate our model.

3.6.5 Comparison with other "yield stress" models for pressure solution

The above analysis predicts the existence of a "yield stress" below which pressure solution is halted due to grain boundary healing by surface energy driven growth of islands. In the poro-visco-plastic compaction model of Revil et al. (2006), the existence of a yield stress with an Arrhenius dependence on temperature is postulated and supported by comparison with the experimental results of Niemeijer et al. (2002). Earlier, Revil (2001) proposed a yield stress for pressure solution, but with a physical basis that differs from our model. Revil assumed a grain boundary structure that, for the purpose of the following discussion, functions like a thin film structure, i.e., a fully wetted grain boundary that supports a normal stress through the action of surface forces. He then applied the following formula for the chemical potential of a surface element of stressed solid in the grain boundary (μ_{ss}):

$$\mu_{ss} = \mu_s + w - \sigma_n \omega + \gamma H \omega \tag{3.34}$$

Here μ_s is the chemical potential of the same surface element in an unstressed/unstrained reference state, w is the change in molar strain energy (including both elastic and plastic strain energy), σ_n is the normal component of the stress at the grain contact (measured positive in compression), and ω is the molecular volume of the solid. The surface energy term $\gamma H\omega$ is neglected in this model. It follows that the potential drop between a surface element of stressed solid in a grain-to-grain contact and a surface element of the same solid on an unstressed free face surface is given by:

$$\Delta\tilde{\mu} = \Delta w - (\sigma_n - P_f)\omega \tag{3.35}$$

Stress enhancement of the solubility and hence pressure solution at the grain contacts were then assumed by Revil to proceed when $(\sigma_n - P_f)\omega \geq \Delta w$, i.e., at negative $\Delta\tilde{\mu}$. A critical effective normal contact stress below which pressure solution does not occur is then given by $(\sigma_n - P_f) = \Delta w/\omega$.

However, if we compare the model of Revil (2001) to the thermodynamic analysis of pressure solution given by for instance Lehner (1990), it is evident that the $\sigma_n\omega$ term in (3.34) should be positive. In other words, both stored strain energy and compressive normal stress lead to an increase in chemical potential at stressed grain interfaces, so that these terms should be added rather than subtracted. This renders the physical basis for the yield stress effect proposed by Revil (2001) invalid. In contrast, the yield stress for pressure solution predicted by our model for grain boundary healing follows directly from the physics of interfacial energy. Our model shows that at grain contact points or islands with a small, negative radius of curvature, the decrease in chemical potential caused by surface curvature can be larger than the increase in chemical potential caused by stored elastic energy related to intergranular stresses. At sufficiently low stress, this leads to grain boundary healing and the cessation of pressure solution.

3.7 Summary and conclusions

Three simple geometric models representing grain boundaries containing a thin continuous fluid film, an island-channel network with cylindrical islands, and an island-channel network with bar-shaped islands have been presented here. These grain boundary structural models have been used as a basis to derive expressions giving the ratio I^*/I for "pressure-dissolving" quartz grain contacts, where I^* is the dissolution rate constant for a rough grain boundary and I is the free face dissolution rate constant as measured in geochemical kinetics experiments. A grain boundary energy/entropy balance approach was used. Previously published, theoretically based models for dissolution controlled pressure solution in quartz sands assuming $I^* = I$ overestimate experimental pressure solution rates by about half an

order of magnitude (Niemeijer et al., 2002). Our models for I^* show only a minor ($\leq$13%) reduction in I^* compared to I and cannot fully account for the observed discrepancy. Our models also predict that the load across a grain boundary with island-channel structure is supported by only a small fraction of the contact area, though the area occupied by non load-supporting islands might be larger.

A further model was derived, predicting a critical stress or "yield stress" below which grain boundary healing prevents pressure solution. In this model, grain boundary healing occurs when the driving force for growth of the islands induced by surface energy exceeds the average driving force for dissolution of the islands caused by a non-hydrostatic stress (c.f. Revil, 2001). Applying this model to the compaction experiments by Niemeijer et al. (2002), performed on quartz sands at temperatures of 400–600°C, effective stresses of 50–150MPa, and fluid pressures of 150–250MPa, shows that grain boundary healing is a possible cause for the sharp decrease in pressure solution compaction rates observed in their experiments at porosities below ~10–15%. The model was also used to estimate the dependence on depth of the minimum porosity that can be attained by compaction of arenitic rocks by pressure solution. A comparison of the estimated trends with porosity-depth data obtained for arenites from the Norwegian continental shelf (Ramm, 1992) showed a reasonable match, for values of α between 0.3 and 0.4. If further study would indicate that grain boundary healing is a limiting factor for pressure solution, this would imply that average pressure solution rates derived from natural rocks assuming continuous pressure solution during burial strongly underestimate actual rates.

4. Kinetic effects of microscale plasticity at grain boundaries during pressure solution

This chapter has been submitted for publication in the Journal of Geophysical Research.

Abstract

It is generally assumed in kinetic models for pressure solution in materials such as quartz that the effective dissolution rate coefficient in grain boundaries is equal to the conventional geochemical dissolution rate coefficient on a free surface. However, predictions based on this assumption usually overestimate both natural and experimental pressure solution rates even when evidence for dissolution rate control is strong. A possible explanation for this discrepancy is that grain boundary structure and dissipative processes such as microscale plasticity in the grain boundary can decrease this effective rate coefficient. Based on a simple grain boundary model assuming an island-channel structure, we have derived a preliminary model for the effect that dissipation by plastic deformation (work hardening flow and creep) of grain boundary islands has on dissolution controlled pressure solution rates. Comparing the predictions of this model to experimental data on quartz pressure solution rates, we see that microscale plasticity at grain boundary islands does slow down pressure solution, and can help explain the discrepancies between observed and theoretical pressure solution rates. When applied to pressure solution creep of sandstones or fault rocks in nature, our model predicts that grain boundary plastic deformation might have a significant effect at depths beyond ~9-10km.

4.1 Introduction

Pressure solution is an important mechanism of compaction and creep in upper and mid crustal rocks and fault zones, progressively giving way at depths beyond 10-20km to plastic flow by dislocation mechanisms (e.g., Rutter, 1983; Bos et al., 2000; Revil, 2001; Niemeijer and Spiers, 2005). In a chemically closed system, the rate of pressure solution is controlled by the slowest of three processes operating in series. These processes are: 1) dissolution of solid in the grain boundary fluid at highly stressed grain contacts, 2) diffusion of the dissolved solid out of the grain boundary, and 3) precipitation at low stress interfaces or on free pore walls (Raj, 1982; Rutter, 1983; Lehner, 1990). In open systems, fluid flow or long-range diffusion can transport dissolved material into or out of the system, slowing down or speeding up pressure solution respectively (Lehner, 1995; Gundersen et al., 2002).

During the last two decades, the structure of grain boundaries undergoing pressure solution has been much discussed, with models varying from thin adsorbed films (Figure 4.1a, 4.1b) (Weyl, 1959**;** Rutter, 1976, 1983; Hickman and Evans, 1991, 1992, 1995; Renard and Ortoleva, 1997; Renard et al., 1997; Alcantar et al., 2003; Meyer et al., 2006), to dynamically stable island-channel networks (Figure 4.1c, 4.1e) (Elliott, 1973; Raj, 1982; Lehner, 1990; Schutjens and Spiers, 1999; Ghoussoub and Leroy, 2001; De Meer et al., 2002, 2005; Dysthe et al., 2003; Van Noort et al., 2006, Chapter 2), and to thin films short-circuited by wider

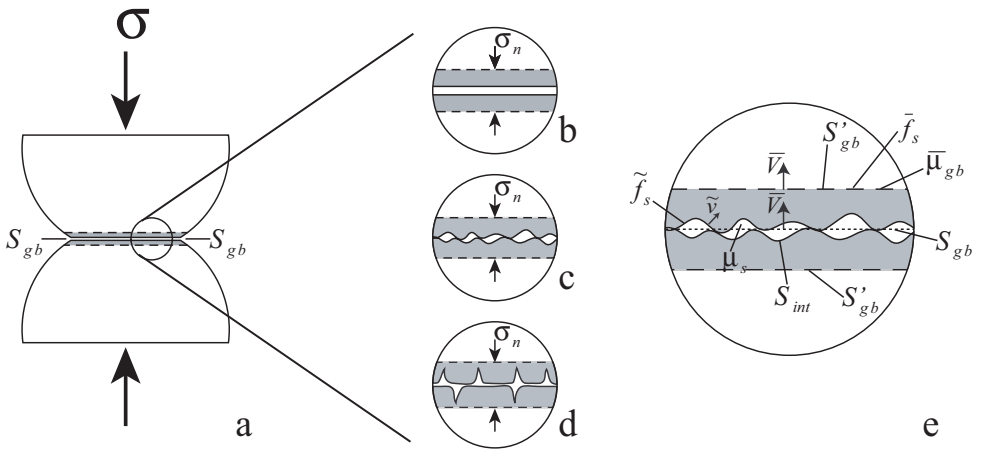

Figure 4.1 A grain contact undergoing pressure solution, and its internal structure viewed at: (a) the grain scale, and (b-e) the scale of the representative elementary volume with (b) a thin fluid film (e.g., Hickman and Evans, 1995), (c) an island-channel network (e.g., Lehner, 1990), and (d) a thin film short-circuited by crack arrays (e.g., Renard et al., 1999). The grain boundary zone is indicated in grey. (e) A close-up view of the island-channel network illustrating various quantities and definitions used in this paper (after: Lehner, 1990). They are: the grain scale grain boundary surface S_{gb}, the average dissolution rate normal to S_{gb}; $\bar{V}$, the margins of the grain boundary zone; S'_{gb}, the average Helmholtz free energy on S'_{gb}; $\bar{f}_s$, and the average chemical potential on S'_{gb}; $\bar{\mu}_{gb}$, the actual solid-fluid interface; S_{int}, the local dissolution rate normal to S_{int}; $\tilde{v}$, the Helmholtz free energy on S_{int}; $\tilde{f}_s$, and the chemical potential of the solid dissolved in the grain boundary fluid; μ_s.

crack or channel arrays (Figure 4.1d) (Gratz, 1991; Den Brok, 1998; Renard et al., 1999). This issue is important because the structure of the contact between two grains undergoing pressure solution can exert a strong influence on the rate of diffusion of dissolved material out of the grain boundary and hence on the rate of pressure solution. Specifically, the effective diffusivity of such grain boundaries is controlled by the degree of grain boundary wetting, the mean thickness of the fluid film, the tortuosity of the diffusion pathway, and by any structuring of the grain boundary fluid due to thin film or surface force effects (Rutter, 1976, 1983; Hickman and Evans, 1995; Alcantar et al., 2003; De Meer et al., 2005).

Despite evidence that pressure solution in silici-clastic rocks may often be dissolution controlled (Schutjens, 1991; Dewers and Hajash, 1995; Niemeijer et al., 2002), much less is known about the effect of grain boundary structure on dissolution controlled pressure solution. Recently, Van Noort et al. (2008, Chapter 3) presented models addressing the structure of island-channel grain boundaries undergoing pressure solution, and the influence that this dynamic structure has on dissolution controlled pressure solution rates. Assuming a purely elastic material, their models predict that the load across the contact between two grains of

quartz undergoing steady state pressure solution is carried by a very small fraction (generally <5%) of the total grain boundary area, and that compared to a free surface, dissolution rates (and hence dissolution controlled pressure solution rates) are reduced by only 10-15%. This cannot account for the relatively low rates of dissolution controlled pressure solution reported in experiments (e.g., Niemeijer et al., 2002). However, as the load-bearing islands are predicted by Van Noort et al. (2008, Chapter 3) to be very highly stressed, in practice plastic flow, fracturing or other surface damage of these points is likely to occur prior to their dissolution. Plastic deformation in particular would lead to the dissipation of energy otherwise available for driving pressure solution. This microscale deformation might range from highly localised surface indentations or dislocation damage, to island-scale yielding or flow at higher temperatures. Such effects might exert an important influence on pressure solution under conditions where plastic deformation becomes significant. In this chapter, we expand the model of Van Noort et al. (2008, Chapter 3), to include the influence of plastic deformation of load-bearing contact points in an island-channel grain boundary on dissolution controlled pressure solution rates. In our approach we will consider both strain hardening plastic deformation and steady state plastic flow.

4.2 The Model

4.2.1 Definitions

Rate equations for the deformation of rock materials by pressure solution have been derived by numerous authors (e.g., Raj, 1982; Lehner 1990, 1995; Niemeijer et al., 2002). For the case of 1-D or uniaxial compaction creep of a porous aggregate, for example, this takes the form:

$$\dot{\varepsilon} = \frac{GC}{d^m}\left[\exp\left(\frac{B(\phi)\sigma_e\Omega_s}{RT}\right) - 1\right]f(\phi) \approx \frac{GC}{d^m}\frac{B(\phi)\sigma_e\Omega_s}{RT}f(\phi) \tag{4.1}$$

In this equation, G is a geometric constant dependent on grain packing, d is grain size (m), σ_e is the effective axial stress (Pa), Ω_s is the molar volume of the solid (m^3mol^{-1}), R is the gas constant ($Jmol^{-1}K^{-1}$), T absolute temperature (K), and $B(\phi)$ and $f(\phi)$ are dimensionless functions of porosity (ϕ) accounting for porosity dependent changes in grain contact area and stress concentration. C is a rate constant dependent on the rate controlling process. The approximation $e^x - 1 = x$ is only valid at low effective stress σ_e (Niemeijer et al., 2002).

For dissolution controlled pressure solution, $m = 1$ and $C = I^*$, where I^* is a phenomenological rate coefficient (Lehner, 1990). To assess the effect of plastic deformation on dissolution controlled pressure solution, it is useful to express I^* in terms of the ratio of

I^*/I, where I is the free face dissolution coefficient of the dissolving material ($v_{dis} = I\Delta\mu/RT$, where $\Delta\mu$ is the potential drop between the solid in the solid phase and the solid in the solution phase). Seen in this context, I^* is a dissolution rate coefficient modified to account for the effect of the internal structure of the grain boundary zone and for all dissipative processes operating within it. It is defined via the relation $\bar{V} = I^* \Delta\bar{\mu}/RT$, where $\Delta\bar{\mu}$ is the average potential drop between the stressed solid in the grain boundary zone and the dissolved solid in the grain boundary fluid phase (Lehner, 1990; see also Van Noort et al., 2008, Chapter 3).

The coefficient I^* is the key kinetic factor in all models for dissolution-controlled pressure solution (e.g., Shimizu, 1995, Niemeijer et al., 2002; Spiers et al., 2004), but it is usually assumed that $I^* = I$ (Shimizu 1995; Renard et al., 1999; Revil, 2001; Gundersen et al., 2002; Niemeijer et al., 2002). This incorrect assumption overestimates I^* for a purely elastic grain boundary, as it neglects the effect of an island-channel network on the available surface area for dissolution (Van Noort et al., 2008, Chapter 3). It must also overestimate I^* for a grain boundary in which plastic deformation occurs, as plastic deformation dissipates part of the energy otherwise available for driving dissolution. Against this background it is important to note that previous dissolution-controlled pressure solution models overestimate experimental pressure solution rates by more than half an order of magnitude (Niemeijer et al., 2002), and also overestimate natural pressure solution rates (e.g., Revil, 2001; Gundersen et al., 2002).

4.2.2 Grain boundary energy/entropy balance

Our model for the effects of grain boundary microplasticity on dissolution controlled pressure solution, that is, on I^*, is based on the approach established by Lehner (1990). Grain boundaries are assumed to posses a microscale island-channel structure. On the grain scale, the grain boundary is considered as a surface (S_{gb}) on which smoothly varying values of free energy and normal contact stress (σ_n) can be defined. On a finer scale, we consider a representative elementary volume of the grain boundary to consist of a pillbox shaped zone, bounded by the surfaces S'_{gb}. Along the rough solid-liquid interfaces (S_{int}) within the grain boundary zone, microscale values of free energy ($\tilde{f}_s$) vary continuously and the normal stress is equal to the fluid pressure (P_f) (see Figure 4.1e). In a purely elastic solid, the following energy/entropy balance applies for an element of the grain boundary zone with area A during steady state dissolution-controlled pressure solution (Lehner, 1990; Van Noort et al., 2008, Chapter 3):

$$\frac{\bar{V}A}{\bar{\Omega}}\left[\left(\bar{f}_s + \sigma_n\bar{\Omega}\right) - \mu_s\right] = \int_{A_{\text{int}}} \frac{\tilde{v}}{\bar{\Omega}}\left[\left(\tilde{f}_s + P_f\tilde{\Omega}\right) - \mu_s\right]ds \tag{4.2}$$

Here $\bar{f}_s$ is the average Helmholtz free energy defined on S'_{gb}, while $\bar{\Omega}$ and $\tilde{\Omega}$ are respectively the average molar volume on S'_{gb} and the local microscale molar volume on S_{int}. The local microscale Helmholtz free energy on S_{int} is $\tilde{f}_s$. The chemical potential of the solid in the grain boundary fluid, μ_s, is approximately equal to the chemical potential of the pore wall during dissolution controlled pressure solution, and (neglecting pore wall curvature) is thus given $\mu_s \approx \bar{f}_s + P_f \bar{\Omega}$. An infinitesimally small element of S_{int} is represented by ds, and A_{int} is the area of surface S_{int} contained in the grain boundary element. The velocities $-\bar{V}$ and $-\tilde{v}$ respectively denote the average relative velocity with which mass moves into the grain boundary zone (through S'_{gb}) and the local relative velocity with which mass moves out of the grain boundary zone into solution (through S_{int}). At steady state, these velocities must balance such that the total mass of solid in the grain boundary zone is constant, i.e., such that

$$\bar{V}/\bar{\Omega} A = \int_{A_{\text{int}}} \tilde{v}/\tilde{\Omega} ds.$$

It can now be seen that the left hand side of equation (4.2) represents the amount of energy moving into the grain boundary zone, through S'_{gb}, while the right hand side represents the amount of energy lost from the grain boundary zone by dissolution of the solid along S_{int} (Lehner, 1990; Van Noort et al., 2008, Chapter 3). In a purely elastic material, energy is stored in the grain boundary zone by elastic deformation, and is dissipated at the same time by dissolution. At steady state, this results in zero net change of Helmholtz free energy, integrated over the grain boundary zone.

Irreversible plastic deformation is a dissipative process. Therefore, if we are to consider the influence that plastic deformation in an island-channel grain boundary zone (Figure 4.1e) has on pressure solution, we must include the dissipation of energy by plastic processes ($\dot{\Delta}_{pl}$) in balance equation (4.2). Again assuming steady state, there is no net storage of Helmholtz free energy stored in the grain boundary zone. Hence, when plastic deformation occurs in the grain boundary, equation (4.2) can be rewritten:

$$\frac{\bar{V}A}{\bar{\Omega}}\left[\left(\bar{f}_s + \sigma_n \bar{\Omega}\right) - \mu_s\right] = \int_{A_{\text{int}}} \frac{\tilde{v}}{\tilde{\Omega}}\left[\left(\tilde{f}_s + P_f \tilde{\Omega}\right) - \mu_s\right] ds + \dot{\Delta}_{pl} \tag{4.3}$$

where $\bar{f}_s$ and $\tilde{f}_s$ now include both elastic and defect stored energy, and where from the second law of thermodynamics $\dot{\Delta}_{pl} > 0$ (Lehner, 1990). In the case of time-independent, strain-hardening plastic deformation, and assuming a steady state grain boundary structure, bulk grain material moves into the grain boundary zone and is instantly deformed plastically. The rate of dissipation by plastic deformation will then be controlled by the rate of grain boundary dissolution and the strain-hardening flow law. Here, the grain boundary dissolution rate determines the amount of material available for plastic deformation, while the flow law determines the amount of plastic deformation this material undergoes. For time-dependent

plastic flow, or creep, the rate of local plastic deformation in the grain boundary depends only on the local stresses and creep properties of the material.

In the pressure solution models of Lehner (1990) and resulting constitutive equations such as equation (4.1), dissipation by plastic deformation is included in the dissolution step through the phenomenological rate coefficient I^*, which accounts for the structure of the grain boundary and all dissipative processes occurring in the grain boundary zone. This definition of I^* then implies that when dissipation is dominated by grain boundary plastic deformation, pressure solution will become dissolution controlled (Lehner, 1990), with I^* determining the absolute rate.

In our previous paper (Van Noort et al., 2008, Chapter 3), we derived models for the influence of a dynamically stable island-channel network with cylindrical and bar-shaped islands (Figure 4.2 and 4.3) on dissolution-controlled pressure solution in an elastic material. In the following, we will first reconsider the mass and energy balances used to derive these models. We will then expand these balances to include the effect of plastic deformation in the grain boundary zone on the ratio I^*/I and hence on the rate of (dissolution-controlled) pressure solution.

4.2.3 The model for an elastic solid

Figures 4.2 and 4.3 show the two hypothetical island-channel grain boundary geometries considered. In both geometries, two distinct dissolution sites can be distinguished, namely island margins (dissolving laterally at average velocity $\tilde{v}_i$) and channel roofs/floors (dissolving perpendicular to the grain boundary at average velocity $\tilde{v}_c$). Under the assumption of a steady state grain boundary structure within a given grain boundary element, $\tilde{v}_i$ and $\tilde{v}_c$ must be

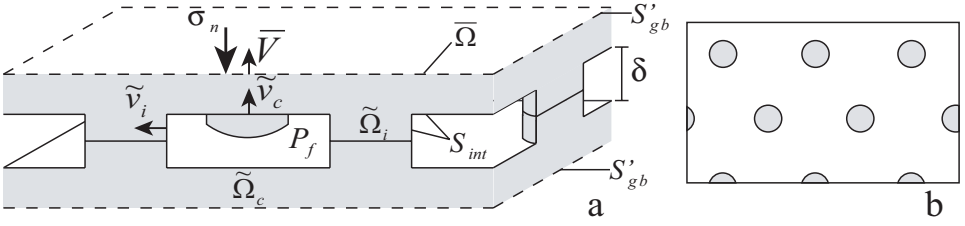

Figure 4.2 (a) A schematic drawing of the grain boundary structure assumed in the island-channel model with cylindrical islands. An element of grain boundary is shown in grey. $\bar{V}$ *indicates the (macroscopic) rate with which the grain boundary zone moves towards the centre of the grain, perpendicular to* S'_{gb}*;* $\tilde{v}_c$ *and* $\tilde{v}_i$ *respectively indicate the average rate of dissolution on channel floors/roofs and of the island margins, perpendicular to the solid-fluid contact* S_{int}*.* $\bar{\Omega}$*,* $\tilde{\Omega}_c$ *and* $\tilde{\Omega}_i$ *are respectively the average solid molar volume on* S'_{gb}*, the solid molar volume in the channel floors/roofs (on* S_{int}*) , and the solid molar volume in the islands (on* S_{int}*).* δ *represents the grain boundary width. (b) A plan view of the island-channel geometry.*

balanced so that the amount of island mass removed by $\tilde{v}_i$ is equal to the amount of mass effectively added to the islands by deepening of the channels (by $\tilde{v}_c$). This then implies that for both structures:

$$\frac{\tilde{v}_c A}{\tilde{\Omega}_c}\alpha = \frac{\tilde{v}_i A}{\tilde{\Omega}_i} M \frac{\delta}{2} c_i \tag{4.4}$$

Here, α is the fraction of this grain boundary occupied by load-supporting solid island contact, $\tilde{\Omega}_i$ and $\tilde{\Omega}_c$ are local average values of the solid molar volume for the islands and the channel roofs/floors (defined on S_{int}), M is the number of islands in the grain boundary (m^{-2}), δ is the width of the grain boundary (in m) and c_i is the average circumference of an island (in m). For cylindrical islands $c_i = 2\pi r_i$, where $r_i = \sqrt{\alpha/M\pi}$ is the mean island radius. For bar-shaped islands $c_i = 2\left(\sqrt{\alpha s/M} + \sqrt{\alpha/Ms}\right)$, where s is the island aspect ratio (island length divided by island width).

In addition, the mass of solid entering our element of grain boundary zone must equal the mass of solid dissolved from the grain boundary zone, so that:

$$\frac{\bar{V}A}{\tilde{\Omega}} = \frac{\tilde{v}_c A}{\tilde{\Omega}_c}(1-\alpha) + \frac{\tilde{v}_i A}{\tilde{\Omega}_i} M \frac{\delta}{2} c_i \tag{4.5}$$

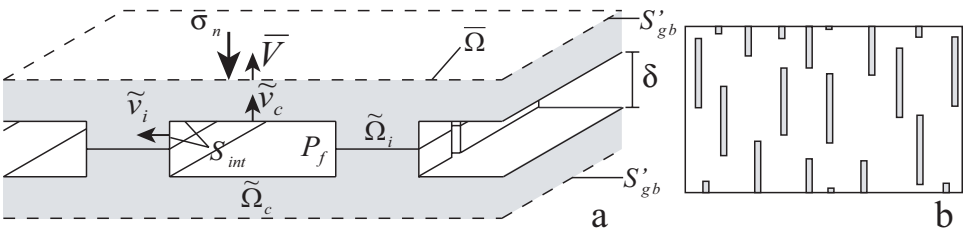

Figure 4.3 (a) A schematic drawing of the grain boundary structure assumed in the island-channel model with bar-shaped islands. An element of grain boundary is shown in grey. $\bar{V}$ indicates the (macroscopic) rate with which the grain boundary zone moves towards the centre of the grain, perpendicular to S'_{gb}; $\tilde{v}_c$ and $\tilde{v}_i$ respectively indicate the average rate of dissolution on channel floors/roofs and of the island margins, perpendicular to the solid-fluid contact S_{int}. $\bar{\Omega}$, $\tilde{\Omega}_c$ and $\tilde{\Omega}_i$ are respectively the average solid molar volume on S'_{gb}, the solid molar volume in the channel floors/roofs (on S_{int}) , and the solid molar volume in the islands (on S_{int}). δ represents the grain boundary width. (b) A plan view of the island-channel geometry.

Likewise, the conservation of energy and entropy also applies to the grain boundary element. Rewriting Lehner's relation for this (equation (4.2)), using the mass balance expressed in equation (4.5) gives:

$$\frac{\bar{V}A}{\bar{\Omega}}\left[\left(\bar{f}_s + \sigma_n\bar{\Omega}\right) - \mu_s\right] = \frac{\tilde{v}_c A}{\tilde{\Omega}_c}(1-\alpha)\Delta\tilde{\mu}_c + \frac{\tilde{v}_i A}{\tilde{\Omega}_i}M\frac{\delta}{2}c_i\Delta\tilde{\mu}_i \tag{4.6}$$

In this equation, $\Delta\tilde{\mu}_i$ and $\Delta\tilde{\mu}_c$ are the local differences in chemical potential between the solid on S_{int} and the solid dissolved in the grain boundary fluid, with $\Delta\tilde{\mu}_i$ applying to the islands and $\Delta\tilde{\mu}_c$ to the channel roofs/floors. Combining mass balance equations (4.4) and (4.5), we can further show that $\bar{V}/\bar{\Omega} = \tilde{v}_c/\tilde{\Omega}_c$, and therefore that

$$\left(\bar{f}_s + \sigma_n\bar{\Omega}\right) - \mu_s = \Delta\tilde{\mu}_c\left[(1-\alpha) + \frac{2\alpha^2}{M\delta c_i}\frac{\tilde{\Omega}_i}{\tilde{\Omega}_c}\right] \tag{4.7}$$

As $\bar{V} = I^*\Delta\bar{\mu}/RT$ and $\tilde{v}_c = I\Delta\tilde{\mu}_c/RT$ it can also be shown that:

$$I^*/I = \frac{\Delta\tilde{\mu}_c}{\left(\bar{f}_s + \sigma_n\bar{\Omega}\right) - \mu_s}\frac{\bar{\Omega}}{\tilde{\Omega}_c}, \tag{4.8}$$

yielding:

$$\frac{I^*}{I} = \frac{1}{\left[(1-\alpha) + \frac{2\alpha^2}{M\delta c_i}\frac{\tilde{\Omega}_i}{\tilde{\Omega}_c}\right]}\frac{\bar{\Omega}}{\tilde{\Omega}_c} \tag{4.9}$$

which is the result reported by Van Noort et al. (2008, Chapter 3) for the elastic case.

4.2.4 Influence of plastic deformation

The above model for I^* during dissolution-controlled pressure solution in an elastic solid will now be extended to include plastic deformation in the grain boundary zone. As shown in equation (4.3) and explained by Lehner (1990), this can be done by including the dissipation of energy by plastic deformation in the energy/entropy balance of the pressure-dissolving grain boundary. At the scale of individual grain boundary islands, part of the work done by plastic deformation will be dissipated, but energy will also be stored in newly generated

dislocations. On the scale of a representative grain boundary element of area A, the rate of energy dissipation within the solid phase ($\dot{\Delta}_{pl}$) by plastic deformation must then equal the total work rate of plastic deformation minus the rate with which energy is stored in dislocations ($\dot{f}_{pl}$):

$$\dot{\Delta}_{pl} = \dot{W}_{pl} - \dot{f}_{pl} > 0 \tag{4.10}$$

Under the assumption of steady state, the total amount of dislocation-stored energy in our element of grain boundary zone, like the total amount of stored elastic energy, will be constant. This means that, while all of the work done by plastic deformation ($\dot{W}_{pl}$) is dissipated, only part is dissipated as a result of plastic deformation ($\dot{\Delta}_{pl}$). The other part ($\dot{f}_{pl}$) is stored first, and then dissipated by dissolution. In a volume of deformed solid, the excess amount of dislocation-stored energy, over a hydrostatically stressed solid, (f_{pl}, Jm^{-3}) is given (e.g., by Humphreys and Hatherly, 1996) as

$$f_{pl} = \rho W = \beta \rho G b^2 \tag{4.11}$$

where β is a material dependent constant, ρ is the dislocation density (m^{-2}), G the shear modulus (Pa), and b the Burger's vector (m). In addition, the dependence of the dislocation density on the differential stress (σ) in a plastically deformed material can be approximated as (Takeuchi and Argon, 1976; Humphreys and Hatherly, 1996; Dresen et al., 1997):

$$\rho = \left(\frac{\sigma}{\kappa G b} \right)^2 \tag{4.12}$$

Here, κ is a material dependent constant. Inspection of the data presented by De Bresser (1996) shows that, for calcite, equation (4.12) not only applies to steady state creep, but also to strain hardening deformation. A quadratic correlation between stress and dislocation density is also reported during strain hardening plastic flow in periclase (Kohlstedt and Weathers, 1980), halite at least at strains below 4% (Davidge and Pratt, 1964), and in fluorite (Evans and Pratt, 1970), while a similar relation with a coefficient of ~1.5-2, is also found for quartz and olivine (Kohlstedt and Weathers, 1980; De Bresser, 1996). In our modelling, we will assume that a quadratic correlation applies during strain hardening plastic deformation of all minerals considered. During pressure solution, significant plastic deformation is expected mainly in and in the neighbourhood of highly stressed contact points (islands). Assuming then that the dislocation stored energy in bulk grains and channel walls is negligible in comparison, the rate with which energy is stored in dislocations in a grain boundary element ($\dot{f}_{pl}$) is given by

the rate with which undeformed solid moves into the islands times the energy that will be stored in this solid (f_{pl}). For the present case, contacting islands support a differential stress given $\sigma_i = (\sigma_n - P_f)/\alpha$, so that from (4.11) and (4.12):

$$\dot{f}_{pl} = \beta \frac{\sigma_i^2}{\kappa^2 G} \tilde{v}_c \alpha A \tag{4.13}$$

In defining the rate of plastic work $\dot{W}_{pl}$ in order to obtain $\dot{\Delta}_{pl}$ in (4.10), two different modes of plastic deformation will be considered. First we will look at strain hardening deformation. Next a model will be defined assuming steady state plastic flow of the islands.

4.2.5 Strain hardening plastic deformation

Strain hardening deformation of a material, such as a single crystal, can be viewed as behaviour characterised by a yield stress which increases as the total amount of strain in the sample increases. The stress-strain behaviour during strain hardening deformation of single crystals can often be approximated quite accurately by a linear relationship of the form $\varepsilon = \sigma/S$, as demonstrated for example by data presented for calcite (De Bresser and Spiers, 1997), for halite (Pratt, 1953; Davidge and Pratt, 1964; Wanten et al., 1996), for fluorite (Evans and Pratt, 1970), or for various metals (e.g., Hirsch, 1964). The plastic work rate associated with compressive deformation of the islands, under the action of the differential stress σ_i, is then given by the amount of (plastically) undeformed mass moving into the islands, times the work done in deforming this mass ($W_{pl} = \sigma^2/2S$), i.e., by

$$\dot{W}_{pl} = W_{pl} \tilde{v}_c \alpha A = \frac{\sigma_i^2}{2S} \tilde{v}_c \alpha A \tag{4.14}$$

where S (Pa) is the linearised work hardening coefficient defined $S = d\sigma/d\varepsilon$. The plastic irreversible dissipation rate is then given using (4.10) and (4.13) by:

$$\dot{\Delta}_{pl} = \dot{W}_{pl} - \dot{f}_{pl} = \sigma_i^2 \left(\frac{1}{2S} - \frac{\beta}{\kappa^2 G} \right) \tilde{v}_c \alpha A > 0 \tag{4.15}$$

Inserting (4.15) into (4.3) now yields the energy/entropy balance

$$\frac{\bar{V}A}{\bar{\Omega}}\left[\left(\bar{f}_s + \sigma_n\bar{\Omega}\right) - \mu_s\right] = \frac{\tilde{v}_c A}{\tilde{\Omega}_c}(1-\alpha)\Delta\tilde{\mu}_c + \frac{\tilde{v}_i A}{\tilde{\Omega}_i}M\frac{\delta}{2}c_i\Delta\tilde{\mu}_i + \frac{\tilde{v}_c A}{\tilde{\Omega}_c}\alpha\tilde{\Omega}_i\sigma_i^2\left(\frac{1}{2S} - \frac{\beta}{\kappa^2 G}\right) \tag{4.16}$$

Fortunately, the mass balance equations (4.4) and (4.5) for the elastic solid still apply for the plastically deforming solid. Using these, the above energy balance can hence be rewritten:

$$\left(\bar{f}_s + \sigma_n\bar{\Omega}\right) - \mu_s = \Delta\tilde{\mu}_i\left[(1-\alpha)\frac{M\delta c_i}{2\alpha}\frac{\tilde{\Omega}_c}{\tilde{\Omega}_i} + \alpha\right] + \alpha\tilde{\Omega}_i\sigma_i^2\left(\frac{1}{2S} - \frac{\beta}{\kappa^2 G}\right) \tag{4.17}$$

This equation then serves as a statement of the fact that the amount of energy going into the grain boundary zone is equal to the amount of energy dissipated by dissolution, diffusion and precipitation plus the amount of energy dissipated as a result of plastic deformation of the islands.

The next step is to evaluate $\Delta\tilde{\mu}_i$, which, it will be recalled, is the average chemical potential difference between the solid at the island-fluid interface in a given grain boundary element ($\tilde{\mu}_i = \tilde{f}_i + P_f\tilde{\Omega}_i$), and the solid dissolved in the grain boundary fluid. As dissolution is rate-controlling, the chemical potential of the solid in the grain boundary fluid is approximately equal to the chemical potential at the pore wall ($\mu_s \approx \bar{f}_s + P_f\bar{\Omega}$), so that if we neglect the minor effect of curvature of the pore wall:

$$\Delta\tilde{\mu}_i = \tilde{\mu}_i - \mu_s = \frac{\sigma_i^2}{2E}\tilde{\Omega}_i + \beta\frac{\sigma_i^2}{\kappa^2 G}\tilde{\Omega}_i + P_f\left(\tilde{\Omega}_i - \bar{\Omega}\right) \tag{4.18}$$

The first term on the far right side of equation (4.18) represents the excess elastic stored energy at the islands compared with the (undeformed) pore wall (E is Young's modulus), while the second term represents the excess dislocation-stored energy in the islands, compared to the pore wall. The third term is P_f times the difference in molar volume between the solid at islands and at pore walls. Generally, this is much smaller than the other two terms (except at very high fluid pressures) and it is henceforth neglected. As, from (4.4) and (4.5), $\bar{V}/\bar{\Omega} = \tilde{v}_i M\delta c_i/\left(2\alpha\tilde{\Omega}_i\right)$, again using $\bar{V} = I^*\Delta\bar{\mu}/RT$ and $\tilde{v}_i = I\Delta\tilde{\mu}_i/RT$, we can now write:

$$\frac{I^*}{I} = \frac{M\delta c_i}{2\alpha} \frac{\Delta\tilde{\mu}_i}{\left[\left(\bar{f}_s + \sigma_n\bar{\Omega}\right) - \mu_s\right]} \frac{\bar{\Omega}}{\tilde{\Omega}_i} \tag{4.19}$$

which, upon inserting (4.17) for $\left(\bar{f}_s + \sigma_n\bar{\Omega}\right) - \mu_s$ and (4.18) for $\Delta\tilde{\mu}_i$ becomes:

$$\frac{I^*}{I} = \frac{\Psi M\delta c_i}{\Psi\left[(1-\alpha)M\delta c_i \frac{\tilde{\Omega}_c}{\tilde{\Omega}_i} + 2\alpha^2\right] + 4\alpha^2 EX} \left(\frac{\bar{\Omega}}{\tilde{\Omega}_i}\right) \tag{4.20}$$

where $\Psi = \left(\kappa^2 G + 2\beta E\right)$ and $X = \left(\kappa^2 G/(2S) - \beta\right)$ are material dependent constants. This gives the ratio I^*/I for a grain boundary where islands deform by strain hardening plastic flow.

4.2.6 Time dependent plastic flow

The second mode of plastic deformation considered here is time-dependent, steady state plastic flow of the islands, for example described by a Dorn-type power law. In this case, again assuming a steady state grain boundary structure, the mass and energy balances defined above for the elastic and hardening models still apply, but the solid material in the islands is continuously deforming or creeping. The plastic work rate, $\dot{W}_{pl}$, is now given by the amount of material in the islands, multiplied by the island strain rate normal to the grain boundary ($\dot{\varepsilon}_i$) times the differential stress supported by the islands:

$$\dot{W}_{pl} = \dot{\varepsilon}_i \sigma_i \alpha A \frac{\delta}{2} \tag{4.21}$$

Assuming equations (4.11) and (4.13) still apply for the amount of dislocation stored energy and the rate with which energy is stored in the islands during plastic flow, the dissipation rate is now given by:

$$\dot{\Delta}_{pl} = \dot{W}_{pl} - \dot{f}_{pl} = \dot{\varepsilon}_i \sigma_i \alpha A \frac{\delta}{2} - \frac{\tilde{v}_c A}{\tilde{\Omega}_c} \alpha\tilde{\Omega}_i \beta \frac{\sigma_i^2}{\kappa^2 G} \tag{4.22}$$

We stress again that, as plastic deformation is an irreversible process, $\dot{\Delta}_{pl} > 0$ must apply. Inserting (4.22) into (4.3) then gives the following result:

$$\frac{\bar{V}A}{\bar{\Omega}}\left[\left(\bar{f}_s + \sigma_n\bar{\Omega}\right) - \mu_s\right] = \frac{\tilde{v}_c A}{\tilde{\Omega}_c}(1-\alpha)\Delta\tilde{\mu}_c + \frac{\tilde{v}_i A}{\tilde{\Omega}_i}M\frac{\delta}{2}c_i\Delta\tilde{\mu}_i + \dot{\varepsilon}_i\sigma_i\alpha A\frac{\delta}{2} - \frac{\tilde{v}_c A}{\tilde{\Omega}_c}\alpha\tilde{\Omega}_i\beta\frac{\sigma_i^2}{\kappa^2 G} \tag{4.23}$$

Using the mass balance equations (4.4) and (4.5) we can now rewrite equation (4.23) as:

$$\left(\bar{f}_s + \sigma_n\bar{\Omega}\right) - \mu_s = \Delta\tilde{\mu}_i\left[(1-\alpha)\frac{M\delta c_i}{2\alpha}\frac{\tilde{\Omega}_c}{\tilde{\Omega}_i} + \alpha\right] + \alpha^2\tilde{\Omega}_i\frac{\dot{\varepsilon}_i\sigma_i}{\tilde{v}_i Mc_i} - \alpha\tilde{\Omega}_i\beta\frac{\sigma_i^2}{\kappa^2 G} \tag{4.24}$$

Inserting equation (4.18), the above result and $\tilde{v}_i = I\Delta\tilde{\mu}_i/RT$ into equation (4.19) then yields:

$$\frac{I^*}{I} = \frac{I\Psi^2M^2\delta c_i^2\bar{\Omega}}{I\Psi^2\tilde{\Omega}_i\left[(1-\alpha)M^2\delta c_i^2\frac{\tilde{\Omega}_c}{\tilde{\Omega}_i} + 2Mc_i\alpha^2\right] + 8E^2\kappa^4G^2\alpha^3RT\dot{\varepsilon}_i\sigma_i^{-3} - 4IMc_i\alpha^2\beta E\Psi\tilde{\Omega}_i} \tag{4.25}$$

This equation thus gives the ratio I^*/I for a grain boundary where islands deform by time dependent, steady state plastic flow.

4.2.7 Constraints on contact geometry

The above models are based on the balances of energy and mass derived by Lehner (1990), and applied here in the form of equations (4.7), (4.17), and (4.24). The excess chemical potential of the bulk grain material at the margin of the grain boundary zone (S'_{gb}) relative to the pore wall, as found in these equations, is given by:

$$\left(\bar{f}_s + \sigma_n\bar{\Omega}\right) - \mu_s = (\sigma_n - P_f)\bar{\Omega} \tag{4.26}$$

Note that this assumes that there are no significant grain scale gradients in free energy, due to gradients in elastic and plastic deformation of the bulk grain material. For the elastic model with no plastic deformation, combining equations (4.7) and (4.26) implies that:

$$(\sigma_n - P_f)\bar{\Omega} = \frac{\left[(\sigma_n - P_f)/\alpha\right]^2}{2E}\left[(1-\alpha)\frac{M\delta c_i}{2\alpha}\tilde{\Omega}_c + \alpha\tilde{\Omega}_i\right] \tag{4.27}$$

This shows that at a given effective contact stress (given σ_n and P_f), and assuming a steady state structure, only 2 out of 3, or 3 out of 4, of the parameters determining the grain boundary geometry (α,δ, M, and s) are independent. Analogous results and interdependencies are also found for the hardening and plastic flow models by combining equation (4.26) and either equation (4.17) or equation (4.24).

4.3 Model predictions and discussion

Equations (4.20) and (4.25) give approximations for the influence of grain boundary structure and plastic deformation on the rate of grain boundary dissolution by pressure solution. We will now apply these models in order to evaluate this influence on quartz pressure solution under conditions where the onset of plastic deformation or dislocation damage can be expected, by inserting suitable flow laws. Then, using our new model, we will determine values for the variable α (or M) at specific values of δ, s, and M (or α), using a modified balance equation (4.27). Next we will calculate I^*/I ratios, which can be used to calculate compaction strain rates due to dissolution controlled pressure solution by insertion into equation (4.1). Finally, we will compare our predictions for pressure solution including grain boundary microplasticity to those of Niemeijer et al. (2002) and to their experimental data for dissolution controlled pressure solution in quartz.

4.3.1 Pressure solution in quartz

Recent experiments indicate that dissolution is the rate controlling mechanism for pressure solution in quartz in nature and experiment (e.g., Niemeijer et al., 2002). Therefore, any plastic deformation occurring within the grain boundaries is likely to influence pressure solution rates. In addition, recent SEM and EBSD analysis of quartzites that were faulted in nature at low temperatures (200-250°C) and fluid pressures (2-3kbar) has shown that high stresses at grain contacts initially lead to dauphiné twinning followed by low temperature (work hardening) plasticity and/or microcracking (e.g., Lloyd, 2000). However, since there is almost no quantitative data available on time-independent strain-hardening flow in quartz at high stresses, we will only consider the creep behaviour of grain boundary islands. Steady state creep models are available. To describe the dislocation creep behaviour we take the following equation presented by Hirth et al. (2001):

$$\dot{\varepsilon} = 10^{-41.2} f_{H_2O} \sigma^4 \exp\left(135000/RT\right) \tag{4.28}$$

where water fugacity f_{H_2O} and the differential stress σ are given in Pa. This flow law is widely considered to describe plastic flow of quartz both in experiments and nature, and has been calibrated against flow rates in a quartzite rock deforming in nature at ~250-300°C (Hirth et al., 2001). The weakening effect of water present in the quartz crystal lattice (hydrolytic

weakening effect, e.g., Blacic and Christie, 1984) is included in this equation via the water fugacity term. As we consider plastic deformation in the very thin grain boundary zone only, (4.28) can be included in (4.25) to describe plastic flow of the islands, with the water concentration in the deforming islands assumed to be in equilibrium with the water fugacity of the pore fluid, thus assuming the grain boundary island structure to be water weakened. In other words, we assume equilibration of dissolved water content in the grain boundary zone.

For our calculations of I^*/I from (4.25), we use the dissolution rate constant I given by (Rimstidt and Barnes, 1980):

$$I = k_+ \Omega_s = \Omega_s \times 10^{(1.174 - 0.002028T - 4158/T)} \tag{4.29}$$

This model for I is used here, as it was also used by Niemeijer et al. (2002), and thus gives a better comparison between our models than using a different model for I, such as that of Tester et al. (1994), would. Inserting (4.28) for $\dot{\varepsilon}$ into (4.25), we calculated I^*/I ratios for quartz pressure solution including grain boundary plastic deformation, using the following values: $E = 96$GPa (Simmons and Wang, 1971), $G = 44$GPa (Simmons and Wang, 1971), $\kappa = 2$ (Dresen et al., 1997; Kohlstedt and Weathers, 1980), and $\beta = 0.5$ (Humphreys and Hatherly, 1996). The island circumference c_i depends on whether we used cylindrical or bar-shaped islands. In the latter case the island aspect ratio was chosen as $s = 20$ (Van Noort et al., 2008, Chapter 3).

Figures 4.4 and 4.5 show the predicted dependence of area fraction α (calculated using equation (4.27) modified for the plastic case) and of I^*/I (calculated using equations (4.25) and (4.28)) on island density M at set values of grain boundary width δ (5, 10 and 50nm) and island aspect ratio s, for the experimental conditions used in the quartz compaction experiments of Niemeijer et al. (2002) (500°C, 200MPa P_f, 100MPa σ_{eff}). Values for the grain boundary width are generally estimated to fall in the range 1-100nm (e.g., Nakashima, 1995; Shimizu, 1995; Renard and Ortoleva, 1997; Spiers et al., 2004). Our curves are plotted for normal contact stresses of 695 and 486MPa, equivalent to porosities of either 30% or 20% ($\phi/\phi_0 = 0.63$and 0.42) in the framework of the pressure solution compaction model used by Niemeijer et al. (2002) to compare with their experimental data. This model assumes a simple cubic packing of initially spherical grains. Figure 4.4 shows that α falls in the range 0.01 to 0.1 for cylindrical islands, with lower values for lower δ and effective normal contact stress. Minimum values of α occur for M values in the range $2\text{x}10^{10}$ to $2\text{x}10^{12}\text{m}^{-2}$. For bar-shaped islands, α falls in the range 0.01 to 0.07, and has minimum values for M in the range $2\text{x}10^{9}$ to $5\text{x}10^{10}\text{m}^{-2}$. Figure 4.5 shows that I^*/I ratios increase with increasing values of M. Higher values for I^*/I are obtained for higher values of δ, and lower effective normal contact stresses.

Next, we compare the quartz compaction data of Niemeijer et al. (2002), their pressure solution compaction model (i.e., equation (4.1) assuming $C = I$), and their compaction model

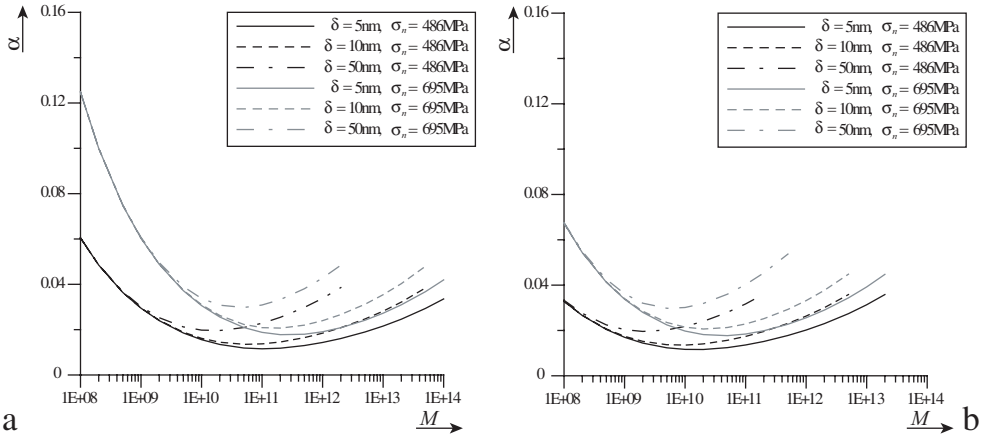

Figure 4.4: Predicted dependence of the grain boundary area fraction taken up by islands (α) on the number of load bearing islands per square meter in the grain boundary (M in m^{-2}), with grain boundary widths (δ) of 5, 10 and 50nm, at effective normal contact stresses of 486 and 695MPa (equivalent to 20 and 30% porosity in the experiments of Niemeijer et al. (2002)). (a) Cylindrical islands. (b) Bar-shaped islands.

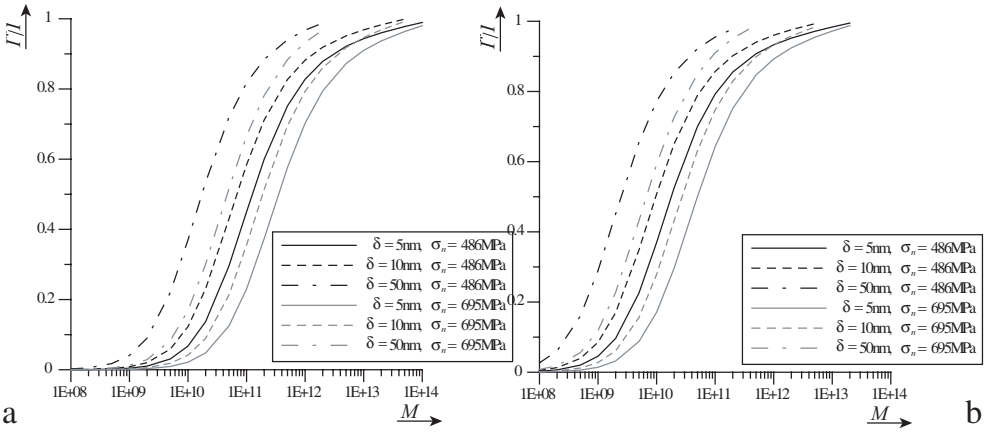

Figure 4.5 Predicted dependence of the ratio of the phenomological rate constant for grain boundary dissolution (I^*) over the geochemical rate constant for free-face dissolution (I) on the number of load bearing islands per square meter in the grain boundary (M in m^{-2}), with grain boundary widths (δ) of 5, 10 and 50nm, at effective normal contact stresses of 486 and 695MPa (equivalent to 20 and 30% porosity in the experiments of Niemeijer et al. (2002)). (a) Cylindrical islands. (b) Bar-shaped islands.

applied using our model for I^*/I. Values for the ratio I^*/I were calculated for different porosities (different effective normal contact stresses) assuming constant values of δ and s, and assuming the minimum value of α for which the energy balance (the plastic equivalent of equation (4.27)) could be solved. This value of α is chosen simply as a reference value, with specific physical reason. The corresponding value for M at each porosity is also found from the modified equation (4.27), and decreases with decreasing effective normal contact stress (see also Figure 4.4). Solving our system of equations using these values for α and M, yield a roughly constant value for the effective island stress at all porosities. The ratio I^*/I is also found to be more or less independent of porosity (see Figure 4.6a). Furthermore, I^*/I is only very weakly dependent on δ ($I^*/I = 0.45$ for $\delta = 5$nm and $I^*/I = 0.48$ for $\delta = 50$nm). Moreover, the predicted I^*/I ratios are independent of island shape, though higher numbers of cylindrical islands (~7 times higher) are predicted. The grain boundary geometry predicted does depend on δ, however, with larger numbers of islands (M ~6.6-6.8 times higher) taking up less area (α ~0.59-0.6 times lower) at lower grain boundary widths. The effective island stresses predicted by our model are rather high (more than 20GPa), indicating that surface fracturing and other surface damage is very likely to occur. Finally, Figure 4.6a compares the data from experiment CPf8 of Niemeijer et al. (2002) with their model (equation (4.1)) applied using I, and their model applied using I^* determined from our I^*/I ratios assuming minimum α values. Our I^*/I ratios do show a reduction of pressure solution rates due to the effects of grain boundary plasticity. However, they do not significantly improve the comparison between theory and experiment, and also do not fully explain the observed discrepancies, which increase with decreasing porosity.

As an alternative way of solving the balance equation (4.27) for the plastic model, we can assume that the number of contact points per grain boundary is always minimal, by choosing the number of contact points per square meter of grain boundary (M) such that the number of solid-solid contacts in an average sized grain contact is three at all porosities, see also Van Noort et al. (2008, Chapter 3). This implies decreasing values of M with decreasing porosity, as grain contact sizes increase. From solving our equation (4.27) for each porosity, we then find that α also decreases with decreasing porosity, resulting in increasing effective island stresses. Equation (4.25) then shows that the ratio I^*/I increases with decreasing porosity. Values for the I^*/I ratio fall in the range 0.019-0.82 (though lower values would be obtained for higher grain sizes, i.e., for lower values of M). Figure 4.6b compares experimental data with the Niemeijer et al. (2002) model, and that model modified using I^*/I ratios calculated assuming that the number of solid-solid contacts in a grain boundary is three. Though the discrepancies between experiment and theory fall in the range of values predicted by our model, the experimental compaction trend again is not reproduced.

A better agreement between experimental and theoretical compaction rates, with changes in I^*/I compensating very well for increases in the discrepancy between experimental and theoretical rates, at least down to porosity ratios ϕ/ϕ_0 of ~0.55 is obtained by assuming a

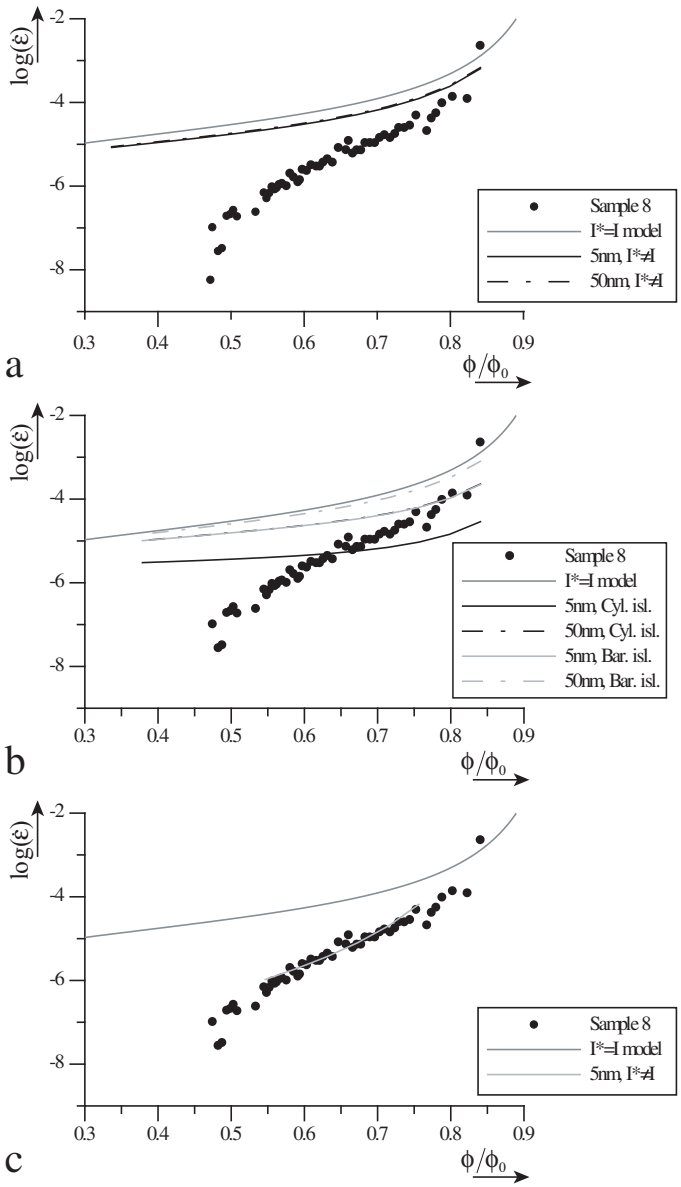

Figure 4.6 A comparison between the data obtained from quartz compaction experiment CPf8 of Niemeijer et al. (2002), his pressure solution model applied assuming $I^* = I$*, and an equivalent pressure solution model applied using our expression for* I^**, assuming (a) minimum values for the grain boundary area fraction (*α*) taken up by islands, (b) the minimum of three points of actual contact per grain boundary (i.e., minimum* M*), and (c) a constant value of* $\alpha = 0.022$ *for grain boundary width* $\delta = 5nm$*, and* $\alpha = 0.038$ *for* $\delta = 50nm$*.*

constant value of α ($\alpha = 0.027$with $\delta = 5$nm) and the minimum associated value for M, at all porosities (Figure 4.6c), though we have no physical basis for this. Note that using this assumption, the energy balance cannot be solved for very high porosities ($\phi/\phi_0 > 0.76$) and predicts very low values of M (implying less than one island per contact) at lower porosities ($\phi/\phi_0 < 0.55$when assuming cylindrical islands). The range over which our model can be applied can be broadened by allowing α to evolve with porosity.

The above examples show that including the effects of microscale plasticity in the grain boundary in dissolution controlled pressure solution models can reduce predicted compaction rates to rates comparable to those observed in the experiments of Niemeijer et al. (2002). A detailed agreement between model and experiment can be obtained, but we have no physical basis for the assumptions on the grain boundary structure made to achieve these solutions to our grain boundary energy/entropy balance. We point out once again that our model is based on very simple assumptions of grain boundary structure. Furthermore, it is questionable if the steady state model for plastic creep in quartz used here is applicable to the high stresses in the islands, and if actual stresses in the grain boundary islands might be lower due to surface forces when grain boundary widths are of the order of a few nanometers (e.g., Alcantar, 2003). The high stresses at the contact points predicted also indicate that fracturing of such contact points, followed by surface energy driven dissolution, is likely to occur. In essence the detailed physics of the (dissipative) processes occurring in a grain boundary during pressure solution are still poorly understood. Our model, however, indicates that in quartz plastic deformation in the grain boundary zone might be an important process. Experimental investigations of such contacts are required to determine if this is indeed the case.

When considering the deformation of sandstones or granular fault rocks in nature, applying equation (4.1), including our microplasticity model for the ratio I^*/I allows us to estimate that the effects of plastic flow of grain boundary islands on dissolution controlled pressure solution rates only become important at depths greater than ~9-10km (assuming a geothermal gradient of 30°Ckm^{-1}, hydrostatic fluid pressures and lithostatic rock pressures). Another interesting point, which we hope to address in a future paper, is that it is possible to derive a criterion for grain boundary healing that includes dislocation stored energy, and hence plastic deformation by including the second term on the far right side of equation (4.18) (i.e., the excess dislocation stored energy term) in equation (3.31).

4.4 Summary and conclusions

Models for dissolution controlled pressure solution, neglecting the influence of grain boundary structure and dissipation by plastic deformation, generally overestimate experimental compaction rates by more than half an order of magnitude. Assuming a very simple steady-state island-channel structure, we have derived a simple, preliminary model for the influence of work hardening plastic deformation and dislocation creep of grain boundary islands on the kinetics of dissolution controlled pressure solution. We applied our model to the compaction

of granular quartz, assuming microplasticity at grain boundary islands due to hydrolytically weakened flow. Our calculations show that plastic flow of grain boundary islands could slow down dissolution controlled pressure solution rates by several orders of magnitude, and helps explain the discrepancies observed between experimental and theoretical pressure solution rates. However, a better understanding of the properties of quartz grain boundaries is required to thoroughly test our model. Our model further indicates that the kinetic effect of plastic flow of grain boundary islands on pressure solution in granular quartz rocks only becomes significant at depths greater than ~9-10km. To better apply our model to pressure solution in quartz in nature and experiment, a more thorough investigation of the structural properties of pressure dissolving quartz grain boundaries is required. Furthermore, (experimental) studies supporting or disproving the occurrence of grain boundary plasticity during pressure solution would also be of interest. Thanks to the general nature of our model, it can readily be applied to estimate the kinetics of dissolution controlled pressure solution in any other material in which strain-hardening plastic flow or dislocation creep are of significance.

5. Structure and properties of loaded silica contacts during pressure solution: Impedance spectroscopy measurements under hydrothermal conditions

This chapter has been submitted for publication in Physics and Chemistry of Minerals.

Abstract

In order to investigate directly the structure and properties of grain boundaries in silicate materials undergoing pressure solution, in situ measurements of these properties are required. We report electrical impedance spectroscopy measurements, performed, under hydrothermal conditions, on individual glass-glass and glass-quartz contacts undergoing pressure solution. Resulting estimates of the average grain boundary diffusivity product ($Z = D\delta_{av}C^*$) for silica transport and of the average grain boundary fluid film thickness (δ_{av}) fall in the ranges $6.3\pm1.4\times10^{-18}m^3s^{-1}$ and 380±140nm respectively. However, the average values for Z and δ_{av} obtained were likely influenced by cracking and irregular dissolution of the dissolving contact surfaces, rather than representing uniformly wetted grain boundary properties. Post-mortem SEM observations indicate that the contact surfaces established during pressure solution were internally rough on the (sub)micrometer scale. Taken together our data support the notion that during pressure solution of quartz, grain boundary diffusion is relatively rapid, and interface processes (dissolution and precipitation) are more likely to be rate-limiting than diffusion.

5.1 Introduction

It is well established that the structure and properties of fluid-filled grain boundaries play a key role in controlling the kinetics of compaction and deformation of wet crustal rock systems by processes such as intergranular pressure solution (e.g., Rutter, 1976, 1983; Lehner, 1990, 1995). Much useful experimental work has been done on polycrystalline samples of rock-salt (e.g., Spiers et al., 1990; Zubtsov et al., 2004), quartz (e.g., Schutjens, 1991; Dewers and Hajash, 1995; Niemeijer et al., 2002) and calcite (Zhang et al., 2002; Zhang and Spiers, 2005) in an attempt to quantify pressure solution kinetics at the sample scale, and theoretical studies have identified the grain boundary parameters that need to be determined to characterise the process (Lehner, 1990, 1995; Shimizu, 1995). Of particular importance amongst these grain boundary parameters, and highly controversial for many years, is the question of the effective thickness and diffusivity of wetted grain boundaries, expressed in terms of the grain boundary diffusivity product, defined $Z = D\delta_{av}C^*$, where D is the diffusion coefficient of the dissolved solid in the grain boundary fluid, δ_{av} is the average thickness of the grain boundary fluid film, and C^* is the concentration of solid dissolved in the grain boundary fluid phase in m^3m^{-3}. This product Z controls the rate of grain boundary diffusion controlled

pressure solution in materials with wetted grain boundaries, but is very poorly constrained (e.g., Rutter, 1976, 1983; Revil, 2001).

The magnitude of Z has, to some extent, been investigated by means of single contact (or bi-crystal) pressure solution rate measurements conducted on halite-glass contacts (Hickman and Evans, 1991, 1992, 1995; Schutjens and Spiers, 1999; De Meer et al., 2002), halite-clay-glass contacts (Hickman and Evans, 1995) and even quartz-quartz (c.f. Hickman and Beeler, 1997) or quartz-indenter (Gratier et al., 2006) contacts, with some success under conditions avoiding neck growth (e.g., see Schutjens and Spiers, 1999; Visser, 1999; Van Noort et al., 2008, Chapter 3). However, because of the associated technical challenges, direct in situ probing of the structure and diffusive properties of grain boundaries during pressure solution is rare, limiting the extent to which the process is understood at the fundamental level. Nonetheless, several such studies have been carried out on halite. For instance, De Meer et al. (2002) and Van Noort et al. (2006, Chapter 2) studied the diffusivity of annular halite-glass contacts by measuring the electrical resistivity of such contacts during pressure solution of the halite. These authors report values for the grain boundary diffusivity product $Z = D\delta_{av}C^*$ of 3×10^{-20}–2×10^{-18}m^{3}s^{-1}, at room temperature. They also found an inverse dependence of Z on normal stress and a clear effect on Z of the crystallographic orientation and associated roughness of the dissolving contact. The Z values obtained are about an order of magnitude higher than values derived from pressure solution rate measurements made in experiments on both polycrystalline halite and on single contacts (Spiers et al., 1990; Hickman and Evans, 1995; Schutjens and Spiers, 1999). In an attempt to independently determine δ_{av} and the product DC in Z, De Meer et al. (2005) performed Fourier Transform Infrared (FTIR) spectroscopy measurements on grain boundary fluid films developed during pressure solution of a halite crystal pressed against a fluorite crystal. Their findings indicate that the fluid films occupied continuously evolving, rough, non-equilibrium structures – i.e., an island-channel structure. Interestingly, a thicker (~85-185nm thick) fluid film formed on dissolving (111) planes than on (100) planes (~40nm). Furthermore, on the (111) plane, at fluid film thicknesses below 200nm, the water molecules showed increased polymerisation towards an ice-like structure, or "hard water" (Nakashima et al., 2001, 2004). Diffusion through this structured grain boundary fluid was found to be about an order of magnitude slower than in bulk water.

Though not addressing actively dissolving interfaces (i.e. interfaces undergoing active pressure solution), various studies have been conducted using the surface forces apparatus (Israelachvili, 1986; Horn et al., 1989; Vigil et al., 1994; Alcantar et al., 2003) to study the properties of thin aqueous films bound between solid surfaces at room temperature. Such studies have provided data on fluid film thicknesses, fluid viscosities, and hence diffusion coefficients - through the Stokes-Einstein relation (e.g., Israelachvili, 1986; Horn et al., 1989; Vigil et al., 1994). They have shown that thin aqueous films can be maintained in a stressed contact by surface forces such as repulsive electrostatic forces or hydration forces. In the case of silica, a gel-like surface layer of silanol and silicic acid groups may form, and a fluid film can be maintained by steric repulsion and bonding between these surface groups. Significantly, the viscosity of water trapped between silica surfaces in films only a few nanometers thick has been shown to be comparable to the bulk water viscosity (Horn et al., 1989). Recently,

Alcantar et al. (2003) used the surface forces apparatus to study interactions between mica surfaces in various electrolyte solutions. At contact normal stresses between 10 and 50MPa at 21°C, they found fluid film thicknesses ranging from 0 to 3nm. From in situ observations of changing fluid film thicknesses, contact areas and contact forces, induced by changing the electrolyte concentration, ion diffusion rates in thin films of 0.3-1.5nm thick were found to be reduced compared to bulk water diffusion, but only by a factor of 2 to 40 at most. This, and the similarly limited decrease in thin film diffusion rates reported recently for grain boundary diffusion in "pressure dissolving" halite (e.g., De Meer et al., 2002, 2005; Van Noort et al., 2006, Chapter 2), contrast strongly with the decrease of up to 5 orders of magnitude predicted in early theoretical studies (e.g., Rutter, 1976, 1983). Agreement is much better, however, with more recent models in which values for D, in fluid films a few nanometers thick, are estimated to be up to 1 or 2 orders of magnitude lower than in bulk water (e.g., Renard et al., 1997; Revil, 2001).

Despite the above surface forces studies, and in situ probing work on halite, no in situ data are presently available on grain boundary structure and properties in quartz, calcite or other minerals undergoing active pressure solution, e.g., under hydrothermal conditions. The work reported here was aimed at directly probing the in situ properties and diffusivity of wetted grain boundaries in pressure dissolving silica and/or quartz. To achieve this, a special cell was developed allowing the electrical impedance of a single, annular, pressure-dissolving contact between a silica tube and a quartz or silica anvil to be measured, at high temperatures and pressures. Silica glass rather than quartz tubes were used in this first attempt at such a study, as the kinetics of silica dissolution are faster at lower temperatures. Reliable measurements proved difficult to make. However, in the more successful experiments, measured impedances gave composite Z values dependent on the concentrations of various ions present, which in turn, assuming ionic diffusion rates equal to diffusion rates in bulk water, suggested average grain boundary fluid film thicknesses in the range 200-500nm. Since these values were likely influenced by contact imperfections such as dissolution pits and/or cracks, they probably overestimate active film thicknesses.

5.2 Theoretical background

5.2.1 Principle of the measurement method

In the experiments reported here, impedance spectroscopy was used to investigate the diffusive properties of annular "grain boundaries" formed at silica glass contacts during pressure solution under hydrothermal conditions. The principle behind these measurements is similar to that employed in the experiments of De Meer et al. (2002) and Van Noort et al. (2006, Chapter 2), who investigated the diffusive properties of annular halite-glass and halite-halite contacts undergoing pressure solution at room temperature, by probing the electrical conductivity of the brine-filled contact in combination with in situ microscopic observation of the evolving contact ring.

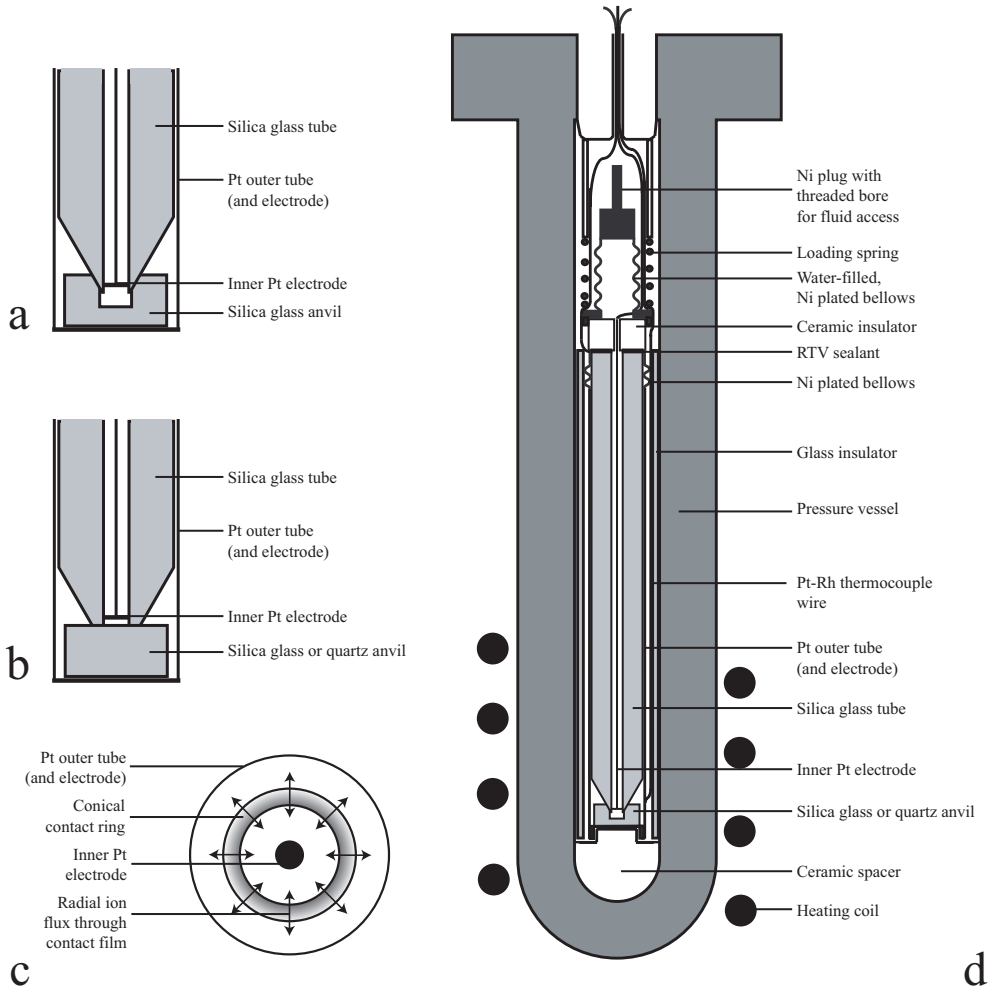

Figure 5.1 Schematic drawing of the experimental setup. (a) and (b) Close-ups of the contact between the silica glass tube and (a) a silica anvil with central hole or (b) a quartz/silica anvil without hole. (c) Plan view of the contact ring formed during pressure solution of the contact between the cone-tipped silica tube and the anvil. (d) Schematic illustration of the water-filled experimental cell and the cold-seal pressure vessel used to pressurise it.

The geometry of the annular, "pressure dissolving" contact created in our experimental apparatus is illustrated in Figures 5.1a-c. The electrical resistance (Ω) of a ring-shaped contact of this kind is given (De Meer et al., 2002):

$$\Omega = \frac{w}{2\pi r \delta_{av} \kappa} \tag{5.1}$$

where r is the contact radius (m), w is the contact width (m), and κ ($\Omega^{-1}m^{-1}$) is the conductivity of the fluid in the grain boundary. The conductivity of a solution of known composition, containing a variety of ionic species (i) can be approximated using $\kappa = \sum \kappa_i$, where κ_i, the contribution of ionic species i to the solution conductivity, is given by the Nernst-Einstein equation:

$$\kappa_i = \frac{D_i C_i z_i^2 F^2}{RT} \tag{5.2}$$

In this equation, D_i is the diffusion coefficient (m^2/s) of ionic species i, C_i its concentration ($molm^{-3}$), z_i its ionic charge number, F the Faraday constant ($Cmol^{-1}$), R the gas constant ($Jmol^{-1}K^{-1}$), and T absolute temperature (K). Combining equations (5.1) and (5.2) with the relation $\kappa = \sum \kappa_i$, we obtain the result:

$$\delta_{av} \sum D_i C_i z_i^2 = \frac{w}{2\pi r \Omega} \frac{RT}{F^2} \tag{5.3}$$

Then, using this result for the various ionic species present in our system (mainly monovalent impurity ions), and knowing r and w from post-experimental observations, a composite Z-like value ($Z^c = \delta_{av} \sum D_i C_i z_i^2$) can be obtained for these ions in the grain boundary fluid, by measuring the contact resistance Ω. This assumes the contact to be overwhelmingly the highest resistance in the cell circuit, which simple tests, performed at room temperature and atmospheric pressure, have shown to be the case. By assuming values for D_i equal to the ionic diffusivities in bulk water, and using concentrations obtained as explained below, an apparent value for δ_{av} can hence be estimated, which, if large enough (>~5nm) to obviate significant thin film effects on the diffusion coefficient (e.g., Alcantar et al., 2003), would justify the bulk diffusivity assumption. In such a case, we can then use δ_{av} to go on to estimate the grain boundary diffusivity product $Z = D\delta_{av} C^*$ for total dissolved silica transport.

5.2.2 Grain boundary fluid composition at experimental conditions

From the above, it is clear that to estimate the conductivity of the grain boundary fluid phase in our experimental set-up, and hence to evaluate the product $Z^c = \delta_{av} \sum D_i C_i z_i^2$ and estimate the average grain boundary thickness δ_{av}, it is necessary to know the ionic composition of the grain boundary fluid, i.e., the concentration C_i of the dissolved ionic species. Ions are

introduced into the fluid by the dissociation of water, the dissolution and dissociation of silica, and the dissolution of any contaminant ions present in the cell at startup. Contaminant ion concentrations were the dominant conducting species (providing >92% of κ), and were directly measured after our experiments. The concentrations of other (minor) ionic species

Reaction	Equilibrium constant	Reference
$H_2O \rightleftharpoons H^+ + OH^-$	$-\log(K_w) = 9.76$ at 300MPa and 300°C $-\log(K_w) = 9.61$ at 300MPa and 350°C	IAPWS, 1980
$SiO_2 + 2H_2O \rightleftharpoons H_4SiO_4$	$\log(K_{am.silica}) = -8.476 - \frac{485.24}{T} - 2.268 \times 10^{-6} T^2 + 3.068 \times \log(T)$	Gunnarsson and Arnorsson, 2000
$H_4SiO_4 \rightleftharpoons H_3SiO_4^- + H^+$	$-\log(K_1) = \frac{3375.5}{T} - 8.0355 + 0.021748 \times T$	Volosov et al, 1972
$H_3SiO_4^- \rightleftharpoons H_2SiO_4^{2-} + H^+$	$-\log(K_2) = \frac{4465.2}{T} - 8.354 + 0.021962 \times T$	Volosov et al, 1972

Table 5.1 Reactions and equilibrium constants used to calculate the ionic composition of fluids in our cell at experimental conditions.

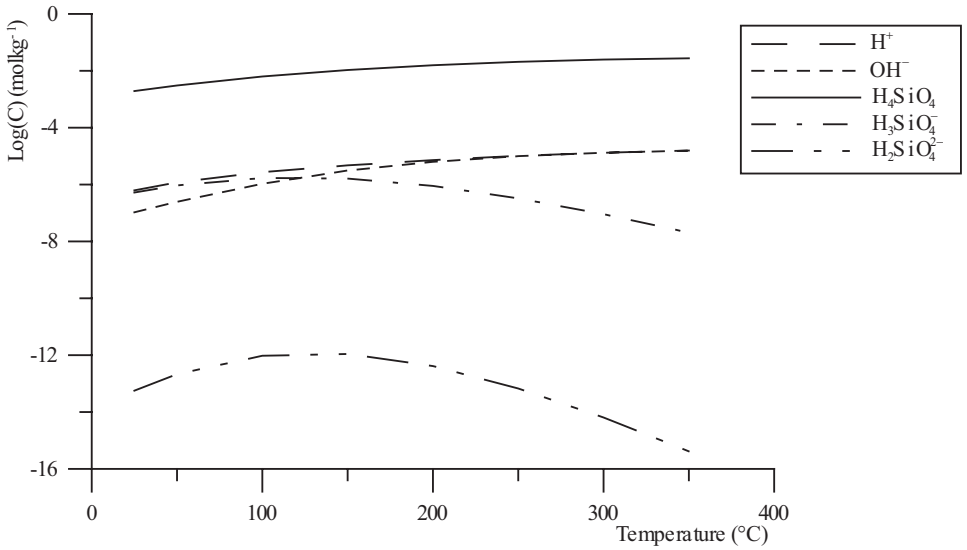

Figure 5.2 Predicted concentrations of (ionic) species present in pure silica-water solutions at temperatures between 25 and 300°C and pressures of 300MPa, based on solubilities given by Gunnarsson and Anórsson (2000), silica dissociation constants given by Volosov et al. (1972) and water dissociation constants given by the IAPWS (1980).

(H^+, OH^-, $H_3SiO_4^-$, $H_2SiO_4^{2-}$) and of undissociated, dissolved silica (H_4SiO_4 monomers, c.f. Volosov et al., 1972; Hiemstra and Van Riemsdijk, 1990; Rimstidt, 1997, Gunnarsson and Arnorsson, 2000) were calculated for our experimental conditions from the literature data shown in Table 5.1. In the present study, we combined the dissociation constants for the various silica species, with those of water (see Table 5.1), to lead to a model for the ionic composition of a saturated silica solution at given pressure and temperature conditions. Figure 5.2 shows the predicted ionic concentrations at 25-350°C and 300MPa. Coupling this model with equations (5.2) and (5.3) allowed us to determine the quantity Z^c and to estimate δ_{av}, as described above.

5.3 Experimental method

5.3.1 Impedance cell

The cell we constructed to determine the electrical impedance of single wetted grain boundaries in silicate materials during pressure solution at hydrothermal conditions is illustrated in Figure 5.1d. During operation, the water-filled cell is placed inside an externally heated, cold-seal pressure vessel, which is pressurised using argon. The electrical impedance of the (pressure dissolving) contact ring, formed between a silica glass tube with conical tip and silica glass or quartz anvil (Figures 5.1a-c), is measured using an Impedance/Gain-Phase Analyser.

In detail, the cell consists of an outer tube of platinum, sealed with a welded platinum cup at the lower end and supported at the bottom of the pressure vessel by a ceramic spacer. Spot-welded to the outside of this tube is a platinum-rhodium wire, forming an S-type thermocouple near the tip of the platinum tube. At the top end of the platinum tube, a small nickel bellows is soldered onto the tube, and soldered to this is a nickel-clad, alumina-ceramic insulating block, providing an insulated lead-through for the inner electrode wire. This is further soldered to a second nickel bellows, which compensates for expansion and contraction of fluids in the cell. The second bellows and whole assembly is closed, at the top, with a soldered-in nickel plug containing a threaded bore for priming the cell with fluid. This can be sealed with a small screw that is soldered into place after filling the cell. All soldering was done using tin-silver solder, fluxed with Fluox S.

Inside the cell, the quartz or silica glass anvil, in some experiments with a hole drilled into the centre, is located against the platinum end-cup. The silica glass tube with conical tip is pressed against this anvil, or into the hole, by means of a calibrated spring (placed outside the cell) compressed using spacers of various lengths to provide the desired load on the contact (see Figure 5.1d). Note that the spring load determined at room temperature and atmospheric pressure is not necessarily the same as that at experimental conditions, as small differences in (thermal) expansion between the silica glass tube and the (pressurised) vessel might result in a different (likely slightly lower) load. Our estimates suggest a corresponding uncertainty in load of ~±3N. Inside the silica tube, an inner platinum wire electrode, in some experiments

with a platinum disc at the tip to increase its surface area, is supported in a silica glass capillary. This inner electrode wire passes through the ceramic insulator and is then soldered to the connection between the nickel-ceramic insulator assembly and the upper bellows. The upper (cool) end of the main silica glass tube was glued onto the alumina-ceramic insulator, around the lead-through, using a silicone-based room temperature vulcanising (RTV) sealant, designed for use at high temperatures (up to 260°C) and in humid environments (Comma Instant Gasket). The platinum outer tube (below the ceramic insulator) functioned as the second electrode for impedance measurements. The whole cell was encased in an outer glass tube to insulate it from the wall of the pressure vessel. Outside the cell, the two electrodes and additional thermocouple wire from the cell were connected, via insulated sections, to cone-sealed, high-pressure lead-outs, to provide connections to the measurement apparatus.

The silica glass tubes used in the experiments were cut from stock silica glass tubing. They were ground and hand-polished on a lap, in a specially constructed holder to produce a conical tip with apical angle of 60°. Care was taken to ensure that the conical tip was centered on the hole in the tube, so that a contact ring of even width was formed. In early experiments, the silica glass anvils were cut from a silica glass rod. In later experiments they were cored out of a silica glass plate or optically clear, natural quartz crystal (with top surfaces parallel to the $\{10\bar{1}0\}$ form), as the glass rod was found to contain elongated pores parallel to the extrusion axis, which sometimes short-circuited our set-up. All anvils were polished by hand on a lap using P-4000 grade polishing paper. When an anvil with a central hole was used, the top surface of the anvil was ground and polished until the hole had a sharp edge. In one experiment (GC03, see also the list of experiments provided in Table 5.2), a skirt of platinum foil and a platinum filler piece enveloped the loaded cone-anvil contact at the tip of the silica glass tube, in an attempt to minimise convection and the amount of free fluid around the contact. In addition, the sides of the silica glass tube were painted with platinum paint, with subsequent heat treatment to drive off all volatiles, in an attempt to reduce dissolution and precipitation.

The electrical impedance of the cell was measured between the inner electrode (inside the silica glass tube and conical tip) and the outer electrode (the platinum tube). Impedance spectroscopy was performed using a Solarton SI1260 Impedance/Gain-Phase Analyser (see

Exp. No.	Dur. (d)	T (°C)	P (MPa)	Load (N)	Anvil
GC01	5	301	300	17±3	Silica glass from rod, with
GC02	9	353	300	22±3	Silica glass from plate, solid.
GC03	7	305	300	12±3	Silica glass from plate, solid.

Table 5.2 Experimental conditions for the three experiments reported here. Between experiments GC01 and GC02 the whole experimental set-up was inverted so that the hot tip of the cell was at the top rather than at the bottom, in an attempt to reduce the driving force for convection.

also Watanabe and Peach, 2002), which, in later experiments (including GC02 and GC03; see Table 5.2) was connected to a Solartron 1296 Dielectric Interface. Measurements were performed using a sinusoidal excitation voltage, with root mean square amplitude of 500mV. Impedance spectra were measured over a frequency range between 10^{-1}-10^{6}Hz, with 5-10 points per decade. Using just the Solartron SI1260, impedances could be measured in the range 100mΩ to 10MΩ with an accuracy of better than 1%. Using the dielectric interface gives improved accuracy over an increased range of impedances.

Trial experiments with a similar contact geometry as the hydrothermal temperature experiments were performed at room temperature and atmospheric pressure, and using a solution of known composition. Varying the contact spacing (i.e. the distance between the anvil and the tube) showed that the resistance of an unloaded contact was 10× as high as the resistance of the open fluid pathway between the electrodes.

5.3.2 Experimental procedure

The first step in setting up an experiment was the grinding and polishing of the silica glass parts. Next, the inner platinum-wire electrode was assembled, coated with platinum black by electrolysis of a solution containing lead acetate and chloroplatinic acid in water to make the surface rough, and slid into place in the silica glass capillary and tube. The tube was then glued with RTV against the ceramic insulator in the upper part of the cell. After the RTV had set, the glass or quartz anvil was placed into the bottom of the platinum cell tube, and the conically tipped glass tube was slid into place, along with the top part of the cell (from the lower bellows up), and the nickel lower bellows was soldered onto the platinum tube. The assembled cell was then filled through the small port (threaded bore) located in the nickel top plug. This was achieved by evacuating and then flooding the cell with demineralised and degassed water. After several rinses (to remove any residual flux or other contaminants), the port then was either closed with a tight fitting screw and soldered, or temporally sealed to check for changes in fluid resistivity over a few days until the resistance of the cell (after refilling) became stable, and then closed. Once closed, the cell was placed in the Tuttle-type cold seal vessel, and load was applied to the glass tube-anvil contact via the calibrated spring, which was loaded by closing the vessel. The cold-seal vessel, plus whole assembly, was then mounted into the external heater, connected to the argon gas pressure system, and held at room temperature and atmospheric pressure for one day to make sure no more changes in cell impedance occurred.

To bring the cell to the desired pressure and temperature conditions, the vessel pressure was first raised to 100MPa using argon gas. This pressurised the water in the cell to 100MPa via the action of the bellows. The tube furnace around the tip of the vessel was then switched on, and the rising temperature was monitored. At around 100°C, the argon and hence cell pressure was raised to 200MPa, and at ~200°C it was raised once more to almost 300MPa. The temperature was then further increased to the experimental temperature of 300 or 350°C, while keeping the pressure constant at 300MPa. Once the cell temperature was stable at the desired value, impedance analyses were performed at regular intervals of 20 or 30 minutes. Note that during the experiments, only the tips of the pressure vessel and the cell were heated

to the indicated temperature, whereas the other end of the vessel was water-cooled, so that a strong temperature gradient existed over the cell.

Experiments were allowed to run for up to 27 days. In terminating an experiment, the furnace was switched off and removed, and compressed air was used to cool the vessel. Once the cell temperature (at the cell tip) had decreased to 200°C, the argon pressure was decreased to 200MPa. The pressure was then further decreased to 100MPa at 100°C, and to atmospheric pressure at room temperature. After removing the cell from the vessel, the port in the nickel plug at the top of the cell was opened to bleed out the fluids, which were retained for chemical analysis by Inductively Coupled Plasma Optical Emission Spectrometry (ICP-OES). The cell was then carefully dismantled. In some cases, the silica glass tube was stuck inside the platinum tube due to local silica precipitation. The end-cup was then cut off the platinum tube to save the contact, and the remaining glass tube was removed more forcefully. Optical microscope analysis and Scanning Electron Microscopy (SEM) using Secondary Electron (SE) analysis were used to study the anvil and tube-tip after the experiments.

5.4 Results and discussion

A total of 13 experiments were performed while attempting to create a well-sealed silica-silica contact. In most of these experiments, an increase in contact resistance with time was not observed, but a decrease was observed instead. In these tests, the tubes and anvils in all cases showed signs of dissolution and precipitation. Convection, identified through precipitation

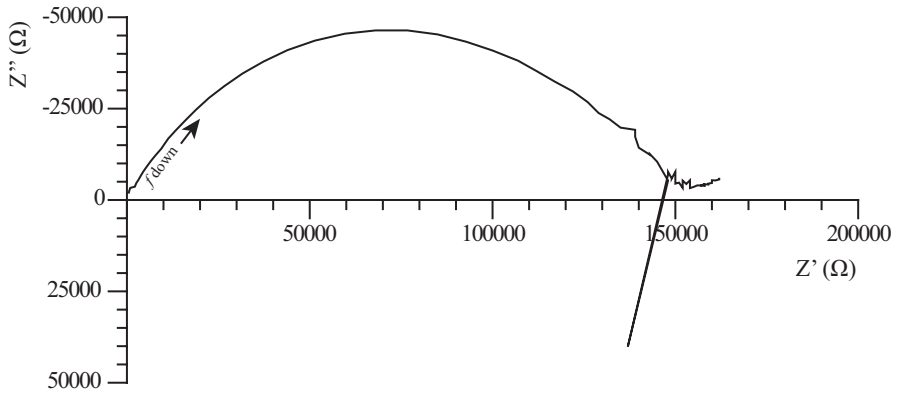

Figure 5.3 Example complex impedance plot, showing imaginary impedance (Z'') versus real impedance (Z'), typical of the curves observed in experiments GC01, GC02 and GC03. The complex plot shown here displays the last contact impedance spectrum measurement in experiment GC01 (frequency (f) range from 10^6 to 10^{-1} Hz). The sharp spike in the data is caused by mains supply interference at 50Hz.

patterns on the silica glass tube and the large total amounts of dissolved/transported material, also seemed to play a role in most experiments. Cracking was observed in the tube tip after some of the experiments, and might have resulted in decreased electrical impedance values by providing additional pathways for conduction. Another possible cause for the decrease in cell resistance observed during the early experiments might have been the release of ions held in the platinum black surface coating on the tube and inner electrode, overprinting any increase in resistance due to the formation of a closed contact. In five of our experiments, an increase in contact resistance was observed. In three of these five experiments it was possible to preserve the tip of the tube and enough cell fluids for useful study. The results of these three experiments will be presented and discussed here. They are named GC01, GC02 and GC03 for convenience. The experimental details of these three experiments are listed in Table 5.2.

In all three experiments discussed here, the complex impedance plots obtained from the Solartron measurements showed a single, slightly depressed arc (Figure 5.3), indicating that our cell behaved as a system consisting of a resistance and a capacitance acting in parallel (e.g. Barsoukov and Macdonald, 2005). At low frequencies (in the range 10^{0}-$10^{2.5}$Hz), our cell showed almost purely resistive behaviour, with phase shift angles of generally less than 3° (and always less than 5°). At higher frequencies, capacitance effects dominated the electrical behaviour of the cell. Electrical resistance values for the cell, and hence for the contact, were determined from each impedance plot by curve fitting (GC01) or by selecting the point with the least phase shift (GC02 and GC03). As phase shift angles were close to zero at these points, the electrical behaviour of the cell at was almost purely resistive. Compared to curve fitting, this then resulted in minimal errors (<~5%).

5.4.1 Experiment GC01

In experiment GC01, the conical tip of the silica glass tube was pressed into a 3mm central hole machined into the silica glass anvil. A spring load of ~17±3N was used, resulting in a final contact normal stress of about 15±2MPa. The experiment was run at a temperature of 301°C and fluid pressure of 300MPa. The experimental duration was approximately 5 days. Figure 5.4a shows the increase in cell resistance with time. The resistance remained constant at ~15kΩ for approximately 2 days, and then increased over the next 3 days to ~150kΩ, at which point the experiment was ended.

After the experiment, SEM study was performed on the silica glass anvil and tip. Both showed only limited signs of dissolution on their free surfaces. However, a contact ring was clearly visible on the edge of the hole in the glass anvil (see Figures 5.4b-c) and around (part of) the conical tip of the glass tube (see Figure 5.4d), which we believe to be a "pressure dissolved" contact ring. A composite SEM image of the contact ring formed on the anvil is shown in Figure 5.4b. The ring is not of uniform width. This is caused by the fact that the hole in the anvil was slightly off-centre. On the top surface of the anvil, several deep, cylindrical pits, with diameters up to ~300µm have formed due to dissolution, possibly concentrating on impurities or voids (see Figure 5.4b). The surface of the contact ring (Figure 5.4c) is covered in shallow, concave, reniform depressions, up to ~100µm long and ~50µm wide, and up to a ~5µm deep, with their long axes oriented parallel to the contact circumference.

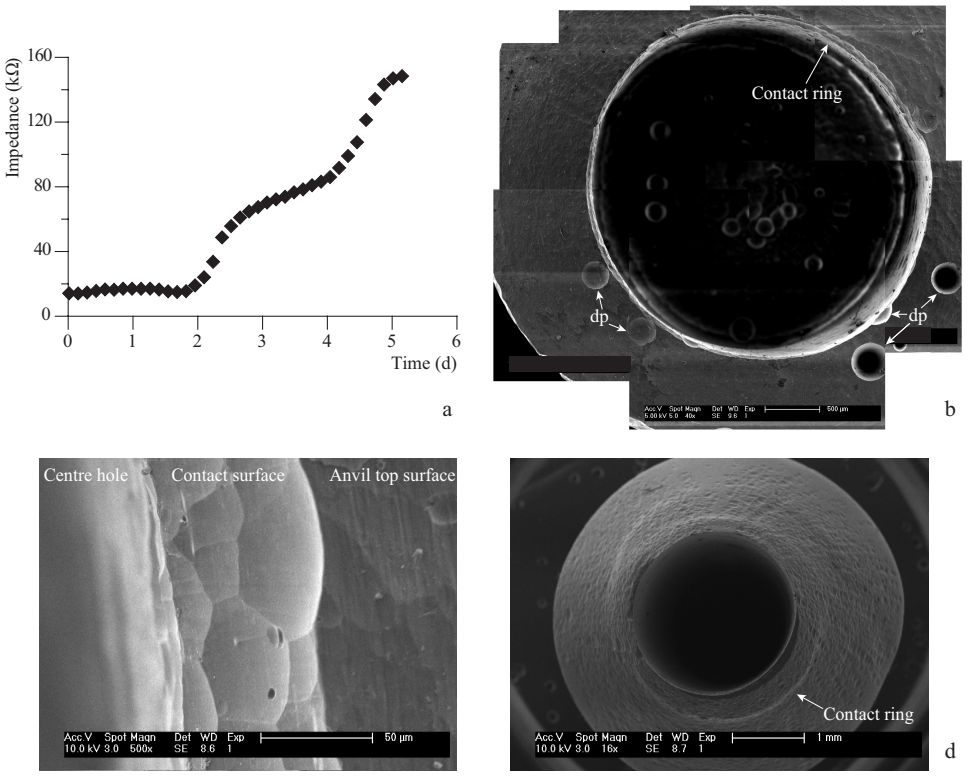

Figure 5.4 Results from experiment GC01. (a) Graph showing the evolution of the contact impedance with time. (b) A compound SEM SE image of the contact ring formed on the glass anvil. Dissolution pits on the top surface of the anvil are indicated "dp". (c) Close-up SEM SE image of the contact ring, showing shallow concave depressions. (d) SEM SE image of the tip of the glass tube used in the experiment. A contact ring can be observed on its surface, indicating the operation of pressure solution.

Unfortunately, one of the (much deeper) dissolution pits observed on the free anvil surface intersects the contact ring (Figure 5.4b).

On the free surfaces of the tube tip (Figure 5.4d), dissolution resulted in a pitted surface, covered with shallow depressions up to ~100×60µm in size. The small step in the conical surface corresponds to the pressure-solution contact with the anvil. On this step, the same texture is found as on the rest of the conical surface. The texture looks very similar to that on the contact ring on the glass anvil. As this texture is found on free surfaces as well as loaded contact surfaces, it is inferred that it mainly formed as a result of dissolution, and not cracking.

From the composite SEM image of the contact ring (Figure 5.4b), an estimate can be

Element	GC01 C (molkg^{-1})	GC02 C (molkg^{-1})	GC03 C (molkg^{-1})
Si	0.015	0.059	0.011
Ca	0.00012	0.000005	0.00071
Cl	0.0009	0.00028	0.00078
Fe	0.00005	0.000004	0.00048
Ni	0.00007	0.00003	0.00001
Pb	0.000005	0.000001	0.000003
Zn	0.00004	0.000008	0.00002
Na	-	0.00004	0.00029
K	-	0.00001	0.00011
Al	-	-	0.000007
B	-	-	0.0017
Mg	-	-	0.000008
Mn	-	-	0.000008
S	-	-	0.00004
Sn	-	0.00004	-

Table 5.3 Chemical compositions of cell fluids during the experiments.

made of the contact diameter (3.1mm, assuming an annular contact) and average contact width (~60μm) at the end of the experiment. Inserting these estimates and the final contact resistance value into equation (5.3) then shows that $\delta_{av} \sum D_i C_i z_i^2 = 2.12 \times 10^{-14}$mols^{-1}.

The results of the chemical analysis done on the cell fluids are shown in Table 5.3. The silica concentration is lower than the solubility at 300°C, but it is assumed that the fluids were silica saturated during the experiment, and that the remaining silica precipitated during cooling and/or in the time between the experiment and the analysis. Other ionic concentrations are well below room temperature solubilities and are assumed to represent experimental concentrations. The main ionic species present is Cl^-. Its concentration is considerably higher than the estimated concentrations of H^+, OH^- and charged silica species at 300°C and 300MPa. Assuming the presence of a similar concentration of monovalent cations for charge balance (see Table 5.3), representing all positively charged ions other than H^+ present in the fluid, we can then estimate both the fluid conductivity using equation (5.2), or the value of the sum $\sum D_i C_i z_i^2$. The diffusion coefficients of H^+, OH^-, Na^+ and Cl^- in bulk water at room temperature are given by Atkins and de Paula (2002) as 9.31, 5.03, 1.33 and 2.03×10^{-9}m^{2}s^{-1} respectively. From these values and assuming an Arrhenius temperature dependence and activation energy of ~15kJmol^{-1} (Nakashima, 1995), diffusion coefficients of Na^+ and Cl^- at experimental conditions (neglecting the effect of pressure) can be estimated as 2.4 and 3.7×10^{-8}m^{2}s^{-1}. The diffusion of silica is somewhat slower than the diffusion of alkali metal ions, though still of the same order of magnitude (Nakashima, 1995), and the diffusion coefficient of silica is taken here as equal to that of Na^+ as an upper estimate. The activation energy for the diffusion of H^+ and OH^- was calculated to be ~10kJmol^{-1} from the data of Morash et al. (1994), thus giving values for the diffusion coefficients of H^+ and OH^- at 300°C of 6.4 and 3.5×10^{-8}m^{2}s^{-1}. Using equation (5.2), the electrical conductivity of the fluid

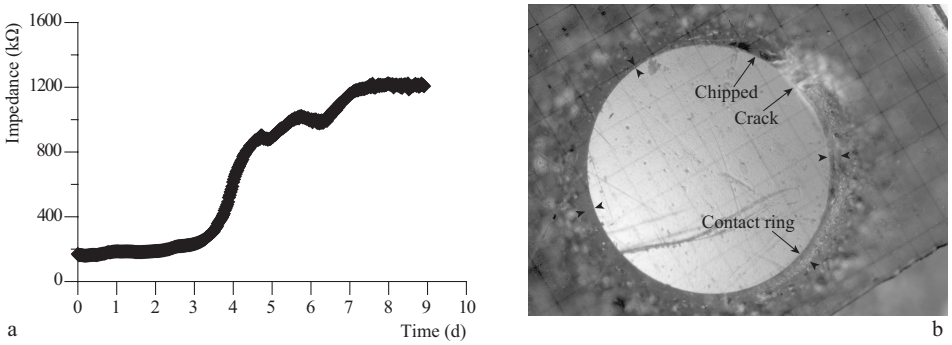

Figure 5.5 Results from experiment GC02. (a) Graph showing the evolution of the contact impedance with time. (b) Optical microscope reflected light image of the contact formed on the glass tip. A 400μm grid is shown over the tip for scale.

in the tip (assuming bulk diffusivities to be appropriate) is then estimated to be ~0.10$\Omega^{-1}m^{-1}$.

Using equations (5.1) and (5.2) and the conductivity estimated above, it emerges that the average apparent fluid film thickness, δ_{av}, was about ~400nm in experiment GC01. This is much greater than the values at which surface forces or water structuring effects are expected to reduce diffusion coefficients compared with bulk fluid values (up to ~200nm – Nakashima et al., 2001, 2004). Our estimate of $Z = D\delta_{av}C^*$ for the silica glass pressure solution contact then becomes ~$6.2\times10^{-18}m^3s^{-1}$, assuming that the diffusion coefficient of orthosilicic acid in the grain boundary fluid phase is the same as in bulk water, and assuming that the concentration of silica in the grain boundary fluid phase is equal to the bulk water solubility of amorphous silica.

5.4.2 Experiment GC02

In experiment GC02, the silica glass tube was pressed against a solid silica glass anvil cored from a silica glass plate. The experiment was conducted at a temperature of 353°C at the contact, and a fluid pressure of 300MPa. A spring load of ~22±3N was used to load the contact, which resulted in an initial contact normal stress of ~12±1.5MPa (calculated from the pre-experimental tip surface area determined from a micrograph). The experiment was stopped after 9 days. As can be seen in Figure 5.5a, the cell resistance remained constant at ~200kΩ for approximately 3 days, then increased over the next 4 days to ~1.2MΩ, then remaining constant for another 2 days, at which point the experiment was ended. The initial and final resistance values are about an order of magnitude higher than the initial and final resistance values measured in GC01, probably because more care was taken to clean the inside of the cell while setting up GC02.

An image of the tip of the tube after the experiment is shown in Figure 5.5b. Post experimental observation again showed the development of a contact ring, presumably by

"pressure dissolution". However, a crack had developed in the tube tip. Also, a small chip was missing from the contact ring on the tip next to the crack. It is unknown whether this damage occurred during the cooling and disassembly stages of the experiment or before heating or measurement. If the crack occurred during the experiment, an observable decrease in contact resistance would be expected, so it seems most likely that the crack occurred while the experiment was being set up, or during termination. Dissolution on the free surfaces of the silica glass anvil and the silica glass tube was more marked than in experiment GC01, as evidenced by the rugged texture developed on the outer surfaces of the tube and anvil, the conical shape of the initially cylindrical anvil, and an observed decrease rather than increase in contact width. This might have been the result of the higher experimental temperature driving more convection, which in turn, together with faster dissolution kinetics and higher silica solubility, caused increased silica transport rates away from the hot zone. Note that between experiments GC01 and GC02, the set-up was turned upside down, so that the hot spot was now at the top. This was done in order to reduce convection in the system, but had no discernable effect. The image of the tip of the tube (Figure 5.5b) shows a contact ring of uneven width (as indicated by the black arrowheads). This variation in width around the ring is caused by the hole in the silica glass tube not being exactly centered.

The composition of the cell fluid after the experiment was again analysed, and the results of the analysis are shown in Table 5.3. The very high Si concentration (higher than the silica saturation at 350°C) might be caused by colloidal silica suspended in the fluid, as the fluid looked somewhat milky. From the microscope image (Figure 5.5b), the final diameter (2.4mm) and average final width (~83μm) of the contact were determined as before. From this and equation (5.3), we calculated that $\delta_{av}\sum D_i C_i z_i^2 = 5.00 \times 10^{-15}$mols^{-1}. Furthermore, using the composition of the fluid, and assuming a solution in which all metal cations were monovalent (such as Na^+) with a concentration high enough to create charge balance, we can evaluate $\sum D_i C_i z_i^2$, to yield an estimate of the conductivity of the fluid around the tip (~0.04Ω^{-1}m^{-1}). From the sum $\sum D_i C_i z_i^2$, using equation (5.3), we can also estimate that the average fluid film thickness at the end of the experiment was ~230nm. This results in an estimated value for Z for amorphous silica transport of ~4.9×10^{-18}m^{3}s^{-1}.

5.4.3 Experiment GC03

In the final experiment, GC03, the silica glass tube was coated on the outside with a thin platinum layer (sintered platinum paint) to limit dissolution/precipitation. This tube was pressed against a solid crystalline quartz anvil cored from a natural crystal perpendicular to the {100} form. The test was performed at a tip temperature of 305°C and a fluid pressure of 300MPa, and using a spring load of ~12±3N, resulting in an initial contact stress of ~22±5MPa. As shown in Figure 5.6a, the cell resistance decreased from 20kΩ to below 10kΩ in the first 4 days. After that, the resistance steadily increased for 17 days to a maximum contact resistance of 80kΩ. In the last 6 days of the experiment, the contact resistance continuously decreased to a final value of 67kΩ, and the experiment was halted after ~27 days. Due to a large degree of dissolution, transport, precipitation and possibly microcracking, the tube tip was weakened, and only part of the tip could be safely recovered after the experiment. Dissolution (and

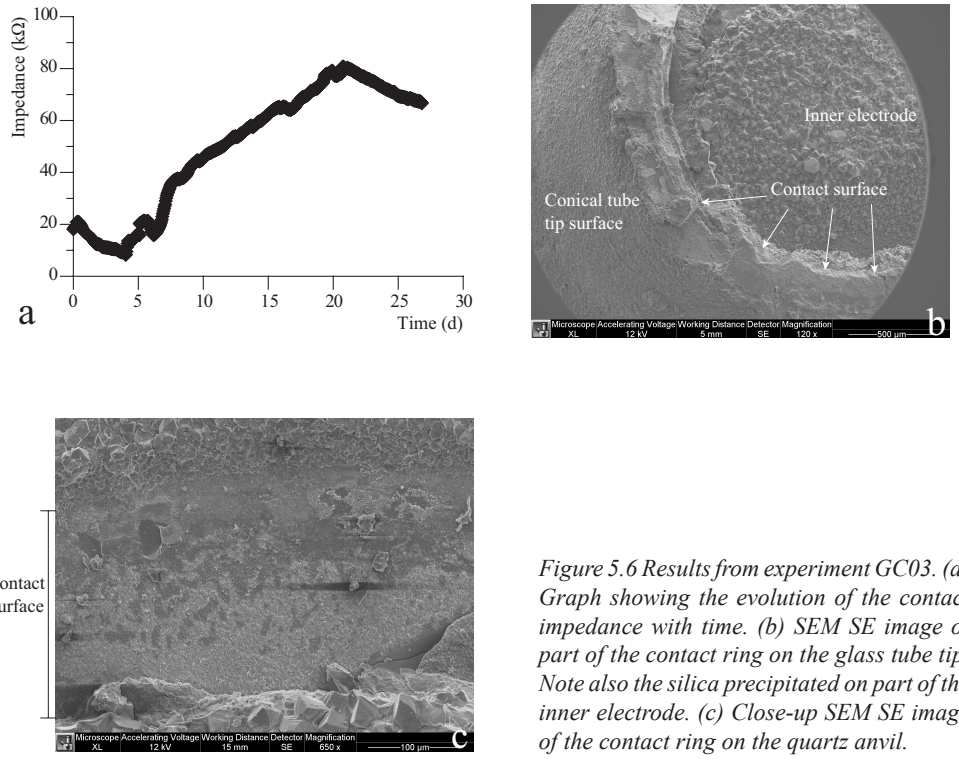

Figure 5.6 Results from experiment GC03. (a) Graph showing the evolution of the contact impedance with time. (b) SEM SE image of part of the contact ring on the glass tube tip. Note also the silica precipitated on part of the inner electrode. (c) Close-up SEM SE image of the contact ring on the quartz anvil.

cracking) lead to undercutting of the platinum painted surface, partly hollowing out the tip of the tube. SEM study of what remains of the contact surface on the tube tip (Figure 5.6b) shows some micrometer-scale roughness and some smoother patches. On the quartz anvil (Figure 5.6c), the contact surface is visible as a slight depression. Optical analysis indicated that some dissolution took place on this contact surface, but subsequent precipitation cannot be excluded. The contact surface on the quartz anvil also shows roughness with a lateral length scale of a few micrometers, and with sub-micrometer scale amplitude. The rough texture on both the tip and the anvil contact surfaces is much finer than, and does not show the reniform appearance of the roughness observed on the contact in experiment GC01. Unfortunately, it cannot be determined with certainty whether these textures represent dissolution or precipitation features.

An estimate of the contact width (~95μm) and diameter (~2.3mm) was made for GC03 from the SEM micrographs, assuming that a contact with even width existed during the experiment. These values, coupled with equation (5.3) then give: $\delta_{av} \sum D_i C_i z_i^2 = 1.01 \times 10^{-13}$mols^{-1}. In combination with the fluid composition analyses (Table 5.3), and again simplifying the fluid conductivity calculation by assuming that all charge from contaminant ions is carried by Na^+ and Cl^- (resulting in a value of $\kappa \approx 0.40\Omega^{-1}m^{-1}$), estimates of the average grain boundary

fluid film thickness and of the grain boundary diffusivity product (Z) for amorphous silica transport were made. The values obtained are 500nm and ~7.7×10^{-18}m^{3}s^{-1} respectively. However, since only part of the tube tip could be recovered intact after the experiment, we cannot be certain that a completely closed contact ring had formed. Moreover, as seen in Figure 5.6b, during this experiment a large amount of precipitation of silica occurred, also on part of the disc-surface of the inner electrode. This might have been a cause for the observed increase in cell resistance, rather than closure of the contact. Such an effect should not become a problem, however, until the surface area of the (inner) disc-electrode available for conduction becomes similar to the cross-sectional area of the fluid pathway between the tube and anvil, which is >3 orders of magnitude smaller. It is not expected that silica precipitation on the electrode influenced our measurements in this experiment.

5.4.4 Synthesis

Our three experiments have yielded estimates of the average fluid film thickness (δ_{av}) in silica-glass/silica-glass or silica-glass/quartz contacts undergoing pressure solution, between 230 and 500nm, and estimates for the silica diffusivity product ($Z = D\delta_{av}C^*$) for these contacts between 4.9×10^{-18}m^{3}s^{-1} and 7.7×10^{-18}m^{3}s^{-1}, assuming there are no thin film effects on diffusivity (i.e. assuming diffusivities in bulk water). Our δ_{av} estimates are similar to the contact surface roughness in some of our dissolved contact rings (Figure 5.4c). However, they are much higher than the values of ~0-5nm for fluid films between smooth silicate surfaces, determined at room temperature using the surface forces apparatus (e.g., Vigil et al., 1994; Alcantar et al., 2003). This is perhaps not surprising since little or no surface dissolution is expected during surface forces experiments performed at room temperature. Higher values for δ_{av} in the range 1-100nm have been estimated from post-experimental observations on granular quartz compacted by pressure solution (Cox and Paterson, 1991), from comparisons of experimental pressure solution rates with theoretical models (e.g., Gratier and Guiguet, 1986) and from a model of a Debye-Hückel double layer combined with osmotic pressure (Renard and Ortoleva, 1997). These values are still lower than the values reported here, though. As a result of our high mean fluid film thickness and assumed bulk diffusion coefficients, our estimated values for $D\delta_{av}$ (and therefore Z) are between a half and four orders of magnitude higher than generally derived in quartz pressure solution models that assume diffusion to be rate-limiting (Gratier and Guiguet, 1986; Shimizu, 1995; Revil, 2001; Revil et al., 2006).

The most likely cause for our high δ_{av} estimates is the rough contact structure with an additional possibly major effect of incomplete "closure" of the contacts due to larger scale cracking and pitting. In experiment GC01, for example, the dissolution pit intersecting the contact ring (Figure 5.4b) might have formed a fast pathway for conduction. The non-uniform contact width also made estimates of the average width (w) of the contact difficult, as most conduction would occur through the narrow part of the contact ring, though such effects are unlikely to yield order of magnitude errors. Likewise, the possibility of microcracking

and a non-uniform contact width may have influenced our results in experiments GC02 and GC03.

As already mentioned, our SEM studies indicate that our (pressure dissolving) silica contacts were rough. The scale of the rough texture varies between experiments GC01 and GC03 from reniform depressions of up to 100×50μm and up to ~5μm deep, to a rough network of islands on a micrometer-scale, with sub-micrometer scale amplitude. Note, though, that the structure observed on GC03 might have resulted from precipitation rather than dissolution. An island and channel texture on pressure dissolving quartz grain boundaries has previously been reported by Cox and Paterson (1991) and Den Brok (1998). Examining their results in more detail, Cox and Paterson (1991) report an irregular network of ridges and channels with a lateral length scale of 0.05-3μm developed on a quartz contact that underwent pressure solution at 927°C, 200MPa fluid pressure and 300MPa confining pressure. Den Brok (1998) shows a pressure solution contact from a quartzite with a similar island-channel grain boundary structure, but which is slightly coarser (0.5-5μm) and in which the channels are deeper and interpreted as cracks. Rough pressure dissolving contacts were thus reported in both of these studies, and were observed in our work (in experiment GC01, and possibly in experiment GC03). However, the scale and morphology of the island-channel networks reported by Cox and Paterson (1991) and Den Brok (1998) are different from the scale and morphology observed here, especially compared with the reniform structures seen in GC01. Furthermore, Cox and Paterson (1991) estimate the roughness to have an amplitude of up to 100nm, which is of the same order as, though still smaller than, the grain boundary fluid film thicknesses estimated here. This strengthens our belief that our data overestimate grain boundary film thicknesses. Though larger scale cracking might have occurred in some of our experiments (most notably GC02), the contact structures observed here did not appear to be related to cracking normal to the contact as described by Den Brok (1998).

In contrast to the above reports, Dewers and Hajash (1995) show SEM images of contacts on grains that underwent pressure solution at only 150°C. Their better-developed contacts are quite flat (especially compared to their free faces) but do show some pits on the scale of a few micrometers. Their observations, thus, are quite different from the rough contact structures reported here and by Cox and Paterson (1991) and Den Brok (1998).

Drawing the above information together, the rough structures observed on our dissolving contacts, and the associated cracking, support previous inferences and model calculations (Gratz, 1991; Schutjens, 1991; Dewers and Hajash, 1995; Renard et al., 1999; Niemeijer et al., 2002), that diffusion during pressure solution in quartz grain boundaries is likely to be very fast. Our results thus support the notion that, during quartz pressure solution, interface kinetics, i.e., either dissolution or precipitation, are probably the rate-limiting process.

5.4.5 Future experiments

As discussed above, our experiments did not result in accurate estimates of δ_{av} and Z, as several unsolved problems probably prevented a continuous, uniformly structured contact from forming. A challenging problem was convection driven silica dissolution and transport from the contact area. Precipitation patterns, and the amount of precipitation, demonstrated

for instance by the silica glass tube getting stuck inside the platinum outer tube in some experiments, show that convection driven transport is a factor in our experiments. It is also a possible factor affecting contact from formation. Post-experimental observations did show that the precipitation-free electrode surface area remained much larger than the estimated tube tip window through which conduction took place, indicating that precipitation on the electrodes did not cause the observed increases in impedance in our experiments, with possible exception of GC03. Several attempts to reduce convection, such as inverting the cell (from tip-down to tip-up), reducing the amount of fluid in the cell by including platinum spacers, blocking convection with a platinum skirt, and preventing dissolution with a coating of platinum on the silica tube met with only limited success. The convection problem thus needs a better solution for future experiments. Another factor was cracking. Though room temperature and atmospheric pressure tests showed no cracking at contact stresses higher than those used here, cracking still seemed to be an issue, especially in experiments GC02 and GC03. Finally, it was unfortunately not possible to accurately calculate the changes in contact load during heating and pressurisation. Using a spring with a lower spring constant would mean that differences in thermal expansion of the vessel and cell would influence the applied load less, and would result in a more constant and more reliably estimated load throughout the experiment.

5.5 Conclusions

In an attempt to investigate the structure and diffusive properties of grain boundaries in silicate materials during pressure solution, we performed experiments in which a silica glass tube was pressed against a silica glass or quartz single crystal anvil under hydrothermal conditions. Impedance spectroscopy was used to monitor the electrical impedance and hence diffusive properties of the contact. In many experiments, a continuous contact did not form, but we report the results of three experiments in which a reasonably continuous pressure solution contact was produced. Post-experimental optical microscopy and SEM study was used to determine the diameter, width and surface texture of the contact rings that formed in these three moderately successful experiments. After each experiment, the chemical composition of the fluids in the experimental cell was determined after the experiment by mass spectroscopy. Using this composition, plus calculations of the concentrations of H^+, OH^-, $H_3SiO_4^-$ and $H_2SiO_4^{2-}$ present in the fluids in our cell at experimental conditions, the conductivity of the fluids in the contact was estimated (through the Nernst-Einstein equation). From this the mean contact width (δ_{av}) and grain boundary diffusivity product (Z) for quartz pressure solution were estimated.

In the three experiments reported here, we found an average grain boundary fluid film thickness of ~230-500nm, which is one to two orders of magnitude higher than generally assumed for quartz grain boundaries during pressure solution. This is similar to the internal grain boundary roughness observed post-mortem in some of our tests. From this thickness, relatively high values for the silica grain boundary diffusivity product $Z = D\delta_{av}C^*$ were

estimated in the range 4.9-7.7$\times 10^{-18}$m^{3}s^{-1}. Though considerable roughness was observed within the dissolved contacts, our estimates for the grain boundary fluid film thickness, and the grain boundary diffusivity product, are likely too high due to non-uniform development of our contacts related to microcracking and/or irregular dissolution pitting.

Rough contact structures, though with a different morphology than the contact structures observed in some of the present experiments, were reported previously by both Cox and Paterson (1991) and Den Brok (1998) for grain boundaries in granular quartz aggregates compacted by pressure solution. Cox and Paterson estimated an amplitude on the order of up to 100nm for this roughness, which is smaller than our estimates of the average contact fluid film thickness. Taking into account the roughness observed in our contacts, and the tendency for microcracking and irregular dissolution, our results support earlier predictions and conclusions (e.g., Renard et al., 1999; Dewers and Hajash, 1995; Niemeijer et al., 2002) that during pressure solution diffusion through quartz grain boundaries is likely to be relatively fast, especially where cracks and other irregularities provide fast diffusion pathways short-circuiting the thin film. Our results accordingly point to quartz pressure solution being interface reaction controlled (dissolution or precipitation controlled), at least under hydrothermal conditions.

6. Compaction of granular quartz under hydrothermal conditions: Controlling mechanisms and grain boundary processes

Abstract

We report isostatic compaction experiments performed on granular quartz under hydrothermal conditions (3-129μm initial grain size, 300-600°C, 200MPa fluid pressure, 25-100MPa effective pressure). From microstructural evidence, it was determined that whereas microcracking controlled pre-compaction at room temperature, pressure solution was the main compaction mechanism during hydrothermal compaction, though a role of microcracking could not be excluded entirely. Our mechanical data, together with theoretical pressure solution rate models, further indicated that pressure solution was controlled by interface kinetics, with dissolution being the most likely rate-controlling mechanism. An empirical relation of the form $\dot{\varepsilon} = 10^{-7.8}\left(\phi/\phi_0\right)^{10.0}\sigma_e^{3.4}d^{-1}\exp\left(-105000/RT\right)$ *was fitted to our data to describe experimental compaction rates. Electron Backscatter Diffraction (EBSD) analysis performed on one sample showed limited evidence for plastic deformation (Dauphiné twinning and lattice bending) at grain contact points under high stress. Contact microstructures formed during compaction were studied using quartz single crystal discs, or a mica plate as reference surfaces. This showed that, in all contacts, contact microstructures were rough, with a micrometer scale roughness. Many contacts also showed internal microcracking, and it is inferred that microcracking is likely an important mechanism for creating and maintaining rough contacts during quartz pressure solution, at least under the present experimental conditions. Extrapolation of our empirical equation for compaction rates to natural conditions is consistent with previous observations that during burial and diagenesis of a sandstone, pressure solution starts to operate at depths of about ~1.5-2km, becoming the dominant compaction mechanism at depths greater than ~2.5-3km. The extrapolation gives good agreement with porosity-depth trends reported for natural, arenitic sandstones.*

6.1 Introduction

It is widely accepted throughout the geological literature that grain scale microfracture and intergranular pressure solution, with accommodation by intergranular sliding and rotation, are principle mechanisms of compaction and deformation of quartz-rich sediments and fault rocks under upper crustal conditions (Tada et al., 1987; Houseknecht, 1988; Wahab, 1998; Gratier et al., 1999; Karner et al., 2003, 2005). All evidence points to (subcritical) microcracking dominating at shallow depths and low temperatures, with pressure solution becoming increasingly important at depths beyond 2.5-3km (Ramm, 1992), and ultimately dominant at mid crustal conditions (e.g., Wintsch and Yi, 2002). A considerable amount of experimental work has been done on pressure solution in quartz, notably through compaction experiments on sands (De Boer et al., 1977; Gratier and Guiguet, 1986; Schutjens, 1991; Cox and Paterson, 1991; Dewers and Hajash, 1995; Niemeijer et al., 2002), and recent experiments

are providing new data on compaction controlled by subcritical crack growth (Chester et al., 2004; Chester et al., 2007). However, quantifying the rates of these processes through experiments, and obtaining a mechanism-based theoretical description or constitutive model to accurately constrain extrapolation of laboratory data to nature, remains problematic (see Niemeijer et al., 2002; Van Noort et al., 2008, Chapter 3, Chapter 4). A particular problem is that individual deformation mechanisms are difficult to isolate in experiments, i.e. to activate as the dominant process, and therefore difficult to quantify independently.

This chapter focuses on improving our understanding of the mechanism and rate of intergranular pressure solution in granular quartz via compaction experiments performed under high temperature (hydrothermal) conditions expected to favour the process. A large number of experimental studies on pressure solution in quartz have been reported over the last decades, providing some evidence for dissolution as the rate limiting processes for quartz pressure solution. However, consistency between studies is poor (Rutter, 1976, 1983; Schutjens, 1991; Revil, 2001; Niemeijer et al., 2002; Revil et al., 2006), theoretical rate models for pressure solution compaction do not yet accurately predict experimental pressure solution rates under conditions favouring the mechanism (e.g., Niemeijer et al., 2002), and the operation of other deformation mechanisms during the experiments performed to date cannot be excluded with certainty. Better quality compaction data, obtained over a wide range of temperatures, effective pressures and grain sizes, combined with an extensive study of the microstructures formed and deformation mechanisms operating (including the possible roles of microcracking and grain boundary plasticity), are thus required to constrain pressure solution models better. Additionally, the structure of wetted grain boundaries in quartz undergoing pressure solution, and the influence of this on grain boundary diffusion, grain boundary dissolution kinetics, and hence pressure solution rates, have seen only limited investigation, and urgently need elucidating.

In this chapter, we report new isostatic compaction creep experiments on granular quartz aggregates, performed at fluid pressures of 200MPa, temperatures between 300 and 600°C, effective pressures of 25-100MPa, and initial grain sizes between 3 and 129μm. We also report observations on the structure of grain boundaries developed during pressure solution, made by adding polished single crystal discs of quartz to the experiments, and by investigating the contacts formed on these discs using Scanning Electron Microscopy (SEM). Electron Backscatter Diffraction (EBSD) was used on one sample in order to search for evidence of any intragranular plastic deformation processes operative during our experiments, such as lattice bending, subgrain development, Dauphiné twinning (a rotation of 180°, or apparent rotation of 60°, around the (0001) axis – e.g. see Lloyd, 2000) or microcracking. Our results indicate that dissolution-controlled pressure solution was the main mechanism of compaction. We found that grain boundaries during compaction were rough on the micrometer scale, and that this roughness was often associated with microcracking. Our EBSD work also shows some evidence for plastic deformation processes operating at highly stressed contact points.

6.2 Background

6.2.1 Previous compaction experiments

Before describing our own experiments, it is useful to briefly review previous experimental and theoretical work on compaction of granular quartz by pressure solution and associated mechanisms. Previous compaction experiments on wet quartz sand at pore fluid pressures of 12.5 to 15.5MPa, and at applied effective stresses up to 15MPa needed to get measurable compaction rates, have shown that pressure solution becomes a principal deformation mechanism at temperatures above about 250-350°C (e.g., Schutjens, 1991). At temperatures in the range ~300-927°C, the development of grain indentation, truncation and overgrowth microstructures clearly indicates pressure solution as a principal compaction mechanism in aggregates with mean grain sizes between 3-125μm (Cox and Paterson, 1991; Schutjens, 1991; Niemeijer et al., 2002) or even coarser (150-250μm - cf. Den Brok and Spiers, 1991). Strain rates at these temperatures tend to be highly sensitive to effective stress, showing an equivalent power law n-value at fixed porosity of typically 3.5 (Niemeijer et al., 2002), similar to the (exponential) sensitivity predicted by pressure solution models predicted at high stress (e.g. Niemeijer et al., 2002). Apparent activation energies in the range 61-76kJmol^{-1} (hence similar to quartz dissolution kinetics - Schutjens, 1991; Niemeijer et al., 2002), and an inverse, nearly linear dependence of compaction rate on grain size (Niemeijer et al., 2002), point to dissolution as the rate-controlling process for pressure solution at these high temperatures. At the same time, however, a possible role of microcracking, or of diffusion or precipitation limited pressure solution, in controlling deformation behaviour is hard to eliminate.

At experimental temperatures below ~300°C, (time-dependent) microcracking becomes more important, though evidence for pressure solution is still seen (Schutjens, 1991; Elias and Hajash, 1992; Dewers and Hajash, 1995). Apparent activation energies for compaction at these lower temperatures are again found to lie in the range 61-76kJmol^{-1} (Schutjens, 1991; Dewers and Hajash, 1995), consistent with values for quartz dissolution or subcritical crack growth (c.f. Atkinson, 1984). Schutjens (1991) infers microcracking to be the dominant compaction mechanism in angular sands at these low temperatures and at effective stresses up to 20.7MPa. In contrast, Dewers and Hajash (1995) conclude, based on microstructural evidence and an apparent activation energy for quartz compaction of 73kJmol^{-1}, that dissolution-controlled pressure solution was the main compaction mechanism in their experiments, performed on well-rounded (St-Peter) sands at temperatures of 150°C and 200°C and effective pressures up to ~50MPa. They also report an inverse relation between strain rate and grain size raised to the power 2.3, and an exponential relation between strain rate and stress (though a linear correlation fits well at lower effective pressures), which is broadly consistent with a pressure solution mechanism. On the other hand, in more recent compaction experiments at these lower temperatures, He et al. (2007) have found that microgranulation at quartz grain boundaries, resulting in high energy ultrafines, might be an important factor for driving grain boundary dissolution.

Significantly, in compaction experiments performed on granular quartz at temperatures of 22 and 150°C, under dry (vented) conditions, and in the presence of water vapor, liquid water

and percolating water, strong microstructural evidence has recently been reported indicating that subcritical grain scale microcracking was the dominant compaction creep mechanism (Chester et al., 2004; Chester et al., 2007). Contrary to high stress compaction tests on loose sand (Brzesowsky, 1995), strain rates showed an inverse linear dependence on grain size at all water contents (Chester et al., 2007). Furthermore, compaction rates were observed to increase with increasing water content. It should be noted, however, that the total strain attained in the experiments by Chester et al. (2004, 2007) was low (typically <10%), so that porosities and grain contact stresses were high.

6.2.2 Theoretical background

Not only has intergranular pressure solution been studied in experiments, it has also been widely studied in theory, with the purpose of deriving a rate law for both compaction and deviatoric deformation by pressure solution. To provide a background to assess better if pressure solution was the main compaction mechanism in our experiments, we will now briefly consider the results of these theoretical studies. Note that, with the exception of a preliminary model presented by Brzesowsky (1995), no microphysical models for creep of granular aggregates by subcritical cracking have appeared in the open literature to date.

Pressure solution is a compaction and deformation mechanism the rate of which is determined, under closed system conditions, by the slowest of its three constituent processes, namely dissolution, diffusion and precipitation (Rutter, 1976, 1983; Raj, 1982; Lehner, 1990, 1995). Theoretically derived rate laws have been proposed by numerous authors assuming fluid-filled grain boundaries with either a thin film or an island-channel structure (e.g. Lehner, 1990, 1995; Mullis, 1993; Shimizu, 1995; Niemeijer et al., 2002). These models essentially give the same result, with differences only in the geometric terms dealing with porosity and grain packing. Rate laws for uniaxial or isostatic compaction of a granular aggregate by dissolution controlled, diffusion controlled or precipitation controlled pressure solution respectively, are given by Niemeijer et al. (2002) as:

$$\dot{\varepsilon}_s = A_s \frac{I^*}{d}\left[\exp\left(\frac{B(\phi)\sigma_e\Omega}{RT}\right) - 1\right] f_s(\phi) \approx A_s \frac{I^*}{d}\frac{B(\phi)\sigma_e\Omega}{RT} f_s(\phi) \tag{6.1}$$

$$\dot{\varepsilon}_d = A_d \frac{D\delta C}{\tau d^3}\left[\exp\left(\frac{B(\phi)\sigma_e\Omega}{RT}\right) - 1\right] f_d(\phi) \approx A_d \frac{D\delta C}{\tau d^3}\frac{B(\phi)\sigma_e\Omega}{RT} f_d(\phi) \tag{6.2}$$

$$\dot{\varepsilon}_p = A_p \frac{I_p}{d}\left[\exp\left(\frac{B(\phi)\sigma_e\Omega}{RT}\right) - 1\right] f_p(\phi) \approx A_p \frac{I_p}{d}\frac{B(\phi)\sigma_e\Omega}{RT} f_p(\phi) \tag{6.3}$$

Here, $\dot{\varepsilon}$ (s^{-1}) denotes volumetric strain rate, while σ_e (Pa) is the applied effective stress (effective isostatic pressure, or axial stress for 1-D compaction). The factor $B(\phi)$ is a stress multiplier, which accounts for the evolving stress concentration at grain contacts in a

compacting porous aggregate. The subscripts s, d and p indicate quantities associated with dissolution, diffusion, and precipitation controlled creep, A is a geometric constant, d (m) is the grain size, δ (m) the average thickness of the grain boundary fluid phase, C (m^3m^{-3}) the solubility of the solute in the grain boundary fluid, D (m^2s^{-1}) is its diffusivity, R ($Jmol^{-1}K^{-1}$) the gas constant, T (K) the absolute temperature, Ω (m^3mol^{-1}) the molar volume, and $f_x(\phi)$ is a dimensionless function of porosity (ϕ) which depends on the rate controlling process (x=s,d,p). The grain boundary tortuosity, τ is often assumed 1, or neglected altogether (e.g., Niemeijer et al., 2002). In the case of reaction controlled pressure solution, I^* (ms^{-1}) is the macroscopic rate constant for grain boundary dissolution (i.e. the velocity of dissolution at grain boundaries for a driving force of 1RT - see Van Noort et al., 2008, Chapter 3), while I_p (ms^{-1}) is the rate constant for precipitation on free pore walls. Note finally that the approximation $e^x - 1 \approx x$ made to obtain the right hand member of equations (6.1) to (6.3) is valid only at low applied effective stress (see Niemeijer et al., 2002).

In the above, I^* is often assumed equal to I, the dissolution rate coefficient for a free surface defined $I = k_+\Omega$, where k_+ ($mol{\cdot}m^{-2}s^{-1}$) is the standard geochemical dissolution rate coefficient as defined for example by Rimstidt and Barnes (1980). However, this assumption neglects the influence of grain boundary structure and effects such as plastic deformation of grain boundary islands on dissolution rates so that in general we expect $I^* < I$ (Lehner, 1990; Van Noort et al., 2008, Chapter 3, Chapter 4).

Finally, note that provided pressure solution is the dominant compaction mechanism, equations (6.1) to (6.3) predict a dependence of $\dot{\varepsilon}$ on d^{-1} (dissolution or precipitation control), or d^{-3} (diffusion control), an exponential dependence of $\dot{\varepsilon}$ on σ_e, and an apparent activation energy for creep that is determined by the activation energies for I^*, the product DC or I_p and by the term $\left[\exp\left(B(\phi)\sigma_e\Omega/RT\right) - 1\right]/\Omega$. As already indicated, only a preliminary model is available for compaction creep by subcritical crack growth (Brzesowsky, 1995). Interestingly, this predicts a positive dependence of creep rate on grain size.

6.3 Experimental method

In an attempt to investigate the kinetics and the rate controlling mechanism of compaction creep of granular quartz under conditions expected to favour pressure solution, we have performed 24 isostatic compaction experiments on granular samples with mean initial grain sizes of 3-129μm, at 200MPa pore fluid pressure, temperatures between 300 and 600°C, and effective isostatic pressures of 25-100MPa (see Table 6.1 for a list of experiments). All samples were pre-compacted by means of cold isostatic pressing, at an effective pressure of 150-155MPa and a pore fluid (water) pressure of 10MPa, to obtain a homogeneous starting microstructure. As a result of microcracking, the grain size at the end of the hot isostatic compaction stage was reduced to between 2 and 30μm. In order to investigate the structure of

Experiment No.	d_i (μm)	ϕ_0 (%)	D (d)	T (K)	P_f (MPa)	P_c (MPa)	d_f (μm)	ϕ_f (%)	e_v (%)	
QC01	20.0±9.0	35.98	5.8	763	200	300	11.1±8.2	13.33	26.14	
QC02	79.4±54.3	32.20	6.8	768	200	300	21.8±24.5	13.22	21.87	
QC03	20.0±9.0	36.19	12.9	763	200	300	10.8±7.6	12.17	27.35	
QC04	9.8±5.7	36.60	7.7	757	200	300	7.9±4.4	14.42	25.92	
QC05	129.1±38.9	29.56	10.7	762	200	300	25.3±33.7	12.50	19.49	
QC06	46.9±26.3	34.57	9.8	763	200	300	13.5±13.5	11.91	25.72	
QC07	3.1±2.1	41.09	10.8	762	200	300	2.9±1.8	16.31	29.61	
QC08	79.4±54.3	30.47	9.7	764	200	300	17.3±21.0	10.86	22.00	
QC203	20.0±9.0	35.58	6.8	779	200	252	11.8±8.0	19.56	19.91	b
QC204	20.0±9.0	38.16	6.6	683	200	251	9.2±6.7	24.05	18.58	
QC205	20.0±9.0	37.25	1.9	777	200	305	11.9±7.5	18.13	23.36	b
QC206	20.0±9.0	37.59	7.8	631	200	252	17.7±9.2*	25.42	16.31	
QC207	20.0±9.0	36.49	6.7	777	200	271	10.7±7.9	15.83	24.47	
QC209	20.0±9.0	33.39	0.75	874	200	252	9.7±7.0	20.17	17.33	b
QC211	20.0±9.0	34.00	1.1	875	200	253	10.2±6.8	21.08	16.37	b
QC212	20.0±9.0	35.41	6.7	776	200	222	11.0±7.5	24.12	14.88	
QC213	20.0±9.0	36.55	2.8	775	200	252	11.2±7.1	18.81	21.85	b
QC214	20.0±9.0	37.49	3.7	729	200	251	9.3±6.9	21.40	20.47	1
QC215	129.1±38.9	29.81	1.7	777	200	250*	21.3±36.3	18.26	13.84	2
QC216	20.0±9.0	-	-	RT	10	163	16.1±9.3*	-	-	
QC218	20.0±9.0	34.75	6.9	585	200	252	8.9±7.0	24.99*	13.00	3
QC219	20.0±9.0	35.55	1.0	775	200	234	10.7±7.9	26.41	12.42	4
QC221	129.1±38.9	27.78	1.0	777	200	250*	-	22.62	6.66	2
QC222	20.0±9.0	34.65	-	RT	10	163	8.4±7.4	34.65*	-	

Table 6.1 Experimental conditions, intial and final sample grain sizes, starting and final porosities, and final volumetric strains (e_v) of the 24 isostatic compaction experiments reported here. The experimental duration (D) is given for the hot compaction stage only. Experimental temperatures were corrected for non-linearity of the thermocouple output, and for temperature differences between the inside and the outside of the vessel wall. The final grain sizes of samples QC206 and QC216 were analysed using a Malvern particle sizer, rather than the linear intercept applied to SEM micrographs of other samples. Note that the volumetric strain only gives the strain due to hot compaction. A "b" in the last column indicates that compaction was halted due to blocking of the pore fluid tube by precipitated quartz. 1) Experiment QC214 was ended when the capsule started leaking. 2) In experiments QC215 and QC221 a gas pressure leak occurred. 3) In experiment QC218 a possible leak of gas into the sample occurred at the end of the test. 4) In experiment QC219 the effective pressure was not constant.

grain contacts undergoing pressure solution, polished single crystal discs were added to the quartz aggregates in some experiments, providing reference surfaces suitable for observing dissolution pitting. A mica plate was added to one experiment in order to study the contacts formed at quartz-mica interfaces.

6.3.1 Materials

The granular quartz used in our experiments was obtained in grain size fractions of <15, <30, <49, <75 and <125µm from the US Silica Corporation (MIN-U-SIL and SIL-CO-SIL products). According to the supplier's analyses, the samples consisted of at least 99.2% pure, ground silica. XRD analysis showed a representative sample (i.e., MIN-U-SIL 15), to consist of crystalline quartz only. Specific grain size fractions were prepared by gravitational settling in a column of water. During this process, aggregation was prevented by ultrasonic treatment between settling runs. The grain size fractions obtained were characterised using a Malvern Instruments Fraunhofer diffraction particle sizer. The grain sizes of the samples obtained were accordingly 3.1±2.1, 9.8±5.7, 20.0±9.0, 46.9±26.3, 79.4±54.3, 129.1±38.9µm.

Single crystal discs 6mm in diameter and ~2mm thick were prepared from an optically pure, natural crystal of quartz cored perpendicular to the $\{10\bar{1}0\}$ form, by sawing the core into slices. The discs produced were then polished by hand, using water as a lubricant, on a polishing lap with paper grades down to P-4000, this yielded a high quality, optically flat surface. The mica plate added to one experiment was a cleaved grade v-5 muscovite mica crystal obtained from SPI supplies. The pore fluid used in all experiments was demineralised and degassed water.

6.3.2 Experimental apparatus

The isostatic compaction apparatus used in our experiments is illustrated in Figure 6.1. It consists of a much-improved, servo-controlled version of the manually adjusted apparatus described by Niemeijer et al. (2002). The sample is enclosed in a silver/titanium capsule assembly (Figures 6.1a-b). This is connected to the pore fluid system, which includes a servo-controlled volumetric pump, a reservoir, a pressure transducer (resolution ~0.2MPa) and a vacuum pump. The sample assembly is located in an externally heated, cold seal, Tuttle-type pressure vessel, which is pressurised with argon to apply a predetermined confining pressure and hence effective isostatic pressure (Figure 6.1a).

Focusing on the sample assembly (Figure 6.1b), the silver capsule (inner diameter 10mm, wall thickness 0.2mm) and associated titanium components form the high temperature section of the fluid system, whereas 316L stainless steel is used in the cooler parts, and for parts that are not in direct contact with the main fluid pathway. This was done in order to minimise electrochemical corrosion effects and metallic ion contamination of the pore fluid. The silver capsule and titanium tubing strongly reduce such effects because of the similar electrochemical potentials of titanium and silver. In this way, major metallic ion contamination of the pore fluid can be excluded as an influence on observed compaction rates (c.f. the explanation for the inhibition of creep put forward by Niemeijer et al., 2002).

The system's servo-controlled volumetric pump ensures that the fluid pressure is kept constant during the experiments, and that measurements can be logged at regular intervals of 10s. The movement of the pump is monitored using a linear displacement transducer (a linear potentiometer), linked to the pump motion via a play-free gearing system. The minimum measurable increment of pore volume change is 0.3µl at room temperature, equivalent to 0.5µl at a sample temperature of 500°C and 200MPa pore fluid pressure. External argon

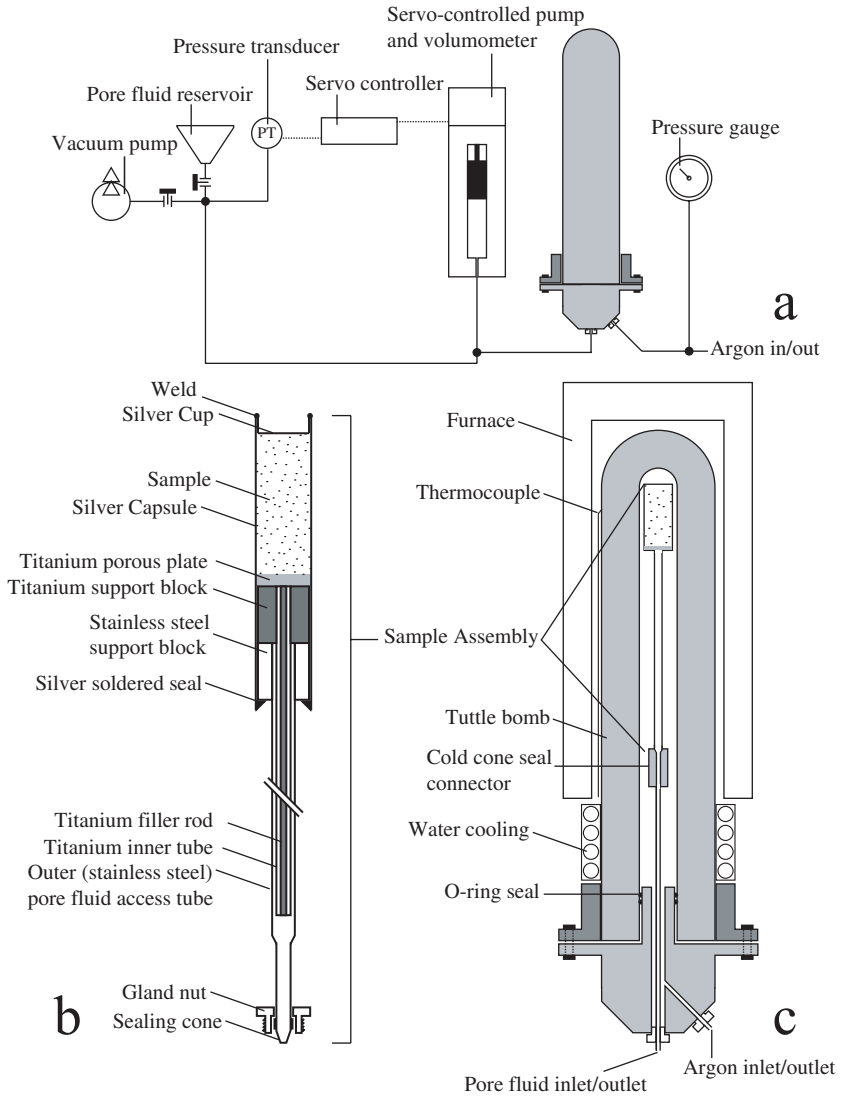

Figure 6.1 Schematic diagrams of the isostatic compaction apparatus used. (a) The general set-up. (b) The sample assembly. (c) The sample assembly placed in the Tuttle-type pressure vessel.

confining pressures are generated using a remote intensifier system, and are measured using a Bourdon type pressure gauge calibrated against the pressure transducer employed in the fluid system. Type K thermocouples located on the outside of the vessel (see Figure 6.1c), and on the pore fluid pipe near the servo-operated pump, are used to monitor the temperature of the vessel/sample and the pump (approximately at room temperature) respectively. Sample temperatures and control temperature settings were calibrated against vessel skin temperature using a thermocouple translated along the inside wall of the vessel at atmospheric pressure. Temperature gradients along the length of the sample were found to be of the order of a few degrees using the temperature control settings of the QC2 series of experiments, but may have been larger in other experiments (QC01-QC08).

6.3.3 Experimental procedure

In setting up individual experiments, the sample assembly was prepared by silver-soldering an open-ended silver tube onto the stainless steel support block and outer pore fluid access tube, as shown in Figure 6.1b. The titanium support block, inner tube, filler rod and porous plate (2μm pore size) were then inserted into the capsule-tube assembly through the open (top) end of the capsule. Next, a granular quartz sample of known mass (~2.5-3.0g) was loaded into the silver capsule and the capsule was sealed at the top by welding-in a silver cup (Figure 6.1b). The sample assembly was then placed into the pressure vessel (Figure 6.1c). Subsequently, the sample and pore fluid system were evacuated and flooded with water from the pore fluid reservoir (Figure 6.1a). Each sample was then cold-pressed in order to produce a reproducible starting porosity, and to minimise strain by grain rearrangement and cataclasis during hot compaction (c.f. Niemeijer et al., 2002). Cold-pressing was done at room temperature, 10MPa fluid pressure and 160-165MPa confining pressure (i.e., 150-155MPa effective pressure) for a duration of approximately one hour. Volume changes were recorded during this cold-pressing stage. After the loading stage, during which any open spaces in the capsule were closed and some time-independent compaction took place, pore pressures stabilised and only a small amount of time-dependent strain or creep occurred (<~0.2-1% total strain after the initial time-independent deformation).

After the cold-pressing stage, the pore fluid pressure was increased to ~160MPa, to yield a near-zero effective stress, and the external furnace was switched on. While the setup was heating up, the fluid pressure was kept within 10MPa of the confining pressure, by incrementally raising the fluid pressure or by decreasing the confining pressure, until both fluid and confining pressure reached 200MPa at the chosen test temperature. When the temperature had stabilised, the confining pressure was raised almost instantly to the desired test value (between 225 and 300MPa) and compaction creep initiated. As compaction progressed at the imposed effective pressure of 25-100MPa (i.e. well below the cold-pressing value of 150MPa), the fluid pressure was kept constant by the servo pump, and the system volume change was monitored. In most experiments, the external (argon) confining pressure decreased somewhat initially, presumably due to sample compaction, but changes over the duration of the entire experiment were generally less than a percent.

Experiments were stopped after 6-13 days, or when compaction was no longer measurable. In doing so, the confining pressure was first decreased from the test value to ~205MPa.

The pressure vessel was then quenched with compressed air, resulting in an average cooling rate, down to room temperature, of ~30°C per minute. During cooling, care was again taken to maintain the fluid pressure slightly (~5MPa) below the confining pressure. Finally, the cylindrical, indurated sample was removed from the capsule, and dried in an oven at 60°C for at least 48 hours. The final porosity of the sample was determined using Archimedes' method, i.e., by measuring the weight of the water-saturated sample (pores filled under vacuum) in water and in air, and the weight of the dried sample in air. The porosity of each sample was measured at least twice and, showed an absolute variability generally less than ±0.1%. Subsequently the dried sample was impregnated with resin and cut into thin sections along its long axis for optical microscopy and SEM study.

6.3.4 Data acquisition and processing

The volumeter displacement, vessel temperature, pump temperature (approximately at room temperature) and fluid pressure output signals were logged at 10 second intervals during the experiments, using a 16-bit AD-convertor and a personal computer. To keep data-files to a manageable size, only every 10^{th} data point was used in subsequent data processing (i.e., data points at 100s intervals).

As already explained, changes in sample pore volume were measured via the change in volumetric pump position required for maintaining constant fluid pressure. The raw volume changes measured by the servo pump were first corrected for variations in room temperature (maximum 3°C diurnally, with up to 5°C variations over the duration of individual experiments), using an empirically calibrated volume change versus temperature change relation. The resulting volumetric data was then smoothed using a moving averaging procedure over 35 data points (i.e., 3500 seconds). Finally, the data were converted to pore volume changes occurring in the sample at test temperature. This was done by multiplying the smoothed volumetric data by the ratio of the density of water at pump temperature to its density at sample temperature, assuming that the mass of fluid in the pipe system was constant. The density of water under the various experimental conditions employed was calculated using the equation of state of Wagner and Pruß (2002).

From the resulting data, and the sample pore volume determined after the experiment, the pore volume evolution of each sample was calculated. Assuming the porosity to be fully connected, the porosity ϕ, the porosity ratio ϕ/ϕ_0 (instantaneous porosity over starting porosity) and cumulative volumetric strain (e_v) were also calculated as a function of time. Finally, the volumetric strain rate at each instant in time during the experiment was calculated, from the time interval associated with a moving sample volume change interval of 0.01ml. As the random variability in the measured sample volume change was typically less than ±0.001ml, this implies an uncertainty in our strain rate calculations of less than ±10%.

6.3.5 Microstructural methods

Microstructural analysis was performed on polished thin sections of the deformed samples using both optical microscopy, and backscatter electron microscopy (BSE) performed using

a Philips XL30SFEG scanning electron microscope (SEM). Grain sizes and porosities were determined from representative SEM images at 650x magnification using the linear intercept method. Mean intercept grain sizes were corrected to equivalent spherical grain diameters (see Table 6.1) using a stereological correction factor of 1.62 (Underwood, 1970; Russ, 1986). Sample porosities were also determined using the linear intercept method. The grain sizes of unconsolidated samples QC206 (compacted wet at 350°C) and QC216 (cold-compacted only) were measured with the Malvern particle sizer. The loose grains of these samples were studied in the SEM. Quartz and mica reference discs added to samples QC05, QC215 and QC221 were also studied in the SEM, as were the parts of the samples that contacted them.

To investigate the possibility of any dislocation substructure development or other evidence of crystal plastic deformation, Electron Backscatter Diffraction (EBSD) analysis was performed on a section of sample QC02 (79μm average initial grain size), compacted at ~500°C and 100MPa effective pressure. We used Electron Backscatter Patterns (EBSPs) to discern the relative orientations of grains and Forescattered Electron (FSE) images to identify orientation contrasts. To enable EBSD study, this section was polished with Syton™ colloidal silica (30nm grain size). The polished sample was then gold-coated, and subsequently wiped using a soft polishing cloth, leaving a conductive gold coating in depressions formed at resin-filled pores. The sample was then coated with a thin layer of carbon to minimise overall charging effects.

EBSD data were collected and analysed using a Nordlys CCD camera integrated with the Philips XL30 SFEG SEM and HKL Channel 5 software. The microscope was operated at 20kV voltage and 2nA current using a working distance of 20mm and sample tilt of 70° with respect to the electron beam. EBSD maps were constructed using a step size of 1μm, mapping a total area of $1.7\times10^5\mu m^2$, containing 100-150 original grains. A minimum of 6 diffraction bands and 80 {hkl} reflectors were used to analyse the patterns. Non-indexed patterns were automatically saved and re-analysed. Some 50-70% of the patterns were successfully indexed in the first pass; re-analysis of non-indexed patterns gave a final, total indexing of between 60-80%. Our EBSD maps were further processed using the HKL software to replace non-indexed pixels that had at least 6 indexed neighbours with an orientation of a neighbouring pixel. Isolated pixels that showed a 60° misorientation about the [0001] direction with respect to all neighbouring pixels, were considered to be misindexed and were replaced with a neighbour pixel orientation. As Dauphiné twins in quartz show the same apparent twin-host misorientation relationship as this common quartz misindexing problem, FSE images were used to distinguish real twins from misindexing artefacts. Other artefacts, related to surface charging and sample topography adjacent to pores and grain contacts, also affected EBSD analysis to some extent. Charging deflects the beam, changing the analysed grain orientations. Topographic effects also lead to small errors in orientation determination and reduce indexing success rates. To avoid such artefacts, images of sample QC02 were selected for detailed study, and about 30 grain contacts were examined for small changes in lattice orientation. The resolution of the orientations acquired by EBSD from this sample is estimated to be better than 2°.

6.4 Results

Table 6.1 gives the experimental conditions and final volumetric strains of the 24 isostatic compaction experiments reported here. Note that, in our samples, the absolute difference between sample porosities determined by Archimedes method and by linear intercept is generally less than ~3% in value.

6.4.1 Cold compaction and initial porosity data

The initial cold compaction stage of our experiments was characterised by instantaneous compaction followed by very slow creep (0.2-1% in total), and resulted in a net decrease in porosity from an estimated value before cold compaction of ~38-48% to around 28-42% (Table 6.1). This second value is taken as the initial porosity (ϕ_0) for hot compaction and was back-calculated after completion of each experiment, from the final sample porosity and the volume change measured during hot compaction. Thermal expansion and elastic compaction of the sample at test temperature and pressure, compared to room temperature and atmospheric pressure, can be shown to be minor (c.f. Fei, 1995; Bass, 1995) and were neglected. Variations in starting porosity (ϕ_0) are likely the result of different initial sample grain sizes (higher initial porosities were obtained in samples with lower grain sizes), but also of different heating rates and/or of small variations in effective pressure during heating. Because of these differences in initial porosity, comparisons between creep rates obtained in different experiments will be made at fixed values of the porosity ratio ϕ/ϕ_0, rather than at set porosities, as this is expected to reduce the effect of varying starting porosity on compaction rates under otherwise identical conditions (see also Niemeijer et al., 2002).

6.4.2 Hot compaction creep data

Rapid compaction creep (at rates of ~10^{-4}-10^{-5}s^{-1}) was observed at the start of the hot compaction stage of the tests, decelerating continuously thereafter (see Figure 6.2). In many of the experiments performed at 500°C or more (see Table 6.1), compaction rates first decreased continuously, but then, after a few hours to a few days, suddenly fell below measurement resolution. When this happened, the experiments were generally terminated. Post-experimental observations showed that in these cases, the pore fluid tube was always blocked near the sample by precipitated quartz, preventing further compaction.

Our results for the dependence of creep rate ($\dot{\varepsilon}$) on grain size (d), effective stress (σ_e) and temperature (T), at fixed ϕ/ϕ_0 values, are reported in Figure 6.3. Our data on grain size dependence (experiments QC01-QC08) are given in Figure 6.3a, which is a plot of $\log(\dot{\varepsilon})$ versus $\log(d)$ at fixed values of normalised porosity ϕ/ϕ_0. Assuming a power law dependence of strain rate on grain size, linear regression fits to the data indicate a grain size exponent between 0.92 and 1.05 with an average value of 0.97.

Our data on stress dependence (experiments QC203, QC205, QC207, QC212, QC213 and QC219) show that compaction strain rates increase with increasing effective stress at set

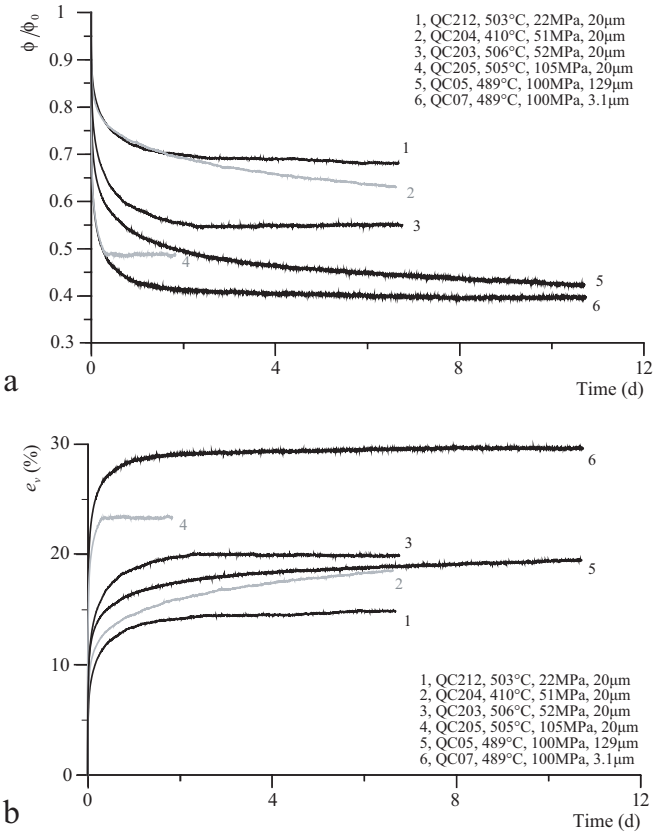

Figure 6.2 Example curves of (a) the porosity ratio (ϕ/ϕ_0) and (b) the volumetric strain (e_v) versus time (in days) for the experiments indicated. Note the sudden cessation of creep in experiments QC203 and QC205 caused by quartz precipitation blocking the pore fluid pipe. Also note the effect of grain size (curves 5 and 6), effective stress (curves 1, 2 and 3) and temperature (curves 2 and 3).

values of the porosity ratio ϕ/ϕ_0, though scatter is considerable (Figure 6.3b). Assuming a power law dependence of strain rate on stress in this log-log representation, linear regression fits give a stress sensitivity of strain rate at fixed ϕ/ϕ_0 of between 3.0 and 4.2, with an average value of 3.4. Note that experiment QC212 (performed at 25MPa effective stress) is not included in Figure 6.3b at $\phi/\phi_0 = 0.7$, as strain rates at this porosity level were rapidly dropping due to blocking of the pore fluid tube.

Our data on the influence of temperature on compaction rate at fixed ϕ/ϕ_0 (experiments QC203, QC204, QC206, QC209, QC211, QC213, QC214 and QC218) are shown in the Arrhenius plot of Figure 6.3c. These data show a strong increase in compaction rate with temperature. Assuming an Arrhenius dependence, linear regression fits (Figure 6.3c) give an apparent activation energy for compaction creep between 91 and 121kJmol^{-1}, with an average value of 105kJmol^{-1}.

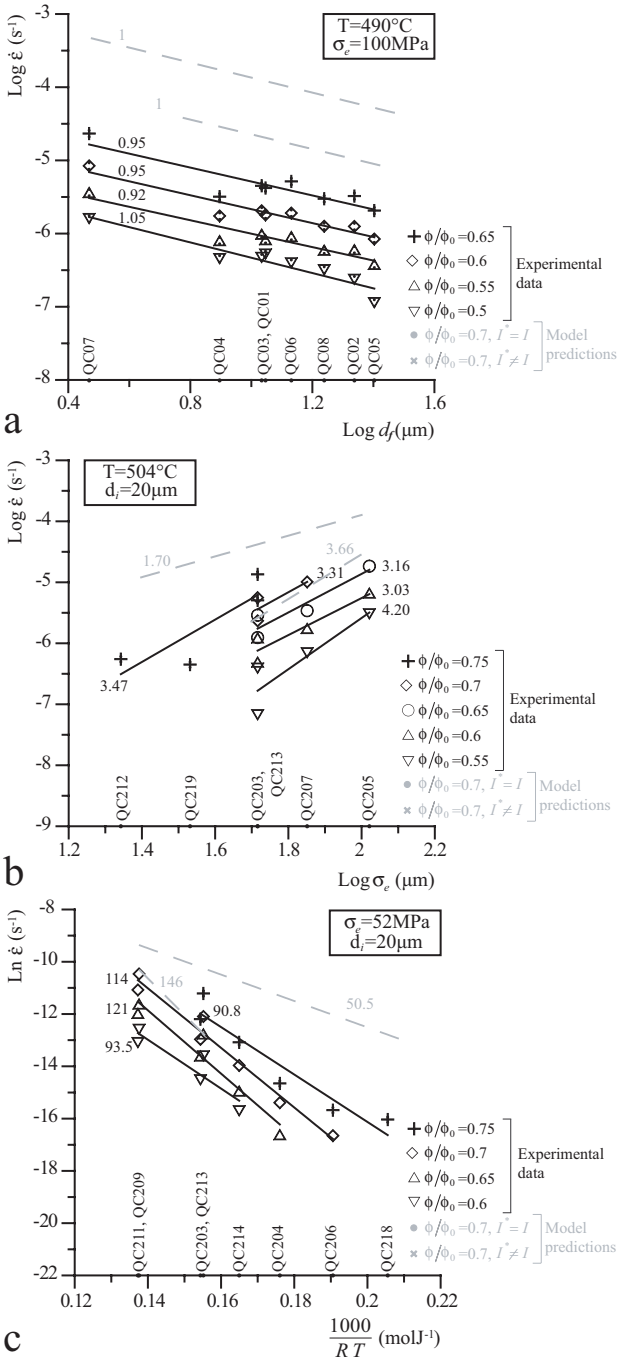

Figure 6.3 Plots demonstrating the dependence of strain rate on grain size, on effective stress and on temperature at fixed normalised porosities (ϕ/ϕ_0), as determined in our experiments (black symbols and lines). Modelling results (grey) are shown for comparison. (a) The logarithm of strain rate versus the logarithm of final grain size. (b) The logarithm of strain rate versus the logarithm of effective stress. (c) The natural logarithm of strain rate versus 1000/RT. The best fit lines show the corresponding grain size sensitivity, stress sensitivity and apparent activation energy for compaction. The symbol size is larger than the uncertainty in the experimental strain rates (±10%). Note that during experiment QC219, a leak in the pressure vessel caused the effective pressure to decrease significantly (from 39 to 32MPa) - this is accounted for in plot (b).

6.4.3 Microstructural observations

SEM study of our starting material after gravitational settling (the 20μm mean grain size fraction) demonstrated our uncompacted grain fractions to consist of highly angular grains with mainly (conchoidally) fractured surfaces, though a few percent of the surfaces showed heavy pitting.

Grain size analysis of the sample that underwent cold compaction only (QC216), using the Malvern particle sizer, showed that the mean grain size was reduced from the initial value of 20μm to 17μm. However, linear intercept analysis performed on an SEM image of a similar cold-compacted-only sample (QC222) indicated a reduction from an initial mean of 20μm to 8.4μm, with a large number of very fine grains (smaller than a few micrometers in diameter). Optical analysis of this same sample showed undulatory extinction within the grains, though no more than in sieved only material.

Hot isostatic compaction resulted in porous, indurated samples showing a homogeneous spatial distribution of porosity and grain sizes in SEM and optical examination. Grain shape varies with test temperature from angular up to 400°C to rounded at temperatures of 450°C or more. Mean final grain sizes depend systematically on initial mean grain sizes (see Table 6.1), but are reduced significantly due to the presence of large numbers of micrometer size grains that broaden the grain size distribution, especially in the (initially) coarser samples. No clear trend of final grain size with experimental temperature is found. Significantly, final grain size of the samples tested at 500°C (see Table 6.1) also shows no correlation with effective stress in the range 25-100MPa, suggesting that grain size reduction occurred through microcracking mainly in the cold compaction stage.

Transmission optical study of the hot-compacted samples showed undulatory extinction similar to that seen in the starting material. In the optical microscope and SEM, all samples showed the formation of grain-to-grain indentations (Figures 6.4a-d), grain truncations (Figure 6.4d), and sutured grain boundaries (Figures 6.4c, e), providing evidence that intergranular dissolution occurred. Intragranular and transgranular cracks (Figures 6.4e-f) are found in all samples, but especially in those with larger initial grain sizes. In finer grained samples (<20μm mean initial grain size), mainly isolated trans-/intragranular fractures are observed, often emanating at high angles from grain boundaries and sometimes in association with contact granulation or crushing features (such as those shown in Figure 6.4e). By contrast, coarser grained samples show complex trans- and intragranular fracture systems, usually emanating from or connecting contact points, and often arranged in parallel or radial arrays (e.g., Figure 6.4g). Such fracture systems completely fragment some grains in these samples, whereas other grains remained unaffected. The grain size dependence of microcracking is shown in Figure 6.5, which shows SEM micrographs for 4 samples with different grain size all compacted at ~490°C and 100MPa effective pressure. As seen from Table 6.1, during cold compaction of these coarse samples, a high degree of microcracking caused a significant decrease in mean grain size. Qualitatively speaking, open cracks are more prevalent in the low temperature experiment QC218 than in the higher temperature experiments, but no relationship was evident between crack density and effective pressure in samples of the same grain size. In some of our samples (especially the 600°C experiments QC209 and QC211), evidence for grain boundary healing was found (Figure 6.4h).

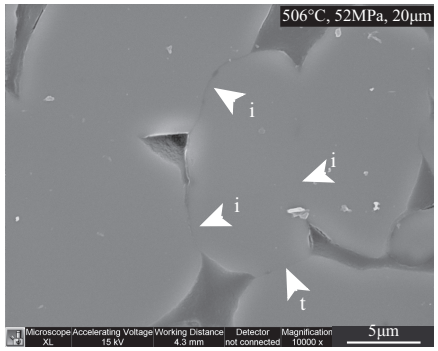
506°C, 52MPa, 20µm
i
i
i
t
Microscope Accelerating Voltage Working Distance Detector Magnification
XL 15 kV 4.3 mm not connected 10000 x
5µm

a

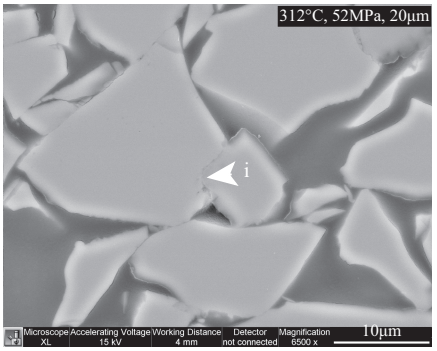
312°C, 52MPa, 20µm
i
Microscope Accelerating Voltage Working Distance Detector Magnification
XL 15 kV 4 mm not connected 6500 x
10µm

b

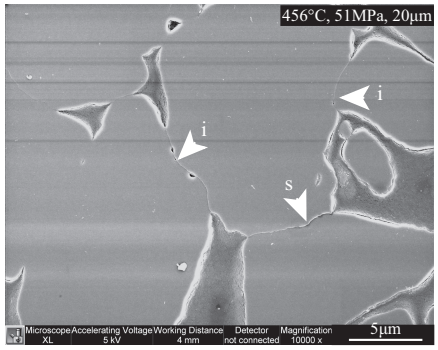
456°C, 51MPa, 20µm
i
i
s
Microscope Accelerating Voltage Working Distance Detector Magnification
XL 5 kV 4 mm not connected 10000 x
5µm

c

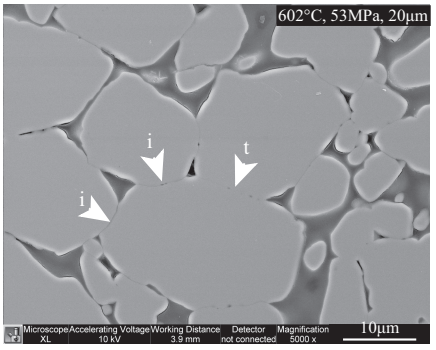
602°C, 53MPa, 20µm
i
t
i
Microscope Accelerating Voltage Working Distance Detector Magnification
XL 10 kV 3.9 mm not connected 5000 x
10µm

d

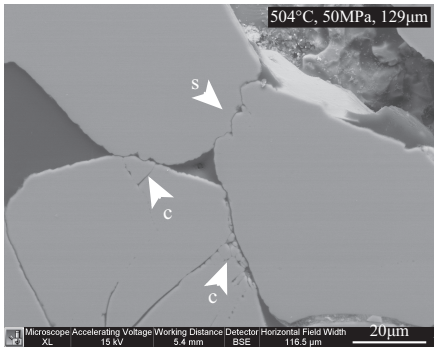
504°C, 50MPa, 129µm
s
c
c
Microscope Accelerating Voltage Working Distance Detector Horizontal Field Width
XL 15 kV 5.4 mm BSE 116.5 µm
20µm

e

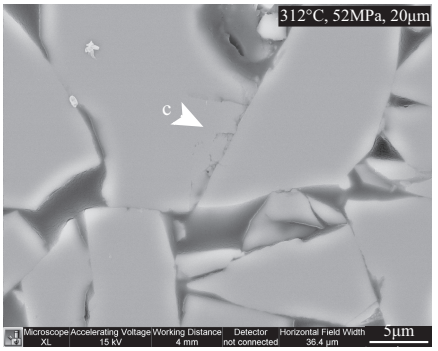
312°C, 52MPa, 20µm
c
Microscope Accelerating Voltage Working Distance Detector Horizontal Field Width
XL 15 kV 4 mm not connected 36.4 µm
5µm

f

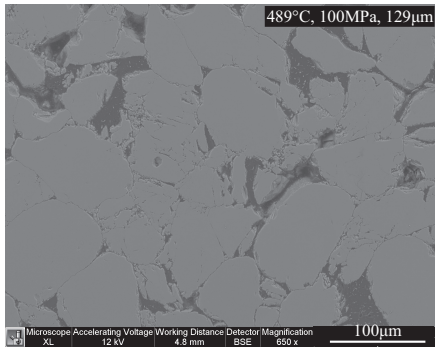
489°C, 100MPa, 129µm
Microscope Accelerating Voltage Working Distance Detector Magnification
XL 12 kV 4.8 mm BSE 650 x
100µm

g

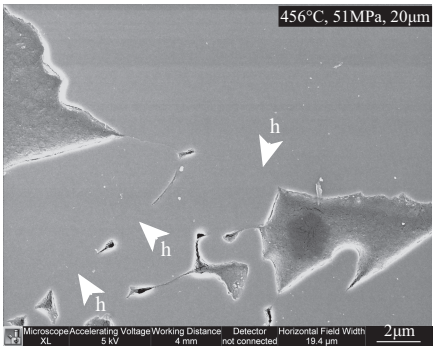
456°C, 51MPa, 20µm
h
h
h
Microscope Accelerating Voltage Working Distance Detector Horizontal Field Width
XL 5 kV 4 mm not connected 19.4 µm
2µm

h

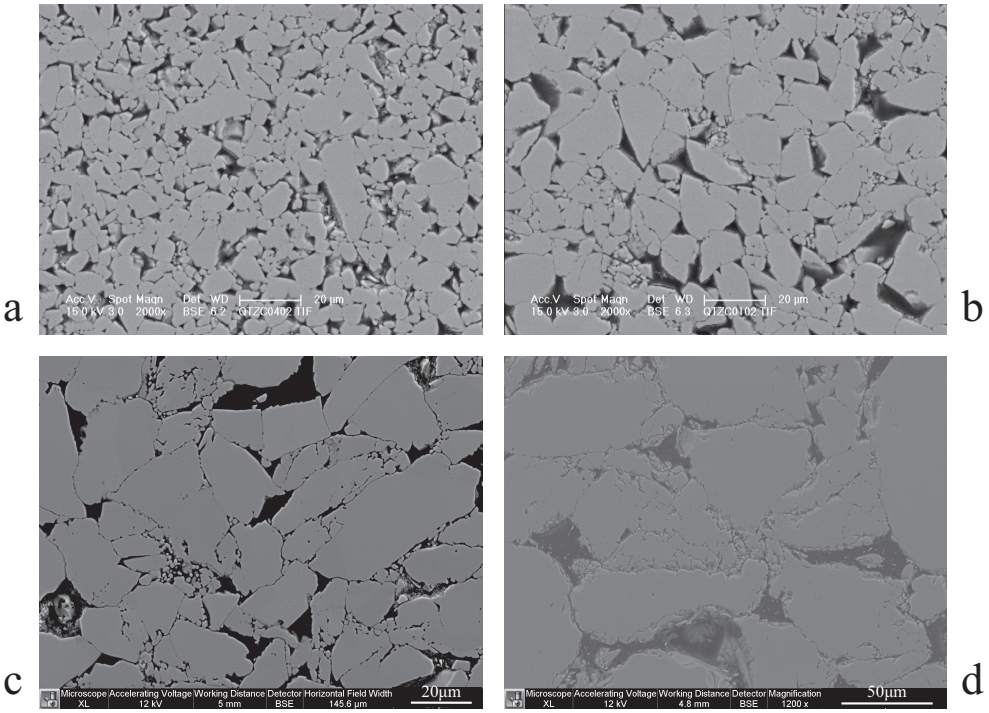

Figure 6.5 SEM BSE micrographs showing the influence of (initial) grain size on microcracking. All samples shown were deformed at ~500°C, 200MPa fluid pressure, and 100MPa effective pressure. Note that not all images are the same scale. (a) QC04; mean initial grain size of 9.8µm. This sample shows very little cracking. (b) QC01; mean initial grain size of 20µm. This sample shows an increase in the amount of grain scale cracking. (c) QC06; mean initial grain size of 47µm. This sample shows again more cracking, and complex fracture systems in parallel or linear arrays, often emanating from contacts. (d) QC05, mean initial grain size of 129µm. A further increase in the amount of cracking and again more complex fracture systems are visible.

Opposite page:
Figure 6.4 SEM BSE images of polished sections of our compacted samples showing various features. (a-e) Grain indentations, truncations, and sutured grain boundaries. (e-f) Intragranular cracks emanating from a grain boundary. (g) Complex fracture networks. (h) Healed grain boundaries. Images taken on sections from experiments QC203, QC218, QC214, QC211, QC221, QC218, QC05, and QC214 respectively. Temperature, pressure and initial mean grain size are indicated in the top right corner of each image. Arrowheads point out grain indentations (i), grain truncations (t), sutured grain boundaries (s), intragranular cracks (c), and healed grain boundaries (h).

6.4.4 EBSD

Selected microstructural maps obtained for the single sample studied using EBSD (QC02; 495°C, 100MPa effective pressure, initial mean grain size of 79μm) are displayed in Figures 6.6, 6.7 and 6.8. Figure 6.6 shows a grain-to-grain contact, with grain A indenting into grain B. The main image displays variations in crystallographic orientation of up to 5° relative to selected pixels. The grey background is a band contrast image, giving a measure of the quality of the EBSP's. The inset is an FSE image. Two intragranular boundaries with a sharp misorientation contrast not attributable to charging effects are observed in grain A. The first (white arrow) is associated with a microcrack in the FSE image. The second misorientation boundary is not related to any visible microcrack. Other (minor) variations in orientation are observed throughout both grains, but these variations occur in horizontal bands, suggesting they are caused by charging effects.

Figures 6.7a and 6.7b both display EBSD images in which colouring illustrates sample orientations according to the inverse pole figure legends shown (i.e. not relative to selected pixels). The insets again show FSE images of the same respective regions. As in Figure 6.6, pink lines indicate Dauphiné twin boundaries. Dauphiné twinning is observed in all grains displayed, and is visible in both EBSD and FSE images. Many of these twin boundaries, such as the twins in grains C, D and E, emanate from grain-to-grain contact points. Grain F in Figure 6.7a displays a complex fracture system, as commonly observed in the coarser grained samples, with >2° misorientations across the fractures.

Figure 6.8a, shows an FSE orientation contrast image with a typical microstructure for sample QC02. Orientation contrast within grains was identified from EBSD as mostly Dauphiné twinning. Figure 6.8b displays the area indicated in Figure 6.8a, with colours indicating variations in relative crystallographic orientation of up to 5° relative to selected pixels. The microstructural relation between grains H and I (seen in Figures 6.8a-b) suggests that they have formed by fracture of one parent grain. This is confirmed by a Dauphiné twin boundary that continues beyond the crack (arrow in Figure 6.8a). This further shows that, in this specific case, the grain fractured after twinning occurred. Dauphiné twinning, related to grain contacts, is again observed in these grains. Furthermore, in both grains G and H, we observe small, gradual and consistent changes in lattice orientation. These are interpreted as lattice bending. Zones of lattice misorientation of more than 2° are also observed along twin boundaries, grain contacts (as pointed out by the arrows) and cracks as indicated by the varying colours towards and along these features. Sharp orientation contrast boundaries, which cannot be directly related to microcracks on the FSE image, are observed in grain H (one is indicated by a white arrowhead). Figure 6.8c, which displays variations in crystallographic orientation within grain I, shows Dauphiné twinning, and lattice bending along the contact with grain J, and along the twin boundary. Figure 6.8d shows a "flame" shaped subgrain (see also Lloyd, 2000), that is also visible in the FSE image (Figure 6.8a). This subgrain formed at a contact and has a misorientation of approximately 2° compared to the parent grain.

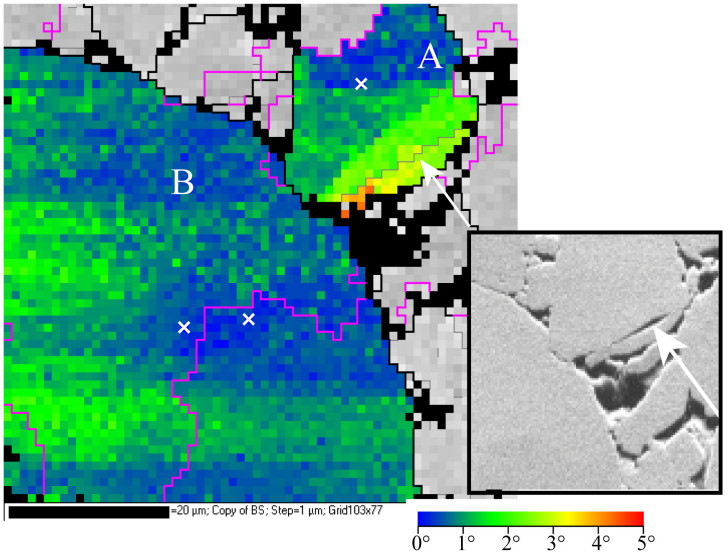

Figure 6.6 Image showing variations in crystallographic orientation within two grains in contact in sample QC02 (495°C, 200MPa fluid pressure, 100MPa effective pressure). The inset shows an FSE orientation contrast image. Black lines indicate grain boundaries (>10˚ misorientation), grey lines indicate misorientation boundaries with a misorientation across them of >2˚, pink lines indicate Dauphiné twin boundaries. White crosses indicate the three points from which relative orientations are displayed in colour according to the legend (one point in grain A, and two points in grain B). The white arrows in both the image and the inset point to the same feature, a microcrack. In grain A also note the sharp misorientation boundary that is not clearly related to a microcrack. Horizontal bands of orientation contrast are mainly caused by charging effects. The grey background colour in the main image gives a measure of the quality of the EBSP for each pixel (i.e., a band contrast image).

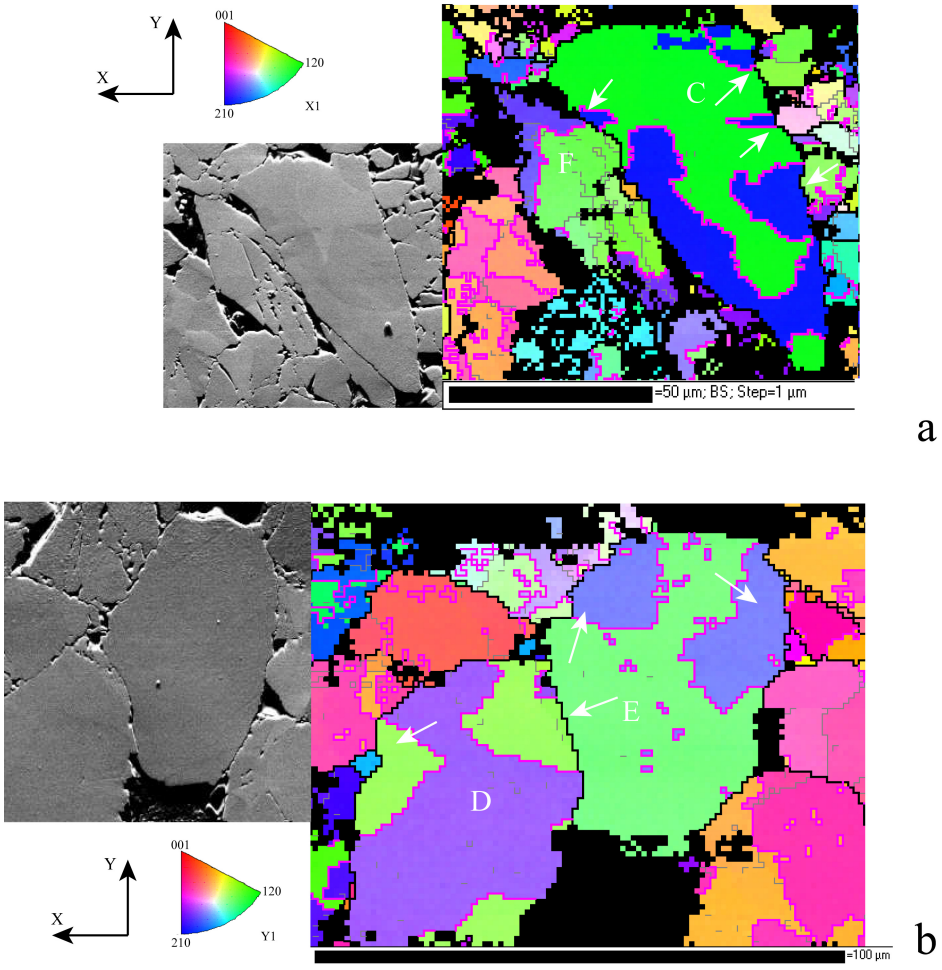

Figure 6.7 EBSD images of microstructures from sample QC02 (495°C, 200MPa fluid pressure, 100MPa effective pressure). The insets show FSE orientation contrast images. In the EBSD images, the black lines indicate grain boundaries (>10˚ misorientation), grey lines indicate misorientation boundaries with a misorientation across them of >2˚, pink lines indicate Dauphiné twin boundaries. Colouring illustrates different sample orientations, according to the inverse pole figure legends. In (a) the x-direction is shown, in (b) the y-direction is shown. All grains show Dauphiné twinning, and twins commonly emanate from grain-to-grain contacts, as pointed out by the white arrows.

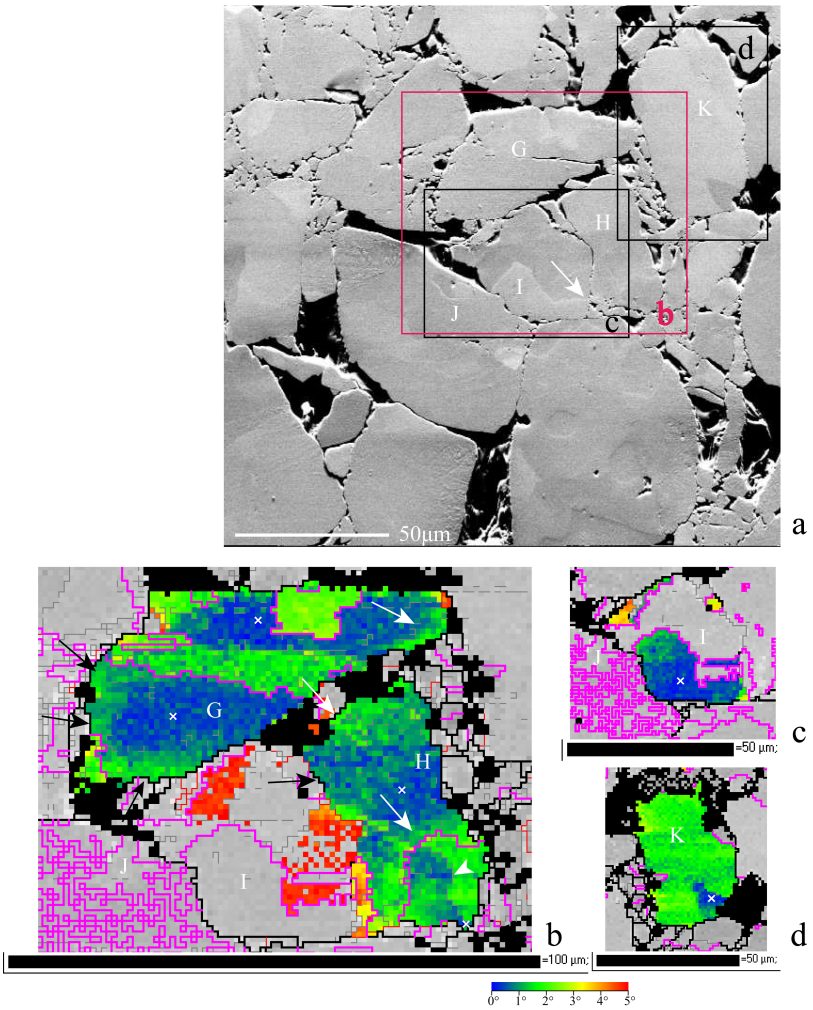

Figure 6.8 An FSE image and images showing relative crystallographic orientations of quartz grains in sample QC02 (495°C, 200MPa fluid pressure, 100MPa effective pressure). Black lines indicate grain boundaries (>10°) and pink lines indicate Dauphiné twin boundaries. (a) FSE image showing orientation contrast. (b) Relative orientation image. Red lines indicate misorientations of >5°, grey lines indicate misorientations of >1°. White crosses indicate the 4 points from which relative orientations (with up to 5° misorientation) are displayed. Relative orientation patterns show subtle lattice bending along twin boundaries, grain contacts and cracks (black and white arrows). The white arrowhead points to a sharp misorientation line (>1°) that is not obviously related to any microcrack visible in the FSE image (a). Note also the twin boundary in grain I that can be followed into grain H. (c) Relative orientation image of grain I. The reference point is again indicated by a white cross. Relative orientations show subtle lattice bending along the contact with grain J and along the twin boundary. (d) This relative orientation image shows a 'flame' shaped subgrain formed at a contact with a misorientation of approximately 2° compared to the parent grain. The grey background in images (b-d) is a band contrast image, and giving a measure of the quality of the EBSP's measured.

6.4.5 Contact microstructures

It will be recalled that, in experiments QC05, QC215 and QC221 (all with a mean starting grain size of 129μm), polished quartz single crystal discs were added as reference surfaces for studying grain contact microstructures. After each of these experiments, the disc was removed from the sample, and its surface, plus the surfaces on the grains in contact with it, were studied using SEM. Figure 6.9 shows some of the contacts observed. The single crystal discs show many shallow pits formed on the scale of the grain size, i.e., several 10's of micrometers in diameter and up to several micrometers deep – Figures 6.9a-b). On the internal surfaces of these pits, we observed a rough texture of generally angular islands and channels (Figures 6.9a-c), sometimes with a granular appearance (e.g., see Figure 6.9b), with a length scale of up to a few micrometers, and sub-micrometer amplitude. Many of the pits display small microcracks (a few to 10s of micrometers in length) within the contact (Figure 6.9a-c). Larger cracks spreading well beyond the contact were also observed, mainly on the crystal included in experiment QC215 (see Figure 6.9d). These larger cracks on the disc from QC215 often connect neighbouring pits. The single crystal disc from experiment QC05 was fractured and subsequently healed during the experiment, as evidenced by several healed fracture planes seen in the disc after the experiment (Figure 6.9e).

The contacts formed on grains impinging upon the included quartz plates (Figures 6.9f-h) show similar roughness, i.e., similarly scaled island-channel microstructures, to the pits seen on the single crystal discs. In addition, very fine (1-3μm), flat, subcircular, plate-like islands or asperities are observed on these contacts, giving the contacts a granular or scaly appearance (Figure 6.9h). Intervening channels are often flat-bottomed and are frequently associated with cracks visible at the contact margins (e.g. Figure 6.9g). Microscale cracking is widespread on grain contact surfaces, with cracks occurring in complex arrays probably controlled by crystal orientation (Figures 6.9f-h).

Figure 6.10 shows micrographs of contacts formed on quartz grains that were in contact with the mica crystal added to experiment QC221. From Figure 6.10a it can be seen that a flattened contact formed against the mica plate by the dissolution of the contacting grains. As the mica crystal was pulled off the sample, flakes of mica remained attached to many of the contact surfaces and to the margins of the pores. Figure 6.10b shows a single contact formed on a quartz grain in contact with the mica crystal. A flake of mica is still attached to the centre of the contact, and the mica sheets are visible at the edges of the flake. The underlying contact surface of the quartz crystal, where visible, is rough. This contact roughness is similar in

Opposite page:
Figure 6.9 SEM images of the contacts formed on and against the quartz single crystal discs. (a-b) Contact indents on the single crystal disc from experiment QC05. (c) A close-up of the contact microstructure on the disc in experiment QC215. Note the microcracks in (a-c), indicated by white arrows. (d) Contacts and connecting cracks on the surface of the disc added to experiment QC215. (e) A healed crack in the single crystal disc added to experiment QC05. (f-h) Microstructures formed on the contact surfaces of grains pressure dissolving against the single crystal disc in experiment QC215. The arrows on (g) indicate microcracks at the contact margins associated with channels in the contact.

Hydrothermal compaction of granular quartz

a

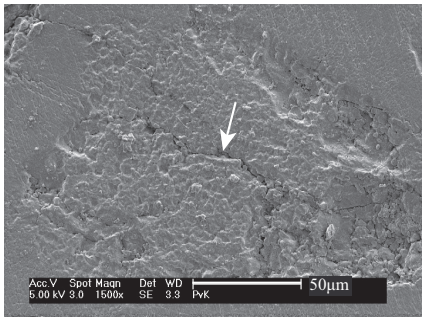

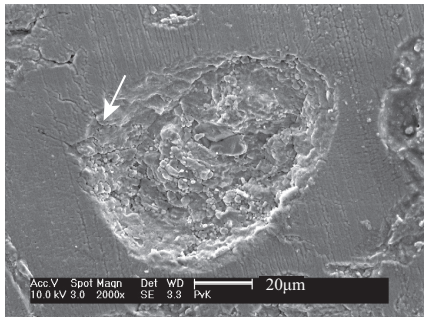

b

c

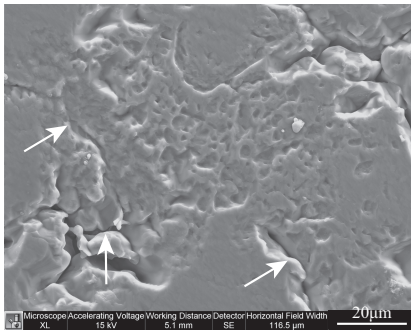

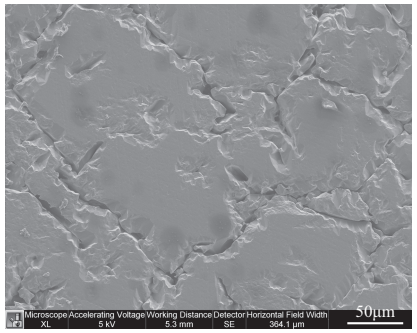

d

e

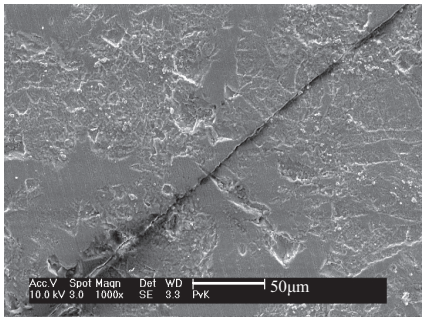

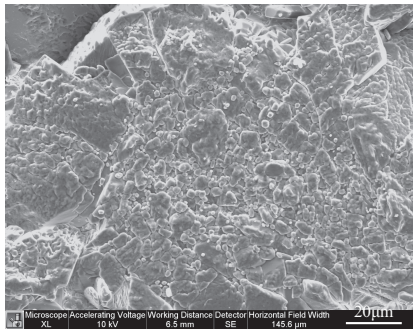

f

g

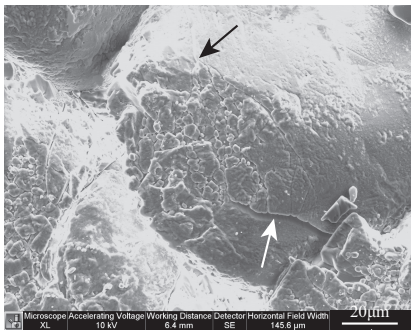

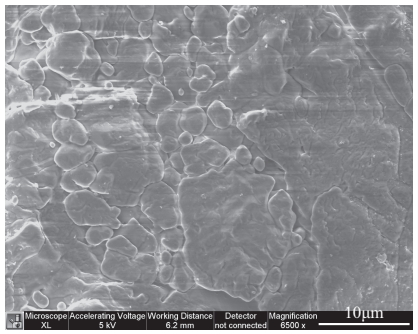

h

a 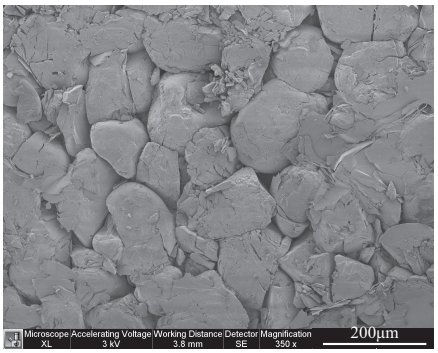

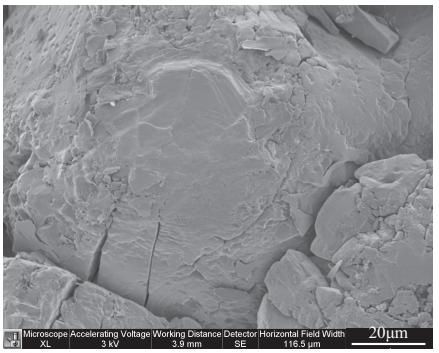

b

Figure 6.10 SEM images of the contacts formed on quartz grains that pressure dissolved against a mica plate in experiment QC221. (a) Several quartz grains in a flattened contact formed against the mica plate. Note the flakes of mica that remained attached to many of the contact surfaces and to the margins of the pores. (b) A single contact. A flake of mica covers the centre of this contact (note the mica sheets visible at the edge of the flake). Around this flake, a rough contact microstructure is visible. The free faces of the quartz grain is relatively smooth.

scale and texture to the roughness observed at quartz-quartz contacts (see Figure 6.9). The free faces of the quartz grains show dissolution pitting, but are otherwise relatively smooth (Figure 6.10b).

6.5 Discussion

We have performed new, servo-controlled experiments on the compaction of granular quartz by pressure solution, at temperatures in the range 300-600°C, effective stresses of 25-100MPa, and using initial mean grain sizes of 3-129µm. We now proceed to interpret our results, discussing the compaction mechanisms operating during cold and hot (hydrothermal) compaction, the rate-controlling processes and the structure of quartz grain boundaries. We then compare our results to the results of other workers and consider the implications of our findings.

6.5.1 Mechanisms controlling cold compaction

We address this issue by recalling that an effective isostatic pressure of 150-150MPa applied to our (wet) samples at room temperature resulted in instantaneous compaction, followed by a stage of very slow compaction creep (~0.2-1% strain in one hour, i.e. a volumetric strain rate $\dot{\varepsilon}$ of 10^{-6}-$10^{-7}s^{-1}$). Microstructural and grain size analyses of cold compacted sample QC222 showed that grain scale cracking was widespread, resulting in major grain size reduction

(from 20 to 8.4μm). Grain indentations or truncations and sutured grain boundaries were not observed. Undulatory extinction was observed in cold the compacted material, but was no more prevalent than in our starting material. It is inferred that microcracking, accompanied by intergranular slip and grain rearrangement, was the main compaction mechanism in our cold compacted samples. Despite having the same initial grain size of 20μm, the final grain size of cold-pressed sample QC216, which was measured using a Malvern particle sizer rather than by linear intercept, was around 17μm, thus considerably larger than the final grain size of sample QC222. However, as cracking during cold compaction led to the formation of a large number of very fine grains, we suspect that these micrograins stuck to other grains during particle size analysis, thus leading to an overestimate of average grain size for sample QC216 (and QC206 – see Table 6.1).

6.5.2 Mechanisms controlling hot compaction

Hot isostatic pressurization of our granular quartz samples led to rapid initial compaction creep (at rates of ~10^{-4}-$10^{-5}s^{-1}$), followed by continuously decelerating compaction. Faster compaction creep occurred in samples with smaller mean grain sizes, and in samples tested at higher temperatures and at higher effective pressures (Figure 6.3). An approximately linear inverse dependence of compaction strain rates on grain size ($\dot{\varepsilon} \propto d^{-0.97}$) was found, along with a mean apparent activation energy for compaction of 105kJmol^{-1} and an approximately power law dependence of strain rate on stress ($\dot{\varepsilon} \propto \sigma_e^{3.4}$). Noting that the exponential dependence of $\dot{\varepsilon}$ on σ in equations (6.1) to (6.3) is roughly equivalent a power law dependence with power ~2 for our test conditions (effective contact stresses between ~90-800MPa for effective stresses in the range 25-100MPa and ϕ/ϕ_0 values between 0.5 and 0.75), these trends in mechanical data are qualitatively consistent with theoretical expectations for pressure solution, notably reaction controlled pressure solution (see section 2.2). However, they do not rule out other creep mechanisms, such as subcritical microcracking.

Microstructural analysis done on our samples using SEM, showed that in all samples grain interpenetrations, grain truncations and sutured grain boundaries were prevalent, supporting the idea that pressure solution was important. Though microcracks are observed in all samples (especially the lower temperature samples), and resulted in considerable grain size reduction in the coarser grained samples, the finding that hot compacted samples (such as QC203, QC205 and QC213) show grain coarsening rather than grain size reduction compared with the cold-pressed sample QC222, suggests that cracking was not a major creep mechanism during hot compaction. This is supported by the lack of any effect of stress on the grain size of hot compacted samples (see Table 6.1). The slight increase in mean grain sizes in hot compacted samples compared to cold compacted sample QC222 is probably the result of the (initial) dissolution of micrograins, and possibly also of crack healing. Similarly, grain rounding seen in high temperature experiments is likely caused by the (initial) dissolution of the sharper extremities of angular grains. That some crack healing occurred in our hot tests is supported by our EBSD observations of sharp crack-like orientation-contrast features without visible voids. Our SEM observations similarly provided evidence for grain boundary healing in the higher temperature experiments.

The grain size dependence of compaction found in our experiments is clearly comparable to the grain size dependence commonly reported for interface reaction controlled pressure solution in quartz (e.g., Niemeijer et al., 2002; though not Dewers and Hajash, 1995). However, a similar grain size dependence is also reported by Chester et al. (2007) for time-dependent compaction of quartz aggregates by microcracking at temperatures up to 150°C, so it is hard to eliminate microcracking on this basis. It should also be noted, though, that the experiments of Chester et al. (2007) reached maximum total strains of only ~10% of which up to ~5% was instantaneous. Moreover, extrapolating our compaction rates (using the apparent activation energy of 105kJmol^{-1}) to 150°C indicates that the compaction rates of Chester et al. (2007) are at least an order of magnitude faster than might be expected for pressure solution. Coupled with our microstructural evidence, we therefore conclude that, while limited microcracking may have occurred during the hot compaction stage of our experiments, its influence on compaction rates was probably minor.

Another possible mechanism for the compaction observed in our experiments is time-dependent crystal plastic deformation. Undulatory extinction, indicating lattice bending, was observed in our samples both before and after hot compaction, suggesting that some degree of crystal plastic deformation was present in the samples before the hot compaction stage. Lloyd (2000) discusses crystal plastic deformation in quartzites during faulting at 200-250°C and 200-300MPa fluid pressure, evidenced by Dauphiné twinning microstructures emanating from grain contacts, and "flame" shaped subgrain structures or zones of diffuse low angle misorientation (indicative of crystal slip) emanating from grain-to-grain contact points. Our EBSD studies, aimed at identifying whether such plastic deformation processes occurred in our samples (specifically QC02), showed similar microstructures (see Figures 6.6, 6.7 and 6.8), though Dauphiné twinning was the most pervasive. The observed correlation of these microstructures with grain contacts suggests that they formed during our compaction experiments. Since significant dislocation motion and recovery are unlikely at room temperature on experimental time scales (Hirth et al., 2001; Rutter and Brodie, 2004), we can thus conclude that some low temperature plastic deformation probably occurred during compaction by pressure solution. Though rate laws for time dependent plastic flow in quartz (Hirth et al., 2001; Rutter and Brodie, 2004) predict a similar dependence of strain rate on differential stress as observed here, the grain size dependence and low apparent activation energy of 105kJmol^{-1} observed in our experiments (compared to 120-240kJmol^{-1} for plastic flow), coupled with the limited microstructural evidence for plastic flow, lead us to conclude that time-dependent plastic deformation was not a significant creep mechanism during hot compaction. This is further supported by the results of Niemeijer et al. (2002), who showed that at 500°C and at effective pressures of 60 or 300MPa, compaction of natural quartz sand in the absence of pore water is much slower than wet compaction.

In summary of this analysis of the deformation mechanisms operating during hot compaction, our microstructural observations can all be explained by pressure solution being the dominant compaction mechanism. In particular, the deep grain indentations and truncations and the sutured grain boundaries observed (Figures 6.4, 6.9-6.10) suggest that the removal of mass from highly stressed contact points was a major straining mechanism. Our observations of healed microcracks and healed grain boundaries further indicate the operation of mass transport. Finally, the observed grain size and stress dependence of creep

rate are roughly comparable to what is expected for interface reaction controlled pressure solution. Some brittle deformation did occur on the grain scale during our experiments, but this was likely limited mainly to the cold compaction stage.

Our microstructural observations on contacts formed between quartz grains and an inserted quartz plate show that during experimental pressure solution grain boundaries developed a rough structure of channels, cracks and load-bearing islands. Significant corruption of these post-mortem grain boundary microsctructures, by quartz precipitation during the cooling and depressurization stages of our tests, is unlikely as the solubility of quartz at 500°C and 200MPa is most ~0.1molkg^{-1} (6gr·kg^{-1}) – Manning, 1994). In forming and maintaining these rough structures, both dissolution/precipitation processes (e.g. Figures 6.9a-c, see also Lehner, 1990; Spiers and Schutjens, 1990; Van Noort et al., 2008, Chapter 3) and microcracking at high angles to the grain boundaries (e.g. Figures 6.9f-h, see also Gratz, 1991; Den Brok, 1998; Gratier et al., 1999) clearly played a role. In addition, locally intense microcracking or contact crushing might have lead to grain boundary microgranulation (Figure 6.9h, see also He et al., 2007), creating an increase in surface free energy and thus providing a driving force for grain boundary dissolution processes. We infer that, during pressure solution in quartz at 500°C, microcracking and dissolution/precipitation processes interact to create a dynamic, rough grain boundary microstructure, in which open fluid channels and microcracks enable dissolution and fast diffusion, and where microgranulation may contribute to the driving force for dissolution.

6.5.3 Hot compaction creep behaviour versus pressure solution theory

We have inferred above, on qualitative grounds, that pressure solution is the most likely mechanism dominating our hot compaction experiments. We will now compare our hot compaction data to absolute rates of creep predicted by theoretical models for pressure solution creep to gain insight into the likely rate controlling process.

Theoretical models of pressure solution predict either an inverse linear dependence of compaction rate on grain size (interface reaction controlled pressure solution, equations (6.1) and (6.3)), or an inverse cubic dependence (diffusion controlled pressure solution, equation (6.2)). As already indicated, the nearly inverse linear grain size dependence found in our experiments (Figure 6.3a), then, agrees well with the models for dissolution or precipitation controlled pressure solution, while diffusion controlled pressure solution can be discounted.

We will now compare our experimental data with the compaction rate model of Niemeijer et al. (2002), which takes into account all three processes operating during pressure solution (dissolution, diffusion and precipitation), as expressed in the exponential forms of equations (6.1) to (6.3), assuming in equation (6.1) that $I^* = I$, where $I = k_+\Omega$ is calculated from the k_+ data of Rimstidt and Barnes (1980). Following Niemeijer et al. (2002 – see also Lehner, 1995; Renard et al., 1999; Gundersen et al., 2002), we assume a granular aggregate microstructure consisting of initially spherical quartz grains arranged in a simple cubic packing (for which $A_d = 6$). The functions $f_x(\phi)$ and $B(\phi)$ are determined by the geometric evolution of the system, assuming that dissolving contacts remain flat and that uniform precipitation occurs on the spherical grain walls (see Lehner, 1995; Renard et al., 1999; Gundersen et al., 2002;

Niemeijer et al., 2002). Comparison of the model predictions of equations (6.1) and (6.2) shows that at our experimental conditions (e.g. 500°C, 200MPa fluid pressure, 50MPa effective pressure), even when assuming a thin film contact with a fluid film thickness (δ) of 1nm, grain boundary tortuosity (τ) of 1, diffusivities (D=10^{-9}m^{2}s^{-1}) ~10× slower than in bulk water, and a grain size of 20μm, diffusion is predicted to be faster than dissolution. Thin film diffusion was already discounted as a rate controlling mechanism based on the observed inverse linear dependence of strain rate on grain size. If we now consider the rough, micrometer scale contact structures observed in this study, average fluid film thicknesses must have been much greater than the 1nm assumed above. In addition, any thin film diffusion pathways were very likely short-circuited by fast diffusion pathways formed by cracks or channels (e.g., see Gratz, 1991; Gratier et al., 1999; Renard et al., 1999). Thin film diffusion lengths thus were typically very short (less than 1μm on average), further discounting thin film diffusion as a rate limiting process for creep. At sample porosity ratios (ϕ/ϕ_0) down to 0.5, the predicted compaction rates for precipitation controlled pressure solution are faster than for dissolution controlled pressure solution by at least a factor 1.4 (see also Niemeijer et al., 2002), so that whereas dissolution is expected to be the main rate controlling mechanism during our experiments, precipitation may also influences rates, especially at the porosities reached in the later stages of our experiments.

Comparison of our measured compaction rates to those predicted by the theoretical rate model taking $I^* = I = I_p$ shows that the experimental rates are generally about one or sometimes two orders of magnitude slower than the predicted values, with larger discrepancies at lower temperatures (Figure 6.3). Similar discrepancies were also observed by Niemeijer et al. (2002) between their experimental data and the compaction model. For porosity ratios (ϕ/ϕ_0) between 0.55 and 0.75, our experimental strain rates (500°C, 200MPa fluid pressure, 25-100MPa effective pressure) show an apparent power law dependence on effective pressure, with an average exponent of 3.4 (Figure 6.3b). This is higher than the values between 1.4-1.9 predicted by the model for ϕ/ϕ_0 values in the range 0.55-0.75 (at 500°C, 200MPa fluid pressure, 25-100MPa effective pressure). In the temperature range 300-600°C, our experimental data show an average apparent activation energy for compaction of 105kJmol^{-1} (Figure 6.3c). This is considerably higher than the mean apparent activation energy of ~51kJmol^{-1} predicted by the model for ϕ/ϕ_0 values in the range 0.55-0.75. Though the observed discrepancies between model and experiment are significant, the broad agreement with expectations for (dissolution controlled) pressure solution remains evident. Possible causes for these discrepancies include the effects of additional mechanisms, such as subcritical microcracking, which may have played some role in controlling mechanical behaviour, or possibly the effects of grain boundary structure on the rate of dissolution controlled pressure solution, as discussed by Van Noort et al. (2008, Chapter 3). Their findings indicate that, for an elastic solid, an island-channel structure has a relatively minor effect on dissolution controlled pressure solution rates, slowing it down by a maximum of only 13% through reducing I^* relative to I. The work reported in Chapter 4 on the other hand considers the effect of plastic deformation of highly stressed contact asperities on dissolution controlled pressure solution rates. The model presented shows that plastic dissipation in grain

boundaries reduces the driving force for dissolution and could slow down pressure solution rates by more than one order of magnitude, i.e., to values similar to those observed here.

We will now directly compare our experimental results with model predictions for our experimental conditions made using the formulation for I^* ($\neq I$) presented in Chapter 4 for pressure solution with grain boundary microplasticity. Following Chapter 4, we assume a grain boundary thickness (δ) of 5nm, minimum values for the number of islands (M) per square meter of grain boundary, plus grain boundary area fractions (α) between 0.018 and 0.024. This model gives physically viable predictions (i.e., satisfying the conservation of energy/ entropy with at least one contact point per grain boundary) only in the range of conditions for which it is displayed in Figure 6.3. Within this range, it yields a better agreement with our experimental data than the model assuming $I^* = I$. It more accurately predicts strain rates, as well as stress dependence. However, it predicts an apparent activation energy some 40% higher than observed in our experiments. The model presented in Chapter 4, assuming grain boundary plasticity, can thus give better agreement with our data. Application of this model and our choice of grain boundary parameters are, however, highly speculative. Other factors, such as the contamination of the pore fluid by metal ions, might also lead to decreased creep rates by decreasing dissolution and/or precipitation rates (cf. Niemeijer et al., 2002; Niemeijer and Spiers, 2002). Alternatively, the observed grain boundary microcracking/granulation might have a strong effect on creep rate. The models presented in Chapters 3 and 4 predict very high stresses at contact asperities, and may imply unavoidable (coupled) grain boundary microcracking effects. As discussed earlier, our contact microstructural observations do seem to point to grain boundary microcracking as a mechanism for creating and maintaining rough grain boundaries during pressure solution.

In summary of the foregoing, we have compared our experimental hydrothermal quartz compaction data to theoretical compaction rate models for pressure solution. This comparison shows the best agreement for with reaction controlled models, notably the dissolution controlled case, though agreement is still rather poor. The dissolution controlled compaction rates predicted making the classical assumption that $I^* = I$, overestimate actual pressure solution compaction rates by about one order of magnitude. Moreover, while an inverse linear dependence of compaction rates on grain size is predicted and was observed, experimental strain rates depended much more strongly on effective pressure and on temperature than predicted. Further comparison of our compaction data with the model predictions presented in Chapter 4, which consider the influence of plastic deformation of highly stressed contact points on dissolution controlled pressure solution rates, showed that this model may partly explain the discrepancies observed. On the other hand, while our EBSD analyses suggested limited low temperature plastic deformation at/near grain contacts, our observations on contacts formed on quartz single crystal discs added to some experiments, showed widespread contact microcracking. We therefore infer that microscale contact cracking at highly stressed contact points, followed by surface energy driven dissolution, might have been an important mechanism in creating and maintaining a rough grain boundary structure, as previously speculated (Gratier et al., 1999; He et al., 2007). As contact points fracture, other contact points form, and become load-bearing, ensuring that this is a dynamic structure.

6.5.4 Comparison with previous experimental work

Next, we will compare our experimental results with previous experimental results. Recall that Schutjens (1991) reported a transition from microcracking to dissolution controlled pressure solution as the dominant compaction mechanism at temperatures of around 250-350°C.

In our experiments, we found an inverse linear dependence of compaction rates on grain size. A similar dependence of compaction rates on grain size was also observed by Niemeijer et al. (2002), during experimental compaction of granular quartz by dissolution controlled pressure solution, and by Chester et al. (2007) during compaction of quartz sand by microcracking at 150°C. Our microstructural observations, however, indicate that mass removal from grain boundaries by dissolution, i.e., some form of pressure solution, rather than the direct effects of microcracking, more likely dominated compaction. Dewers and Hajash (1995) report a grain size coefficient of –2.3 associated with what they associate to be dissolution controlled pressure solution compaction at temperatures up to 200°C. Niemeijer et al. (2002) ascribe this high coefficient to differences in starting porosity between different grain size fractions used. The mean apparent activation energy for compaction found in our experiments (105kJmol^{-1}) is considerably higher than apparent activation energy values in the range –67 to -76kJmol^{-1}, generally reported in the literature for pressure solution compaction of quartz (Schutjens, 1991; Dewers and Hajash, 1995; Niemeijer et al., 2002). As these commonly found values are close to the activation energy for free-face dissolution of quartz at temperatures up to 300°C (Rimstidt and Barnes, 1980; Dove and Crerar, 1990), this is often used as an argument for dissolution rate control of pressure solution. Note, however, that the apparent activation energy for pressure solution creep predicted by the commonly used theoretical rate equation (equations (6.1) to (6.3)), assuming the dissolution kinetics of Rimstidt and Barnes (as done by Niemeijer et al., 2002), is lower than this value (~51kJmol^{-1}). A relatively high activation energy for quartz free-face dissolution of 89kJmol^{-1} is given by Tester et al. (1994) for a temperature range of 25-625°C, and using their model a slightly better comparison between experimental and theoretical apparent activation energies for pressure solution can be obtained. The relatively high apparent activation energies obtained in our experiments could be the result of different starting material properties such as the angularity of the grains or intracrystalline water contents. These factors might have resulted in a higher relative importance of grain boundary plasticity or microfracture processes through higher contact stress concentrations. Hydrolytic weakening effects (e.g., see Blacic and Christie, 1984) seem unlikely in view of our experimental conditions. A similarly high apparent activation energy for creep (114.5kJmol^{-1}) was reported by Rutter and Wanten (2000) for the compaction of phyllosilicate-bearing quartz sands. The stress sensitivity found in our experiments (3.4) at constant ϕ/ϕ_0 is similar to the values reported by Niemeijer et al. (2002) and Rutter and Wanten (2000), and falls in the range reported by Schutjens (1991).

It is interesting to note that in most of our higher temperature experiments, performed at 500-600°C, a rapid drop in compaction rates was observed after a few hours to a few days, similar to the rapid drops in strain rate reported by Niemeijer et al. (2002) at sample porosities of ~10-15%. In our experiments, this drop was demonstrably caused by quartz precipitation in the tip of the pore fluid pipe, blocking fluid flow. It is possible that in the experiments of

Niemeijer et al. (2002) the rapid drop in compaction rates often observed was also caused by blocking of the fluid pipe, though no such blocking was reported by these authors.

6.5.5 Influence of mica on quartz pressure solution

From microstructural and experimental observations, it is widely believed that the presence of phyllosilicates enhances pressure solution rates in quartz and halite, presumably due to increased grain boundary diffusion rates or enhanced reaction kinetics (e.g., Hickman and Evans, 1995; Renard et al., 1997; Rutter and Wanten, 2000; Niemeijer and Spiers, 2002). It has also been proposed that this effect may be due to the prevention of grain boundary healing in polymineralic materials due to the different surface energies of phase boundaries compared with grain boundaries (e.g., Bos and Spiers, 2000; Van Noort et al., 2006, 2008, Chapters 2 and 3). In our experiment QC221, a mica plate was added to the compacting quartz aggregate so that the contact structures on the quartz grains contacting the mica plate could be studied. The rough structures formed were similar to the structures formed between quartz grains. Unfortunately, strain rates could not be determined due to a confining pressure leak. Our observations suggest, however, that there were no special effects of mica due to specific contact structures forming on abutting quartz grains.

6.6 Implications: Compaction of sandstones in nature

We now look at the implications of our results for the compaction of sandstones in nature. As we have been unable to demonstrate good agreement between our results and theoretically based rate laws, we can approach this only by deriving an empirical rate equation for the compaction behaviour measured in our experiments. The equation we obtain, for porosity ratios (ϕ/ϕ_0) in the range 0.75-0.4, takes the form:

$$\dot{\varepsilon} = \frac{\Psi}{d}\sigma_e^{3.4}\exp\left(-105000/RT\right) \tag{6.4}$$

where the factor Ψ depends on geometry and on ϕ/ϕ_0. This is empirically determined, by best fitting of a simple power law function, yielding the result:

$$\Psi = 10^{-7.8}\left(\phi/\phi_0\right)^{10.0} \tag{6.5}$$

Using the empirical rate equation thus obtained, we can cautiously extrapolate our results to predict porosity loss during burial and diagenesis of a sandstone, by the compaction mechanisms that operated during our experiments, i.e., mainly pressure solution. Note that,

as our experiments were essentially performed in a system closed to the long-range transport of material, this model does not include lateral or vertical transport of silica, and possible cementation effects. Note also, that this equation will predict much slower pressure solution compaction rates under natural conditions than previously predicted based on theoretical models for dissolution controlled pressure solution, such as the model of Niemeijer et al. (2002).

A similar, empirically based porosity-depth prediction was made by Chester et al. (2007) for time dependent compaction by subcritical microcracking, based on their low strain compaction experiments. We will assume conditions similar to those assumed by them, i.e., a burial rate of 100m/My, geothermal gradient of 20°Ckm^{-1}, lithostatic loading (rock density 2200kgm^{-3}), hydrostatic pore pressure (water density 1000kgm^{-3}), a starting porosity of 35% and a mean (rather fine) grain size of 100μm. Note that this is finer than assumed by Chester et al. (250-350μm – 2007) to compensate for grain size reduction by microcracking at shallow levels.

The predicted porosity versus depth curve for these conditions is shown in Figure 6.11. Our empirical rate model predicts very little compaction by pressure solution for depths less than 2km. At depths around 2km, pressure solution starts to operate significantly, and between 3km and ~10km, pressure solution results in major porosity loss from ~32 to 5%. Our empirical model, combined with that of Chester et al. (2007) and assuming a geothermal gradient of 20°Ckm^{-1} thus suggests that microcracking is the most important compaction mechanism for sandstone compaction at depths down to ~3km, where pressure solution starts to become the dominant mechanism. This agrees quite well with observations made on compacted natural quartz arenites, which show pressure solution to become an important mechanism at depths below about 2.5-3km (e.g., Ramm, 1992). Figure 6.11b shows a comparison between the porosity measurements of Ramm (1992) and our empirical model, assuming geothermal gradients of 20 and 40°Ckm^{-1} (as on parts of the Norwegian continental shelf – Ramm, 1992). For a geothermal gradient of 40°Ckm^{-1}, our model predicts that pressure solution starts to operate at about 1.5km depth, and starts to dominate at ~2.5km. The porosity-depth curves predicted by our model with a geothermal gradient of 40°Ckm^{-1} agree quite well with the porosities measured by Ramm (1992). In a previous paper (Van Noort et al., 2008, Chapter 3), we showed that the porosity-depth trends of Ramm (1992) might also be explained by a cessation of rapid pressure solution by grain boundary healing. Detailed microstructural analysis is thus required to help distinguish which mechanisms operate to determine final porosities in compacting sandstones under natural conditions.

Experimental evidence suggests that pressure solution only becomes important at temperatures greater than 250-300°C (Schutjens, 1991). Our predictions now show that while at lower temperatures, between ~70 and 250-300°C, microcracking might be the more important mechanism in experiments (Schutjens, 1991; Chester et al., 2004; Chester et al., 2007), under natural conditions, pressure solution is more important. Unfortunately, experiments at timescales required to investigate a possible change in operating mechanism are impossible to perform. Detailed, quantitative microstructural analysis of various clean sandstones compacted under well-constrained natural conditions, however, could provide further answers on this change in mechanisms (e.g., Houseknecht, 1988; Dickinson and Milliken, 1995).

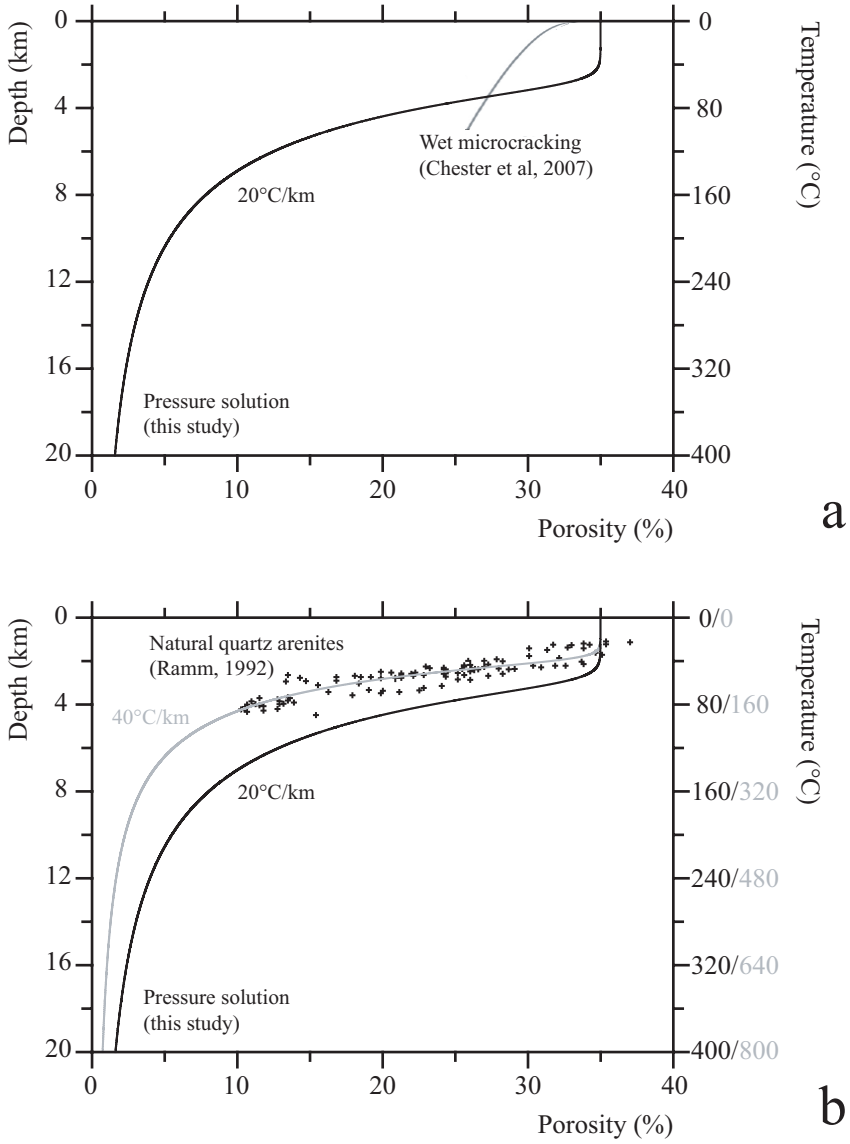

Figure 6.11 Predicted porosity versus depth curves, using our empirical compaction equation. We assume lithostatic rock pressure and hydrostatic pore fluid pressure. (a) A comparison of our empirical model with the porosity versus depth curve predicted by Chester et al. (2007) for wet microcracking in St Peter sand with an initial grain size between 250-300μm, assuming a geothermal gradient of 20°C/km and a burial rate of 100m/My (as assumed by Chester et al., 2007) and a mean grain size of 100μm. (b) A comparison of porosity-depth curves predicted by our empirical model with porosity measurements on well-sorted arenitic sandstones from the Norwegian continental shelf where the geothermal gradient is between 33 and 41°C/km (Ramm, 1992). After Ramm (1992), a mean grain size of 500μm and a burial rate of 25m/My are assumed here.

6.7 Conclusions

In order to determine the compaction of quartz by intergranular pressure solution, we have performed isostatic compaction experiments at temperatures between 300-600°C, effective pressures up to 100MPa, on granular quartz samples with final mean grain sizes between 2 and 30μm. Furthermore, EBSD analysis was performed on one sample in order to investigate whether plastic deformation took place during our experiments. In some experiments, single crystal quartz reference discs or a mica plate were added to the samples. Subsequently, the structures formed at the contacts formed between grains and plates were studied using SEM.

Microstructural evidence suggests that, whereas microcracking was the main compaction mechanism during cold precompaction, during hot compaction at temperatures of 300-600°C, pressure solution was the main mechanism of compaction. Though limited microcracking during hot compaction may have occurred, grain size and qualitative microstructural analyses indicate that its influence as a direct strain accumulating mechanism was small. EBSD analysis showed Dauphiné twinning, lattice bending up to ~2° in zones of a few micrometers wide, and flame-shaped substructures near highly stressed contact points, comparable to the observations on faulted quartzites reported by Lloyd (2000). These occurrences are interpreted to indicate that minor plasticity did indeed take place during our compaction experiments, presumably during the hot compaction stage.

SEM study of the indentations formed on, and the contacts formed against the single crystal quartz reference discs added to certain samples showed that all contacts were rough, with a micrometer scale island-channel network with sub-micrometer scale amplitude. Furthermore, almost all contacts showed some degree of microcracking, varying from very fine cracks (on the scale of and associated with the roughness) to larger cracks (beyond the scale of the contacts). The contacts formed on quartz grains contacting a mica plate were also rough, with a texture that was similar in scale and appearance to the contacts formed between a quartz grain and a quartz single crystal disc.

From an analysis of the independent effects of varying d, σ_e and T our mechanical data indicate a nearly linear inverse dependence of strain rates on grain size (coefficient of –0.97), a power law dependence of strain rates on effective stress with exponent ~3.4, and an apparent activation energy of 105kJmol^{-1}. The grain size dependence of the compaction rates is consistent with the possibility that pressure solution was controlled by interface reactions. From a comparison with theoretical models, we conclude that pressure solution rates were most likely controlled by dissolution in the grain boundary though agreement is rather poor. Comparing our data with the pressure solution rate models of Niemeijer et al. (2002) indicates that our compaction rates are slower than predicted for dissolution control, and show greater sensitivity to σ_e and T. Extending the model of Niemeijer et al. with the modifications suggested in Chapter 4, that considered the effect of grain boundary plastic deformation on dissolution controlled pressure solution rates, offers possible insight into these discrepancies, though the influence of grain boundary microcracking on grain boundary structure and on pressure solution rates may be equally or more important.

An empirical rate equation, based on our experimental results was used to extrapolate

our measurements, and to predict porosity change with depth for an arenitic sandstone during burial and diagenesis. The extrapolation (assuming geothermal gradients between 20-40°Ckm^{-1}) showed that pressure solution starts to operate at depths between 1.5-2km, and leads to considerable compaction and porosity loss at depths between ~2-10km. When compared with the data and predictions of Chester et al. (2007) our empirical model shows that at shallower depths (down to ~3km for 20°Ckm^{-1}), microcracking is the dominant compaction mechanism, but that at greater depths, compaction is likely controlled by pressure solution. When compared to porosity measurements on arenitic sandstones from the Norwegian continental shelf (Ramm, 1992), our empirical model shows good agreement for a geothermal gradient of 40°Ckm^{-1}.

As a final note, we conclude, from a combination of our microstructural and mechanical observations, our EBSD work, our contact structures and the model for the effects of grain boundary microplasticity on pressure solution presented in Chapter 4, that pressure dissolving grain boundaries in quartz have a microstructure in which highly stressed contact points take up a fraction of the grain boundary area. Stress concentrations in the points of actual contact will lead to fracturing and may lead to local plastic deformation. As contact points fracture, other contact points form, and become load-bearing, while dissolution at the previous contact points continues, driven by surface energy. In this way, a dynamic island-channel network, that allows fast diffusion, enabling (dissolution-controlled) pressure solution, can be maintained.

Chapter 6

7. Conclusions and suggestions for future research

7.1 Conclusions

In this study, the structure and properties of grain boundaries in geological materials undergoing intergranular pressure solution, and the influence of these grain boundary properties on pressure solution kinetics were investigated. This was done through in-situ contact experiments on single halite and silica contacts, hydrothermal compaction experiments on granular quartz aggregates, and theoretical modelling of grain boundary structure/properties and their influence on grain boundary dissolution rates. The general conclusions of this study are summarised below in relation to the research questions and aims posed in the introductory chapter.

1) Orientation effects on grain boundary diffusion

a) From the halite–glass single contact pressure solution experiments and associated electrical impedance measurements reported in Chapter 2, we conclude that there is a marked dependence of the grain boundary diffusivity product (Z) on the type of halite face (F-, S- or K-face) that forms the contact. SEM observations showed that contact surfaces parallel to F-, S- and K-faces have markedly different post-mortem structures, but that contacts with similar roughness are characterised by grain boundary diffusivity products of similar magnitude. Our results support the notion that orientation is important in determining contact diffusivity primarily through a PBC-dependent crystallographic control on contact roughness, at least in the case of halite.

b) Our halite–halite contact observations and impedance measurements have shown that contact type and contact misorientation, likely through surface energy effects, have a strong influence on the rate of neck growth. Whereas halite–glass contacts showed pressure solution, halite–halite contacts showed neck growth, with faster neck growth occurring in a contact with low (zero) misorientation than in a contact with high (45°) misorientation. Furthermore, the diffusivity product of a halite–halite contact with low misorientation was considerably lower than in halite–glass contacts, whereas the diffusivity product of a halite–halite contact with high misorientation was considerably higher, suggesting that grain boundary diffusivities may be influenced by grain boundary misorientation. These results imply that at low stresses polymineralic rocks may deform faster by pressure solution than monomineralic rocks due to the inhibition of neck growth and possibly due to faster grain boundary transport. This finding is supported by previous work on pressure solution in polymineralic systems (calcite/halite mixtures – Zubtsov et al., 2004). Clearly, care should be taken when applying data obtained from experiments on contacts between two dissimilar materials to contacts between two similar materials and vice versa.

c) Lastly, the above imply that, contrary to conventional thinking on diffusion creep mechanisms, pressure solution may be capable of leading to the development of significant lattice-preferred orientations in highly deformed rocks. This follows from the fact that certain contacts, with specific grain-to-grain misorientation relationships, will allow faster dissolution and diffusion than others, whereas yet other contact combinations will be characterised by neck growth. Such a lattice-preferred orientation, plus resulting preferred orientation of wetted grain boundaries, can in turn lead to seismic and electrical anisotropy.

2) Grain boundary dissolution and healing during pressure solution of elastic solids

Using an energy/entropy balance approach for a representative element of grain boundary, the effect of grain boundary structure on the grain boundary dissolution rate coefficient (I^*) for pressure solution has been examined. In another model, the issue of whether a dynamically wetted island-channel structure can be maintained in a grain boundary under non-hydrostatic stress, as opposed to healing by surface energy driven growth of islands, has also been addressed.

a) When applied to quartz, the models derived here for the apparent dissolution rate coefficient (I^*) in a pressure dissolving grain boundary with island-channel structure in a purely elastic material, show only a minor ($\leq$13%) reduction in I^* compared to the free surface dissolution rate coefficient (I). This cannot fully account for the observed discrepancy of typically one order of magnitude observed between theoretically predicted pressure solution rates (assuming dissolution control with $I^* = I$) and the lower rates measured in quartz aggregates under hydrothermal conditions.
b) The above models also predict that the load across a grain boundary with island-channel structure undergoing pressure solution is supported by only a very small fraction of the contact area. The area occupied by non load-supporting islands might be larger, however.
c) Our model for surface energy driven grain boundary healing predicts a critical effective stress or "yield stress" below which grain boundary healing prevents pressure solution. Below this critical stress, the driving force term for growth of the islands to reduce surface energy and curvature exceeds the average driving force for dissolution of the islands caused by elastic strain energy imparted by the applied effective stress.
d) The "yield stress" for pressure solution predicted by the grain boundary healing model implies that at any given depth, compaction of sediments by pressure solution will proceed and porosity will be reduced until a critical minimum porosity is reached at which the grain contact stress equals the local yield stress value. Applying the model to the compaction of arenitic rocks by pressure solution in nature, we mapped the critical minimum porosity that can be attained as a function of depth. Comparison of the porosity-depth trends obtained with porosity-depth data obtained from arenites from the Norwegian continental shelf showed a reasonable match for values of the grain boundary area fraction taken up by islands between 0.3

and 0.4. If grain boundary healing of this type is a limiting factor for compaction by pressure solution, the implication is that average pressure solution compaction rates, derived from natural rocks by assuming continuous pressure solution during a given interval of geological time (burial history) will strongly underestimate actual rates.

3) Grain boundary microplasticity

a) The grain boundary dissolution model for pressure solution in elastic solids has been expanded to include the effect of dissipation by grain boundary microplasticity, within an island-channel grain boundary structure, on the grain boundary dissolution rate coefficient (I^*). When applied to hydrolytically weakened quartz under hydrothermal conditions, this predicts that plastic flow of grain boundary islands could slow down dissolution controlled pressure solution rates in experiments by more than one order of magnitude, at least under certain conditions. This result offers a possible, though still highly speculative explanation for the discrepancies observed between experimental and theoretical pressure solution rates under hydrothermal conditions.

b) Like its elastic counterpart, the model for I^* including grain boundary microplasticity implies very small solid-solid contact areas within pressure dissolving grain boundaries, and associated high contact stresses, for the case of quartz. This raises the possibility that microfracture within grain boundaries may be an essential coupled component of intergranular pressure solution in quartz, contributing for example to grain boundary roughening (with or without grain boundary plasticity).

c) The kinetic effect of plastic flow of grain boundary islands in quartz rocks under basin conditions predicts that the phenomenon only becomes significant at depths greater than ~9-10km.

4) Silica contacts undergoing pressure solution

a) From the contact impedance experiments reported here, on contacts between silica glass and silica glass or between silica glass and quartz under hydrothermal conditions, average grain boundary fluid film thicknesses of 380±140nm were inferred. This is one to two orders of magnitude larger than generally assumed for quartz grain boundaries during pressure solution. From this thickness, a (relatively high) mean value of $6.3\pm1.4\times10^{-18}$m^{3}s^{-1} was estimated for the silica grain boundary diffusivity product $Z = D\delta_{gb}C^*$. These estimates for the grain boundary fluid film thickness and the grain boundary diffusivity product are likely overestimates, due to incomplete "closure" or partial "short-circuiting" of our contacts as a result of irregular dissolution and/or cracking.

b) Despite the above, post-experimental observations on preserved contacts showed rough contact structures with. A preserved glass-glass contact showed reniform depressions, caused by dissolution. These depressions were up to 5μm deep and had lateral dimensions of up to ~100×50μm. A glass-quartz contact showed islands and channels on a length scale of up to several micrometers, and with sub-micrometer scale amplitude. However, precipitation on this contact could not be excluded.

c) Our rough grain boundary structures, cracked contacts and high mean fluid film thicknesses and grain boundary diffusivity products support the concept that diffusion through grain boundaries is relatively fast during pressure solution of materials such as quartz, as a result of fast or short-circuit diffusion pathways, and that pressure solution in quartz is likely interface reaction (dissolution or precipitation) controlled in nature.

5) Hydrothermal compaction of granular quartz

Isostatic compaction creep experiments have been performed on granular quartz aggregates (mean initial grain sizes between 3 and 129μm) under hydrothermal conditions (300-600°C, 200MPa fluid pressure, 25-100MPa effective stress).

a) At fixed normalised porosity (ϕ/ϕ_0) values, the results showed a nearly inverse linear dependence on grain size ($\dot{\varepsilon} \propto d^{-0.97}$), an apparent power law dependence on effective pressure ($\dot{\varepsilon} \propto \sigma_e^{3.4}$), and an Arrhenius dependence on temperature with apparent activation energy of 105kJmol^{-1}.

b) From microstructural observations, it is concluded that while grain scale microcracking was important during cold pre-compaction at high stresses, pressure solution was the main compaction mechanism during hydrothermal compaction. Based on the mechanical data, especially the grain size dependence, and on theoretical model predictions, it was inferred that compaction rates were controlled by interface reaction kinetics, and that of these interface reactions, grain boundary dissolution was the most likely rate controlling process, probably coupled with internal grain boundary microcracking.

c) EBSD analysis provided evidence for limited plastic deformation (Dauphiné twinning and lattice bending) during pressure solution at 500°C, 200MPa fluid pressure and 100MPa effective pressure, at or in the neighbourhood of highly stressed grain contacts. Contact indentations formed during hydrothermal compaction were rough, with a micrometer scale roughness of islands and channels with (sub)micrometer scale amplitude. Most contacts showed internal microcracking. Microgranulation may also have occurred. From this, it is proposed that during pressure solution in quartz under the present conditions, stress concentrations at contact points in the grain boundary lead to fracturing of these points, and possibly local plastic deformation. As the contact points fracture, new contact points form, and become load-bearing, while surface energy drives dissolution at previous contact points. In this way, a dynamic island-channel network that allows fast diffusion, and hence dissolution controlled pressure solution, can be maintained.

d) Using an empirical rate model, the experimental compaction rates were extrapolated to predict porosity change versus depth curves for an arenitic sandstone during burial and diagenesis. This showed that pressure solution starts to operate at depths between 1.5-2km for geothermal gradients in the range 20-40°Ckm^{-1}. Comparison with a similar porosity versus depth curve for subcritical cracking, predicted by Chester et al. (2007), shows that pressure solution is the dominant compaction mechanism from ~2.5-3km, as observed by Ramm (1992) for arenitic sandstones from the

Norwegian continental shelf. Our empirical model also shows good agreement with sandstone porosity versus depth data measured by Ramm (1992). This suggests that cessation of pressure solution by grain boundary healing (of the type demonstrated in Chapter 3) is not necessarily required to predict these porosity-depth curves.

7.2 Future research

The results obtained and problems encountered, in the work reported here, have raised new questions and ideas for improvements, and have opened new pathways for further research. Below, we discuss suggestions for future research.

1) The halite-glass contact experiments presented in Chapter 2 show that contact orientation has an effect on contact diffusivity and roughness, but due to the experimental setup used we could not investigate contacts with a single orientation. Attempts to address this using a wedge-shaped glass lens pressed into a slot in a halite single crystal (rather than a conical lens pressed in a circular hole) failed, as electrical conduction at the ends of the lens could not be prevented. A possible way forward might be to implant electrodes (or an electrode array) in a flat indenter applied to a halite (or other mineral) surface of specific orientation.
2) The halite-halite contact experiments of Chapter 2 yielded some interesting results on the influence of contact misorientation on contact evolution (pressure solution versus neck growth). Further investigation, studying the influence of a wider range of misorientations and the influence of contact load on contact evolution and contact conductivity, would be very useful to expand our understanding of the interaction between pressure solution and neck growth. This would also provide a means of testing the grain boundary healing model developed in Chapter 3, with appropriate extension to include plastic deformation effects.
3) The results reported in Chapter 2 imply that polymineralic contacts can allow faster deformation by pressure solution than monomineralic contacts by preventing healing through surface energy effects. So far, this effect has received only limited attention and it would benefit from further investigation. For example, such effects may explain the observation that phyllosilicates enhance quartz pressure solution in natural rocks, in terms of inhibited healing rather than enhanced pressure solution.
4) The geometric model for a grain boundary with an island-channel structure presented in Chapter 3 is clearly oversimplified. The model presented in Chapter 3, and expanded in Chapter 4 to include grain boundary microplasticity would be greatly improved by accounting for a more complex structure. This is clearly a highly problematic issue, however, as the models developed in Chapters 3 and 4 predict that the grain boundary structure will tend to evolve to a state that satisfies the energy/entropy balance and kinematic constraints that apply. A possible way to progress here might be to attempt a moving boundary finite element analysis of a pressure dissolving grain boundary, extending the approach used by Ghoussoub

and Leroy (2001). A second possibility would be a cellular automaton modelling approach to grain boundary structural evolution.

5) Possibly as a result of the over-simplified grain boundary structure used in the model of Chapters 3 and 4, both the elastic and plastic model predict very high stress values at load-bearing contact points, when applied to quartz. These stresses can be of an order that is similar to or even greater than the stresses at which quartz single crystals fracture in indentation experiments. Grain boundary models of the type presented in this thesis would thus further benefit if the effect of grain boundary microfracturing, leading to the creation and subsequent surface energy driven dissolution of ultrafines and unstable surfaces, were included. This might be possible using some kind of microscale averaging approach (c.f. Lehner, 1990) or perhaps a cellular automaton modelling method.
6) As already implied under point 2 above, the grain boundary healing model presented in Chapter 3 might be further improved by including the effect of grain boundary microplasticity. Plastic deformation of the islands in the grain boundary, by storing additional Helmholtz free energy, will lead to a larger driving force for island dissolution, and thus for maintaining a dynamically wetted grain boundary and active pressure solution. A suggestion on how to include the effect of grain boundary microplasticity in the grain boundary healing model of Chapter 3 is given in Chapter 4. In essence, this could be done by including dislocation-stored energy in the description of the driving force for pressure solution (by including the second term on the far right side of equation (4.18) in equation 3.31).
7) The main problem encountered during our silica contact impedance experiments reported in Chapter 5 was the temperature-gradient-driven convection of fluid in the cell, and associated mass transport processes. Several attempts to limit convection, including inverting the cell (placing it upside-down), limiting the amount of fluid in the cell by adding a spacer, blocking convection using a platinum skirt and preventing dissolution/precipitation by painting the silica glass tube with platinum paint, had only limited success. This problem has to be solved if the method is to be applied usefully in the future. One possible solution might be to use a shorter tube, with a strongly reduced temperature gradient achieved by multistage furnace design. This might require a more temperature resistant seal between the silicate tube and the alumina insulator (i.e. replacing the room temperature vulcanizing silicone rubber seal). The second problem encountered with the set-up was cracking of the tube tip near the contact, possibly caused by variations in the contact load during test initiation. Using a less stiff spring and lower contact load might solve this problem. Another solution for limiting cracking might be to create a stable contact before insertion into the pressure vessel.
8) Our quartz compaction experiments indicate that pressure solution is the dominant strain accumulating deformation mechanism in wet, fine-grained quartz at temperatures between 300 and 600°C and effective pressures of up to at least 100MPa. However, some degree of microcracking, notably at grain contacts, could not be excluded and EBSD analysis showed that at 500°C limited crystal plastic deformation phenomena also occurred. A closer investigation of the influence of

these other mechanisms on creep rate would be useful, especially the possible role of grain boundary microcracking and microgranulation. To the best possible description of the data, and thus the best estimates of parameters such as the activation energy or the stress sensitivity, multidimensional regression analysis and Bayesian treatment of uncertainties is needed, following the approach suggested by Fitzenz et al. (in press), for example. More microstructural work is also needed on natural rocks compacted and deformed under upper crustal conditions to clarify the interaction between pressure solution, subcritical cracking, and grain boundary microcracking. Lastly, various ionic species commonly present in natural pore fluids are known to influence quartz dissolution and/or precipitation rates. Such effects might drastically influence pressure solution and subcritical cracking rates in nature. A systematic investigation of the effect of fluid composition on pressure solution rates and subcritical cracking is therefore needed to assess and improve the quality of existing rate models. Such work might also help distinguish better between rate-controlling processes of pressure solution or crack growth, as the effects of impurity ions on free surface reactions are to some extent known. Finally, recalling the inference from our halite contact experiments that polymineralic rocks may often deform faster by pressure solution than monomineralic rocks, an experimental study of this effect in for instance granular quartz-feldspar mixtures might yield interesting results relevant to natural systems.

As discussed earlier in this thesis, recent experimental research on single, pressure dissolving contacts has provided fascinating insights into the micro- and nanoscale mechanisms that operate in pressure dissolving grain boundaries. More systematic study of such contacts, on a wider range of materials, crystal planes and under a wider range of conditions would lead to a much better description and understanding of the structures of grain boundaries. Especially the mean fluid film thickness and the area fraction of grain boundary taken up by solid-solid contacts seem to be important variables, and direct, in-situ measurements of these variables will be vital for future modelling exercises on processes operative in grain boundaries undergoing pressure solution. Another important step will be the study of quartz (and other minerals) aggregates with grain sizes similar to or smaller than the finest grain sizes investigated here at stresses low enough to avoid grain scale cracking, so that pressure solution is truly isolated.

Chapter 7

References

Alcantar, N., J. Israelachvili, and J. Boles (2003), Forces and ionic transport between mica surfaces: Implications for pressure solution, *Geochim. Cosmochim. Acta 67*, 1289-1304.

Angevine, C.L., D.L. Turcotte, and M.D. Furnish (1982), Pressure solution lithification as a mechanism for the stick-slip behavior of faults, *Tectonics 1*(2), 151-160.

Anzalone, A., J. Boles, G. Greene, K. Young, J. Israelachvili, and N. Alcantar (2006), Confined fluids and their role in pressure solution, *Chem. Geol. 230*, 220-231.

Arsic, J., D.M. Kaminski, N. Radenovic, P. Poodt, and W.S. Graswinckel (2004), Thickness-dependent ordering of water layers at the NaCl(100) surface, *J. Chemical Phys. 120*(20), 9720-9724.

Asaro, R.J. and W.A. Tiller (1972), Interface morphology development during stress corrosion cracking: Part I. Via surface diffusion, *Meta. Mater. Trans. B3*(7), 1789-1796.

Atkins, P., and J. de Paula (2002), *Atkins' Physical chemistry, 7th edn*, Oxford University Press, New York, p 1104.

Atkinson, B.K. (1984), Subcritical crack-growth in geological-materials, *J. Geophys. Res. 89*(B6), 4077-4114.

Bass, J.D. (1995), Elasticity of minerals, glasses and melts, in: T.J. Ahrens (ed.), *Mineral physics and crystallography: A handbook of physical constants*, American Geophysical Union, Washington, pp 45-63.

Barsoukov, E., and J.R. Macdonald (eds.) (2005), *Impedance spectroscopy theory, experiment, and applications, Second edition*, John Wiley & Sons, Hoboken, New Jersey, p 595.

Becker, A. (1995), Quartz pressure solution: Influence of crystallographic orientation, *J. Struct. Geol. 17*(10), 1395-1405.

Bisschop, J. and D.K. Dysthe (2006), Instabilities and coarsening of stressed crystal surfaces in aqueous solution, *Phys. Rev. Lett. 96*, 146103 - 1 - 146103 - 4.

Blacic, J.D., and J.M. Christie (1984), Plasticity and hydrolitic weakening of quartz single crystals, *J. Geophys. Res. 89*(B6), 4223-4239.

Bos, B., C.J. Peach, and C.J. Spiers (2000), Slip behavior of simulated gouge-bearing faults under conditions favoring pressure solution, *J. Geophys. Res. 105*(B7), 16669-16718.

Bos, B., and C.J. Spiers (2000), Effects of phyllosilicates on fluid-assisted healing of gouge-bearing faults, *Earth Planet. Sci. Lett. 184*, 199-210.

Bos, B., and C.J. Spiers (2002a), Frictional-viscous flow of phyllosilicate-bearing fault rock: Microphysical model and implications for crustal strength profiles, *J. Geophys. Res. 107*(B2), doi: 10.1029/2001JB000301.

Bos, B., and C.J. Spiers (2002b), Fluid-assisted healing processes in gouge-bearing faults: Insights from experiments on a rock analogue system, *Pure Appl. Geophys. 159*, 2537-2566.

Brzesowsky, R.H. (1995), Micromechanics of sand grain failure and sand compaction, *Ph. D. thesis*, Utrecht University, Utrecht.

Chester, J.S., S.C. Lenz, F.M. Chester, and R.A. Lang (2004), Mechanisms of compaction of quartz sand at diagenetic conditions. *Earth Planet. Sci. Lett. 220*, 435-451.

Chester, F.M., J.S. Chester, A.K. Kronenberg and A. Hajash (2007), Subcritical creep compaction of quartz sand at diagenetic conditions: Effects of water and grain size, *J.*

References

Geophys. Res. 112, B06203, doi:10.1029/2006JB004317.

Cox, S.F., and M.S. Paterson (1991), Experimental dissolution-precipitation creep in quartz aggregates at high temperatures, *Geophys. Res. Lett. 18*, 1401-1404.

Čyžienė, J., N. Molenaar, and S. Šliaupa (2006), Clay-induced pressure solution as a Si source for quartz cement in sandstones of the Cambrian Deimena Group, *Geologija 53*, 8-21.

Davidge R.W., and P.L. Pratt (1964), Plastic deformation and work-hardening in NaCl, *Phys. Stat. Sol. 6*, 759-776.

De Boer, R.B., P.J.C. Nagtegaal, and E.M Duyvis (1977), Pressure solution experiments on quartz sand, *Geochim. Cosmochim. Acta 41*, 257-264.

De Bresser, J.H.P. (1996) Steady state dislocation densities in experimentally deformed calcite materials: Single crystals versus polycrystals, *J. Geophys. Res. 101*(B10), 22189-22201.

De Bresser, J.H.P. and C.J. Spiers (1997), Strength characteristics of the r, f, and c slip systems in calcite, *Tectonophysics 272,* 1-23.

De Meer, S. and C.J. Spiers (1995), Creep of wet gypsum aggregates under hydrostatic loading conditions, *Tectonophysics 245*, 171-183.

De Meer, S., C.J. Spiers, and C.J. Peach (1997), Pressure solution creep in gypsum: Evidence for precipitation reaction control, *Phys. Chem. Earth 22*(1-2), 33-37.

De Meer, S. and C.J. Spiers (1999a), On mechanisms and kinetics of creep by intergranular pressure solution, in: B. Jamtveit and P. Meakin (eds.) *Growth, dissolution and pattern formation in geosystems*, Kluwer Academic Publishers, Dordrecht, pp 345-366.

De Meer, S. and C.J. Spiers (1999b), Influence of pore-fluid salinity on pressure solution creep in gypsum, *Tectonophysics 308*, 311-330.

De Meer, S., C.J. Spiers, and C.J. Peach (2000), Kinetics of precipitation of gypsum and implications for pressure-solution creep, *J. Geol. Soc. Lond. 157*, 269-281.

De Meer, S., C.J. Spiers, C.J. Peach, and T. Watanabe (2002), Diffusive properties of fluid-filled grain boundaries measured electrically during active pressure solution, *Earth Planet. Sci. Lett. 200*, 147-157.

De Meer, S., C.J. Spiers, and S. Nakashima (2005), Structure and diffusive properties of fluid-filled grain boundaries: An in-situ study using infrared (micro)spectroscopy, *Earth Planet. Sci. Lett. 232*, 403-414.

Den Brok, B. and C.J. Spiers (1991), Experimental evidence for water weakening of quartzite by microcracking plus solution-precipitation creep, *J. Geol. Soc. Lond. 148*, 541-548.

Den Brok, B. (1998), Effect of microcracking on pressure-solution strain rate: the Gratz grain-boundary model, *Geology 26*, 915-918.

Den Brok, B., J. Morel, and M. Sahid (2002), In situ experimental study of roughness development at a stressed solid/fluid interface, in: S. de Meer, M.R. Drury, J.H.P. de Bresser, and G.M. Pennock (eds.) *Deformation mechanisms, rheology and tectonics: Current status and future perspectives*. Geological Society Special Publications 200, London, pp 73-83.

Den Brok, B. and J. Morel (2001), The effect of elastic strain on the microstructure of free surfaces of stressed minerals in contact with an aqueous solution, *Geophys. Res. Lett. 28*(4), 603-606.

Dewers, T.A. and P. Ortoleva (1990), A coupled reaction/transport/mechanical model for

References

intergranular pressure solution, stylolites, and differential compaction and cementation in clean sandstones, *Geochim. Cosmochim. Acta 54*, 1609-1625.

Dewers, T.A., and A. Hajash (1995), Rate laws for water-assisted compaction and stress-induced water-rock interaction in sandstones, *J. Geophys. Res. 100*(B7), 13093-13112.

Dickinson, W.W. and K.L. Milliken (1995), The diagenetic role of brittle deformation in compaction and pressure solution, Etjo sandstone, Namibia, *J. Geol. 103*, 339-347.

Dove, P.M., and D.A. Crerar (1990), Kinetics of quartz dissolution in electrolyte solutions using a hydrothermal mixed flow reactor, *Geochim. Cosmochim. Acta 54*, 955-969.

Dresen, G., J. Duyster, B. Stöckhert, R. Wirth, and G. Zulauf (1997), Quartz dislocation microstructure between 7000 and 9100 m depth from the Continental Deep Drilling Program KTB, *J. Geophys. Res. 102*(B8), 18443-18452.

Durney, D.W. (1976), Pressure-solution and crystallization deformation, *Phil. Trans. R. Soc. Lond. A 283*, 229-240.

Dysthe, D.K., F. Renard, F. Porcheron, and B. Rousseau (2002a), Fluid in mineral interfaces – Molecular simulations of structure and diffusion, *Geophys. Res. Lett. 29*,7,10.1029/2001GL013208.

Dysthe, D.K., Y. Podladchikov, F. Renard, J. Feder, and B. Jamtveit (2002b), Universal scaling in transient creep, *Phys. Rev. Lett. 89*, 24, 10.1103/PhysRevLett89.246102.

Dysthe, D.K., F. Renard, J. Feder, B. Jamtveit, P. Meakin, and T. Jøssang (2003), High-resolution measurements of pressure solution creep, *Phys. Rev. E Stat. Nonlin. Soft Matter Phys. 68*, doi: PhysRevE.68.011603.

Dysthe, D.K., R.A. Wogelius, C.C. Tang, and A.A. Nield (2006), Evolution of mineral-fluid interfaces studied at pressure with synchrotron X-ray techniques, *Chem. Geol. 230*, 232-241.

Elias, B.P. and A. Hajash, Jr. (1992), Changes in quartz solubility and porosity due to effective stress: An experimental investigation of pressure solution, *Geology 20*, 451-454.

Elliott, D. (1973), Diffusion flow laws in metamorphic rocks, *Geol. Soc. Am. Bull. 84*, 2645-2664.

Evans, A.G., and P.L. Pratt (1970), Work hardening in ionic crystals, *Philos. Mag. 21*, 951-970.

Fei, Y. (1995), Thermal expansion, in: T.J. Ahrens (ed.), *Mineral physics and crystallography: A handbook of physical constants*, American Geophysical Union, Washington, pp 29-44.

Fitzenz, D.D., A. Jalobeanu, S.H. Hickman, and N. Sleep (in press), Integrating laboratory compaction data with numerical fault models: a bayesian framework, Bayesian inference and maximum entropy methods, in: *Science and engineering: 25th International Workshop on Bayesian Inference and Maximum Entropy Methods in Science and Engineering*, August 2005, San Jose, California, American Institure of Physics, Melville, N.Y..

Gal, D., A. Nur, and E. Aharonov (1998), Stability analysis of a pressure solution surface, *Geophys. Res. Lett. 25*(8), 1237-1240.

Ghoussoub, J., and Y.M. Leroy (2001), Solid-fluid phase transformation within grain boundaries during compaction by pressure solution, *J. Mech. Phys. Solids 49*, 2385-2430.

Gratier, J.-P., and R. Guiguet (1986), Experimental pressure solution-deposition on quartz grains: The crucial effect of the nature of the fluid, *J. Struct. Geol. 8*, 845-856.

Gratier, J.-P., F. Renard, and P. Labaume (1999), How pressure solution creep and fracturing

processes interact in the upper crust to make it behave in both a brittle and viscous manner, *J. Struct. Geol. 21*, 1189-1197.

Gratier, J.-P., L. Muquet, R. Hassani, and F. Renard (2005), Experimental microstylolites in quartz and modeled application to natural stylolitic structures, *J. Struct. Geol. 27*, 89-100.

Gratier, J.-P., R. Guiguet, F. Renard, and L. Jenatton (2006), Experimental pressure solution creep of quartz by indenter technique, AGU Fall Meeting 2006, San Francisco.

Gratz, A.J. (1991), Solution-transfer compaction of quartzites: Progress toward a rate law, *Geology 19*, 901-904.

Green, H.W. (1984) "Pressure solution" creep: Some causes and mechanisms. *J. Geophys. Res. 89*, 4313-4318

Gundersen, E., F. Renard, D.K. Dysthe, K. Bjørlykke, and B. Jamtveit (2002), Coupling between pressure solution creep and diffusive mass transport in porous rocks, *J. Geophys. Res. 107*(B11), doi: 10.1029/2001JB000287.

Gunnarsson, I., and S. Anórsson (2000), Amorphous silica solubility and the thermodynamic properties of H_4SiO_4 in the range of 0° to 350°C at P_{sat}. *Geochim Cosmochim Acta 64*, 2295-2307.

Hartley, N.E.W., and T.R. Wilshaw (1973), Deformation and fracture of synthetic α-quartz, *J. Mater. Sci. 8*, 265-278.

Hartman, P., W.G. Perdok (1955), On the relation between structure and morphology of crystals I, *Acta Crystallogr. 8*, 49-52.

He, W., A. Hajash, and D. Sparks (2003), Creep compaction of quartz aggregates: Effects of pore-fluid flow - A combined experimental and theoretical study, *Am. J. Sci. 303*, 73-93.

He, W., A. Hajash, and D. Sparks (2007), Evolution of fluid chemistry in quartz compaction systems: Experimental investigations and numerical modeling, *Geochim. Cosmochim. Acta 71*, 4846-4855.

Heald, M.T. (1959), Significance of stylolites in permeable sandstones, *J. Sediment. Petrol. 29*, 251-253.

Heidug, W.K. (1991), A thermodynamic analysis of the conditions of equilibrium at nonhydrostatically stressed and curved solid-fluid interfaces, *J. Geophys. Res. 96*(B13), 21,909-21,921.

Hickman, S.H., and B. Evans (1991), Experimental pressure solution in halite: The effect of grain/interphase boundary structure. *J. Geol. Soc. London, 148*, 549-560.

Hickman, S.H., and B. Evans (1992), Growth of grain contacts in halite by solution-transfer: Implications for diagenesis, lithification, and strength recovery, in: B. Evans and T.F. Wong (eds.), *Fault mechanics and transport properties of rocks*, Academic Press, San Diego, pp 253-280.

Hickman, S.H., and B. Evans (1995), Kinetics of pressure solution at halite silica interfaces and intergranular clay films, *J. Geophys. Res. 100*(B7), 13113-13132.

Hickman, S.H., R.H. Sibson, R.L. Bruhn (1995), Introduction to special section: Mechanical involvement of fluids in faulting. *J. Geophys. Res. 100*(B7),12831-12840.

Hickman, S.H., and N.M. Beeler (1997), Direct measurements of diffusive contact growth in quartz at hydrothermal conditions, with implications for interseismic strength recovery. AGU 1997 Fall Meeting, San Francisco.

Hiemstra, T., and W.H. Van Riemsdijk (1990), Multiple Activated Complex Dissolution of

References

metal (Hydr)oxides: A thermodynamic approach applied to quartz, *J. Colloid. Interf. Sci. 136*, 132-150.

Hiraga, T., O. Nishikawa, T. Nagase, and M. Akizuki (2001), Morphology of intergranular pores and wetting angles in pelitic schists studied by transmission electron microscopy, *Contrib. Mineral. Petrol. 141*, 613-622.

Hiraga, T., O. Nishikawa, T. Nagase, M. Akizuki, and D.L. Kohlstedt (2002), Interfacial energies for quartz and albite in pelitic schist, *Contrib. Mineral. Petrol. 143,* 664-672.

Hirsch, P.B. (1964), A theory of linear strain hardening in crystals, *Discuss. Faraday Soc. 38*, 111-122.

Hirth, G., C. Teyssier, and W.J. Dunlap (2001), An evaluation of quartzite flow laws based on comparisons between experimentally and naturally deformed rocks, *Int. J. Earth Sci. 90*: 77-87.

Holness, M.B. (1992), Equilibrium dihedral angles in the system quartz-CO_2-H_2O-NaCl at 800°C and 1-15kbar: The effects of pressure and fluid composition on the permeability of quartzites, *Earth. Planet. Sci. Lett. 114,* 171-184.

Holness, M.B. (1993), Temperature and pressure dependence of quartz-aqueous fluid dihedral angles: the control of adsorbed H_2O on the permeability of quartzites, *Earth. Planet. Sci. Lett. 117,* 363-377.

Horn R.G., D.T. Smith, and W. Haller (1989), Surface forces and viscosity of water measured between silica sheets, *Chem. Phys. Lett. 162*(4-5), 404-408.

Houseknecht, D.W. (1988), Intergranular pressure solution in four quartzose sandstones, *J. Sediment. Petrol. 58*(2), 228-246.

Humphreys, F.J., and M. Hatherly (1996), *Recrystallization and related annealling phenomena*, Elsevier Science Ltd, Oxford, UK.

International Association for the Properties of Steam (1980), Release on the ion product of water substance May 1980, available from www.iapws.org

Israelachvili, J. (1986), Measurement of the viscosity of liquids in very thin films, *J. Colloid Interf. Sci.* 110(1), 263-271.

Jin Z.M., H.W. Green, and Y. Zhou (1994), Melt topology in partially molten mantle peridotite during ductile deformation, *Nature 372*, 164-167.

Jordan, G., T.H.K. Lohkämper, M. Schellewald, and W.W. Schmahl (2005), Investigation of loaded halite-SiO_2 interfaces undergoing dissolution-precipitation processes, *Eur. J. Mineral. 17*, 399-409.

Karner, S.L., C. Marone, and B. Evans (1997), Laboratory study of fault healing and lithification in simulated fault gouge under hydrothermal conditions. *Tectonophysics 277*, 41-55.

Karner, S.L., F.M. Chester, A.K. Kronenberg, and J.S. Chester (2003), Subcritical compaction and yielding of granular quartz sand, *Tectonophysics 377*, 357-381.

Karner, S.L., J.S. Chester, F.M. Chester, A.K. Kronenberg, A. Hajash (2005), Laboratory deformation of granular quartz sand: Implications for the burial of clastic rocks, *Am. Assoc. Pet. Geol. Bul. 89*(5), 603-625.

Karcz, Z., E. Aharonov, D. Ertas, R. Polizotti, and C.H. Scholz (2006), Stability of a sodium chloride indenter contact undergoing pressure solution, *Geology 34*, 61-63.

Kawabata, K., H. Tanaka, G. Kimura (2007), Mass transfer and pressure solution in deformed

References

shale of accretionary complex: Examples from the Shimanto Belt, southwestern Japan, *J. Struct. Geol. 29*, 697-711.

Koehn, D., D.K. Dysthe, and B. Jamtveit (2004), Transient dissolution patterns on stressed crystal surfaces, *Geochim. Cosmochim. Acta 68*(16), 3317-3325.

Koehn, D., A. Malthe-Sorenssen, C.W. Passchier (2006), The structure of reactive grain-boundaries under stress containing confined fluids, *Chem. Geol. 230*, 207-219.

Kohlstedt, D.L., and M.S. Weathers (1980), Deformation-induced microstructures, paleopiezometers, and differential stresses in deeply eroded fault zones, *J. Geophys. Res. 85*(B11), 6269-6285.

Lagoeiro, L. and F. Fueten (2008), Fluid-assisted grain boundary sliding in bedding-parallel quartz veins deformed under greenschist metamophic grade, *Tectonophysics 446*, 42-50.

Lehner, F.K. (1990), Thermodynamics of rock deformation by pressure solution, in: D.J. Barber and P.G. Meredith (eds.), *Deformation processes in minerals, ceramics and rocks*, Unwin Hyman, London, pp 296-333.

Lehner, F.K. (1995), A model for intergranular pressure solution in open systems, *Tectonophysics, 245*, 153-170.

Lloyd, G.E. (2000), Grain boundary contact effects during faulting of quartzite: An SEM/EBSD analysis, *J. Struct. Geol. 22*, 1675-1693.

Lockner, D.A. and B. Evans (1995), Densification of quartz powder and reduction of conductivity at 700ºC, *J. Geophys. Res. 100*(B7), 13081-13092.

Mair, K., J.F. Hazzard (2007), Nature of stress accommodation in sheared granular material: Insights from 3D numerical modeling, *Earth Planet. Sci. Lett. 259,* 469-485.

Manning, C.E. (1994), The solubility of quartz in H_2O in the lower crust and upper mantle, *Geochim. Cosmochim. Acta 58*, 4831-4839.

Martin, B., K. Röller, and B. Stöckhert (1999), Low-stress pressure solution experiments on halite single-crystals, *Tectonophysics 308*, 299-310.

Masuda, T., T. Hiraga, H. Ikei, H. Kanda, Y. Kugimiya, and M. Akizuki (2000), Plastic deformation of quartz at room temperature: A Vickers nano-indentation test, *Geophys. Res. Lett. 27*, 2773-2776.

Meike, A. (1990), Dislocation enhanced selective dissolution: An examination of mechanical aspects using deformation-mechanism maps, *J. Struct. Geol. 12*(5/6), 785-794.

Meyer, E.E., G.W. Greene, N.A. Alcantar, J.N. Israelachvili, and J.R. Boles (2006), Experimental investigation of the dissolution of quartz by a muscovite mica surface: Implications for pressure solution, *J. Geophys. Res. 111*, B08202, doi: 10.1029/2005JB004010.

Morash, K.R., R.D. Thornton, C.H. Saunders, and A.C. Bevilacqua (1994), Measurement of the resistivity of ultrapure water at elevated temperatures. *Ultrapure Water 11*, 9, 18-26.

Müller, P. and A. Saúl (2004), Elastic effects on surface physics, *Surf. Sci. Rep. 54*, 157-258.

Mullis, A.M. (1993), Determination of the rate-limiting mechanism for quartz pressure dissolution, *Geochimica et Cosmochimica Acta 57*, 1499-1503.

Nakashima, S. (1995), Diffusivity of ions in pore water as a quantitative basis for rock deformation rate estimates, *Tectonophysics 245*, 185-203.

Nakashima, S., S. de Meer, C.J. Spiers, V. Famin, and T. Hirono (2001), Physiochemical properties of water in grain boundaries - "Hard" water in the deep crust and the origin of

References

earthquake? -, *Proc. Intl. Symp on Slip & Flow Processes in and below the Seismogenic Region*, 181-188, Nov 5-8, 2001, Sendai, Japan.

Nakashima, S., S. De Meer, and C.J. Spiers (2004), Distribution of thin film water in grain boundaries of crustal rocks and implications for crustal strength, in: S. Nakashima, C.J. Spiers, L. Mercury, P.A. Fenter, and M.F. Hochella, Jr. (eds.), *Physicochemistry of Water in Geological and Biological Systems - Structures and Properties of Thin Aqueous Films*, Universal Academy Press, Tokyo, pp 159-178.

Niemeijer, A.R., C.J. Spiers, and B. Bos (2002), Compaction creep of quartz sand at 400-600 degrees C: Experimental evidence for dissolution-controlled pressure solution, *Earth Planet. Sci. Lett. 195*, 261-275.

Niemeijer, A.R. and C.J. Spiers (2002), Compaction creep of quartz-muscovite mixtures at 500ºC: Preliminary results on the influence of muscovite on pressure solution, in: S. de Meer, M.R. Drury, J.H.P. de Bresser, and G.M. Pennock (eds.), *Deformation mechanisms, rheology and tectonics: Current status and future perspectives*, Geological Society Special Publications 200, London, pp 61-71.

Niemeijer, A.R., and C.J. Spiers (2005), Influence of phyllosilicates on fault strength in the brittle-ductile transition: Insights from rock analogue experiments, in: D. Bruhn and L. Burlini (eds.), *High strain zones: Structure and physical properties*, Geological Society of London, London, pp 303-327.

Niemeijer, A.R. and C.J. Spiers (2006), Velocity dependence of strength and healing behaviour in simulated phyllosilicate-bearing fault gouge, *Tectonophysics 427*, 231-253.

Parks, G.A. (1984), Surface and interfacial free energies of quartz, *J. Geophys. Res. 89*(B6), 3997-4008.

Paterson, M.S. (1973), Nonhydrostatic thermodynamics and its geologic applications, *Rev. Geophys. Space phys. 11*(2), 355-389.

Paterson, M.S. (1995), A theory for granular flow accomodated by material transfer via an intergranular fluid, *Tectonophysics 245*, 135-151.

Porter, D.A., and K.E. Easterling (1992), *Phase transformations in metals and alloys*, Chapman and Hall, London.

Pratt, P.L. (1953), Similar glide processes in ionic and metallic crystals, *Acta Metallurgica 1*, 103-104.

Raj, R. (1982), Creep in polycrystalline aggregates by matter transport through a liquid phase, *J. Geophys. Res. 87*(B6), 4731-4739.

Ramm, M. (1992), Porosity-depth trends in reservoir sandstones: Theoretical models related to Jurassic sandstones offshore Norway, *Mar. Petroleum Geol. 9*, 553-567.

Renard, F., and P. Ortoleva (1997), Water films at grain-grain contacts: Debye-Hückel, osmotic model of stress, salinity, and mineralogy dependence, *Geochim. Cosmochim. Acta 61*, 1963-1970.

Renard, F., P. Ortoleva, and J.-P. Gratier (1997), Pressure solution in sandstones: Influence of clays and dependence on temperature and stress, *Tectonophysics 280*, 257-266.

Renard, F., A. Park, P. Ortoleva, and J.-P. Gratier (1999), An integrated model for transitional pressure solution in sandstones, *Tectonophysics 312*, 97-115.

Renard, F., J.-P. Gratier, and B. Jamtveit (2000), Kinetics of crack-sealing, intergranular pressure solution, and compaction around active faults, *J. Struct. Geol. 22*, 1395-1407.

References

Renton, J.J., M.T. Heald and C.B. Cecil (1969) Experimental investigation of pressure solution of quartz, *J. Sediment. Petrol. 39*, 1107-1117.

Revil, A. (2001), Pervasive pressure solution transfer in a quartz sand, *J. Geophys. Res. 106*(B5), 8665-8686.

Revil, A., P. Leroy, A. Ghorbani, N. Florsch, and A.R. Niemeijer (2006), Compaction of quartz sands by pressure solution using a Cole-Cole distribution of relaxation times, *J. Geophys. Res. 111*, B09205, doi: 10.1029/2005JB004151.

Rimstidt, J.D., H.L. Barnes (1980), The kinetics of silica-water reactions, *Geochim. Cosmochim Acta 44*, 1683-1699.

Rimstidt, J.D. (1997), Quartz solubility at low temperatures, *Geochim. Cosmochim. Acta 61*, 13, 2553-2558.

Robin, P.Y.F. (1978), Pressure solution at grain-to-grain contacts, *Geochim. Cosmochim. Acta 42*, 1383-1389.

Russ, J.C. (1986), *Practical Stereology*, Plenum Press, New York.

Rutter, E.H. (1976), The kinetics of rock deformation by pressure solution, *Philos. Trans. R. Soc. Lond. A 283*, 203-219.

Rutter, E.H., and D.H. Mainprice (1978), The effect of water on stress relaxation of faulted and unfaulted sandstone, *Pure Appl. Geophys. 116*, 634-654.

Rutter, E.H. (1983), Pressure solution in nature, theory and experiment, *J. Geol. Soc. London 140*, 725-740.

Rutter, E.H., and P.H. Wanten (2000), Experimental study of the compaction of phyllosilicate-bearing sand at elevated temperature and with controlled pore water pressure. *J. Sediment. Res. 70*, 107-116.

Rutter, E.H., and K.H. Brodie (2004), Experimental intracrystalline plastic flow in hot-pressed synthetic quartzite prepared from Brazilian quartz crystals, *J. Struct. Geol. 26*, 259-270.

Schenk, O., and J.L. Urai (2004), Microstructural evolution and grain boundary structure during static recrystallization in synthetic polycrystals of sodium chloride containing saturated brine, *Contrib. Mineral. Petrol. 146*, 671-682.

Schenk, O., J. Urai, and B. Evans (2005), The effect of water on recrystallization behavior and grain boundary morphology in calcite – observations of natural marble mylonites. *J. Struct. Geol. 27*, 1856-1872.

Schenk, O., J. Urai, and S. Piazolo (2006), Structure of grain boundaries in wet, synthetic polycrystalline, statically recrystallizing halite – evidence from cryo-SEM observations, *Geofluids 6*, 93-104.

Schutjens, P.M.T.M. (1991), Experimental compaction of quartz sand at low effective stress and temperature conditions, *J. Geol. Soc. London 148*, 527-539.

Schutjens, P.M.T.M., and C.J. Spiers (1999), Intergranular pressure solution in NaCl: Grain-to-grain contact experiments under the optical microscope, *Oil Gas Sci. Technol. 54*, 729-750.

Schwarz, S. and B. Stöckhert (1996), Pressure solution in siliciclastic HP-LT metamorphic rocks - Constraints on the state of stress in deep levels of accretionary complexes, *Tectonophysics 255*, 203-209.

Shimizu, I. (1995), Kinetics of pressure solution creep in quartz: Theoretical considerations, *Tectonophysics, 245,* 121-134.

References

Simmons, G., and H. Wang (1971), *Single crystal elastic constants and calculated aggregate properties: A handbook*, The M. I. T. Press, Cambridge (MA).

Sleep, N.H., and M.L. Blanpied (1992), Creep, compaction and the weak rheology of major faults, *Nature 359*, 687-692.

Sleep, N.H., and M.L. Blanpied (1994), Ductile Creep and Compaction: A Mechanism for Transiently Increasing Fluid Pressure in Mostly Sealed Fault Zones, *Pure Appl. Geophys. 143*, 9-40.

Sleep, N.H. (1995), Ductile creep, compaction, and rate and state dependent friction within major fault zones, *J. Geophys. Res. 100*(B7), 13065-13080.

Sorby, H.C. (1863), On the direct correlation of mechanical and chemical forces, *Proc. R. Soc. London 12*, 538-550.

Sorby, H.C. (1908), On the application of quantitative methods to the study of the structure and history of rocks, *Q. J. Geol. Soc. 64*(1-4), 171-233.

Spiers, C.J., and P.M.T.M. Schutjens (1990), Densification of crystalline aggregates by fluid-phase diffusional creep, in: D.J. Barber and P.G. Meredith (eds.), *Deformation processes in minerals, ceramics and rocks*, Unwin Hyman, London, pp 334-353.

Spiers, C.J., P.M.T.M. Schutjens, R.H. Brzesowsky, C.J. Peach, J.L. Liezenberg, and H.J. Zwart (1990), Experimental determination of constitutive parameters governing creep of rocksalt by pressure solution, in: R.J. Knipe, and E.H. Rutter (eds.), *Deformation mechanisms, rheology and tectonics*, Geological Society Special Publications 54, London, pp 215-227.

Spiers, C.J. and R.H. Brzesowsky (1993), Densification behaviour of wet granular salt: Theory versus experiment, in: H. Kakihana, H. R. Hardy Jr., T. Hoshi, and K. Toyokura (eds.), *Seventh Symposium on Salt*, Elsevier Science, Amsterdam, pp 83-92.

Spiers, C.J., S. De Meer, A.R. Niemeijer, and X. Zhang (2004), Kinetics of rock deformation by pressure solution and the role of thin aqueous films, in: S. Nakashima, C.J. Spiers, L. Mercury, P.A. Fenter and M.F. Hochella, Jr., *Physicochemistry of Water in Geological and Biological Systems - Structures and Properties of Thin Aqueous Films*, Universal Academy Press, Tokyo, pp 129-158.

Sprunt E.S. and A. Nur (1976), Reduction of porosity by pressure solution; experimental verification, *Geology 4*, 463-466.

Srolovitz, D.J. (1989), On the stability of surfaces of stressed solids, *Acta Metall. 37*(2), 612-625.

Tada R., and R. Siever (1986) Experimental knife-edge pressure solution of halite, *Geochim. Cosmochim. Acta 50*, 29-36.

Tada, R., R. Maliva, and R. Siever (1987), A new mechanism for pressure solution in porous quartzose sandstone, *Geochim. Cosmochim. Acta, 51*, 2295-2301.

Tada, R., and R. Siever (1989), Pressure solution during diagenesis, *Ann. Rev. Earth Planet. Sci. 17*, 89-118.

Takeuchi, S., and A.S. Argon (1976), Steady-state creep of single-phase crystalline matter at high temperature, *J. of Mater. Sci. 11*, 1542-1566.

Tenthorey, E. and S.F. Cox (2006), Cohesive strengthening of fault zones during the interseismic period: An experimental study, *J. Geophys. Res. 111*(B09202), 10.1029/2005JB004122.

Tester, J.W., W.G. Worley, B.A. Robinson, C.O. Grigsby, and J.L. Feerer (1994), Correlating

quartz dissolution kinetics in pure water from 25 to 625ºC, *Geochim. Cosmochim. Acta 58*(11), 2407-2420.

Underwood, E.E. (1970), *Quantitative Stereology*, Addison-Wesley Publishing Company, Reading, Massachusetts.

Vanýsek, P. (2006), Ionic conductivity and diffusion at infinite dilution, in: D.R. Lide (ed.) *CRC Handbook of chemistry and physics, Internet version 2007, 87th edn*. Taylor & Francis, Boca Raton, pp 76-78.

Vigil, G., Z. Xu, S. Steinberg, and J.N. Israelachvili (1994), Interactions of silica surfaces, *J. Colloid. Interface Sci.* 165, 367-385.

Visser, H.J.M. (1999), Mass transfer processes in crystalline aggregates containing a fluid phase, *Ph. D. thesis*, Utrecht University, Utrecht.

Volosov, A.G., I.L. Khodakovskiy, and B.N. Ryzhenko (1972), Equilibria in the system SiO_2-H_2O at elevated temperatures along the lower three-phase curve, *Geochem. Int. 9*, 362-377.

Wagner, W., and A. Pruß (2002), The IAPWS formulation 1995 for the thermodynamic properties of ordinary water substance for general and scientific use. *J. Phys. Chem. Ref. Data 31*, 387-535.

Wahab, A.A. (1998), Diagenetic history of Cambrian quartzarenites, Ras Dib–Zeit Bay area, Gulf of Suez, eastern desert, Egypt, *Sediment. Geol. 121*(1-2), 121-140.

Wang, J.H. (1951), Self-diffusion and structure of liquid water. II. Measurement of Self-diffusion of liquid water with O^{18} as tracer, *J. Am. Chem. Soc. 73*, 4181-4183.

Wanten, P.H., C.J. Spiers, and C.J. Peach (1996), Deformation of NaCl single crystals at 0.27Tm <_ T <_ 0.44 Tm, in: M. Goreychi, P. Bérest, H. Reginald Hardy, Jr., and M. Langer, (eds.), *The mechanical behavior of salt: Proceedings of the third conference*, *Trans. Tech. Publications. 20***,** 117-128.

Watanabe, T., and C.J. Peach (2002), Electrical impedance measurement of plastically deforming halite rocks at 125°C and 50 MPa, *J. Geophys. Res. 107*(B1), 2004, doi:10.1029/2001JB000204.

Weyl, P.K. (1959), Pressure solution and the force of crystallization - A phenomenological theory, *J. Geophys. Res. 64*, 2001-2025.

Wintsch, R.P., and J. Dunning (1985), The effect of dislocation density on the aqueous solubility of quartz and some geologic implications: A theoretical approach, *J. Geophys. Res. 90*(B5), 3649-3657.

Wintsch, R.P., and K. Yi (2002), Dissolution and replacement creep: A significant deformation mechanism in mid-crustal rocks, *J. Struct. Geol. 24*, 1179-1193.

Wright, T.O., and L.B. Platt (1982), Pressure dissolution and cleavage in the Martinsburg shale, *Am. J. Sci. 282*, 122-135.

Yasuhara, H., C. Marone, and D. Elsworth (2005), Fault zone restrengthening and frictional healing: The role of pressure solution, *J. Geophys. Res. 110*, B06310, doi:10.1029/2004JB003327.

Zhang, X., J. Salemans, C.J. Peach, and C.J. Spiers (2002), Compaction experiments on wet calcite powder at room temperature: Evidence for operation of intergranular pressure solution, in: S. de Meer, M.R. Drury, J.H.P. de Bresser, and G.M. Pennock (eds.), *Deformation mechanisms, rheology and tectonics: Current status and future perspectives*,

References

Geological Society Special Publications 200, London, pp 73-83.

Zhang, X. and C.J. Spiers (2005), Compaction of granular calcite by pressure solution at room temperature and effects of pore fluid chemistry, *Int. J. Rock Mech. & Mining Sci. 42*, 950–960.

Zubtsov, S., F. Renard, J.-P. Gratier, R. Guiguet, D.K. Dysthe, and V. Traskine (2004), Experimental pressure solution compaction of synthetic halite/calcite aggregates, *Tectonophysics 385*, 45-57.

References

Samenvatting in het nederlands

Het rheologisch gedrag (vloeigedrag) van gesteentes speelt een belangrijke rol bij vrijwel alle dynamische processen die plaatsvinden in de Aardkorst, zoals bijvoorbeeld de compactie van sedimentaire afzetting en beweging langs breuken. Water bevordert ductiele kruip en heeft daardoor een sterke invloed op dit vloeigedrag. Een belangrijk mechanisme voor kruip in de Aardkorts dat mogelijk wordt door de aanwezigheid van water is drukoplossing. Tijdens dit mechanisme lost materiaal op in natte korrelgrenzen onder hoge mechanische spanning. Vervolgens diffundeert dit opgeloste materiaal door de waterfase in die korrelgrens en slaat het materiaal neer op poriewanden of in korrelgrenzen onder minder hoge mechanische spanning. Deze processen volgen elkaar op wat betekent dat het proces dat het traagst verloopt de snelheid van de andere processen beperkt.

De structuur en andere fysieke eigenschappen van natte korrelgrenzen onder mechanische spanning zijn erg belangrijk in het bepalen van de snelheid waarmee oplossing in en diffusie door de vloeistof in de korrelgrens kunnen plaatsvinden. Er zijn dan ook verschillende modellen opgesteld voor de structuur van zulk een natte korrelgrens. In het eerste model wordt een natte korrelgrens voorgesteld met een dunne (~1nm=10^{-9}m) geadsorbeerde vloeistoffilm. Deze film wordt vastgehouden in het contact, ondanks de mechanische spanning die er op het contact staat, door oppervlakte-interacties. Het tweede model stelt ook zo'n dunne vloeistoffilm voor, maar in dit model vertonen de vaste korrels barsten en bubbels die snelle transportpaden voor opgelost materiaal creëren. In het derde model bestaat er in een natte korrelgrens een dynamisch netwerk van vloeistofkanalen met daartussen eilandcontacten die directe verbindingen vormen tussen de vaste korrels. De vloeistofkanalen laten snel diffusief transport door de korrelgrens toe, terwijl de eilanden de mechanische spanning dragen.

Ondanks de bestaande contraversie is er maar een beperkt aantal experimentele studies uitgevoerd naar de structuur van natte korrelgrenzen onder mechanische spanning. Recent werk gedaan op contacten tussen zoutkristallen en verscheidene andere materialen hebben aangetoond dat natte contacten op zoutkristallen een dynamische structuur bevatten, die vergelijkbaar is met de structuur beschreven in het eiland-kanaal model. Over contacten op andere materialen waarin drukoplossing belangrijk is, zoals kwarts, is er veel minder bekend. Dit komt voor een groot deel door de lage oplosbaarheid en trage oplossingssnelheden van kwarts. Om experimenten uit te kunnen voeren op een haalbare tijdsschaal worden ze daarom meestal gedaan op hoge temperatuur, onder hoge druk, en in zeer fijnkorrelig (<0.25mm) materiaal. Korrelgrensstructuren zijn dan niet of moeilijk te bestuderen.

In dit proefschrift bespreek ik experimenteel en theoretisch werk, gericht op het onderzoeken van de structuur gevormd in natte korrelgrenzen tijdens drukoplossing, en de invloed die deze structuur heeft op de snelheden van de voor drukoplossing belangrijke processen die plaatsvinden in de korrelgrens (oplossing en diffusie).

Allereerst heb ik gekeken naar de invloed van kristaloriëntatie op korrelgrens structuur. Dit heb ik gedaan door middel van het meten van de electrische weerstand van drukoplossingscontacten tussen een glazen lens en een haliet kristal (ook wel bekend als steenzout of keukenzout), daarbij tussen experimenten de oriëntatie van het kristal variërend. De gevormde contacten werden na de experimenten bestudeerd met de electronen microscoop. Dit liet duidelijk zien dat kristaloriëntatie een sterke invloed kan hebben op de gevormde

korrelgrensstructuren. Ook heb ik gekeken naar contacten tussen twee haliet kristallen en naar de invloed van de relatieve oriëntatie van die kristallen ten opzichte van elkaar. Deze contacten vertoonden een geheel ander gedrag en in plaats van drukoplossing vond er nekgroei plaats, de contacten verwijdden zich door oppervlakte-energie gedreven afzetting. Nekgroei was sneller in een contact tussen kristallen met een vergelijkbare oriëntatie. Door vergelijking van de resultaten van de zout-glas contact experimenten met de resultaten van zout-zout contact-experimenten concludeer ik dat contacten tussen verschillende materialen duidelijk ander gedrag kunnen vertonen dan contacten tussen vergelijkbare materialen. Dit werk wordt beschreven in Hoofdstuk 2.

Hoewel de invloed van de natte korrelgrensstructuur op diffusiesnelheden door de korrelgrens veel besproken wordt, gaat er weinig aandacht uit naar de invloed van de korrelgrensstructuur op de snelheid van oplossingsprocessen in de korrelgrens. De snelheid van drukoplossing in kwarts wordt echter gecontroleerd door oplossing en niet diffusie. Het volgende onderwerp waar ik naar gekeken heb is dan ook de invloed van korrelgrensstructuur op oplossingssnelheden in een korrelgrens. Hiervoor heb ik een model gemaakt voor een materiaal dat alleen elastisch deformeert. Dit model is gebaseerd op sterk gesimplificeerde aannames voor de korrelgrensstructuur. Wanneer toegepast op kwarts, laat het zien dat de korrelgrensstructuur waarschijnlijk maar een beperkte invloed heeft op oplossingssnelheden in de korrelgrens. Het model laat ook zien dat in een korrelgrens met een eiland-kanaal structuur, de contactpunten maar een klein deel van het oppervlak beslaan en dus een zeer hoge last dragen.

Of een ruwe, natte korrelgrens überhaupt voor langere tijd kan bestaan tijdens drukoplossing wordt nogal eens betwijfeld. Oppervlakte-energie effecten kunnen door oplossing en precipitatie leiden tot het egaliseren van zo'n ruw contact, waarbij de vloeistof uit het contact geduwd wordt (korrelgrensgenezing). Daarom presenteer ik ook een model dat demonstreert hoe, in een natte korrelgrens onder mechanische spanning, de aandrijfkrachten voor oplossing en korrelgrensgenezing competeren zodat ofwel oplossing of genezing plaatsvindt. Deze beide modellen worden beschreven in Hoofdstuk 3.

Hoewel de invloed van de korrelgrensstructuur op de oplossnelheid in een korrelgrens beperkt is, kunnen ook andere processen die plaatsvinden in een korrelgrens onder mechanische spanning oplossnelheden beïnvloeden. Een voorbeeld daarvan is de plastische deformatie van de contactpunten in de korrelgrens, die immers onder hoge mechanische spanning staan. Tijdens drukoplossing zorgt zulke plastische deformatie voor een verlies van energie die anders beschikbaar zou zijn om drukoplossing aan te drijven. De volgende stap in mijn onderzoek was dan ook het uitbreiden van het model voor korrelgrensoplossing in een elastisch materiaal naar materialen die ook plastisch vervormen. Toegepast op kwarts laat dit model zien dat microplastische vervorming binnen een korrelgrens mogelijk tot een vertraging van de oplossnelheden in die korrelgrens van enkele ordes van grootte kan leiden. Dit is vergelijkbaar met het verschil tussen drukoplossingssnelheden gemeten in experimenten en drukoplossingssnelheden voorspeld met modellen die plastische vervorming in de korrelgrenzen negeren. Dit werk wordt beschreven in Hoofdstuk 4.

Het volgende deel van mijn onderzoek richtte zich op het direct onderzoeken van de structuur en diffusieve eigenschappen van natte korrelgrenzen tijdens actieve drukoplossing in kwartsglas. Dit heb ik gedaan door het electrische gedrag van contacten tussen een

kwartsglazen buis en een kwartsglazen aambeeld of een aambeeld van een kwartskristal te meten over een wijd spectrum van frequenties, onder hydrothermale condities. Uit deze metingen kon vervolgens een schatting gemaakt worden van de diffusiviteit door de korrelgrens en van de gemiddelde dikte en de vloeistoffilm. Helaas werden de metingen beïnvloed door barsten, en oneven oplossing in en rond de contacten. Na de experimenten werden de gevormde contacten onderzocht in de electronenmicroscoop. De gedane observaties toonden dat korrelgrenzen op kwartsglas en op kwarts tijdens drukoplossing onder hydrothermale condities een ruwe structuur hebben. Dit werk wordt beschreven in Hoofdstuk 5.

De samenhang tussen korrelgrensstructuur, processen die plaatsvinden in de korrelgrens, drukoplossing en andere deformatiemechanismen heb ik uiteindelijk bestudeerd in kwarts. Dit heb ik gedaan door middel van compactie-experimenten met alzijdige druk op monsters bestaande uit losse kwartskorrels met een initiële korrelgrootte van 3-129μm, bij temperaturen van 300-600°C, een porievloeistofdruk van 200MPa en effectieve drukken van 25-100MPa. Uit analyse van de tijdens de experimenten gevormde microstructuren bleek dat drukoplossing het voornaamtste compactie-mechanisme was bij onze experimentele condities. Enige invloed van korrelbreuk was echter niet uit te sluiten. Oplossing was waarschijnlijk het traagste en dus snelheidsbeperkende proces. Door middel van Electron Backscatter Diffraction (EBSD) analyses werd enig bewijs gevonden voor plastische deformatie rond korrelcontacten onder hoge mechanische spanning. Bestudering van de gevormde contacten tussen kristallijne kwarts schijfjes die voor sommige experiementen waren toegevoegd aan het monster en losse korrels laat zien dat kwarts-korrelgrenzen tijdens drukoplossing een ruwe structuur ontwikkelen. Kleine breukjes gevonden in en rond de korrel-schijf-contacten tonen aan dat breukvorming op zeer fijne schaal waarschijnlijk een belangrijk mechanisme is voor het creëren en behouden van deze ruwe structuur. Extrapolatie van de gevonden compactiesnelheden naar natuurlijke condities, bijvoorbeeld naar de diagenese en compactie van zandstenen, laat zien dat drukoplossing een belangrijk mechanisme is voor compactie en deformatie vanaf een diepte van ~2.5-3km. Een geëxtrapoleerde voorspelling van porositeit versus diepte geeft bovendien een goede overeenkomst met in natuurlijke zandstenen gemeten diepte-afhankelijkheden van de porositeit. Dit werk wordt beschreven in Hoofdstuk 6.

In Hoofdstuk 7 vat ik nogmaals de belangrijkste conclusies van dit proefschrift samen. Verder geef ik ook enkele aanbevelingen voor toekomstig onderzoek naar de eigenschappen van natte korrelgrenzen onder mechanische spanning en tijdens drukoplossing.

Samenvatting

Dankwoord

Nu, wanneer de opmaak van mijn proefschrift bijna klaar is om naar de drukker gestuurd te worden, is het moment aangebroken om terug te denken aan de afgelopen vier en een half jaar en om de mensen die mij in die tijd geholpen en gesteund hebben te bedanken. Mijn tijd als promovendus was een fantastische periode in mijn leven. Er waren momenten dat ik het zwaar had, maar met hulp van de mensen om mij heen heb ik mij er doorheen kunnen vechten. Wat je niet doodt, maakt je sterker.

First of all, I would like to thank my promotor, Chris Spiers, and my co-promotor, Colin Peach. Chris, we have worked together on various projects now for more than five and a half years. In that time, we have discussed many things. I have always enjoyed our discussions, and rarely came away from one not having learned or realised something new. I'd like to thank you for inspiring and guiding me, and for helping me do this project. Colin, your extensive knowledge and explanations of electrical resistivity and impedance measurements at times made me wonder whether you are really working in the right field. I could not have performed my research without your help at making and interpreting the electrical resistivity and impedance spectroscopy measurements. The same goes for all your help with any computer-related issues I had in the lab.

Geen van de experimenten die ik heb uitgevoerd tijdens mijn onderzoek zou mogelijk zijn geweest zonder de hulp van de technici werkzaam bij het HPT-laboratorium. Met Eimert de Graaff werkte ik samen bij het opzetten van de contactexperimenten beschreven in de hoofdstukken 2 en 5. Ondanks de moeilijkheden met de kwartscel hebben we hier altijd in een optimistische en goede sfeer aan kunnen werken. Gert Kastelein was onmisbaar bij het opzetten van al mijn hoge-druk-experimenten. Dankzij zijn snelle hulp bij het voorbereiden van materialen en het oplossen van problemen kon ik blijven doorwerken. Ook Tony van der Gon wil ik van harte bedanken voor al zijn technische hulp. Met Peter van Krieken heb ik vele uurtjes achter de SEM gezeten. Bovendien was hij mijn aanspreekpunt voor het maken en laten uitvoeren van praktisch alle benodigde analyses. Bij hem kon ik met allerlei kleine en grotere problemen altijd terecht. Met Hans de Bresser heb ik weinig contact gehad, maar ik kon toch bij hem aankloppen met problemen bij het uitvoeren van mijn microstructurele analyses. Magda, tenslotte, heeft mij door de bureaucratische rompslomp die een promotie met zich meebrengt heen geloodst.

I'd also like to thank my co-authors on chapters 3 and 6. Especially Gill Pennock, who did the EBSD analyses with me. Her rapid responses during my last weeks of writing were a great help in improving chapter 6 from my original draft, and I think we managed to get some great results from the EBSD analyses after all. Rian Visser, mijn co-autheur voor hoofdstuk 3 wil ik graag bedanken voor haar hulp met het model voor grain boundary healing. Als laatste wil ik al mijn collega's bij het HPT-lab graag bedanken voor de gezellige werksfeer. Ik heb vooral veel genoten van de koffiepauzes en de praatjes met de andere aio's en studenten. Esther, Sander, Emilia, Siska, André, Arthur en iedereen die ik vergeet, bedankt!

Misschien wel even belangrijk als de hulp op werk, is de steun aan het thuisfront. De afgelopen jaren heb ik mij altijd gesteund geweten door mijn familie. Ik wil mijn ouders, Henk en Elly van Noort, dan ook hartelijk bedanken hiervoor en voor het mij (indirect)

Dankwoord

gegeven hebben van deze kans. Ook mijn zusje, Francisca, haar man, Gerard de Kwant, en mijn schoonouders, Hans en Loes Dankers wil ik van harte bedanken voor alles.

Ik kon de afgelopen jaren op een grote groep vrienden vertrouwen om mij van mijn werk af te leiden. Met de andere leden van de Orde der Noorderwind, vooral Youval, Rouke, Gregal, Jogchem, Araceli, Goulven, Bram, Shanna, Thierry, Maarten en Arjan, heb ik menig weekend gespendeerd op middeleeuwse en fantastische festivals. Met jullie deel ik mijn liefde voor de middeleeuwse krijgskunsten en voor het showvechten. Ook de mensen van Zwaard en Steen wil ik bedanken. Niets ontstresst zo goed als een shinai in je handen en een tegenstander tegenover je. Mijn excuses waar nodig. I'd like to thank Eric Reiter for his expert help in optimally converting my RGB colour images into CMYK images. Tenslotte wil ik nog al mijn vrienden bedanken die ik nu nog niet genoemd heb; Bart, Larissa, Rolf en Ineke, Peter-Bas en Marieke en nog velen anderen: Bedankt!

Tijdens mijn tijd als promovendus heb ik met veel mensen een kantoor gedeeld, maar het grootste deel van de tijd was dat met Suzanne Hangx. We hebben enorm veel tijd samen doorgebracht en samen gewerkt, gewogd, gestresst, en gelachen. Ook buiten het werk om hebben we veel gezelligheid gedeeld, en op 4 juni zal Suzanne één van mijn paranymphen zijn. Guy Calluy was op 6 juni 2006 getuige bij mijn huwelijk. Op 4 juni zal hij mijn tweede paranymph zijn. Ik weet mij altijd gesteund door mijn beste vriend, met wie ik al zoveel heb meegemaakt rond de speeltafel en waar dan ook. Ook Guy wil ik bedanken voor alle hulp, steun en gezelligheid.

De belangrijkste persoon in mijn leven de afgelopen meer-dan-zes-en-een-half-jaar, wil ik als laatste bedanken. Veya van Noort-Dankers, mijn echtgenote, steun, toeverlaat en grote liefde, ik kan niet meer zonder jou. Jouw troost en liefde hebben mij door alle problemen heen gesleept en met jou heb ik alle blijdschap, enthousiasme en opluchtingen van de afgelopen vier en een half jaar kunnen delen. Veya, bedankt voor alle liefde die je mij gegeven hebt en nog zult geven.

Curriculum Vitae

Reinier van Noort

7 August 1980, Dutch
Laan van Vollenhove 1785, 3706GJ, Zeist, the Netherlands
RnrvnNrt@gmail.com

2003-present	PhD Geology, Research position at the Experimental Rock Deformation (HPT) Laboratory at Utrecht University on the structure and properties of fluid-filled grain boundaries under stress in geological materials
2003-2003	MSc. Geology, Utrecht University Specialisation: Earth Materials Thesis on the surface topology and morphology of forsterite Traineeship at ECN (Petten, the Netherlands) on making rock-type materials out of biomass/waste fly ashes
1998-1999	Propaedeutics Geology, Utrecht University (the Netherlands)
1992-1998	Gymnasium, Marnix College, Ede